

©Copyright 2015

Zhe Xu

Design and Control of an Anthropomorphic Robotic Hand: Learning
Advantages From the Human Body & Brain

Zhe Xu

A dissertation submitted in partial fulfillment of the
requirements for the degree of

Doctor of Philosophy

University of Washington

2015

Reading Committee:

Prof. Emanuel Todorov, Chair

Prof. Joshua R Smith, Chair

Prof. Maya Cakmak (Member)

Program Authorized to Offer Degree:
UW Computer Science & Engineering

University of Washington

Abstract

Design and Control of an Anthropomorphic Robotic Hand: Learning Advantages From
the Human Body & Brain

Zhe Xu

Co-Chairs of the Supervisory Committee:

Associate Professor Prof. Emanuel Todorov

Computer Science and Engineering & Applied Mathematics

Associate Professor Prof. Joshua R Smith

Computer Science and Engineering & Electrical Engineering

According to the cortical homunculus, our hand function requires over one quarter of the brain power allocated for the whole body's motor/sensory activities. The evolutionary role of the human hand is more than just being the manipulation tool that allows us to physically interact with the world. Recent study shows that our hands can also affect the mirror neuron system that enables us to cognitively learn and imitate the actions of others. However the state-of-art technologies only allow us to make cosmetically true-to-life prosthetic hands with cadaver-like stiff joints made of mechanical substitutes. And very few research groups know how to design robotic hands that can closely mimic the salient biological features of the human hand. The goal of our project is to reduce cognitive and physical discrepancy, in the cases where we need a pair of our hands interacting with a different environment remotely. Our project will try to answer the following questions: With the great advance of 3D-printing technologies, and promising new materials for artificial muscles and ligaments, can we design a personalized anthropomorphic robotic hand that possesses all the favorable functions of our very own hand? With such a robotic hand, can we reduce the control space, and establish an easy mapping for the human user to effectively control it? Is it possible to teleoperate the robotic hand to perform amazingly dexterous tasks without force feedback as those surgical robots demonstrated? To answer these questions, we are going to investigate

the design and control of our proposed anthropomorphic robotic hand.

TABLE OF CONTENTS

| | Page |
|---|------|
| List of Figures | iii |
| List of Tables | xii |
| Chapter 1: Introduction | 1 |
| 1.1 Related work | 2 |
| 1.2 Human Hand Taxonomy | 6 |
| 1.3 Inspiration from the Human Brain & Body | 10 |
| 1.4 Telemanipulation of the Anthropomorphic Robotic Hand | 15 |
| Chapter 2: The important Anatomy of the human hand | 18 |
| 2.1 The bones | 18 |
| 2.2 Flexor and extensor tendons | 20 |
| 2.3 The tendon sheaths | 23 |
| 2.4 The biological joints | 24 |
| 2.5 The joint ligaments | 29 |
| Chapter 3: Crocheted Extensor hood | 31 |
| 3.1 Crocheting the extensor hood of the human hand | 32 |
| 3.2 Testing the mechanical properties of the crocheted branches | 34 |
| 3.3 Experimental results and discussion | 37 |
| Chapter 4: Design of the biomimetic finger | 40 |
| 4.1 Design of the artificial finger | 43 |
| 4.2 Dynamics of the artificial joint | 51 |
| 4.3 Actuation system | 55 |
| 4.4 Discussion | 70 |
| Chapter 5: Artificial skin | 71 |
| 5.1 Development of the artificial skin | 73 |

| | | |
|---|---|-----|
| 5.2 | Experimental evaluation | 81 |
| 5.3 | Discussion | 86 |
| Chapter 6: Design of a 3-axis fingertip sensor | | 97 |
| 6.1 | Development of the fingertip sensor | 98 |
| 6.2 | Design optimization of the fingertip sensor | 102 |
| 6.3 | Calibration of an optimized fingertip sensor | 108 |
| 6.4 | A case study – designing fingertip sensors for Phantom robots' manipulation tasks | 112 |
| 6.5 | Conclusion | 116 |
| Chapter 7: Low-cost robotic hand | | 117 |
| 7.1 | Development of the anthropomorphic robotic hand | 117 |
| 7.2 | Modeling of the robotic hand | 125 |
| 7.3 | Performance evaluation of the robotic hand | 127 |
| 7.4 | Conclusion | 130 |
| Chapter 8: Proof-of-concept prototype of the anthropomorphic robotic hand | | 131 |
| 8.1 | The rapid prototyping process of the anthropomorphic robotic hand | 131 |
| 8.2 | Teleoperation of our proposed robotic hand | 137 |
| 8.3 | Performance of the biomimetic robotic hand | 141 |
| Chapter 9: Conclusion and future work | | 157 |
| 9.1 | Contributions | 157 |
| 9.2 | Future work | 161 |
| Bibliography | | 163 |

LIST OF FIGURES

| Figure Number | Page |
|---|------|
| 1.1 The representative, anthropomorphic robotic hand systems developed in the past [1–15]. | 5 |
| 1.2 Branching tenons of the human hand (dorsal side) | 7 |
| 1.3 Human hand taxonomy (adopted from [16, 17]) | 8 |
| 1.4 Prioritized list of household objects from [18] | 9 |
| 1.5 The classification process of four basic grasping postures. (a) Pictures of the human hand grasping 39 objects from the prioritized list [18]. (b) Four basic grasping postures are observed based on the relative positions between the thumb and fingers. | 10 |
| 1.6 The models showing cortical homunculus (exhibition from the Natural History Museum, London). | 11 |
| 1.7 Comparison of the mechanical design between the antique prosthetic hand and the state-of-art robotic hand | 12 |
| 1.8 Comparison of the potential tools used for fabricating the antique prosthetic hand and the state-of-art robotic hand | 13 |
| 1.9 The capabilities of the 3D printing technologies [19–21] | 14 |
| 1.10 Snapshots showing human operators executing dexterous tasks with different master-slave systems [22, 23] | 16 |
| 2.1 The definition of the joints and bones of the human left hand (adopted from [24]). <i>Note:</i> The trapezium bone is shown in red. | 19 |
| 2.2 Schematic drawing showing the extensor and flexor tendons of the human right hand. | 21 |
| 2.3 Schematic drawing showing the important function of the extensor hood mechanism. <i>Left:</i> A simplified and geometric representation of the extensor hood. <i>Right:</i> The two small tendons of the lateral bands glide off from the PIP joint during finger flexion. | 22 |
| 2.4 Schematic drawing showing the bulging process of the tendon sheaths (the pulleys) during finger flexion. <i>Left:</i> Different insertion sites of the tendon sheaths. <i>Right:</i> Mechanical analogy of the bending finger showing the increase in moment arms under the effects of elastic pulleys. | 24 |

| | | |
|------|--|----|
| 2.5 | Schematic drawing showing the regular range of motion of the fingers during finger flexion. | 25 |
| 2.6 | Mechanical analogies of the MCP joint of the human fingers. <i>Left:</i> A ball-socket that allows the closest replica of the MCP joint. <i>Middle:</i> A universal joint that supports axial rotation. <i>Right:</i> An elastic joint that has rigid support in axial direction. | 26 |
| 2.7 | Schematic drawing showing the range of motion of the human thumb. | 27 |
| 2.8 | Complex bone shapes at the carpometacarpal joint of the thumb [24]. <i>Top row:</i> The first metacarpal bone (shown in red) of the human left hand. <i>Bottom row:</i> The shape and location of the important trapezium bone (shown in red). | 28 |
| 2.9 | The mechanical analogy adopted for the explanation of the CMC joint. <i>Top row:</i> The definition of the saddle joint. <i>Bottom row:</i> Different statuses of the saddle joint at the corresponding thumb postures. | 29 |
| 2.10 | Schematic drawing showing the function of collateral ligaments at the MCP joint. | 30 |
| 3.1 | Schematic drawings of the crochet technique. <i>Left:</i> Basic crochet stitches used in our study. <i>Right:</i> Standard crochet symbol chart showing different possible variations of stitch types [25]. <i>Note:</i> The three stitches enclosed in the dashed box were adequate enough to prototype the proposed bionic extensor hood. | 32 |
| 3.2 | The prototyping process of the crocheted extensor hood for the index finger of the ACT hand. | 33 |
| 3.3 | Crocheted extensor hood implemented in the Anatomically Corrected Test-bed Hand (ACT) Hand. <i>Left:</i> Manually positioned ACT hand holding a pen. <i>Right:</i> Snapshots showing the extension motion of the thumb and index finger with the help of crocheted extensor mechanisms. | 34 |
| 3.4 | The complex shape of the extensor hood in the human hand (left index finger) and the samples for testing mechanical properties at different branching locations. <i>Top:</i> Crocheted samples for the tensile tests. <i>Bottom:</i> Variations of merging and branching structures observed in the human hand. SS: String string; T1-B: Type1-branching; SC: Single crochet; T2-B: Type2-branching; DC: Double crochet; TC: Triple crochet. | 35 |
| 3.5 | The preparation process of the tensile experiments. <i>Left:</i> Applying Epoxy on the two ends of the test samples. <i>Right:</i> In order to stabilize the flexible section, paper tapes were applied to both sides of the test examples. | 36 |

| | | |
|------|---|----|
| 3.6 | Example of the three stages of a typical tensile test. <i>Left:</i> The test sample was first loosely clamped at both ends. <i>Middle:</i> The two paper legs were cut before the pulling process started. <i>Right:</i> Pulling finished after the test sample reached its yield limit. | 36 |
| 3.7 | Typical Force-Displacement curves from crocheted samples. <i>Note:</i> Dashed lines pass through the points of corresponding breaking strength. | 37 |
| 4.1 | Comparison of the MCP joint design between the previous and new version of the ACT Hand. (a) Structure of the MCP joint in the previous version of the ACT Hand. (b) Our proposed design of the MCP joint. (c) Location and anatomy of the MCP joint in the human hand. | 42 |
| 4.2 | 3D model of the laser-scanned human index finger. | 44 |
| 4.3 | Components of the artificial index finger. (a) Modular design of the index finger. (b) & (c) Steel rings used to anchor the rim of the crocheted finger capsule. (d) Thermoplastic coated articulated surface providing low-friction surface at the finger joint. | 46 |
| 4.4 | Crocheted ligaments of the artificial MCP joint. (a) Basic crochet type I – chain stitch. (b) Basic crochet type II – single crochet. (c) Hyperbolic shape of crocheted joint ligaments limits the range of motion of the MCP joint of the index finger. (d) Partially assembled index finger with crocheted ligaments attached. | 47 |
| 4.5 | Cross section of the fully assembled MCP joint. <i>Bottom Right:</i> The silicon rubber sleeve and the molds used for its fabrication. | 49 |
| 4.6 | Comparison of the extensor mechanism between the human hand [26], the ACT Hand, and the artificial finger. (a) Design evolution of the tendon hood. (b) Schematic drawing of the pulley system of the artificial finger. (c) Cross-section drawing (A-A) of the tendon structures at the MCP joint for a left index finger (the view is towards the distal aspect of the finger). | 50 |
| 4.7 | Left: Experimental setup. Right: typical trials collected from infrared markers for each finger during perturbations. Note that joint angles of the initial finger postures are 45° at the MCP, 35° at the PIP, and 25° at the DIP. | 52 |
| 4.8 | <i>Top:</i> 3D scatter plot of acceleration vs. velocity and position. <i>Bottom:</i> scatter plots of acceleration vs. position and velocity. All data in this figure are from the artificial finger (unloaded thin). | 54 |
| 4.9 | 3D scatter plot of jerk vs. velocity and acceleration. The light dots are the projection of the data on the bottom plane. | 55 |
| 4.10 | The actuation system of the anthropomorphic robotic finger. | 57 |

| | | |
|------|---|----|
| 4.11 | Model of the human index finger. <i>Frame 0:</i> Fixed frame (palm phalange) <i>Frame 1:</i> Adduction/Abduction frame <i>Frame 2:</i> MCP flexion frame <i>Frame 3:</i> PIP flexion frame <i>Frame 4:</i> DIP flexion frame | 58 |
| 4.12 | Desired and actual tendon excursion for central extensor (A), PIP (B) and DIP (C) tendons for the trajectory tracking task. | 61 |
| 4.13 | Pressure difference (D) behavior of pressurization and depressurization at different voltage levels (V_i). | 63 |
| 4.14 | Pressure difference rate (dD/dt) of pressurization and depressurization at intermediate voltage levels (V_i). Solid lines represent original values and dashed lines represent values predicted by model. Pneumatics incurs a latency of 6-7 msec before reaching its maximum effect. | 64 |
| 4.15 | Comparison between the MuJoCo based simulation model and the physical prototype. (a) 3D Visualization of the kinematic model of the robotic finger in OpenGL. (b) Proposed biomimetic artificial finger. | 65 |
| 4.16 | Comparison of measured and estimated tendon excursion data. | 69 |
| 5.1 | Detachable artificial skin pads attached onto the ACT Hand model. <i>Top right:</i> A side view of the thumb's skeleton with steel pins attached. <i>Bottom right:</i> A back view of artificial skin pads mounted onto the thumb. | 72 |
| 5.2 | Schematic drawing of artificial skin's multi-layered structure (Note: Differently colored regions are not in proportion to the real distributions of those layers.) | 73 |
| 5.3 | Components of the molds used for prototyping ACT Hand's fingertip and palm. 74 | |
| 5.4 | Configuration of the tactile sensor (Tekscan Inc., South Boston, MA) as the 2nd layer of the artificial skin. | 75 |
| 5.5 | Tapered cylindrical frame (index fingertip) functioning as the skeleton the artificial skin. | 76 |
| 5.6 | <i>Top Row:</i> The pictures of the ACT Hand with artificial skin attached. <i>Bottom Left:</i> Small pins attached onto the ACT Hand's thumb. <i>Bottom right:</i> Unique design of the thumb web. | 78 |
| 5.7 | <i>Top Row:</i> Eight sets of skin pads with four different textures (from left to right: stripe, pillar, circle and plain) on two types of skin shapes. <i>Bottom left:</i> Molds for tapered cylindrical skin pads. <i>Bottom right:</i> Molds for hexahedral skin pads. | 80 |

| | | |
|------|---|----|
| 5.8 | <i>Left:</i> Experimental setup. <i>Top right:</i> Two different shapes of the probes: the sphere (10 mm in diameter) and the curved surface (47 mm in radius). <i>Bottom right:</i> Initial test position. <i>Note:</i> The difference between the Phantom and sensel frames. | 82 |
| 5.9 | Examples of the skin pad used in the test. (a) CAD model of a tapered cylindrical skin pad. (b) CAD model of a hexahedral skin pad. | 83 |
| 5.10 | Outputs from the experimental setup. (a) Force reading from the sensel. (b) The probe velocity measured from the Phantom's end-effector. (c) The controlled normal and tangential forces from the Phantom robot. (d) Comparison of the calculated (in sensel frame, along Y-axis) and measured (in Phantom frame, along Z-axis) displacement of the probe along vertical direction. | 85 |
| 5.11 | Comparison of the pre-slip curves between skin pads with/without texture. (a) Probe displacement on hexahedral skin pad with plain surfaces (HPL). (b) Probe displacement on stripe patterned, hexahedral skin pad (HS). <i>Note:</i> Spherical probe was used; The location of the forces are moved from the contact point to the center of the probe for easy reading; δ denotes the change of the vertical displacement. | 88 |
| 5.12 | Schematic drawing showing the advantage of having ridges on pre-slip detection. | 89 |
| 5.13 | Slip-ratio measured on tapered cylindrical skin pads with spherical probe. <i>circle cone</i> stands for circle ridges pattern tested on the cylindrical skin pad. | 90 |
| 5.14 | Slip-ratio measured on hexahedral skin pads with spherical probe. <i>circle square</i> stands for circle ridges pattern tested on the hexahedral skin pad. | 91 |
| 5.15 | Schematic drawing showing the deformation of the three ridge patterns (circle, strip, and pillar) under the same tangential force conditions. <i>Left:</i> Shape of the ridges before the start of deformation. <i>Right:</i> Force analysis of ridges during the deformation process, but before the contact breaks. <i>Note:</i> The direction of the normal forces is perpendicular to the paper surface, but the drawing is omitted for easy reading. | 93 |
| 5.16 | Slip-ratio measured on hexahedral skin pads with curved probe. <i>circle square</i> stands for circle ridges pattern tested on the hexahedral skin pad. | 94 |
| 5.17 | Comparison of tapered and non-tapered fingertip during dexterous manipulation. (a) Tapered fingertip possesses smaller moment arm at distal joints. (b) Hyper-extended, non-tapered fingertip achieving the same task with a larger moment arm at distal joints. (c) Transformation from non-tapered to tapered fingertips. | 95 |

| | | |
|------|---|-----|
| 6.1 | Schematic drawing and force analysis of our proposed fingertip sensor. <i>Top left:</i> Schematic drawing of the fingertip sensor showing relative positions of all components. <i>Bottom left:</i> The picture of a Honeywell force sensor used in this paper. <i>Right column:</i> Beam structure of the fingertip sensor when external force (P) applied at the fingertip. | 99 |
| 6.2 | 3D CAD model of the fingertip sensor. | 101 |
| 6.3 | The electrical wiring diagram of a single FSS sensor. | 101 |
| 6.4 | Varying conditions for design optimization. <i>(a)</i> Detachable fingertip cap for minimizing the disturbance to the pre-loading status. <i>(b)</i> Hanging weight method used for loading/unloading difference forces. <i>(c)</i> Under the same force conditions, six different rotational cases were tested during the experiments. (<i>Note:</i> the red, green, and blue colors were used to label the three FSS sensors.) | 103 |
| 6.5 | Examples of the data collected for hysteresis analysis. (<i>Note:</i> the red, green, and blue data points were collected from the three sensors defined in Fig. 6.4(c), respectively.) | 105 |
| 6.6 | The change of the hysteresis of the proposed fingertip sensor at different testing locations. | 106 |
| 6.7 | Force analysis of the fingertip force sensor. | 108 |
| 6.8 | 72 sets of loading forces applied at different locations on an optimized fingertip sensor for calibration purpose. <i>Note:</i> G_1 and G_2 -type forces are labeled with green and red colors, respectively. | 110 |
| 6.9 | Comparison of applied (blue) and measured (red) normal forces of our proposed force sensor. | 111 |
| 6.10 | Fully assembled fingertip sensors mounted at the end-effectors of four 3-DOF Phantom robots for cooperative manipulation tasks. | 113 |
| 6.11 | Experimental setup of the fingertip sensor and definition of different frames. <i>Top:</i> Labeled pictures of a typical trial illustrating the definition of projected angle, sensor-frame, camera-frame, and important components of the experiment. <i>Bottom:</i> Locations of the three FSRs (\$6/unit) in sensor-frame whose X-Y plane is the radial plane). | 114 |
| 6.12 | Comparison of the contact angles between measured and estimated values in the radial plane. | 115 |
| 7.1 | The 3D-printed 20-DOF anthropomorphic robotic hand. | 118 |
| 7.2 | 3D model of the anthropomorphic robotic hand. | 119 |
| 7.3 | Components of each finger unit. | 120 |
| 7.4 | Two examples of assembling a Snap-On joint. <i>Top row:</i> Assembling a DIP hinge joint. <i>Bottom row:</i> Assembling a MCP ROM-ball on to the finger base. 121 | |

| | | |
|------|--|-----|
| 7.5 | Schematic drawing of two possible cable routing types. (<i>a</i>) A 4-DOF finger with four pairs of antagonistic cables (<i>Note</i> : cables originated from the DIP and PIP finger segments were passing through the center of the cable tubes in the real robotic hand, for better illustration, their routings are drawn explicitly). (<i>b</i>) A 3-DOF under-actuated finger with pulley systems. | 122 |
| 7.6 | The configuration of the tactile sensor as the second layer of the artificial skin. | 123 |
| 7.7 | The actuation system of the robotic hand. <i>Left</i> : the pneumatic control unit. <i>Right</i> : Fully assembled actuation unit. | 124 |
| 7.8 | Moment arms at different joints of the index finger of the robotic hand (data are measured from the 3D CAD model). (<i>a</i>) Moment arms at the DIP joint. (<i>b</i>) Moment arms at the PIP joint. (<i>c</i>) Moment arms at the MCP flexion joint. (<i>d</i>) Moment arms at the MCP abduction/adduction joint. (<i>Note</i> : Flexion and abduction motions have positive angles, flexion; extension and adduction motions have negative angles.) | 125 |
| 7.9 | Modeling of our low-cost robotic hand. (<i>a</i>) Kinematic model of the robotic hand visualized in OpenGL(<i>left</i>) and the model of the tendon paths(<i>right</i>). (<i>b</i>) The thumb extensor wrapping at the CMC joint during the flexion motion. | 126 |
| 7.10 | Full finger motion at 3 Hz. <i>Left\Right</i> : Response of the valve pressure (prs) and length sensor (len) of the MCP extensor\flexor with respect to the command signal. | 128 |
| 7.11 | Time stamps. <i>From left to right</i> : T1 – Event Trigger, command written to the pneumatic value, T2 – Pressure wave arrival, T3 – Index finger MCP movement detected. | 129 |
| 8.1 | The full set of 3D-printed finger segments made of ABS plastic. | 132 |
| 8.2 | Simplified joint capsule composed of crocheted Spectra kite string and laser-cut high strength rubber sheet. | 133 |
| 8.3 | The fully assembled biomimetic hand containing the 3D-printed ABS bones from the scan of cadaveric hand bones. <i>Note</i> : The wrist of the hand is immobilized since it is not the focus of this thesis at this stage. | 134 |
| 8.4 | The elastic pulley system implemented on the palmar side of the biomimetic hand. <i>Left</i> : The flexor tendons of the robotic hand are running underneath the laser-cut, elastic tendon sheaths. <i>Right</i> : Snapshots of a separate finger showing the bulging process of the elastic pulleys during finger flexion. | 135 |
| 8.5 | The fully assembled biomimetic hand incorporated with the electric actuators. <i>Left</i> : The palmar aspect of the anthropomorphic robotic hand. <i>Top right</i> : The lateral view of the robotic hand showing the structure of the thumb web. <i>Bottom right</i> : The MX-12W dynamixel servo. | 137 |

| | | |
|------|---|-----|
| 8.6 | The string-potentiometer based data glove. <i>Right:</i> A disassembled string-potentiometer unit. <i>Middle:</i> The palmar view of the data glove showing the four flexors connected to the thumb, index, middle, and coupled ring and little fingers. <i>Right:</i> The dorsal view of the data glove showing the control inputs from the index finger's PIP joint and the ad/b motion of the thumb. | 138 |
| 8.7 | Snapshots showing the teleoperation process of our proposed anthropomorphic robotic hand. <i>Top row:</i> The index and middle fingers can move independently from the coupled ring and little fingers. <i>Middle row:</i> The precision grasp between the index/middle finger and the thumb. <i>Bottom row:</i> The abduction, adduction, and opposition motions of the thumb. | 140 |
| 8.8 | The four hand postures that can be used to bound the common reach and grasp motions of the human hand (adopted from [27]). | 142 |
| 8.9 | Experimental setups for testing the fingertip forces at four different boundary postures. <i>Note:</i> The joint angles are denoted in the form of (MCP, PIP, DIP). | 143 |
| 8.10 | The mechanical coupling between the fingertip and the load cell. | 143 |
| 8.11 | The relationship between the flexor tendon's forces and fingertip forces at four different finger postures. <i>Note:</i> Data are reported as mean +/- standard deviation. | 144 |
| 8.12 | The bulging process of the tendon sheaths (from Posture 1 as shown in Fig. 8.9) when the flexor tendon force increases. | 146 |
| 8.13 | Labeled pictures showing the differential pulley transmission for ring and little fingers and the locations of the reflective makers. <i>Note:</i> All the marker coordinates were recorded with respective to the forearm frame. | 147 |
| 8.14 | The displacement of the fingertips during 20 repetition of flexion and extension motions. (a) XYZ coordinates data from the ring finger. (b) XYZ coordinates data from the little finger. <i>Note:</i> The tracking data were separately recorded for the ring and litter fingers to avoid marker occlusion and confusion. | 149 |
| 8.15 | The ring fingertip's trajectories projected onto the X-Z plane. (<i>Note:</i> The scatter plot is from the 20 repetitions of the full flexion and extension motions.) | 150 |
| 8.16 | The trajectories of the fingertips during our robotic hand movement. <i>Top:</i> 3D scatter plot of fingertip trajectories. <i>Bottom left:</i> The trajectories of the fingertips projected onto the X-Y plane showing the thumb opposition and adduction/abduction motions. <i>Bottom right:</i> The trajectories of the fingertips projected onto the X-Z plane showing the workspaces of the fingers. | 151 |
| 8.17 | The list of objects used in the grasping tasks during tele-manipulation. <i>Note:</i> All the objects were initially placed on the table. The two objects enclosed in the dashed box are the ones that our robotic hand failed to grasp within four trials due to the flatness of the object, the slippery surface of the table, and limited vision at the grasping site. | 153 |

| | | |
|------|--|-----|
| 8.18 | The classification of grasped objects based on their geometrical types. | 154 |
| 8.19 | The hand taxonomy realized by our robotic hand (<i>Note:</i> see Fig.1.3 for comparison). | 155 |
| 8.20 | Snapshots of our robotic hand performing re-grasp of a whiteboard eraser. | 156 |
| 9.1 | The 3D-printed connector that allows 1-DOF forearm rotation. | 162 |

LIST OF TABLES

| Table Number | Page |
|---|------|
| 1.1 Robotic/Prosthetic hands | 3 |
| 3.1 Comparison of mechanical properties between different crocheted conditions. | 38 |
| 4.1 Physical parameters of the artificial finger skeleton | 45 |
| 4.2 Approximate joint motion limits of the artificial finger | 45 |
| 4.3 Comparison of stiffness & damping for the human and artificial MCP joints | 56 |
| 4.4 Denavit-Hartenberg parameters used in the index finger model | 59 |
| 4.5 Moment arms that the simulator computed in the default posture (in mm) | 67 |
| 5.1 Results of slip ratios measured with spherical probe. | 86 |
| 5.2 Results of slip ratios measured with curved probe. | 87 |
| 6.1 Performance characteristics of the FSS force sensor | 102 |
| 6.2 Specifications of the tested fingertip force sensor | 104 |
| 6.3 Specifications of the optimized fingertip force sensor | 109 |
| 7.1 The joint motion limits of the anthropomorphic robotic hand | 120 |
| 7.2 Comparison of characteristic force behaviors | 128 |
| 8.1 The specifications of the Dynamixel servos. | 136 |
| 8.2 The flexor to fingertip force ratios at different finger postures | 145 |

ACKNOWLEDGMENTS

First and foremost, I thank my advisor Professor Emanuel Todorov for his unwavering, strong, and consistent support through all the years of my Ph.D. life. I benefited greatly from inspiring conversation with him about different design approaches and the freedom he gave me to explore my own interests. His broad interests in robotics and astonishing wisdom of control theories always encouraged me to keep curious and explore more across disciplinary boundaries. Without his support of my research from inception to completion, the prototype of our robotic hand might never have been created.

I am grateful to Professor Joshua Smith's continuous support starting even before he came to UW. He generously helped me to get a short-term internship at the Hoaloha robotics and the upcoming postdoc position at Yale. I thank him for reaching out to me when I needed to find a second home in the CSE department. The underactuation system used in our robotic hand was inspired from a discussion with him.

I must thank Professor Blake Hannaford for his path-breaking work. My initial interest in surgical robotics was inspired by his Raven robot. I benefited significantly from the occasional but intriguing discussion with him.

I wish to thank Professor Ashish Deshpande for his mentoring and friendship. When I first joined the former Neurobotics Lab, we spent many sleepless but productive nights together in the lab for preparing demos of the ACT hand. Later I spent three months in his lab at the UT Austin and benefited from the productive environment there.

I thank Professor Maya Cakmak for providing me the opportunity to try something different besides my main project. Her work on Programming by Demonstration inspired me to extract human hand motions for testing our concept prototype of the robotic hand.

I am also grateful to Professor Charles Kemp for his great mentoring when I started my first robotic project at Gatech. Till now, I still see Healthcare Robotics Lab as my first

robotics home.

I thank Professor Christopher Allan for guiding me during the hands-on cadaver hand dissection and arranging meetings to help me understand the important procedures of post-surgery hand rehabilitation.

I would also like to thank Professor Yoky Matsuoka for introducing me to the field of robotic hand research, and the trust she put into me during the first three years of my Ph.D. life. I am privileged to get the chance to work on the ACT hand and still benefit from our discussion.

My thanks also go to my cohort in the CSE at University of Washington. I have presented parts of my research in our department during the past years. Their feedback and questions challenged me to improve my design and make my research accessible to audiences of varied background.

And I would like to take this opportunity to thank my friends who consciously or unconsciously helped me enrich my Ph.D. life. I want to thank Gerry Chu for all the outdoor adventures we did together. They were my biggest treats after each paper deadline. I also want to thank Anand Yang, Edward Rice and other racquetball and handball players for showing me how they balance academic lives with daily exercise on the court. And I would like to thank Qinghua Ding for all the spirit-lifting lunch discussions during the past four years.

I want to thank my mother, Honglu Liu for making the very first crocheted extensor hood for me. She did not know that her handicraft had eventually helped me investigate the mechanical property of the material on the tensile machine. I own my sustained interest in mechanical design to her and my father Haolu Xu, who showed me the secret of hand function through his brilliant dental work since I was a child.

Last but not least, thank you to Ying Zhang for being a wonderful wife, for serving as the first reader of my drafts, and for bringing up discussion about the origin of robotic research with her enthusiasm in history of science.

DEDICATION

To my dear parents Haolu Xu and Honglu Liu,
To my inseparable twin sister He Xu,
And to my beloved wife Ying Zhang

Chapter 1

INTRODUCTION

Human hands can perform many dexterous grasping and manipulation tasks. Hand *dexterity* is the ability to precisely control movements and forces using all the hand's degrees of freedom to perform a variety of tasks. Examples include the ability to play musical instruments, use chopsticks, gesture, and perform daily tasks such as cooking and writing. Currently, we are far from replicating human hand dexterity in robotic hands.

A number of robotic hands have been designed to meet a variety of goals. Most existing robotic hands meet specific task requirements using state-of-the-art technology; they were not designed as a tool for scientific investigation. For example, since prosthetic hands must be comfortably fitted to humans, they must be made of lightweight materials. In contrast, weight is not a constraint for industrial grippers, which must conform to a specific object's shape to assure a stable and guaranteed uniform grasp. Two types of robotic hands will be discussed in this chapter. First, we will describe *prosthetic hands*, which are designed for comfort, lightweight and ease of control while accommodating societal norms of size and hand appearance. Design goals for these prostheses often emphasize their functional needs. Second, we will examine *dexterous hands*, which work in unstructured environments for applications such as space exploration and personal assistance. These hands often mimic the human hand form, degrees of freedom, and motion patterns. Neither type of robotic hand currently exhibits the robust manipulation abilities of the human hand.

High levels of dexterity are achieved in the human hand due to a combination of hand biomechanics (hardware) and neural controls (software). The benefits of investigating anthropomorphic robotic hands have been widely acknowledged. However, it is also widely accepted that the cost of time and funding on developing a research-oriented, custom-designed anthropomorphic robotic hand is often prohibitive. The control of a robotic hand can be affected by many factors, such as the finger length, the range of motion (ROM) of

the joints, the weight of the robotic hand, or transmission types. Many researchers had to shape their control goals due to the limits of commercially available anthropomorphic robotic hands as even the slightest modification on those off-the-shelf robotic hands could easily result in months of waiting.

For those researchers focusing on the hardware aspects of anthropomorphic robotic hands, it is also challenging to modify the design or improve the functionality of an existing system in a short period of time. This is because each of the design iterations needs to go through the validation of physical tests before any useful information can be collected for planning any improvement. Therefore simulation as a promising tool to help evaluating the performance of robotic hands has been adopted to speed up the design process [28].

Many anthropomorphic robotic hands were designed to be cable-driven [2, 5, 7, 29–33]. This approach has several appealing advantages. On the one hand, it is intuitive to mimic the muscle-tendon mechanism of the human hand with cables and wires; on the other hand, a carefully designed cable-driven system is back-drivable, backlash-free, light weight, and flexible for the robotic hand to choose between being fully actuated and being under-actuated depending on needs of different applications. So far numerous efforts have been put into the development of anthropomorphic robotic hands with cable-driven system. Tremendous progresses have been made, yet the ability of most of the existing robotic hands to perform human-level manipulation tasks remains limited.

In this work, we intend to initiate an investigation of an alternative approach to designing an anthropomorphic robotic hand that is anatomically personalizable with fast fabrication process, low-cost for modification and maintenance, and feasible control through teleoperation.

1.1 Related work

To position our proposed anthropomorphic hand in relation to other robotic hands, we now review representative robotic hands that were designed over the past two decades (see Table 1.1).

Table 1.1: Robotic/Prosthetic hands

| <i>Robotic hands</i> | <i># identical fingers</i> | <i># joints / DOF (Total DOFs)¹</i> | <i>Range of motion</i> | <i>Speed of motion</i> | <i>Activation / transmission method</i> | <i>Types of grasps / manipulation</i> |
|--|----------------------------|--|------------------------|------------------------|--|--|
| Hosmer hook [34] | 2 split hooks | 1/1 (1 DOF) | <human hand | <human hand | body-powered | splitting hook pinch |
| Utah Arm / Liberating / OttoBock [35–37] | 2 | T-1/1, I-1/0, M-1/0 (1 DOF) | <human hand | <human hand | EMG signal driven, DC motor, cable | three-finger pinch |
| USC/Belgrade [38] | 4 | T-3/2, I-3/0.5, M-3/0.5, R-3/0.5, P-3/0.5 (4 DOFs) | <human hand | <human hand | DC motor, cable, linkage | grasp: power & finger tip |
| Harvard SDM [39] | 4 | 4×2/1 (1 DOF) | >human hand | <human hand | DC motor, cable, elastic joints | enveloping grasp |
| Gatech Dusty [40] | 1 | 2/1 (1 DOF) | <human hand | — | DC motor, cable, spring hinge joints | nonprehensile grasp |
| Barrett [41] | 3 | T(Right)-2/1.5, T(Left)-2/1.5, I-2/1 (4 DOFs) | >human hand | ≈1.2×human hand | DC motor, worm drives integrated with cable drive and breakaway clutch | grasp: power & finger tip |
| i-Limb [42] | 4 | T-3/1, I-2/1, M-2/1, R-2/1, P-2/1 (5 DOFs) | <human hand | ≈human hand | DC motors, belt transmission | grip: key, hook, power & precision; grasp: spherical & palmar |
| Southampton [43] | 4 | T-2/2, I-3/1, M-3/1, R-3/1, P-3/1 (6 DOFs) | <human hand | ≈0.22×human hand | DC motor, worm-wheel, lead screw | power grasp, lateral pinch |
| Cyber [7] | 5 | T-4/2, I-3/1, M-3/1, R-3/1, P-3/1 (6 DOFs) | ≈0.22×human hand | ≈0.38×human hand | geared DC motor, lead screw, cable, exensor spring | lateral pinch; grasp: cylindrical, spherical & tripod |
| Univ. of Tokyo Hand [44] | 3 | T(R)-3/3, I-2/2, T(L)-3/3 (8 DOFs) | >human hand | =15×human hand | DC motor, harmonic and bevel gear transmission | grasp: power & finger tip; dynamic manipulation |
| Stanford/JPL [45] | 3 | T-3/3, I-3/3, M-3/3 (9 DOFs) | >human hand | — | DC motor, cable | finger tip grasp |
| DARPA hand [46] | 4 | T-3/3, I-3/2, M-3/2, R-3/2, P-3/2 (11 DOFs) | <human hand | <human hand | DC motor, cable, gear transmission | grasp: hook & power |
| Robonaut [2] | 4 | T-5/3, I-4/3, M-4/3, R-3/3, P-3/1 (11 DOFs) | ≈human hand | <human hand | DC motor, flex shaft, lead screw, cable | grasp: power & finger tip; lateral pinch |
| Naist [6] | 4 | T-4/3, I-4/3, M-4/3, R-4/3 (12 DOFs) | ≈human hand | ≈human hand | geared DC motor, bevel gear | power grasp |
| DLR II [47] | 4 | T-4/4, I-4/3, M-4/3, R-4/3 (13 DOFs) | >human hand | =3×human hand | DC motor, belt, harmonic drive, bevel gears | grasp: power & finger tip; lateral pinch |
| Utah/MIT [1] | 4 | T-4/4, I-4/4, M-4/4, R-4/4 (16 DOFs) | <human hand | ≈1.82×human hand | pneumatic actuator, cable | finger tip grasp /manipulation |
| Gifu III [3] | 4 | T-4/4, I-4/3, M-4/3, R-4/3, P-4/3 (16 DOFs) | ≈human hand | ≈1.35×human hand | DC motor, gear transmission, linkage mechanism | power grasp |
| UB III [32] | 4 | T-3/4, I-4/4, M-4/3, R-4/2, P-4/3 (16 DOFs) | <human hand | ≈0.51×human hand | DC motor, cable, helical spring | grasp: power & finger tip |
| Shadow [4] | 4 | T-5/5, I-4/3, M-4/3, R-4/3, P-4/3 (17 DOFs) | ≈human hand | ≈0.5×human hand | air muscle, cable and spring | grasp: finger tip & power |
| Keio [5] | 4 | T-4/4, I-4/4, M-4/4, R-4/4, P-4/4 (20 DOFs) | ≈human hand | ≈2×human hand | ultrasonic motors, elastic elements, cable | grasp: power & finger tip; lateral pinch |

¹T, I, M, R, and P denote thumb, index, middle, ring and, pinky(little) finger, respectively.

1.1.1 Prosthetic Hands

The most frequently used prosthetic hand, a hook-and-cable device designed over a century [43] ago, has only one body-powered degree of freedom. A cable is connected to another part of the body to open/close the hook. Hospitals and insurance companies often provide amputees with these prosthetics at little or no cost. Other prosthetic hands emphasize aesthetics but lack a single degree of freedom [48]. Sophisticated prosthetic hands have one degree of freedom that can be controlled by electromyographic (EMG) signals from the stump [35–37].

The most recent research has focused on developing more functional hands [7, 42, 43, 46]. For example, the i-limb prosthetic hand contains more than 1 DOF and is widely used by amputees. Its popularity shows that amputees desire to have more functional robotic appendages even though they lack the control of human hands. Another critical factor for improving control fidelity is sensory feedback capabilities. Liberating Technologies and i-Limb Hand employ vibration-based sensory feedback that indicates when fingers are experiencing a load [36, 42].

An ideal prosthetic hand would be one that allows natural control through "thoughts" of moving the fingers. Recent studies enable monkeys to control the 3D movement of a robotic arm to achieve self-feeding tasks [49, 50]. Over thirty human arm/hand amputees have received nerve reinnervation surgery to rewire the peripheral nerves that used to go into the hand/arm to the chest muscle instead [51]. The signals amplified by the natural muscle can then be tapped into with surface EMG for prosthetic arm/hand control.

1.1.2 Dexterous/Anthropomorphic Hands

The need for robust and dexterous robotic hands extends to applications such as space exploration and personal assistance. Space exploration entails constant repair of the space station and exposure to environments often dangerous for humans and therefore benefits from robotic help. Personal assistants, such as a robotic arm on a wheelchair or a domestic robot, will soon fetch objects in the house for people with disabilities [40].

Most hand/prosthetics assume a human hand shape because it is so versatile (see

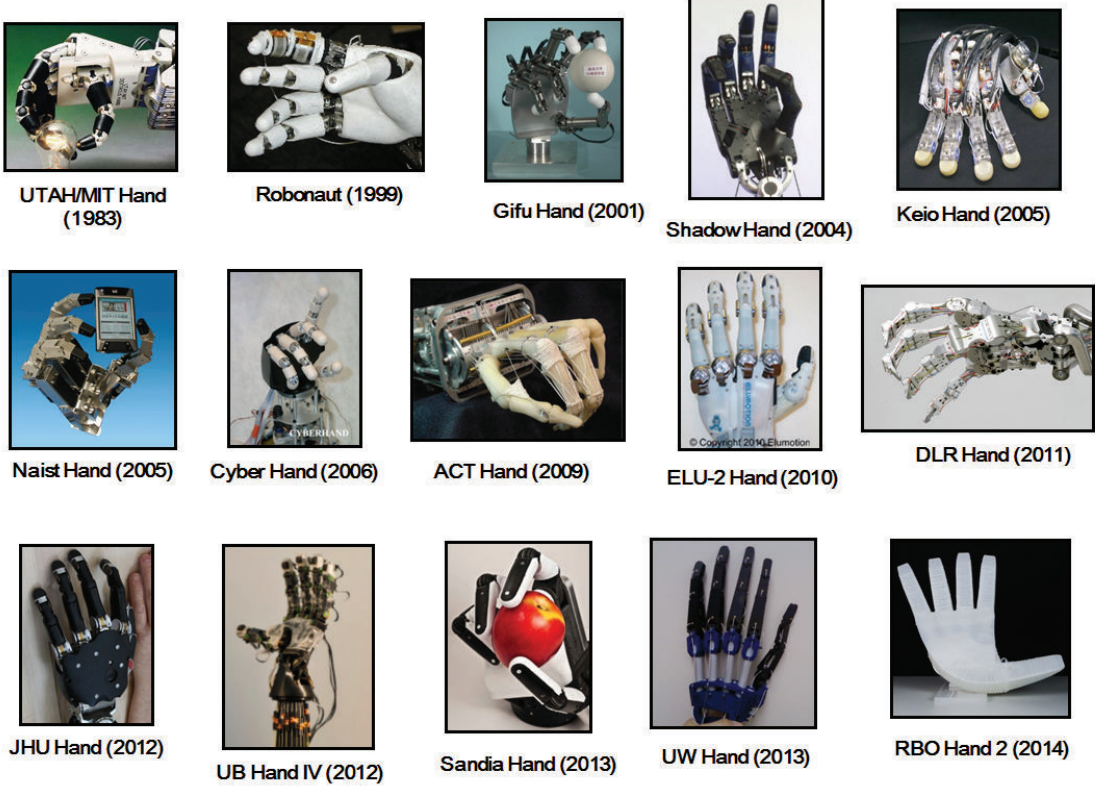


Figure 1.1: The representative, anthropomorphic robotic hand systems developed in the past [1–15].

Fig.1.1). Several important features have been achieved in these anthropomorphic hands, including high degrees of modularity [47], build-in actuators [3,5,6,47], low weights [3,5,32], extra palm DOFs [2,4] and high speed finger motion [1,3,5,47], and 3D-printed with low-cost [13,14].

It is difficult to design a useful, versatile, and robust anthropomorphic robotic hand. When building one, decisions must be made about the number of fingers, joints, DOFs, range of motion, speed, etc. These decisions are constrained by space and weight considerations. Sophisticated controllers must then be able to handle the hand to produce dexterous movements. Most anthropomorphic hands do not demonstrate human levels of dexterity and dynamics even as a preprogrammed sequence. It is likely that hardware specifications,

selected before the hand is built, make it difficult to implement dexterous behavior and that it is inherently difficult to control high DOF systems in a meaningful way. There is also a lack of understanding about how humans realize dexterity both biomechanically and neurologically.

A current trend is to build simpler hands with only a few actuators, augmented by smart mechanisms and passive compliance. For example, BarrettHand [52], one of the most widely used robotic hands in research, attempts to produce robust grasps while providing some versatility [41]. Harvard SDM hand [39] and Gatech Dusty manipulator [40] have only 1 DOF but can grasp a wide range of objects. RBO Hand 2 is made of low-cost compliant materials, and can be pneumatically actuated [15]. The under-actuation in these hands reduces their overall size, weight and complexity of usage. Their mechanical structures and joint compliance allow for grasping objects of different size and shape in unstructured environments without sophisticated controls. However, the ability of these hands to execute human-level manipulation tasks remains limited.

1.2 Human Hand Taxonomy

The dimensionality of the grasp/manipulation space of the human hand could be very large. Based on individual differences in compliance, biomechanics, kinematics, and neuromuscular control strategies, numerous hand postures could be chosen for picking up the same object. Therefore it is impractical to design a universal anthropomorphic robotic hand that can duplicate all the possible hand functions. In fact, it has been found that our human hands also use a small number of key synergies in most of grasps [53]. Hand synergy allows a group of different hand muscles to be evoked at the same time and demonstrates biological couplings resulted from the formation of branching tendons as shown in Fig.1.2.

Thus, before designing and prototyping any anthropomorphic robotic hand, it is crucial to investigate the taxonomy of the human hand and make sure to take into consideration of those essential hand postures. In this way, a reasonable set of design goals could be determined. And this will not sacrifice the dexterity of the resulted robotic hand.

meanwhile this by no means suggests the resulting robotic hand would have limited

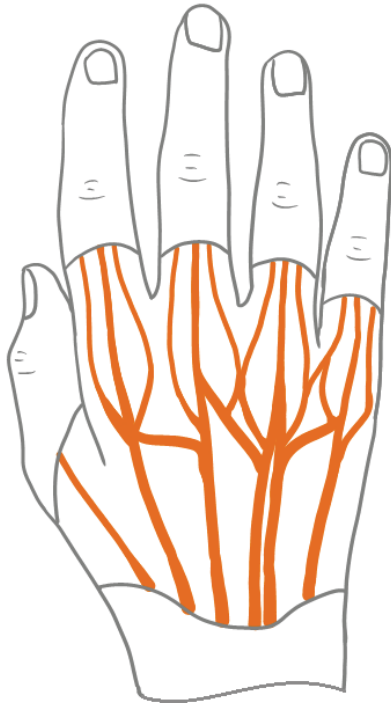


Figure 1.2: Branching tenons of the human hand (dorsal side)

dexterity.

As shown in Fig.1.3, sixteen hand postures are summarized by Cutkosky [16] as the basis for all the common human grasps. It is interesting to note that as the weight and size of the object getting smaller, the grasping sites are gradually moving from the palm to the fingertips. Regarding the common household objects, Kemp's group statistically generated a list of 43 items prioritized by 8 Amyotrophic lateral sclerosis (ALS) patients for robotic retrieval [18]. This list could be used as a reference for answering the question of what types of grasps are most important for people with impaired manipulation ability. Surprisingly, most of the objects from the list could be picked up by using only four basic grasps. That means the important hand postures can be further reduced from 16 to 4 when the environment is bounded by the common household settings.

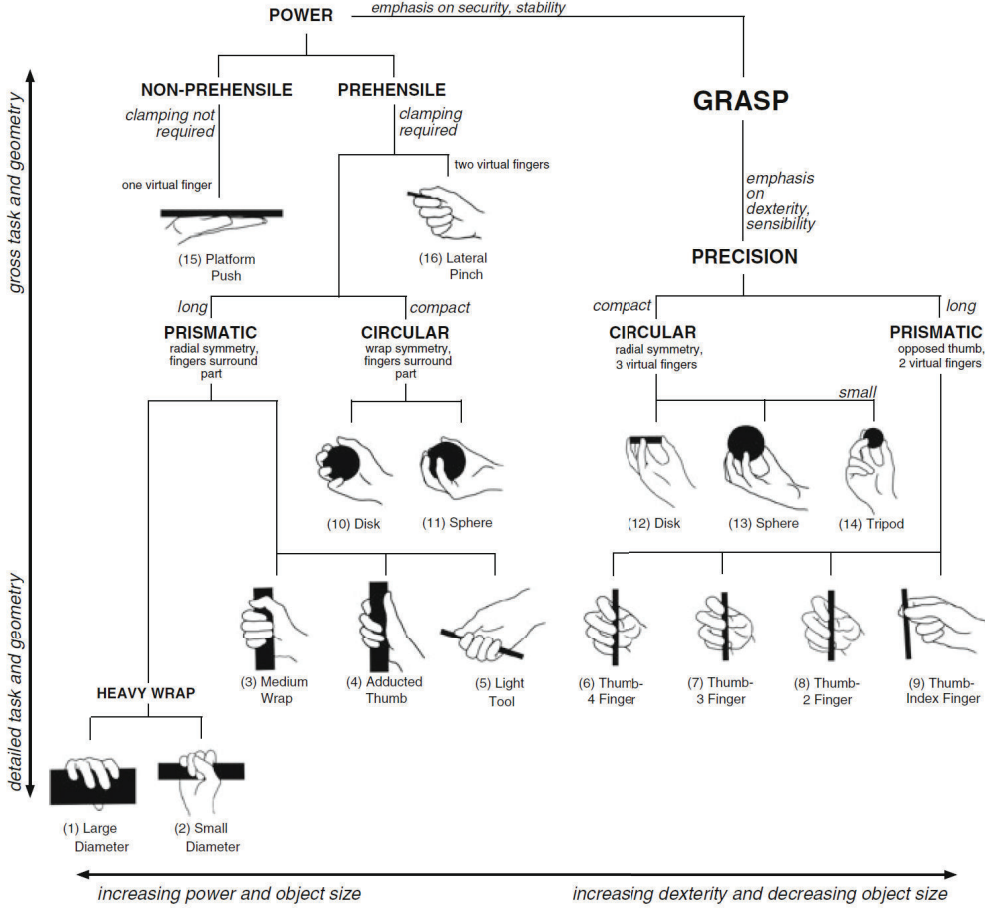


Figure 1.3: Human hand taxonomy (adopted from [16, 17])

Similarly, the anthropomorphic robotic hand we propose will be good at performing a subset of grasp/manipulation tasks that are regarded as essential functions under certain circumstances such as in health care, space exploration, and prosthetics. For different applications, various subsets of the robotic hand motions can also be programmed. For example, it can hold a key to unlock a door and pick up a single pill from the floor, both functions crucial to a person who uses/controls a pair of prosthetic/robotic hands in various scenarios. In addition to performing grasping tasks, we are also interested in testing our proposed anthropomorphic robotic hand in the dexterous manipulation tasks. Particularly, it is of our interest to investigate the fine manipulation of small and light objects during

| Rank | Object Class | Image | Rating Mean | Rating Stdev. | Weight (grams) | Max size (cm) | Rank | Object Class | Image | Rating Mean | Rating Stdev. | Weight (grams) | Max size (cm) |
|------|---------------------|-------|-------------|---------------|----------------|---------------|------|-----------------------|-------|-------------|---------------|----------------|---------------|
| 1 | TV Remote | | 6.64 | 0.57 | 90 | 18 | 22 | Credit Card | | 4.96 | 2.37 | 5 | 8.5 |
| 2 | Medicine Pill | | 6.36 | 1.55 | 1 | 2.2 | 24 | Medicine Box | | 4.88 | 1.88 | 25 | 10 |
| 3 | Cordless Phone | | 6.28 | 1.31 | 117 | 15 | 24 | Bill | | 4.88 | 2.26 | 1 | 13.5 |
| 4 | Prescription Bottle | | 6.08 | 1.31 | 25 | 7 | 26 | Straw | | 4.80 | 2.22 | 1 | 20 |
| 4 | Fork | | 6.08 | 1.12 | 39 | 18 | 26 | Magazine | | 4.80 | 2.02 | 206 | 27.5 |
| 6 | Glasses | | 6.00 | 1.53 | 23 | 14 | 28 | Plastic container | | 4.72 | 2.16 | 49 | 13 |
| 7 | Toothbrush | | 5.96 | 1.81 | 15 | 19 | 29 | Newspaper | | 4.60 | 2.16 | 247 | 31 |
| 8 | Spoon | | 5.92 | 1.19 | 38 | 17 | 29 | Non-disposable bottle | | 4.60 | 2.00 | 709 | 20 |
| 9 | Cell Phone | | 5.88 | 1.69 | 76 | 9 | 31 | Pants | | 4.53 | 2.47 | 539 | 100 |
| 10 | Toothpaste | | 5.72 | 1.84 | 160 | 20 | 31 | Shirt | | 4.53 | 2.47 | 229 | 66 |
| 10 | Book | | 5.72 | 1.46 | 532 | 24 | 33 | Wallet | | 4.48 | 2.33 | 116 | 100 |
| 10 | Hand Towel | | 5.72 | 1.46 | 65 | 58 | 34 | Small Pillow | | 4.44 | 2.08 | 240 | 38 |
| 13 | Mail | | 5.60 | 1.98 | 22 | 24 | 35 | Socks | | 4.40 | 2.08 | 41 | 23 |
| 14 | Cup / Mug | | 5.56 | 1.76 | 267 | 12 | 36 | Hairbrush | | 4.36 | 2.46 | 100 | 24 |
| 15 | Soap | | 5.44 | 2.08 | 116 | 9.5 | 37 | Can | | 4.32 | 2.08 | 350 | 6.4 |
| 16 | Disposable bottle | | 5.40 | 1.66 | 500 | 13 | 38 | Coin | | 4.16 | 2.51 | 6 | 2.5 |
| 17 | Shoe | | 5.36 | 1.98 | 372 | 30 | 39 | Walking Cane | | 3.76 | 2.47 | 1140 | 94 |
| 17 | Dish Bowl | | 5.36 | 1.66 | 154 | 13 | 40 | Wrist Watch | | 3.52 | 2.35 | 86 | 10 |
| 19 | Keys | | 5.28 | 2.28 | 24 | 8.5 | 41 | Scissors | | 3.40 | 2.33 | 25 | 14 |
| 20 | Dish Plate | | 5.24 | 1.85 | 182 | 18 | 42 | Purse / Handbag | | 2.84 | 2.29 | 380 | 24 |
| 21 | Pen / Pencil | | 5.04 | 2.13 | 3 | 14 | 43 | Lighter | | 2.04 | 1.99 | 91 | 6 |
| 22 | Table Knife | | 4.96 | 1.95 | 76 | 24 | | | | | | | |

Figure 1.4: Prioritized list of household objects from [18]

which zero or very few wrist or arm motions are required. In those tasks, success often relies on the execution of a series of highly repetitive hand motions. For instance, the finger motions used to open the lid of a medicine bottle are collaboratively executed between the three dexterous fingers (thumb, index, and middle fingers). In order to validate our design efficacy, a subset of the grasps we are going to use for testing our proposed robotic hand will be extracted from Fig.1.3 based on their priorities ranked by the object list (see Fig. 1.4).

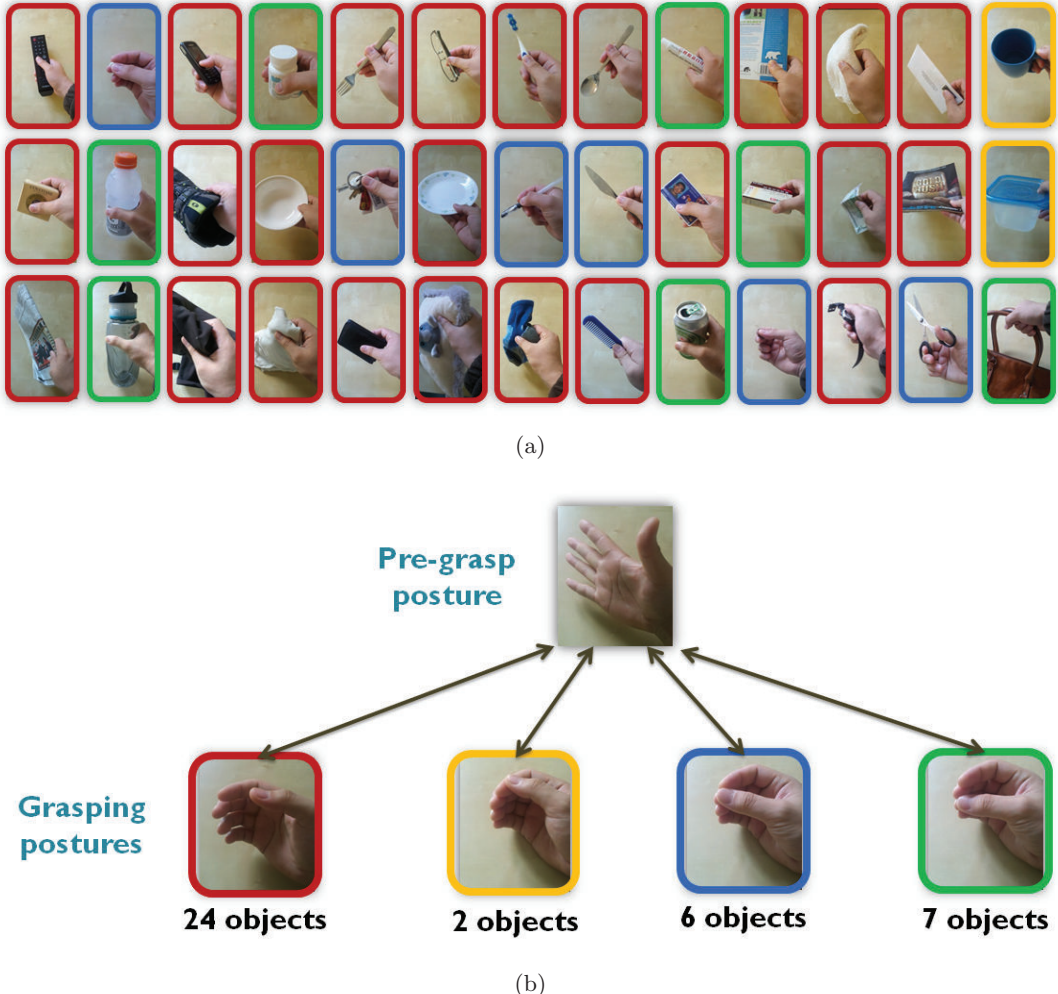


Figure 1.5: The classification process of four basic grasping postures. (a) Pictures of the human hand grasping 39 objects from the prioritized list [18]. (b) Four basic grasping postures are observed based on the relative positions between the thumb and fingers.

1.3 Inspiration from the Human Brain & Body

The cortical homunculus [54] is what a human being would look like if our bodies were built in proportion to the percentage of our motor/sensory cortex mapped to control and feel them. As shown in Fig.1.6, the disfigured human body has a pair of huge hands that account for over 25% of the whole body. According to this homunculus, the functionality



(a) Motor homunculus

(b) Sensory homunculus

Figure 1.6: The models showing cortical homunculus (exhibition from the Natural History Museum, London).

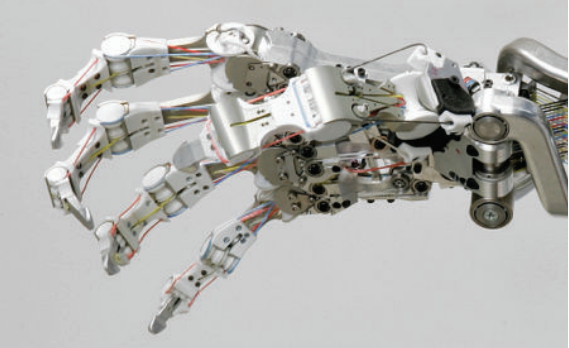
(including both the sensory and motor) of the human hand requires a significant amount of the brain power.

In order to understand how the human brain can smoothly control our hands, many research efforts have been devoted to decoding the electroencephalography(EEG) signals, assuming that the corresponding brain signals for the motor skills can be reliably extracted for controlling prosthetic hands. We argue that solving this problem is equally difficult as investigating any sub-category of artificial intelligence. If we could successfully isolate the grasp/manipulation problem from the rest of the cortical functions and eventually learned everything about it. This would mean that over one quarter of the brain signals from the motor/sensory region could be decoded. Then similarly we should be able to understand the rest of the cortical functions by using divide and conquer method. However, even the most advanced and accurate chronic electrode implants are constantly facing the scaring and biocompatibility issues. Therefore, invasive methods though accurate, may not be suitable solutions for any long-term investigation of brain signals.

While it is challenging to achieve human-level dexterity before we can fully understand how human brains control our hands, it is reasonable to relax the problem and ask whether we can first harness the brain power of human users to teleoperate a robotic hand. In



(a) Prosthetic hand (late 1800s, exhibition from the London Science Museum)



(b) The DLR hand (2011) [10]

Figure 1.7: Comparison of the mechanical design between the antique prosthetic hand and the state-of-art robotic hand

this way, the critical problem becomes how to design the mapping between the user and the anthropomorphic robotic hand so that the human user could easily and seamlessly synchronize his/her control signals to the robotic hand. The key of the success lies in the design of the mapping mechanism which involves both the hardware and software.

The software solution of the mapping could be as simple as the combination of a series of temporally represented joint angles of the hand. If the ultimate goal is to control a pair of anthropomorphic robotic hands remotely, the closer we can design such a robotic hand to match the properties of the human operator's hand, the better chance that the human operator could easily control it. In other words, the proposed robotic hand also needs to be personalized, because an easy mapping for one user to control an anthropomorphic robotic hand could be extremely difficult for another person, even if both of them could control their own biological hands effortlessly. The neuromuscular control strategies, the compliance, and biomechanics of our own hands could all be very different among people, therefore the previously established motor/sensory mappings are subject to any subtitle changes.

For the hardware part, we have not seen fundamental paradigm shift in our ways to physically duplicate the biological counterparts of the human hands. As shown in Fig.



(a) A typical blacksmith workshop (by Alper Orus, 2013) [55]



(b) Rapid prototyping tools with affordable prices [56–58]

Figure 1.8: Comparison of the potential tools used for fabricating the antique prosthetic hand and the state-of-art robotic hand

1.7, the mechanical complexity of the state-of-the-art robotic hand developed in 2011 is very similar to that of the prosthetic hand manually fabricated in 1800s, except for the great advance in the technology of electric motors. However, the tools used during the fabrication process can be very different (see Fig. 1.8(a)). Yet the structure of these hands



Figure 1.9: The capabilities of the 3D printing technologies [19–21]

are drastically different from our biological counterparts. Compared to the past, the modern manufacturing methods enable us to fabricate parts in a more efficient and accurate way, but won't be able to help us achieve a prosthetic arm/hand system that both look and work exactly like our lost one.

Our understanding of the biological structures has far exceeded our ability to replicate them. Current bio-inspired approaches are still trying to mechanize the biological features with conventional mechanical elements such as hinge and gimbal joints. As shown in Fig. 1.1, The finger structure of these robotic hand were generically designed based on minimizing the industrial robot. Although these standard designs can mimic the kinematic behavior of a human joint, they do little to illuminate the salient features that make the human hand irreplaceable for many dexterous tasks. Despite the advances in technology and our seeming prowess in collecting and processing big data, the modern robots still could not outperform nature's solutions in terms of agility, adaptability, fault-tolerance, and energy-efficiency, which are the essential goals of biomimetics. It is therefore necessary to develop biomimetic robotic hand based on accurate physiology in order to quantitatively identify these characteristics.

Hannaford's group has pioneered the design of bio-robotic arm by developing a robotic arm system that is both kinematically and dynamically accurate and can be controlled by artificial muscles through neural network in real time [59].

In recent year, a variety of rapid prototyping tools have been developed to make 3D-printed parts personalizable, strong, durable, and accurate (see Fig. 1.8(b)). By using 3D printing, or direct metal laser sintering, we can now print various parts ranging from prosthesis nose, an exhaust turbine, to a component for surgical robot as shown in Fig. 1.9. The technology allows us to adopt a compelling alternative to conventional mechanical parts by directly copying the unique shapes of human bones. Printed with suitable materials, a resulting biomimetic design could reduce the total number of individual components, achieving an elegant design.

1.4 Telemanipulation of the Anthropomorphic Robotic Hand

Due to the high dimensionality of the grasping space, the control of anthropomorphic robotic hand has been always challenging. Various grasp planning algorithms were developed for both force-closure grasp [28] and dexterous hand movements [60, 61]. However, most of those algorithms were only valid in simulated environments.

In contrast to the development of fully autonomous robotic hand system, the control of prosthetic hand/arm inherently requires the control from human operator. For instance, the amputee patient who recovered after a targeted reinnervation surgery could naturally control her prosthetic arm by using the Electromyogram (EMG) signals extracted from her chest muscles [62]. More recently, researchers have successfully demonstrated that a 7-DOF prosthetic limb can be controlled by a paralyzed patient through two intracortical microelectrode arrays that were directly implanted in the motor cortex of her brain [63]. In spite of their promising results, challenging problems still exist to be resolved. It was reported that the glial scar tissues progressively formed around the array of electrodes can silent the signals only after six weeks of the implantation [64]. Because the chronically implanted devices can cause the foreign body response in the surrounding brain issues that eventually results in degrading performance of the electrode arrays [65]. In addition, the expensive reinnervation surgeries could only extract a limited number of control signals from the intact peripheral nerves. After all, those methods are restricted by the impaired human limb and mainly developed for helping amputee patients to recover partial functions of their lost limbs. In the case of finding a suitable approach to control an anthropomorphic

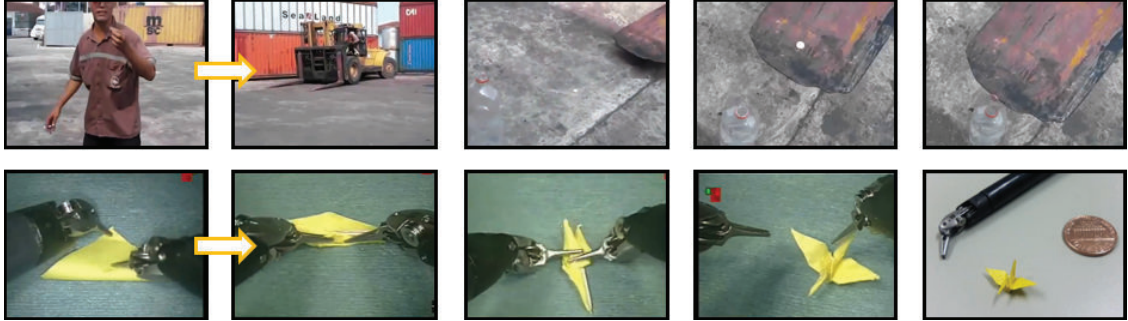


Figure 1.10: Snapshots showing human operators executing dexterous tasks with different master-slave systems [22, 23]

robotic hand that is not intended for prosthesis, intact human hand can be a great resource for extracting fine motor control signals.

It was reported that human operators are only capable of controlling a limited number of degrees of freedom (DOFs) simultaneously (3 DOFs from [66]). However with a smaller number of controllable DOFs and sufficient amount of training, human operators can often establish reliable mappings for different teleoperated master-slave tasks and repetitively execute various tasks with extraordinary precision and dexterity. As shown in Fig. 1.10 (snapshots from the top row), a skilled driver could operate an over-sized forklift to flip a \$0.25 coin from the ground and put the coin into a bottle in about one minute. Using a detached console, a trained surgeon could easily fold a \$ 0.01-size origami with a da Vinci ® surgical robot in a few minutes as well. Surprisingly, many of these successfully demonstrated tasks do not rely on force feedback, but only depend on vision and previous experiences of the human operators.

Although the above two applications are very different from each other, their working processes can be clearly divided into a number of stages during which certain control patterns are either repetitively or consecutively executed (see the snapshots in Fig. 1.10). This observation suggests when it comes to teleoperating a manipulation (telemanipulation) task, as long as the main task can be divided into a series of the consecutive sub-tasks(hand postures/motions) which requires a smaller number of simultaneously controlled DOFs, we

should expect to receive comparable control results from trained human operator as well. In addition, depending on the goal of the task, the separate sub-tasks could either be different from or identical to one another. For instance, the repetitive hand motion used for opening the cap of a bottled water can be divided into several identical hand twisting motions. In other cases like grasping a pen and reorienting to the writing-ready position, the actions require at least three different hand movements, namely prismatic power grasp, in-hand transition grasp, and three-finger grasp. The sub-tasks could be determined according to the definition of different grasps in the hand taxonomy. If the key grasps categorized from hand taxonomy could be organically stitched into a fluid hand movement via a series of transitional postures/motions, many useful tasks could be easily programmed into a robotic hand system.

Therefore we propose to develop an anthropomorphic robotic hand aiming for better compatibility between human cognition and the physical reality of the robotic hand. For example in the two cases we mentioned earlier both the forklift driver and the surgeon who sit behind the different control consoles need to mentally and physically map their hands/bodies' motor skills onto the machinery/instruments' end-effectors that are very different from their biological counterparts. Our goal is to shorten this gap between mental and physical patterns, in the cases where we need a pair of our hands interacting with a different environment remotely. Our project will try to answer the following questions: Can we personalize the end-effector so that it possess all the favorable functions of our very own hand? With such a robotic hand, can we reduce the control space and establish an easy mapping for the human operators to effectively control it? Is it possible to teleoperate the robotic hand to perform dexterous tasks without force feedback as well? Solving these problems will lead us to a paradigm shift in the design of anthropomorphic robotic hand. We will have robotic hands just like the hands of our own with which we have been learning to interact with the surrounding world since we were born, eliminating the hard process of matching with mechanical substitutes.

Chapter 2

THE IMPORTANT ANATOMY OF THE HUMAN HAND

From anatomical point of view, the human hand is composed of bones, joints, ligaments, tendons, muscles, nerves, blood vessels, and layered skin. With our current technologies, we are not able to copy 100% of the human hand with self-healing materials. However we should still be able to directly harvest the wisdom of nature with the help of 3D-scanning and printing technologies, and replicate a subset of these important features in the design of anthropomorphic robotic hands.

Instead of examining the structure of the hand directly from a hand surgeon's perspective, important features of the human hand should be translated into an engineering language so that roboticists can better understand what are the important things to mimic when designing their robotic hands.

In the following sections, we are going to identify the important anatomical features that shape the function of human hand from the following aspects: the bones, flexor and extensor tendons, tendon sheath, biological joints, and joint ligaments,.

2.1 The bones

As shown in Fig. 2.1, the human hand is composed of 27 bones containing 8 tightly packed small wrist bones. A joint is defined as the location where two bones meet. It is of our interest to understand the joint mechanism that enables movement, so the wrist bones are not in scope of our investigation at this stage. Each finger consists of three phalanges and one metacarpal bones. The thumb is an exception, it only has two phalanges besides the metacarpal bone. But the opposable thumb accounts for a big portion of the entire hand function. The trapezium bone located at the base of the thumb has been found to be the critical component that enables the thumb opposition (labeled in red in Fig. 2.1). Together with the thumb's metacarpal bone, they form the carpometacarpal (CMC) joint

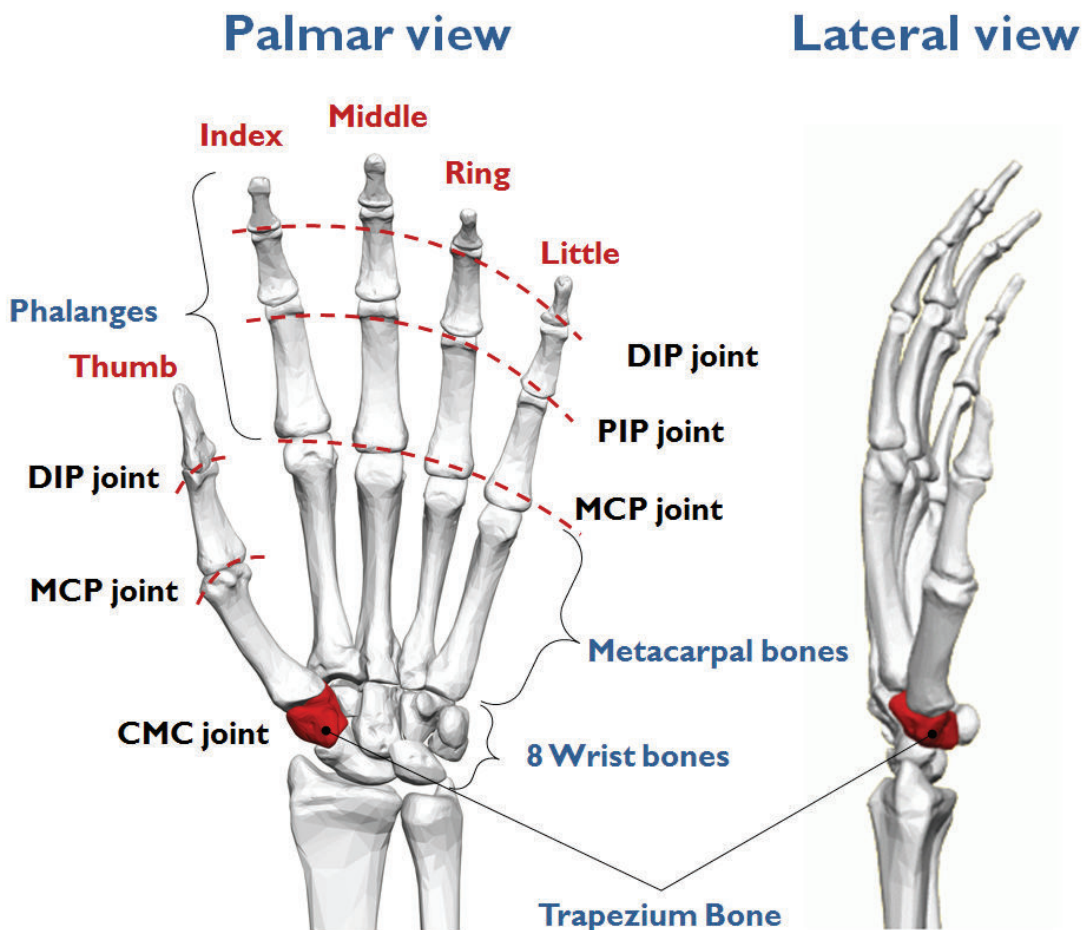


Figure 2.1: The definition of the joints and bones of the human left hand (adopted from [24]).
Note: The trapezium bone is shown in red.

of the thumb. The metacarpophalangeal (MCP) joints are formed by the connection of phalanges to the metacarpals. The MCP joint works like a ball-joint when the finger bends, straightens and wiggles from side to side. Depending on the distance to the MCP joint, there exist two more types of joints, namely, the proximal interphalangeal(PIP) joint and distal interphalangeal(DIP) joint. Based on this definition, the thumb only has one DIP joint between the two thumb phalanges.

2.2 Flexor and extensor tendons

There are two groups of tendons in the human hand. Named according to the function of their contraction motion, the ones straightening the fingers are called extensor tendons, the ones bending the fingers are called flexor tendons. The contraction motions of the tendons originate from the corresponding muscle groups located in the forearm. If we treat the muscles as the actuators that output contraction forces, the tendons of the hand serve as the transmission system that smartly partitions the forces and smoothly delivers torques to each finger joint. As shown in Fig. 2.2, starting from the wrist, the extensor tendons branch out and have multiple insertion sites on the dorsal side of the finger bones. On the other side, after passing through the carpal tunnel, the flexor tendons travel through a series of pulley-like tendon sheaths grown onto the palmar side of the bones and eventually insert at the base of the DIP and PIP joints. The collaborative motions of the two tendon groups make fluent hand movement possible.

The large muscle groups that directly connect to the central branch of the flexor and extensor tendons are called extrinsic muscles. Most of them originate from the elbow and have muscle bellies located in the the forearm. Different groups of the muscles help to realize a subset of hand movements ranging from twisting the wrist to bending the fingers. However there also exist several smaller muscle groups called intrinsic muscles. The majority of these small muscles start from the wrist of hand and connect to the thinner branches of the extensor tendons of each finger near the MCP joint. Most of their muscle bellies are slim enough to reside in the gap between the two adjacent metacarpal bones. One important function of these intrinsic muscles is to stabilize the finger joints during various hand activities.

Most of our daily tasks involving hand motions require the contraction of strong muscles connecting to the flexor tendons. However during this process, the extensor tendons also work as a breaking system that constantly regulates the motion of fingers. The functionality of the breaking system relies on a fibrous structure known as the extensor hood. The extensor hood is a thin, complex, and collagen-based web structure that directly wraps around

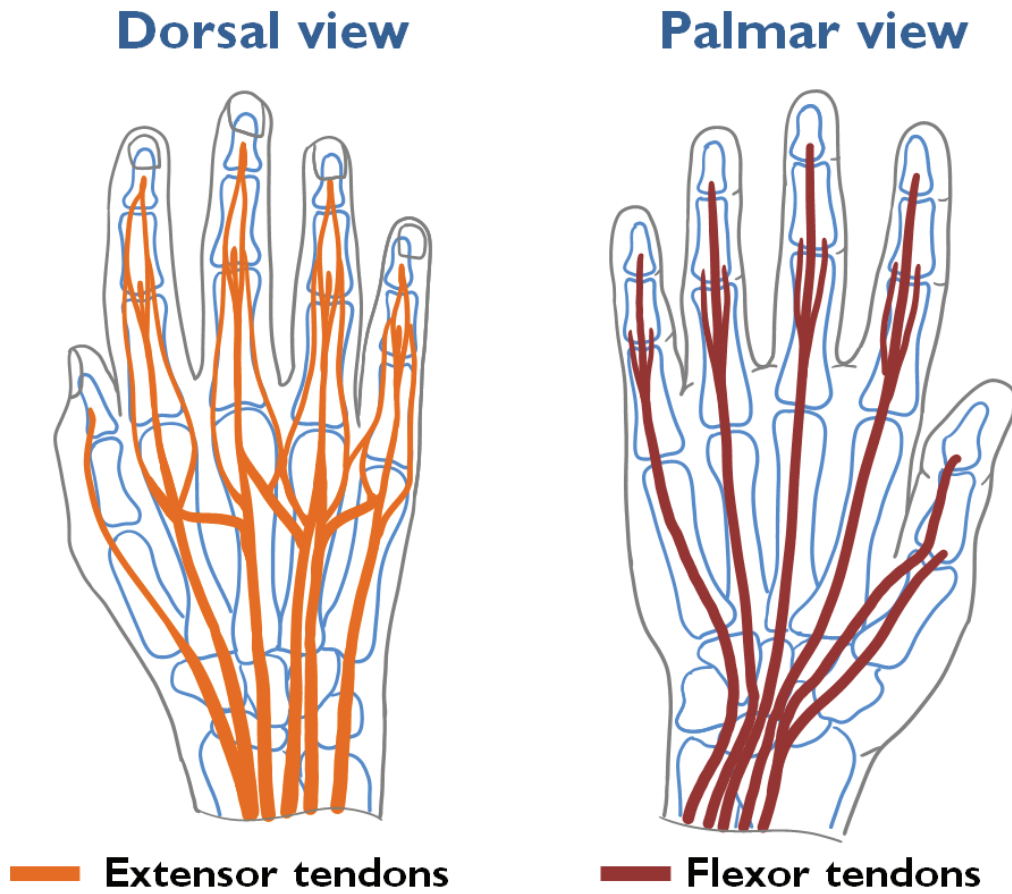


Figure 2.2: Schematic drawing showing the extensor and flexor tendons of the human right hand.

the finger phalanges from the dorsal side. Its structure can be geometrically represented by a two-layer web as shown in Fig. 2.3.

The first layer of the extensor hood is called lateral bands. It has an insertion site at the base of the DIP joint, and split into two small tendons across the PIP joint. This splitting mechanism smartly regulates the breaking forces at the PIP joint based on different status of the finger during its bending process (see Fig. 2.3). As shown in the lateral view, when the finger straightens, the two small tendons are above the rotation axis at the PIP joint

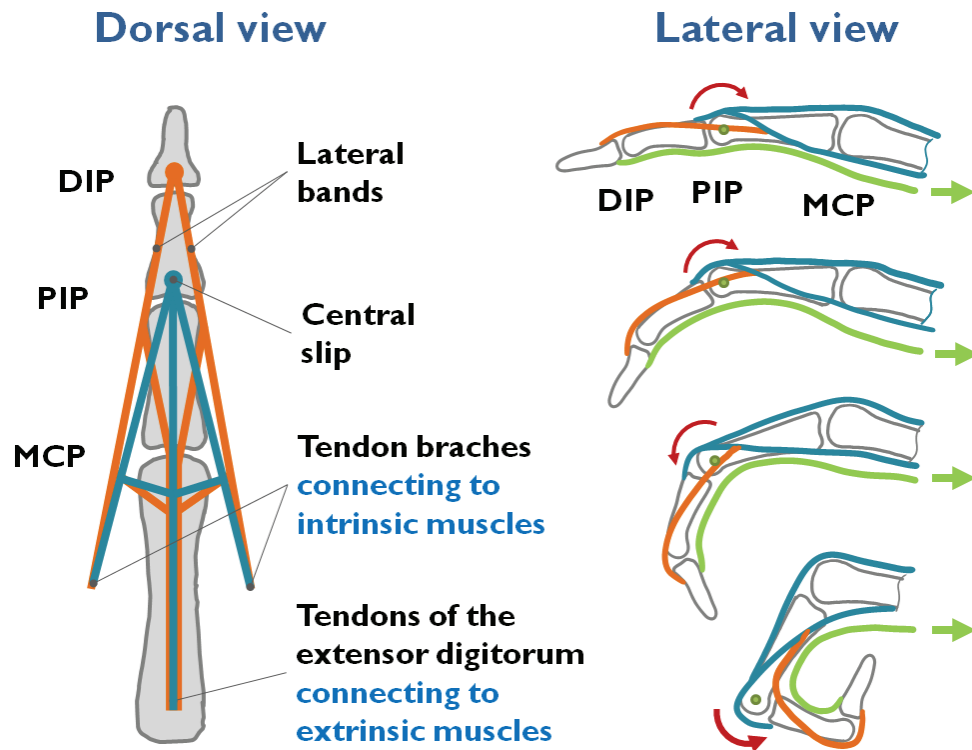


Figure 2.3: Schematic drawing showing the important function of the extensor hood mechanism. *Left:* A simplified and geometric representation of the extensor hood. *Right:* The two small tendons of the lateral bands glide off from the PIP joint during finger flexion.

serving as branches of the extensor tendons. When the flexor tendons keep pulling and extensor tendons getting relaxed, the finger starts its bending process during which the two small tendons continue to glide off from the PIP joint and eventually pass downwards the rotation axis. Hereinafter, although the extensor tendons are still transmitting forces into the two small branches via the web structure, the two small branches are no longer behaving like extensor tendons at the PIP joint, but instead they begin to help flex the finger by providing increasing flexion torques at the PIP joint. When the finger straightens, the above process repeats in the reverse order.

The second layer of the extensor hood is known as the central slip with a insertion point at the base of the PIP joint. Its function is to help extending/flexing the PIP joint. One of its

tendon branches is often connected to a small intrinsic muscle, namely the lumbrical muscle. It has been reported the lumbricals work as flexor tendons at the MCP joints, but can help extend the PIP and DIP joints via the extensor hood mechanism. Due to its variations in size and inserting locations, the function of the lumbricals are not unanimously agreed yet. So we treat them as a part of the intrinsic muscles not emphasizing its uniqueness in Fig. 2.3.

In sum, the complex, web structure of the extensor hood smartly transmits muscle forces to finger joints. This is an important biomechanical advantage that we would like to copy from the human hand.

2.3 The tendon sheaths

As shown in Fig. 2.4, the tendon sheaths are fibrous tissues that wrap around the flexor tendons and have multiple insertions on the dorsal side of finger bones. Although made of tough collagen-based tissues, these pulleys could tear and rupture when they are continuously subject to intense flexion forces during rock climbing. We have briefly mentioned the function of tendon sheaths when introducing the flexor tendons in the previous section. Based on the distance to the MCP joint, each section of the tendon sheaths has been named after a numbered annular pulley in nomenclatures of hand anatomy due to their important functions. Mechanical engineers design different pulley systems to apply forces and transmit power through cables. The tendon sheaths in the human hand work as a series of elastic pulleys to help transmit forces from the muscles to the joints. Since the tendon sheaths can flatten down when the finger straightens and bulge out when the finger bends.

This is another important anatomical feature that we are interested in mimicking. As illustrated in Fig. 2.4, when the finger straightens, no matter how hard the flexion muscles contract, reduced flexion torque are transmitted to the finger due to the decreased moment arms at the fingers. In our daily lives, this won't happen to our hand frequently, unless co-contraction of the hand (contracting both the extensor and flexor muscles simultaneously) is really required. Therefore the elastic pulley system can effectively deliver large torques to the finger joints when a firm grip of objects is needed, but keep the torques at the finger

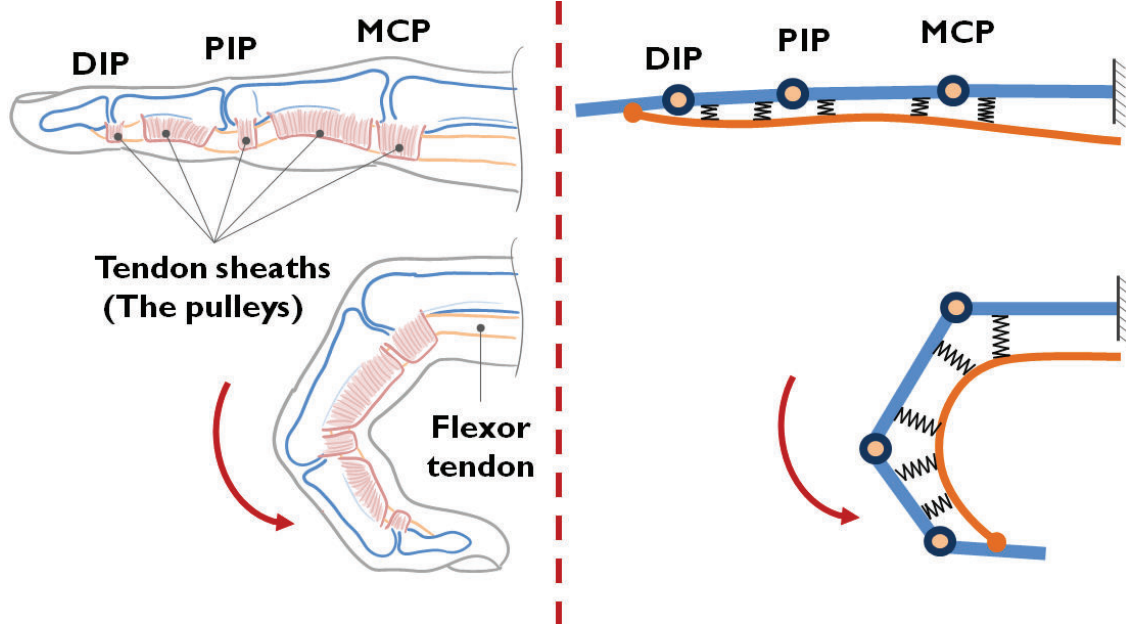


Figure 2.4: Schematic drawing showing the bulging process of the tendon sheaths (the pulleys) during finger flexion. *Left:* Different insertion sites of the tendon sheaths. *Right:* Mechanical analogy of the bending finger showing the increase in moment arms under the effects of elastic pulleys.

joints small when the hand is at rest.

Together with the gliding mechanism of the extensor hood, the elastic pulleys of the fingers are the essential building blocks that greatly affect the dexterity of the human hand. It is of our interest to incorporate these salient features into the design of our anthropomorphic robotic hand.

2.4 The biological joints

A joint is defined based on the contact of two adjacent bones. Their commonly shared contact surfaces decide the possible motions of the joint. Different types of joints facilitate a different set of finger motions, known as the range of motion (ROM). As shown in Fig. 2.5, during the bending motion, the three finger joints work as mechanical hinges. However, the MCP joints have one extra set of active ROM that allows the finger to move from side to side, which are known as the abduction and adduction (ad/b) motions. In addition, the

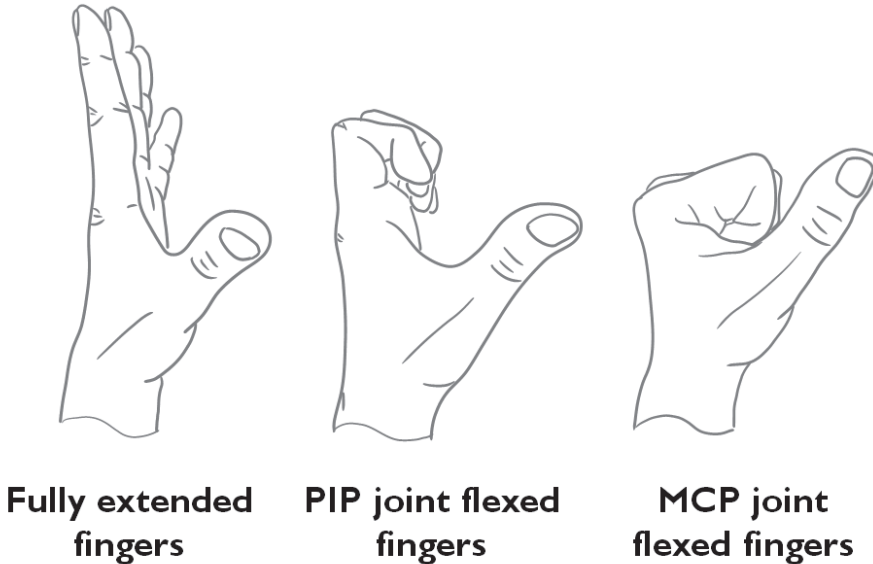


Figure 2.5: Schematic drawing showing the regular range of motion of the fingers during finger flexion.

MCP joints also have one passive ROM that permits twisting motion around the axis of the finger phalanges. Thus, in our following discussion, we are only going to focus on explaining the mechanism of the MCP joint since the 1-DOF hinge joint can be included as a special case.

When it comes to replicating the MCP joint, robotics researchers often have the following three options: a 3-DOF ball-socket joint, a 2-DOF universal joint, and a 3-DOF elastic joint. The universal joint is good at transmitting rotary motion in shafts, but lacks the 1-DOF that allows the finger to passively twist with respect to the axial direction at the MCP joint (see Fig. 2.6). Although the elastic joint can realize all three DOFs, it can not support large load along the axial direction due to the natural compliance of the elastic component. Although not suitable for replacing the MCP joint, successful application of the elastic joints to the design of hinge joints have been widely acknowledged. Compared to the above two designs, the mechanism of the ball-socket joint is simpler and only requires two components. In addition, its structure naturally matches the anatomy of the MCP joint in the human

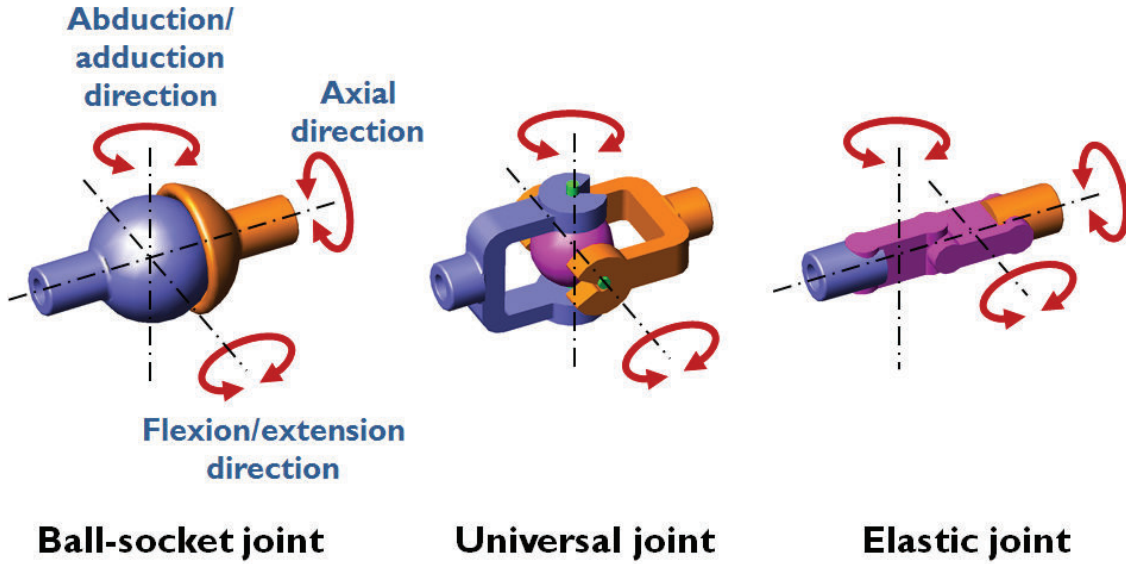


Figure 2.6: Mechanical analogies of the MCP joint of the human fingers. *Left:* A ball-socket that allows the closest replica of the MCP joint. *Middle:* A universal joint that supports axial rotation. *Right:* An elastic joint that has rigid support in axial direction.

finger.

Different from the fingers, the varied thumb movements (see Fig. 2.7) are resulted from the contact between the trapezium and first metacarpal bones at the CMC joint. Due to the irregular shape of the trapezium bone (see Fig. 2.8), the CMC joint has been commonly explained as a saddle joint that allows the thumb a wide ROM – up(adduction) and down(abduction), bent(flexion) and straightened (extension), and the ability to move across the palm (opposition).

When we model the kinematics of human hand with DenavitHartenberg (DH) convention, we could treat the CMC joint as a simplified saddle joint, and in turn all the rotating axes can be nicely fixed (see Fig. 2.9). But in reality, the thumb motion could never be achieved with such a mechanical substitute because the CMC joint requires not only rotating surfaces but also other mechanisms that support sliding and tilting motions. In

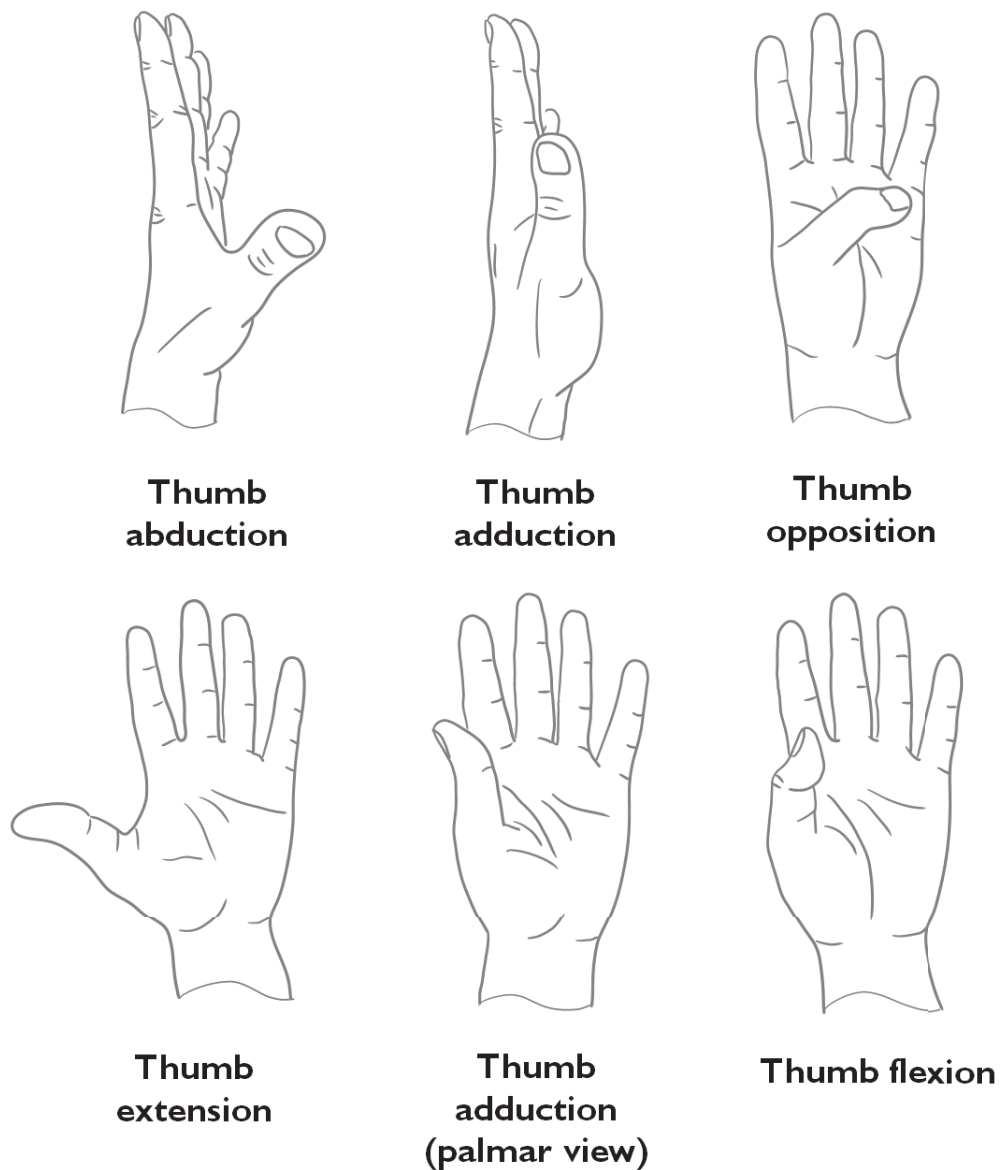


Figure 2.7: Schematic drawing showing the range of motion of the human thumb.

addition, the irregular shapes of articular surfaces are also responsible for stress transfer. It was estimated that a tip pinch of 1 kg will generate 12 kg of joint compression at the CMC joint. For a power grip, the load could become as high as 120 kg [67]

Previous studies on anthropomorphic robotic hand design focus on deriving the closest

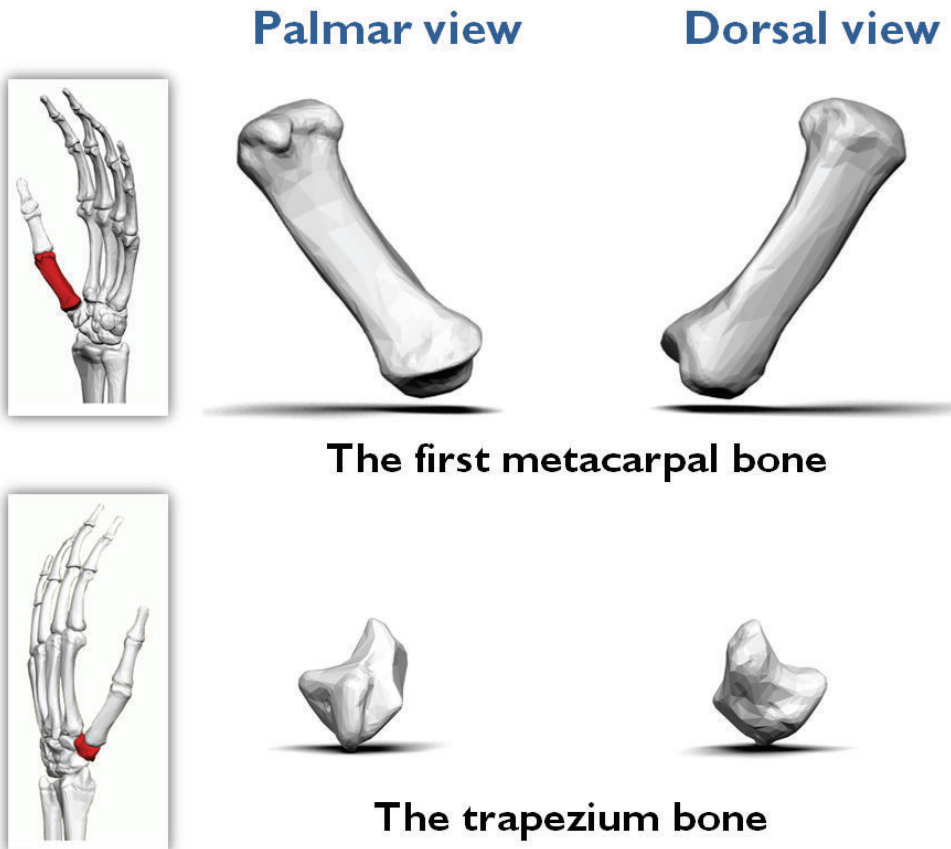


Figure 2.8: Complex bone shapes at the carpometacarpal joint of the thumb [24]. *Top row:* The first metacarpal bone (shown in red) of the human left hand. *Bottom row:* The shape and location of the important trapezium bone (shown in red).

human hand model to build true-to-life robotic hands. Many investigations have been carried out on cadaver hands, but only limited information was extracted and implemented into the robotic hand designs – in most cases just the number of fingers and the length of phalanges. We haven't utilized the geometry of the bone structure, which contains important kinematic information that could be used to greatly simplify the design and prototype of anthropomorphic robotic hand. The biological joints of the human hand have already been proven to work through years of use in daily activities. It is of our interest to

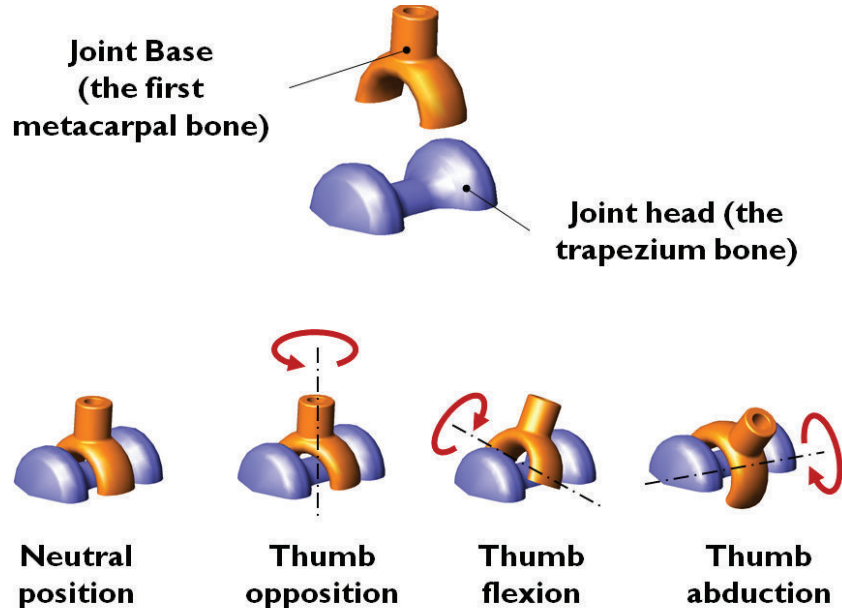


Figure 2.9: The mechanical analogy adopted for the explanation of the CMC joint. *Top row*: The definition of the saddle joint. *Bottom row*: Different statuses of the saddle joint at the corresponding thumb postures.

find out a way to effectively implement its functional features in robotic hand design.

2.5 The joint ligaments

The range of motion at each finger joint is restricted by the length of ligaments. As shown in Fig. 2.10, ligaments are tough bands of fibrous tissues inserted on both sides of the two adjacent bones. Two important branches are called collateral ligaments. Similar structures can be found in all the finger joints with variations in length. Their function is to stabilize the joint, shape the ROM, and prevent abnormal sideways bending of each joint. For example, at the MCP joint, the collateral ligaments originate from the dorsal side of the metacarpal bone and end near the palmar side of the adjacent finger phalanx. In this way, the collateral ligaments get taut when the finger bends, and become relaxed once the finger straightens. This is why our index finger can easily move from side to side when it extends, but has very limited side motions once it fully bends.

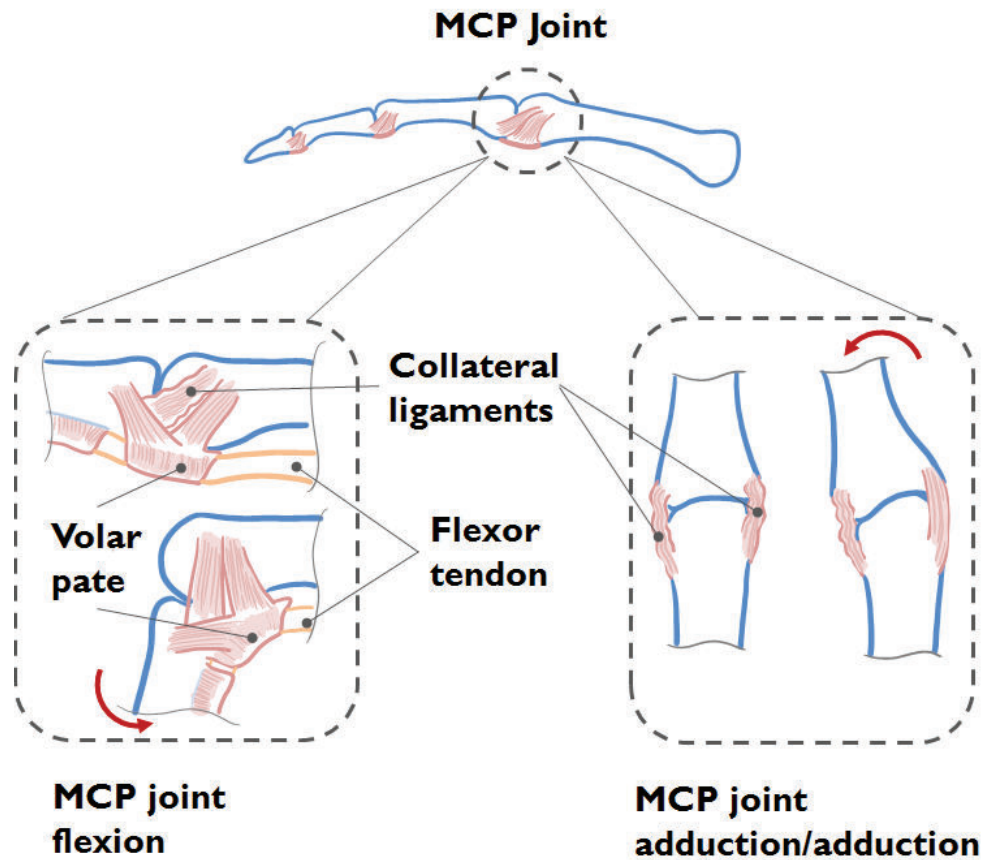


Figure 2.10: Schematic drawing showing the function of collateral ligaments at the MCP joint.

The thick ligament formed on the palmar side of the finger is called volar plate. Like the collateral ligaments, the volar plate also has insertions on both sides of the bones. Its function is to prevent the occurrence of the finger deformity from hyper-extension. The unlabeled ligaments are called accessory collateral ligaments, their function are to help stabilize the finger joint. Together with other ligaments and soft tissues, they form important structure known as the joint capsule.

Chapter 3

CROCHETED EXTENSOR HOOD

Biological tissues and skeletons of the mammals have been actively mimicked along with the advance of material science, from soft skin, muscles to hard cartilage and bones. Resulting innovation and technologies have been successfully applied to diverse fields, ranging from prosthesis, biomimetic robot, and tactile sensing, to clinical transplant, plastic surgery, and tissue engineering. However, important collagen-based tissues have not been studied or replicated due to their complex shapes, layered branches, weaving patterns, and varying positions with respect to bones during the body movement. Ligaments and tendons composed of densely packed collagen fibers are ubiquitously found inside the joints of a wide range of mammals, and biomechanically determine the characteristics of the joints during mammals locomotion. These biological ligaments and tendons are soft and compliant, but at the same time strong and stiff enough to resiliently transfer a large amount of forces from muscle contraction to the body movement exhibiting unique *biosolid* characteristics. However, the complex structure of the ligaments/tendons including the varying thickness, the multiple branches, and the layering formation makes it extremely difficult to replicate them.

The crochet technique may seem to be a realistic solution to the above problem. It has been successfully adopted for materializing hyperbolic shapes in mathematical field, and for visualizing composition of virus cells in biology. The compliance of textile is desirable for fabricating the artificial ligaments/tendons, because it can withstand tensile forces while retaining flexibility. Clinically proven, artificial anterior cruciate ligament (ACL) has a mesh structure made of polyester fibers, and can provide the stiffness and durability similar to those of natural ACL. To achieve the same result, the thin and web-like structure of the extensor hood in the human hand could also be mimicked with a piece of polyester fabric tailored into a similar shape. However the available weaving patterns could not mimic the

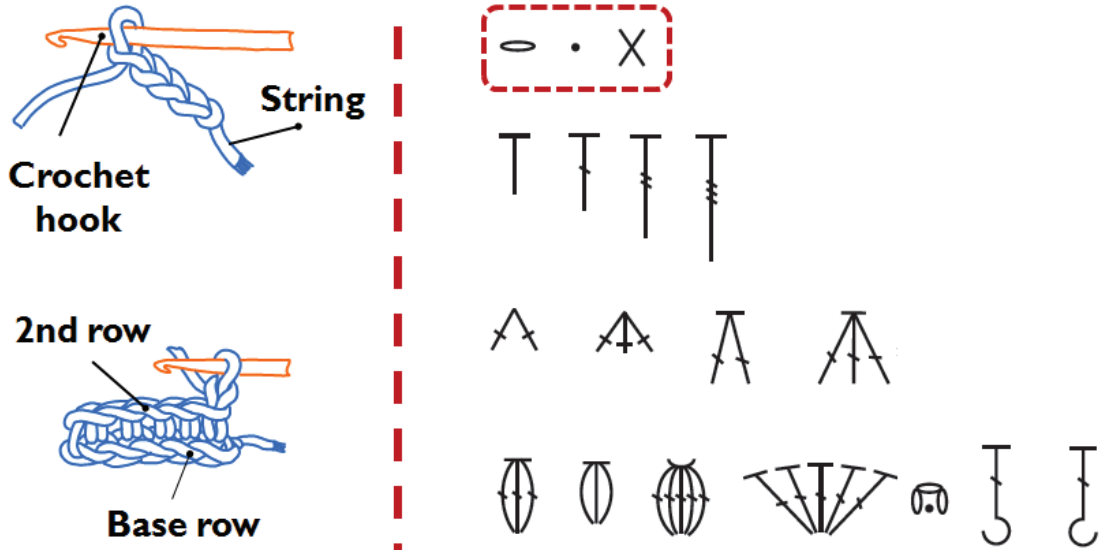


Figure 3.1: Schematic drawings of the crochet technique. *Left:* Basic crochet stitches used in our study. *Right:* Standard crochet symbol chart showing different possible variations of stitch types [25]. *Note:* The three stitches enclosed in the dashed box were adequate enough to prototype the proposed bionic extensor hood.

variations of branching structures without the occurrence of seam fraying. In contrast, we could use crochet technique to fabricate complex 3D shapes with just a hand handful of basic stitches (as shown in Fig. 3.1).

3.1 Crocheting the extensor hood of the human hand

Based on what we learnt from the anatomy of the human hand, we crocheted an artificial extensor hood by using the dimensions extracted from the index finger of the ACT hand. The fabrication process can be divided into six steps as shown in Fig. 3.2.

As shown in Fig. 2.3 in Chapter 2, the extensor hood of the fingers could be divided into two layers. The lateral bands were prepared in the first step since it forms the bottom layer of the extensor hood. And then the top layer called central slip was gradually crocheted onto the lateral bands. The two layers are first merged at the PIP joint insertion points (in Step 2 and 3) and then connected with each other on the two sides of the lateral bands (in

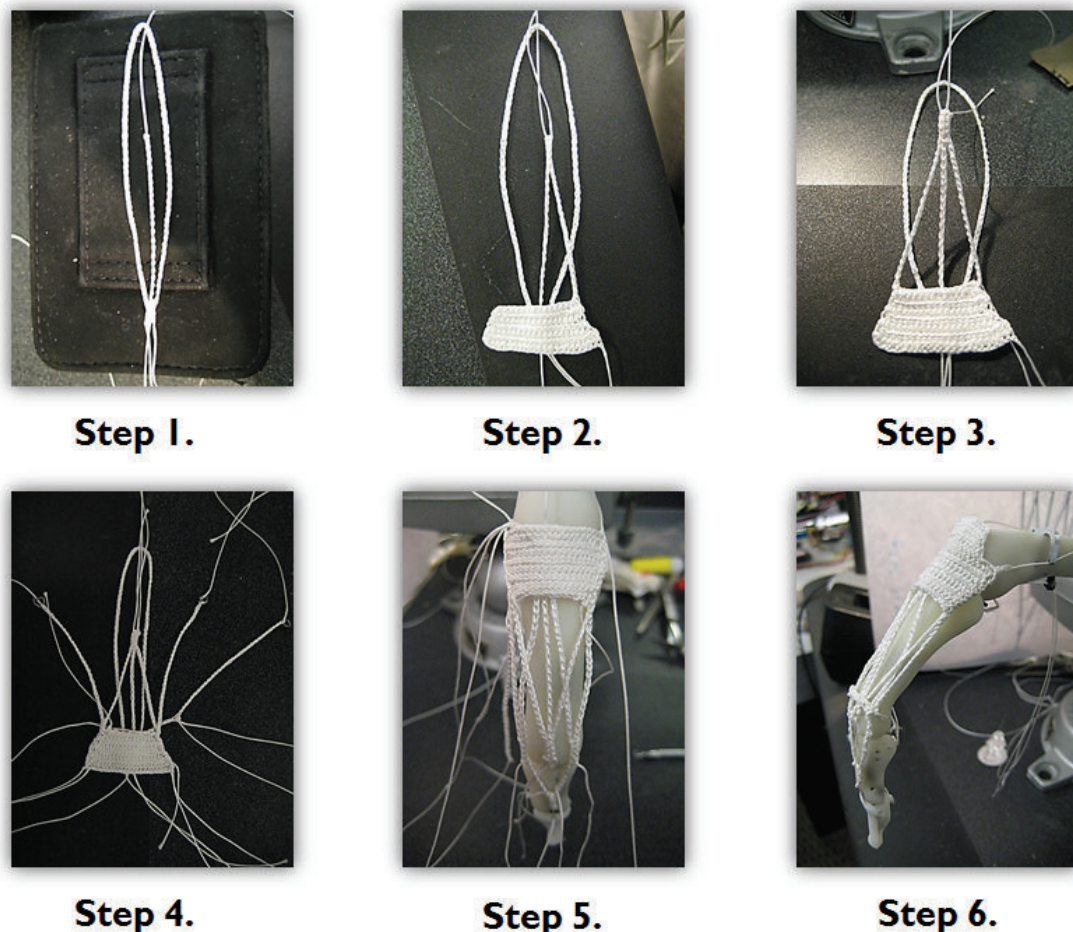


Figure 3.2: The prototyping process of the crocheted extensor hood for the index finger of the ACT hand.

Step 4 and 5). The relative position of the extensor hood with respect to the finger bones is crucial for the finger's ROM (see Fig. 2.5), therefore it needs to be further adjusted after attaching the extensor hood to finger skeleton via insertion points (in Step 6).

The same method was used to crochet the extensor hood of the middle finger. A simplified crocheted mechanism was also fabricated for the thumb to enable its extension movement, but its geometry is not based on any reported anatomical findings. Fig. 3.3 shows

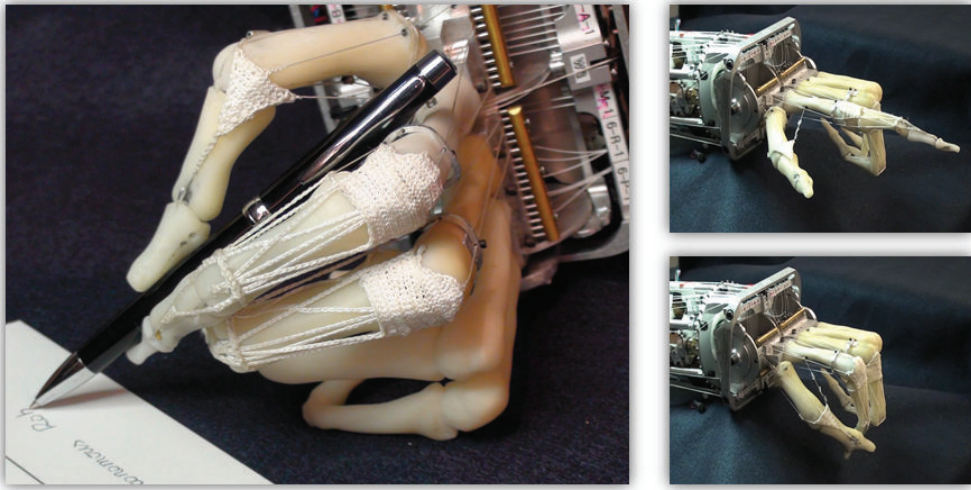


Figure 3.3: Crocheted extensor hood implemented in the Anatomically Corrected Test-bed Hand (ACT) Hand. *Left:* Manually positioned ACT hand holding a pen. *Right:* Snapshots showing the extension motion of the thumb and index finger with the help of crocheted extensor mechanisms.

the picture of the ACT hand equipped with two extensor hoods on its dexterous fingers.

3.2 Testing the mechanical properties of the crocheted branches

It has been demonstrated that the crochet technique can be used to generate complicated 3D shapes with variations of branches. The materials used to crochet the extensor hood is soft and flexible, but also has superior mechanical property (200 N breaking strength). However, several branching structures are used to connect two separate crocheted strings together, the knots and stitches at the merge site may have different mechanical properties, and therefore need to experimentally identified.

As shown in Fig. 3.4, the branching mechanism of the extensor hood can be mainly categorized into five distinctive groups based on the variations of the ligament configurations (e.g., between DC, TC, and SC) and branching types (e.g., between T1-B and T2-B). Since the function of the extensor hood is to transmit forces from the muscle to the joints, it is of our interest to quantitatively validate the efficacy of this novel approach. A series of tensile

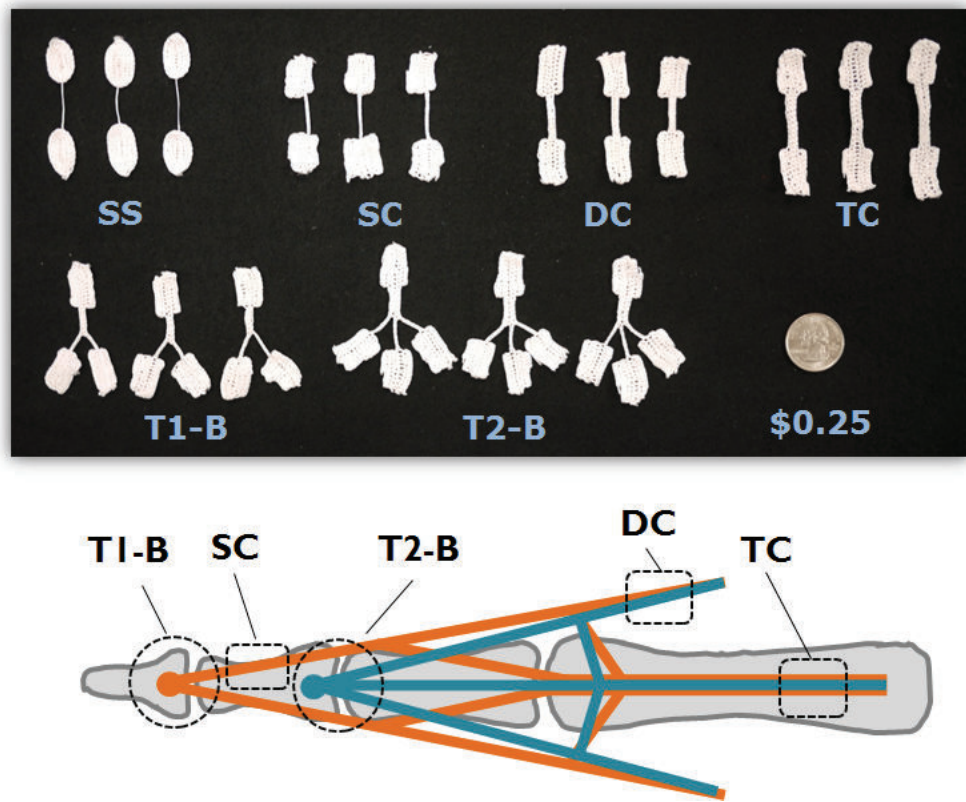


Figure 3.4: The complex shape of the extensor hood in the human hand (left index finger) and the samples for testing mechanical properties at different branching locations. *Top:* Crocheted samples for the tensile tests. *Bottom:* Variations of merging and branching structures observed in the human hand. **SS:** String string; **T1-B:** Type1-branching; **SC:** Single crochet; **T2-B:** Type2-branching; **DC:** Double crochet; **TC:** Triple crochet.

tests were conducted on samples listed in Fig. 3.4.

Before the start of each tensile test, each sample needs to be properly prepared. First, clear epoxy was applied to both ends of the samples in order to increase friction and avoid slip during the following tensile tests. Then each sample was sandwiched by two pieces of paper tapes with the middle parts cut open to form a small window (see Fig. 3.5). In this way, the samples can be better stabilized during the clamping process.

Once the samples were properly prepared, they were clamped vertically by the two grips of the tensile testing machine (Instron 3345, Norwood, MA). Before applying tension to the

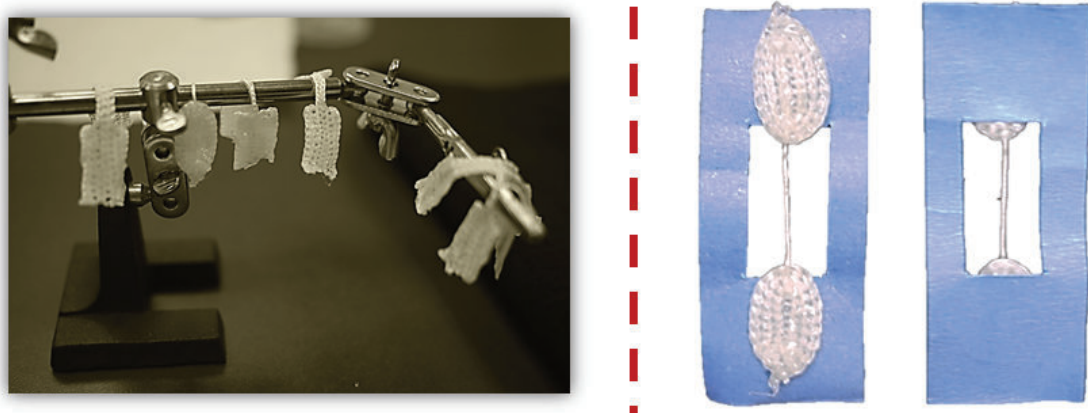


Figure 3.5: The preparation process of the tensile experiments. *Left:* Applying Epoxy on the two ends of the test samples. *Right:* In order to stabilize the flexible section, paper tapes were applied to both sides of the test examples.



Figure 3.6: Example of the three stages of a typical tensile test. *Left:* The test sample was first loosely clamped at both ends. *Middle:* The two paper legs were cut before the pulling process started. *Right:* Pulling finished after the test sample reached its yield limit.

testing sample, necessary adjustment of the sample were made to make sure good alignment. And then the middle section of the paper tapes were eventually cut off without disturbing the crocheted string as shown in Fig. 3.6. The pulling speed was set at 0.5 mm/s. All the

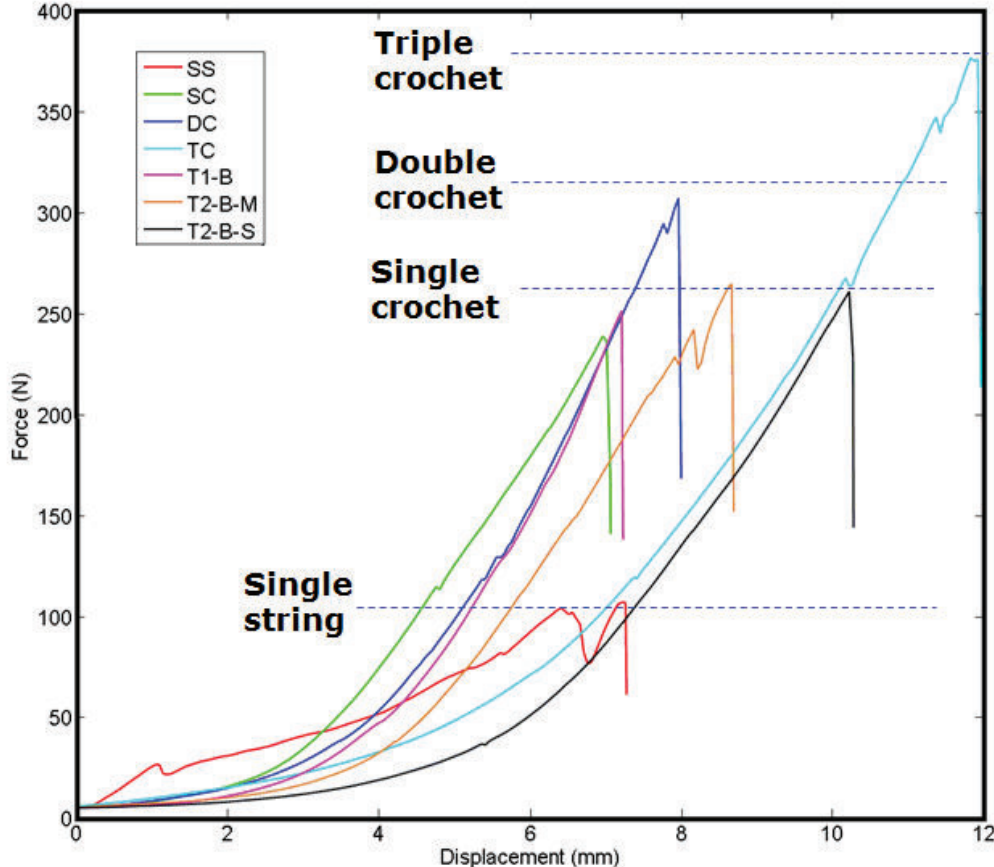


Figure 3.7: Typical Force-Displacement curves from crocheted samples. Note: Dashed lines pass through the points of corresponding breaking strength.

samples were tested until they reached their yield point.

3.3 Experimental results and discussion

The Strain-Stress curve depends on the properties of the materials, and therefore won't be greatly affected by the structure. However, the stiffness calculated from the Force-Displacement curve can be greatly affected by the variation of structures (see Fig. 3.7). Thus we collected data from the 27 tensile tests in order to investigate effect of branching variations on mechanical properties of crocheted mechanisms.

The cross-sectional area of the crocheted string is directly proportional to the number of single crocheted chains that merged together. As shown in Table 3.1, we observed that the breaking strength of string increases drastically after being crocheted into a chain – the breaking strength of a single crochet string exceeds two times of the maximum strength of a single string. And it is interesting to find that the crocheted string exhibits very consistent linear behavior once it passes the pre-tension stage. Under high tension forces, pre-failures were observed when some bundles of the polyester fibers yield firstly. However, the internal tension forces estimated in the extensor hood of the human hand were reported less than 10 N [68].

Table 3.1: Comparison of mechanical properties between different crocheted conditions.

| <i>Samples (n = number of the samples)</i> | <i>Breaking strength (N) Mean ± SD</i> | <i>Linear stiffness (N/mm)¹ Mean ± SD</i> |
|--|--|--|
| Single string (n=3) | 109.3 ± 4.2 | 17.6 ± 4.6 |
| Single crocheted chain (n=3) | 249.5 ± 9.5 | 57.7 ± 7.9 |
| Double crocheted chain (n=3) | 292.2 ± 14.8 | 62.3 ± 13.8 |
| Triple crocheted chain (n=3) | 440.7 ± 150.4 | 61.8 ± 20.1 |
| Type 1-branching (n=6) | 260.1 ± 20.0 | 59.2 ± 14.0 |
| Type 2-branching-middle (n =3) | 277.4 ± 22.2 | 60.5 ± 13.3 |
| Type 2-branching-side (n=6) | 277.6 ± 15.6 | 56.2 ± 10.6 |

¹Linear stiffness values of the crocheted samples are calculated from the linear region of the curves.

Statistical analysis was performed according to the seven categories listed in Table 3.1. It is interesting to find that the stiffness of the single crocheted string is independent of the branching conditions. The averaged stiffness value is 58.4 (N/mm). However, the single crocheted string located in the middle of the branching structure (Type 2-branching-middle) seems to be stronger than the others. It is obvious that breaking strength increases with the number of merged crochet chains. However, due to the nature of manually crafted textile, merged crochet chains (double and triple crocheted chains) often vary in their lengths slightly (within 3 mm), and therefore contribute differently to the overall breaking strength. Again, this won't become a problem when it is used in fabrication of bionic tendon/ligament

for the human hand, since the required forces during finger motion are much smaller compared to the value of their breaking strength. In addition, it is interesting to observe that once a certain length of the string is crocheted into a single crocheted chain, the total length of the chain will be reduced to 60% of the original length but with only 20 % increase in its thickness.

In summary, our crocheted extensor hood can closely resemble its human counterpart by not only replicating important geometry , but also restoring the kinematic functions of the fingers. Our experimental results also suggest that the crocheted chain is stronger than the original string even if different branching methods are used.

Chapter 4

DESIGN OF THE BIOMIMETIC FINGER

Anthropomorphic robotic hands are attracting growing interest of researchers because of their inherent similarity with the human hand that can potentially bring beneficial impact to many aspects of people's lives. Areas such as space exploration, personal assistance, hand prosthetics, and even industrial automation can all be better served with a highly biomimetic artificial hand. Achieving a robotic hand with biomechanics closely resembling our own will allow natural interaction while enabling a leap in prosthetic design. But significant challenges must first be overcome. These challenges include matching the same degrees of freedom (DOFs) of the human hand, possibly for restoring human-level dexterity, replicating human finger compliance to allow safe operation in unstructured human environments, and also designing the actuation system for mimicking the muscle behavior of the human hand. Other large technical obstacles also exist in terms of tactile sensor implementation, weight and size constraints. This chapter focuses on the intrinsic biomechanics required to replicate a human hand.

The challenge of designing a whole robotic hand can be further broken down into individual finger design. The fingers of a human hand possess several salient features that are hard to mimic simultaneously, including (1) the unique shape of the bones at different joints, which determines the degrees of freedom at the joint; (2) a joint capsule formed by fine ligaments, which set the range of motion for the joint and contribute to formation of the finger compliance; (3) cartilage and synovial fluid, enabling low-friction contact between two articulated surfaces [69]; and (4) extensors and flexors, which are originated from the bone insertion points and control the posture and movement of the finger. Most of the existing anthropomorphic robotic hands have not incorporated these biological features due to various constraints [1–7, 32, 38, 42, 43, 46, 47, 70–72].

The first three challenges belong to the domain of robotic hand's joint design. In the

past, two types of joint designs have been widely adopted in anthropomorphic robotic hand research. The first type uses standard mechanical components such as hinges, gimbals, linkages, or gears and belts [1–7, 38, 42, 46, 47, 70, 71]. Several important features have been achieved in these anthropomorphic robotic hands, including high degrees of modularity [47], built-in actuators [5, 6, 47, 73], low inertia [5, 32, 73], and extra palmar DOFs [2, 4]. While this methodology promises excellent performance in achieving the right number of DOFs and even mimicking kinematic characteristics of the human finger, it involves considerable systems-level complexity and implementation costs. In addition few of these types of hands possess built-in compliance which is necessary for a human hand to explore uncertainties in the unstructured real world. The second type uses a simplified design with passive compliance for adaptability. These types of hands are often under-actuated [32, 43, 72, 74], with fewer actuators than degrees of freedom, and therefore reduce overall complexity of the robotic hand’s mechanisms. Mechanical compliance is perhaps the simplest way to allow for coupling between joints without enforcing the fixed-motion coupling relationship inherent with gears or linkages. The hand/graspers made in this way often have superior robustness properties and are able to withstand large impacts without damage [74]. But there is also a trade-off between achieving the desired range of motion of the finger and having a compliant finger joint since the elastic component cannot by itself limit the joint’s range of motion.

As for the last challenge of mimicking the extensors/flexors of the human hand, cables, gears, and linkages have been widely used to transmit the motion from the actuators to finger joints. However, researchers have typically considered it as a part of the joint/finger design rather than emphasize it as an independent component. There are many salient features of the human hand that can only be revealed through dynamic interaction with the different objects. For instance, in order to understand the variable moment arms, which play a significant role in the movement control of the human finger, researchers rely on constantly modifying the cable routing and improving the design of the extensor hood according to the data collected from physical experiments. Once the complicated, and often expensive anthropomorphic robotic hands are prototyped, researchers are reluctant (when using cables) or won’t be able to (when using gears or linkages) modify the transmission

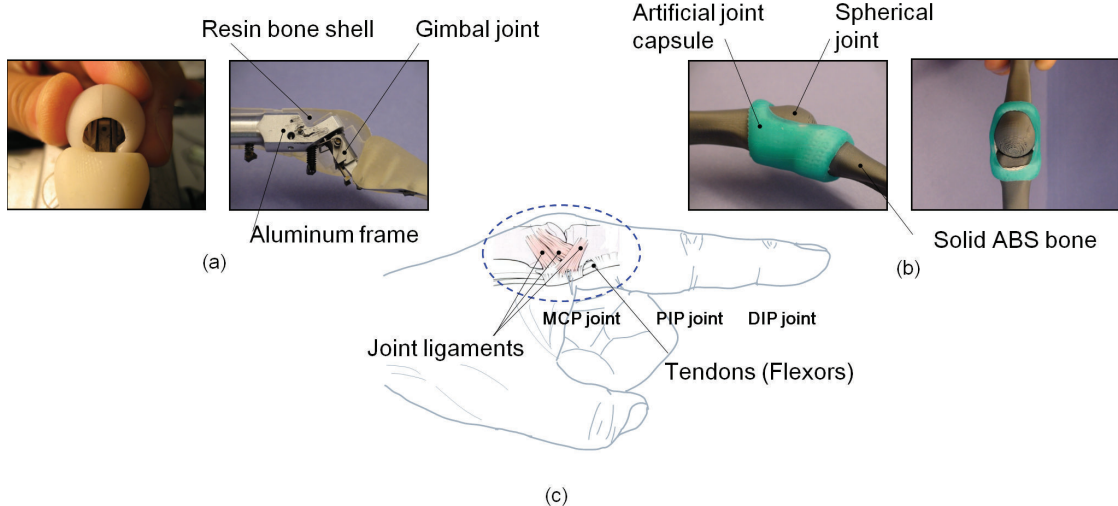


Figure 4.1: Comparison of the MCP joint design between the previous and new version of the ACT Hand. (a) Structure of the MCP joint in the previous version of the ACT Hand. (b) Our proposed design of the MCP joint. (c) Location and anatomy of the MCP joint in the human hand.

pathways without affecting the rest of the components of the robotic hands, resulting in a limited experimental scope.

Although standard design methodology, such as above, can mimic the kinematic behavior of a finger it does little to illuminate the salient features that make the human hand irreplaceable for many dexterous tasks. There is a need for biomimetic artificial fingers, based on accurate physiology, in order to quantitatively identify these characteristics thus providing insight into anthropomorphic robotic hand design.

A compelling alternative to standard mechanical components is to develop mechanisms which directly utilize the unique articulated shapes of human joints, as well as a tendon hood structure to actuate the finger. Following a biologically inspired design also reduces the total number of individual components, resulting in an elegant design.

The artificial finger described in this chapter is inspired by the combination of the above approaches and are used as an essential component for the next generation of the Anatomically Correct Testbed (ACT) Hand [8, 75–77]. This chapter focuses on the design and

control of a biomimetic artificial finger composed of three joint capsules whose mechanical structures and dynamic behaviors is similar to that of the human finger [78]. In the following sections the innovative mechanical design methods are detailed, the dynamic behaviors of the artificial joint are analyzed and compared with the human counterpart, the modeling of the pneumatic actuation system is described, then the simulation of the robotic finger is validated through the experimental results [78].

4.1 Design of the artificial finger

The artificial finger discussed in this chapter is inspired by the previous version of the ACT Hand. Due to a common ancestor from a cadaver hand both fingers share many biomechanical features such as the length of the bone sections, shape of the joint surfaces, and insertion points of the tendons. However, key differences between the two position our proposed artificial finger into a unique category.

As shown in Figure 4.1(c), there are three joints in the index finger: namely, the metacarpophalangeal (MCP), proximal interphalangeal (PIP), and distal interphalangeal (DIP). The PIP joint is located at the distal end of the proximal phalangeal bone, and the DIP joint is located at the distal end of the middle phalangeal bone. The MCP joint has two DOFs: one to achieve flexion-extension and another to realize abduction/adduction finger motion.

The MCP joint of the ACT Hand's index finger for both the previous and our proposed design are compared with the human counterpart. The anatomical drawing of Figure 4.1(c) shows the MCP joint capsule with the extensor hood removed. The previous version of the ACT Hand uses a gimbal joint to realize 2-DOF at the MCP joint. The artificial joint uses a solid sphere which is close to that of a human finger to realize the 2-DOF finger motion (with one extra under-actuated DOF from the 3-DOF spherical joint).

As shown in Figure 4.1(a), the range of motion of the index finger in the previous design of the ACT Hand is prescribed by the shape of the MCP bone shell. The new design uses crocheted joint ligaments to limit the range of motion of the MCP joint with an elastic sleeve to replicate passive biomechanics of the musculo-skeletal structure. Although the kinematics of the MCP joint in the previous version of the ACT hand matches the human

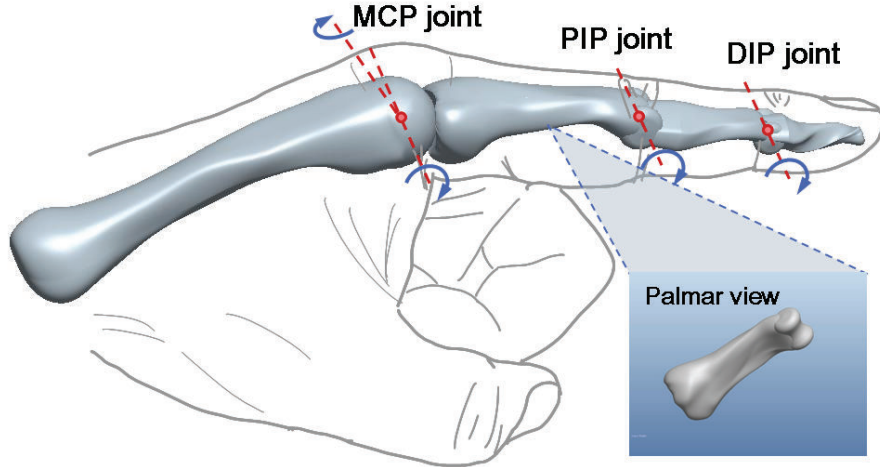


Figure 4.2: 3D model of the laser-scanned human index finger.

hand very well, a complex motor control strategy must be used in order to simulate the passive biomechanics. Shifting the load of simulating passive biomechanics into physical elastic elements at the joints will allow the ACT Hand to reduce its control complexity. This not only saves power but also lowers the chance of saturating the actuators with non task-specific commands.

In the following subsections, each of the components of the artificial finger will be introduced according to its assembly sequence.

4.1.1 Modular design of the bone segments

In order to anatomically match the size and shape of the human finger bones, we used the index finger from a Stratasys Corporation's laser-scan model of human left hand bones supplied in STL format, imported the tessellate facets into Pro/Engineer, and created solid models for each bone by fitting new surfaces to the scanned geometry [76] (As shown in Figure 4.2). Detailed parameters of the artificial finger are listed in Table 4.1 and 4.2.

The adoption of an anatomically correct bone structure would seem to imply a cost

Table 4.1: Physical parameters of the artificial finger skeleton

| <i>Phalange</i> | <i>Length (mm)</i> | <i>Weight (g)</i> |
|-----------------|--------------------|-------------------|
| MCP to PIP | 53.4 | 5.5 |
| PIP to DIP | 32.0 | 2.0 |
| Distal phalange | 23.7 | 1.2 |

Table 4.2: Approximate joint motion limits of the artificial finger

| <i>Joint</i> | <i>Minimum</i> | <i>Maximum</i> |
|--------------|----------------|----------------|
| MCP | 30° extension | 90° flexion |
| | 35° abduction | 35° adduction |
| PIP | 0° extension | 110° flexion |
| DIP | 0° extension | 70° flexion |

intensive and complex manufacturing process. However this cost can be avoided through the innovation of rapid prototyping machines. Each section of the artificial finger joint is 3D printed by the Dimension BST 768 (Stratasys Corp., Eden Prairie, MN). The resolution of the 3D printed parts is 0.025 mm, and it takes only three hours to print all the components of the entire index finger. Additionally the strength of the ABS plastic is sufficient to resist the induced stress of the extensor hood.

Each distal section of the finger joint is designed to be detachable from its base as shown in Figure 4.3 (a). This design serves two functions. The first is for easily mounting a steel ring (0.8 mm in diameter) whose shape conforms to the contour of the cross section of the ABS bone. The rim of the crocheted joint capsule is sewn onto this steel ring (Figure 4.3 (b)) so that the latter forms a continuous attachment zone for the former part along the contour of the cross section near the finger joint. A partially assembled MCP joint section is shown in Figure 4.3 (c).

The second function of this modular design is to provide a platform for future improvement. For instance, the surface of the ABS parts can be further plated with a 0.003 inch

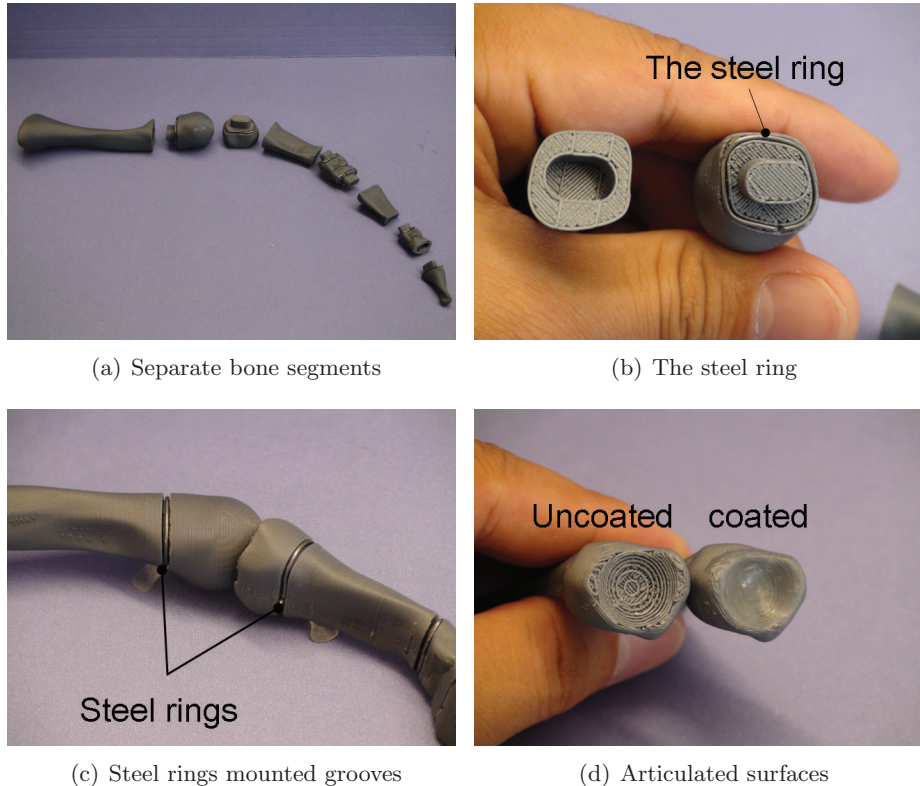


Figure 4.3: Components of the artificial index finger. (a) Modular design of the index finger. (b) & (c) Steel rings used to anchor the rim of the crocheted finger capsule. (d) Thermoplastic coated articulated surface providing low-friction surface at the finger joint.

thickness of chrome to provide a better approach to frictionless contact at the finger joint (RePliForm Corp., Baltimore, MD). An instant benefit of this design is also demonstrated in the experiments where different weights of the distal finger are tested for dynamic identification.

In order to mimic the frictionless surface of the articulated cartilage of the human joint a thermoplastic (Shapelock Corp., Sunnyvale, CA) was used to coat the surface of the socket side of the MCP joint as shown in Figure 4.3 (d). This combination of the joint coupling decreases the friction between the two articulated surfaces. Although, when encountered with the long term tear and wear, commonly engineered materials cannot regenerate like biological tissues, we believe that through low-cost, rapid prototyping technology the modular

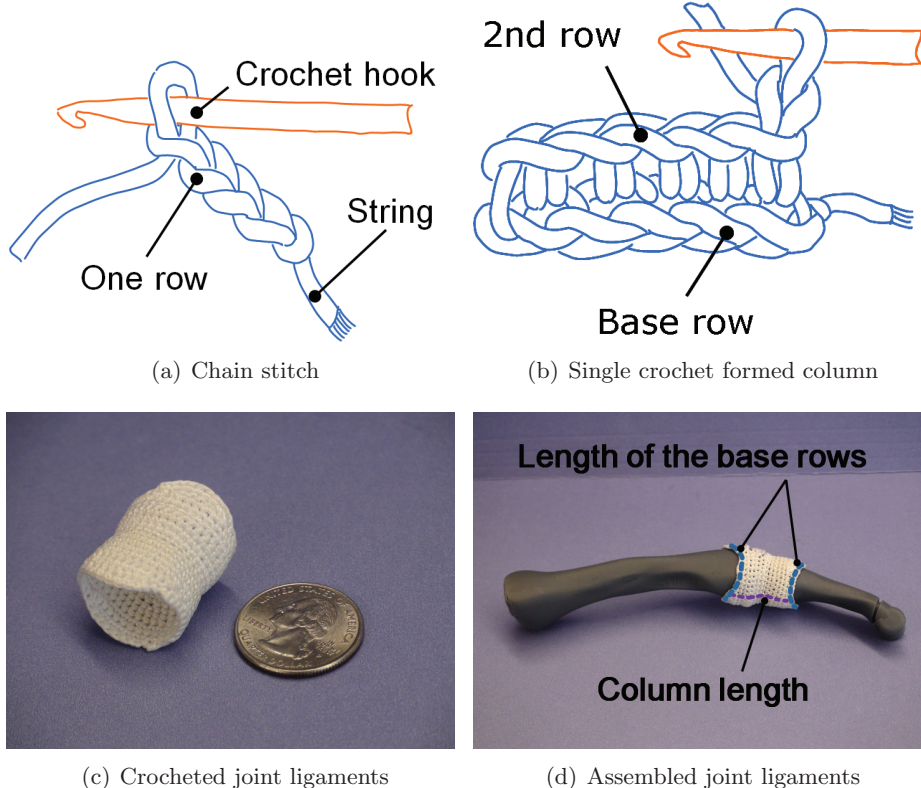


Figure 4.4: Crocheted ligaments of the artificial MCP joint. (a) Basic crochet type I – chain stitch. (b) Basic crochet type II – single crochet. (c) Hyperbolic shape of crocheted joint ligaments limits the range of motion of the MCP joint of the index finger. (d) Partially assembled index finger with crocheted ligaments attached.

design can make maintenance of our proposed artificial finger/hand economically viable.

4.1.2 Crocheted joint ligaments

In the human hand, the joint capsule is a dense fibrous connective tissue that is attached to the bones via specialized attachment zones and forms a sleeve around the joint. It varies in thickness according to the stresses to which it is subject, and is locally thickened to form capsular ligaments, which may also incorporate tendons (see Figure 4.1(c)). It seals the joint space and provides passive stability by limiting movements through its ligaments [79].

In hand surgery surgeons avoid using mechanically complicated replacements for finger

joints. Common prosthetic joints used in hand surgery may include flexible segments made either from titanium alloys, ceramics, or plastics [80] but do not replicate the surface details found on the bone ends. The flexible segments of the prosthetic joint are inserted into holes created inside of neighboring phalanges. The joint is then sealed with the joint capsule. These types of artificial joints have been clinically proven to restore joint function [81]. Without the joint capsule the neighboring phalanges would lose integrity and fall apart, thus it is a critical component of our biologically inspired artificial joint.

Our crocheted joint ligaments are fabricated with 0.46mm Spectra® fiber (AlliedSignal, Morristown, NJ). The fiber was chosen because of its strength (200 N breaking strength), high stiffness, flexibility, and its ability to slide smoothly over the bones.

Two basic crochet stitches were applied during the fabrication of the artificial ligaments. These are the *chain stitch* and *single crochet* as shown in Figure 4.4 (a) and (b). A series of chain stitches is called *a row*, the length of the row is determined by the local perimeter of the joint capsule. A single crochet determines the row width, while a double crochet would increase this width. The total width of the chains formed by single crochet becomes the *column length* of the joint capsule (see Figure 4.4(d)).

A sample of crocheted joint ligaments is shown in Fig 4.4 (c) and (d). This sample illustrates the full hyperbolic shape [82], which covers the area where the extensor hood is typically located. Our design (shown in Figure 4.1) excludes this dorsal area because the extensor hood is considered as an independent component [83]. The hyperbolic shape of the crocheted ligament is well suited for sealing the joint space, and its column length determines the range of motion of the MCP joint.

Given a fixed distance between the two steel rings the column length then determines the amount of slack in the ligaments with the joint in a neutral position. This slack from the crocheted ligaments constrains the joint's range of motion as it moves. The column length was empirically determined based on the dimension of the joint. The base row for each end of the joint ligaments is formed by a chain whose total length is equal to the perimeter of the steel ring. The local thickness of the joint capsule can also be controlled by varying the number of stitches crocheted on a base row. After fabricating the crocheted joint capsule, it is sewn onto the steel ring which snaps into a groove cut into the bone as shown in Figure

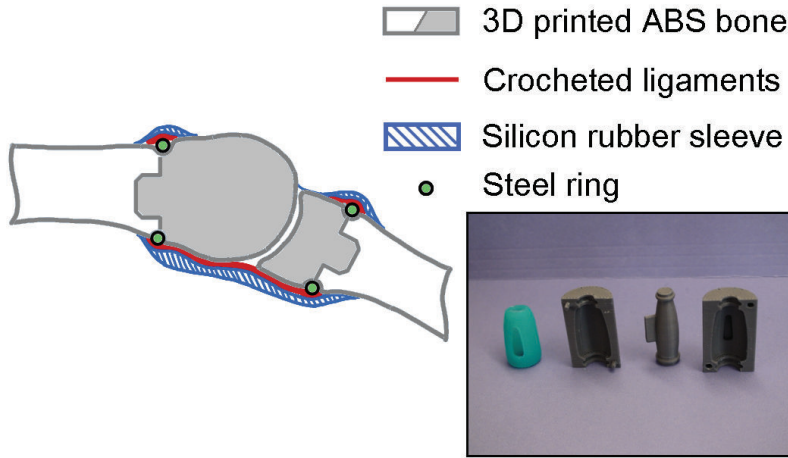


Figure 4.5: Cross section of the fully assembled MCP joint. *Bottom Right:* The silicon rubber sleeve and the molds used for its fabrication.

4.5.

4.1.3 Silicon rubber sleeve

Dynamic properties of the finger joints are largely determined by the passive biomechanics of the muscles and tendons which route along the bone surfaces. Rather than mimic the musculo-skeletal properties with an actuator an elastic sleeve can be designed to act on each joint in combination with the crocheted ligaments, recreating the intended dynamics.

The elastic component of the artificial joint is made of silicon rubber (PlatSil® 71 Series RTV, Polytek Development Corp., Easton, PA) with high shear strength. Its shape is cast by a set of 3D printed molds (see Figure 4.5) which forms a sleeve around the MCP joint providing elastic forces during finger flexion/extension.

To achieve optimal performance and high durability of the silicon rubber, a vacuum chamber was used to remove tiny air bubbles from the silicon mixture before curing. The thickness of the silicon rubber sleeve can be easily modified by using different molds. This feature provides adjustable stiffness and damping for the artificial joint capsule for our dynamic identification.

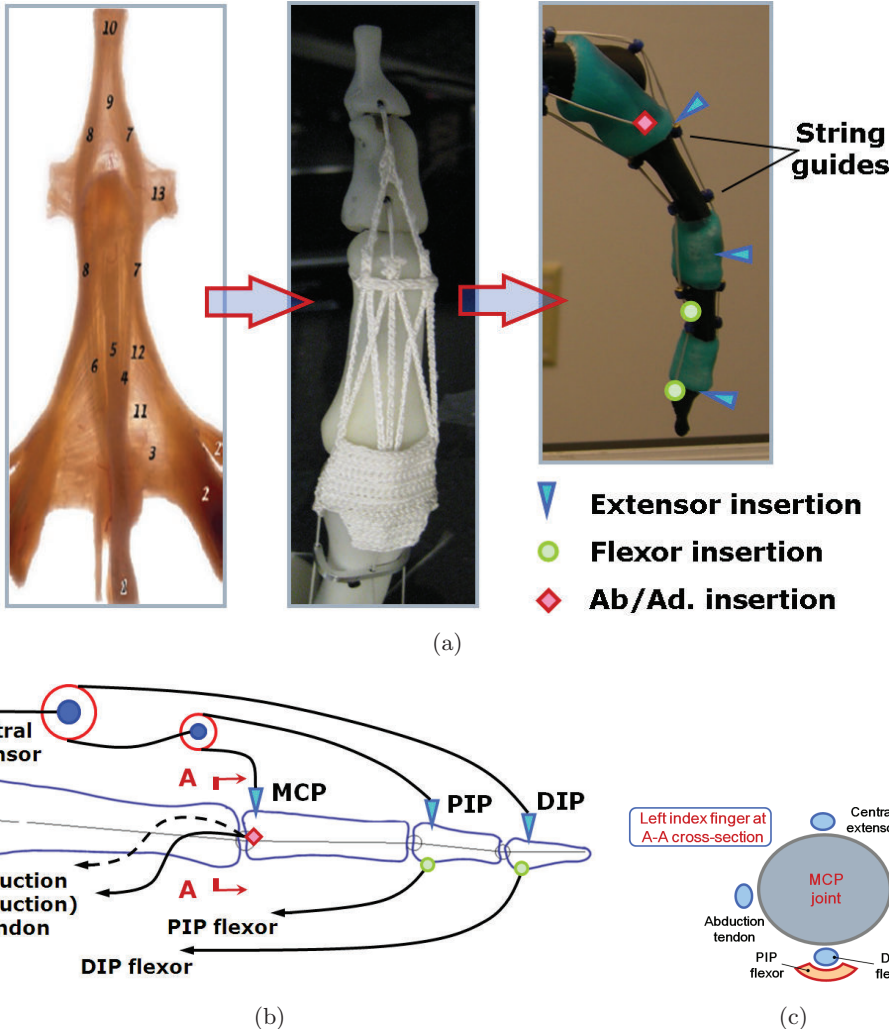


Figure 4.6: Comparison of the extensor mechanism between the human hand [26], the ACT Hand, and the artificial finger. (a) Design evolution of the tendon hood. (b) Schematic drawing of the pulley system of the artificial finger. (c) Cross-section drawing (A-A) of the tendon structures at the MCP joint for a left index finger (the view is towards the distal aspect of the finger).

4.1.4 Tendon hood design and its simplification for the extensor mechanism

Underneath the skin of the human finger over the dorsal side of the finger bone, extension motion of the finger is realized via a complex web structure as shown in the leftmost picture of Figure 4.6(a). On the palmar side of the finger, antagonistic tendons called flexors are

connected from the bone insertion points to the extrinsic muscles located in the forearm to enable the flexion motion.

Previously, a tendon hood for the ACT Hand was designed to mimic the extensor web of the human finger (as shown in the middle picture of 4.6(a)). The artificial extensor is fabricated by crocheting nylon composite to emulate the geometry and functionality of its human counterpart as closely as possible. Instead of adopting the same extensor design, in this chapter we apply what we have learned from the ACT Hand and keep only the tendons essential for the index finger flexion/extension and abduction/adduction in order to focus on the dynamics and control of our artificial finger.

As shown in the rightmost picture of Figure 4.6(a), the locations of insertion points and string guides of the artificial finger are all inherited from its human counterpart. The string guides were 3D printed and securely attached to each section of the finger bones allowing for smooth travel of the extensor/flexors. In the human hand, tendons from the three extensor tendons' insertion points are all merged with the extensor hood at the MCP joint, therefore a pulley system was adopted to make sure each individual tendon is constantly in tension (see Figure 4.6(b)). Our simplified extensor system was designed independently from the joint capsule, thus it reduces the overall complexity of the robotic hand, and makes it cost-effective and flexible enough for future improvement.

4.2 Dynamics of the artificial joint

Together, all of the above components set the stage to enable the artificial finger joint to closely mimic the kinematics and dynamics of the human joint. We quantitatively validated the efficacy of the artificial joint by comparing its dynamic characteristics with that of two human subjects' index fingers by analyzing their impulse response with linear regression. The experimental setup is illustrated in Figure 4.7. In order to focus on the dynamics of the MCP joint, the base of the hand, DIP, and PIP joints were all immobilized during the experiments both for the human and artificial finger. The human subjects were instructed to relax and close their eyes, so as to avoid voluntary responses as much as possible.

120 perturbations were applied manually at roughly 1s intervals at the fingertip. In

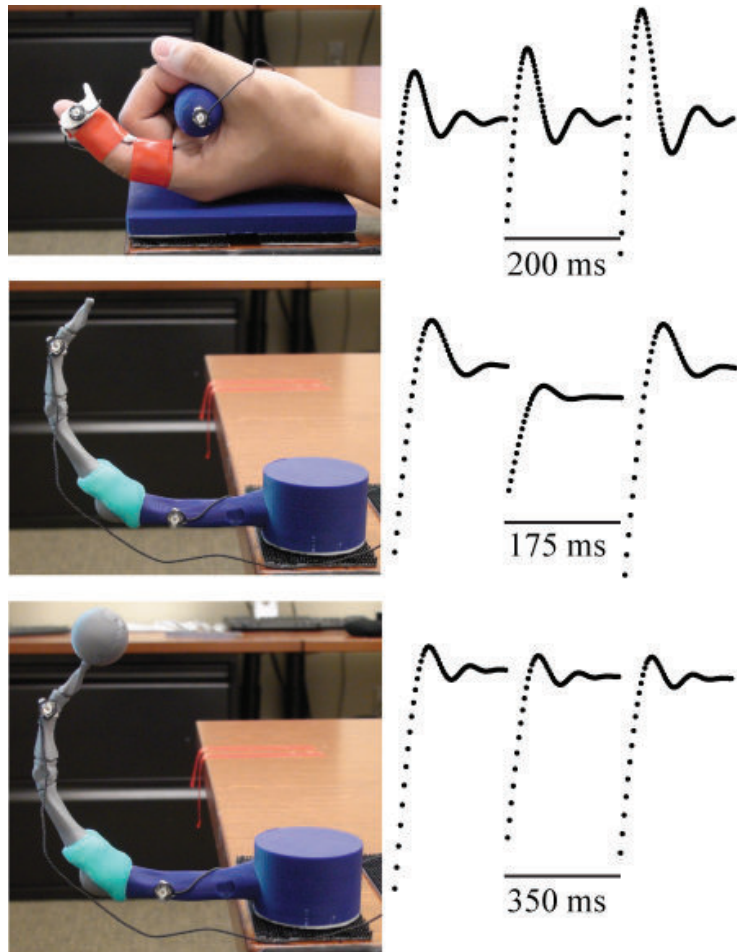


Figure 4.7: Left: Experimental setup. Right: typical trials collected from infrared markers for each finger during perturbations. Note that joint angles of the initial finger postures are 45° at the MCP, 35° at the PIP, and 25° at the DIP.

each perturbation the experimenter extended the finger (human or artificial) to a randomly chosen position, and suddenly released it. Infrared markers (PhaseSpace Inc., San Leandro, CA) were attached to the base and distal segments of each finger. The markers' 3D coordinates were measured at 480 Hz using a 7-camera system. The motion capture data was recorded continuously and parsed into individual trials off-line. In some trials a 7.5g mass was also added to the distal segment (8.7g) for investigating the effect of force/torque

sensors commonly incorporated at the fingertip (as shown in Figure 4.7 bottom). The rationale was that, if the fingers behaved like mass-spring-damper systems [84], the stopping phase would be particularly revealing with regard to their dynamic properties.

All models were fitted using linear regression (Matlab Statistics toolbox), and all fits reported were significant ($p < 0.05$). A simple mass-spring-damper model (model M1) was first chosen to fit all data sets:

$$\ddot{\theta} = -k\theta - b\dot{\theta} + a_0 + a_1 \cos(\theta) + a_2 \sin(\theta) \quad (4.1)$$

This model was chosen because inertial measurements for the human finger was not viable. Instead of duplicating every detail of the tissues from the human finger, the goal of this artificial joint is to mimic their combined property which can be properly modeled as a spring-damper system. Thus k, b here are the stiffness and damping coefficients divided by the moment of inertia. The term a_0 accounts for the spring reference point, as well as any other potential biases. The trigonometric terms account for gravitational forces.

Model M1 fit the human data quite well (with $R^2 = 0.92$), but provided a rather poor fit for artificial fingers (with average $R^2 = 0.55$), indicating that the latter dynamics are more complex. This problem suggested that the acceleration of the robotic finger may not be a well-defined function of position and velocity, but instead the system may have higher-order dynamics. Plotting the raw data as a 3D scatter plot confirmed our suspicion. The 3D plot and two projections of this 3D plot are shown in Figure 4.8. It is found that the surface often has two different accelerations for the same point in position-velocity space.

Therefore the data were re-analyzed under the assumption of 3rd-order dynamics. Fig 4.9 shows the 3D scatter plot of jerk (derivative of acceleration) as a function of velocity and acceleration. It is observed that this function is well-defined (even though there are some positional effects not included in the figure). This prompted us to achieve the final acceleration-based model as follows (M2):

$$\ddot{\theta} = -k\theta - b\dot{\theta} + a_0 + a_1 \cos(\theta) + a_2 \sin(\theta) + c_1\psi + c_2\theta^2 + c_3\dot{\theta}^2 \quad (4.2)$$

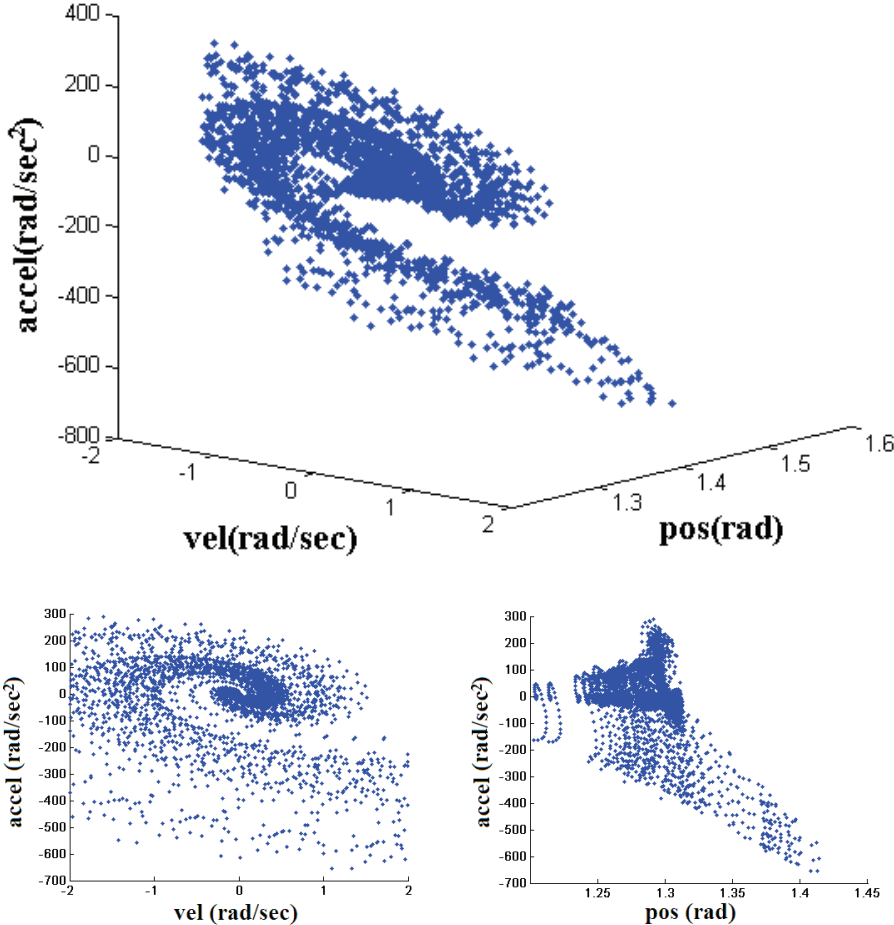


Figure 4.8: *Top:* 3D scatter plot of acceleration vs. velocity and position. *Bottom:* scatter plots of acceleration vs. position and velocity. All data in this figure are from the artificial finger (unloaded thin).

where

$$\psi(t) = \int_0^t \tanh(\dot{\theta}(\tau)) d\tau \quad (4.3)$$

The quadratic terms $\theta^2, \dot{\theta}^2$ were added so as to allow nonlinear stiffness and damping. The sigmoid (tanh) term was included as a model of friction. By adopting Model M2, good fits are observed both in the human ($R^2 = 0.97$) and the artificial joint of the index finger ($R^2 = 0.95$). To obtain values for stiffness and damping that can be compared to the

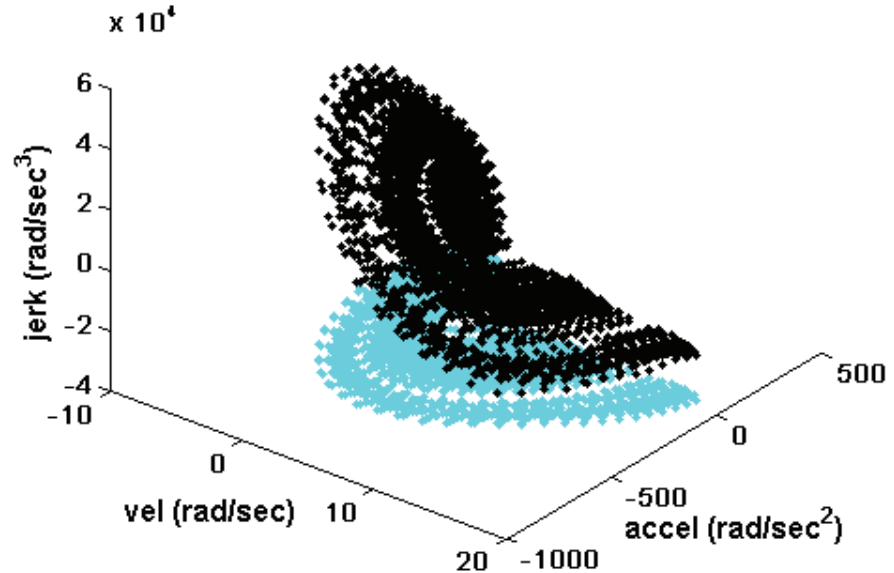


Figure 4.9: 3D scatter plot of jerk vs. velocity and acceleration. The light dots are the projection of the data on the bottom plane.

values estimated for human finger in [84], a simplified version of model M2 is constructed by removing the quadratic and trigonometric terms. We used an inertia of $0.0006 \text{ kg} \cdot \text{m}^2$ for the unloaded finger (Estimated in Pro/E model) and averaged the results for the thick and thin capsules in the unloaded condition. The comparison is shown in Table 4.3, the values are quite similar indicating our artificial joint has similar stiffness and damping.

4.3 Actuation system

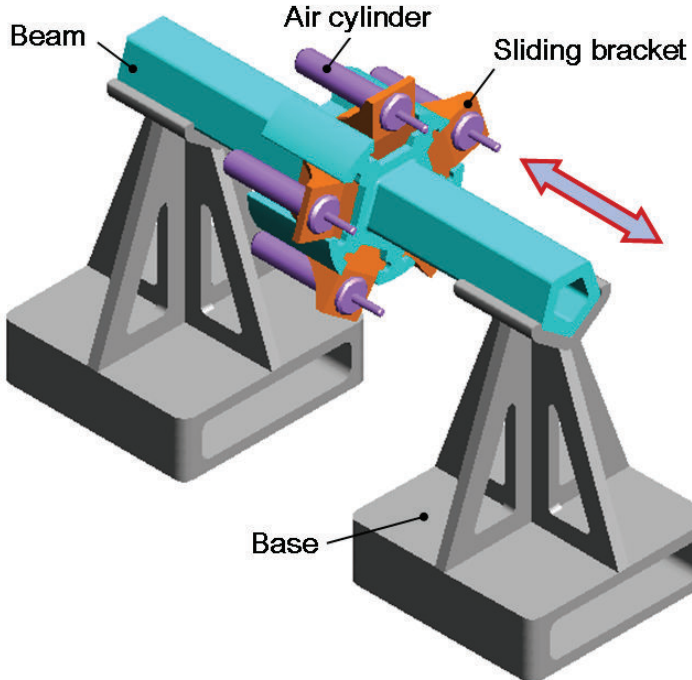
The artificial finger is actuated using a “Pulling-only pneumatic actuation system” (see Figure 4.10a). Because of its robustness, smooth dynamics and inherent damping properties, pneumatic actuation seems promising for modeling muscle behaviors. The robotic finger system consists of five double-acting cylinders (Airpel-anti stiction cylinders, model M9D37.5NT2) evenly mounted along the perimeter of a cylindrical beam through five slid-

Table 4.3: Comparison of stiffness & damping for the human and artificial MCP joints

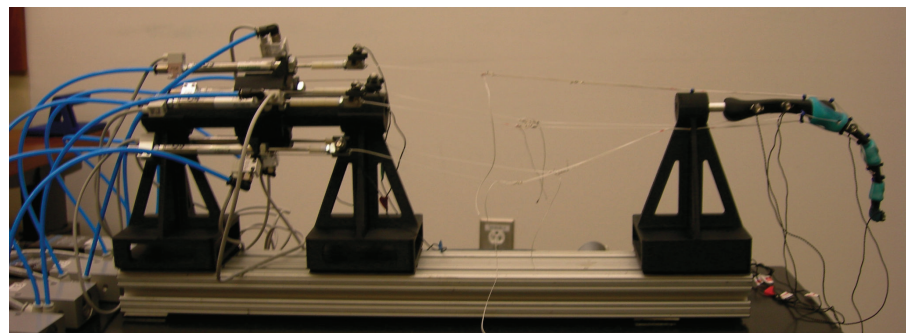
| <i>MCP joint of the index finger</i> | <i>Stiffness K (Nm/rad)</i> | <i>Damping B (Nms/rad)</i> |
|--------------------------------------|---|-----------------------------------|
| Human joint | 0.50 (averaged bewteen -0.2 to 1 radians) | 0.0142 (SD = 0.23) |
| Artificial joint | 0.534 +/- 0.025 (95% confidence interval) | 0.024 +/- 0.0003 ($R^2 = 0.87$) |

ing brackets. The sliding brackets are designed to eliminate any potential slack between the tendons and actuators. The pistons of the five cylinders are connected to the central extensor, abduction and adduction tendons, DIP and PIP flexors, respectively.

The front chamber of each cylinder is connected to a proportional 5/3 pressure valve (Festo, model MPYE-5-M5-010-B). When pressurized the front chamber resembles the muscle contraction and the back chamber is left open to the atmospheric pressure as tendons cannot push the finger (Pulling-only actuation). The valve receives a command voltage from a National Instruments D/A board. This voltage (0-10V) specifies the position of a linear actuator inside the valve, which in turn sets the aperture connecting the front chamber to the compressor (90 PSI above atmospheric pressure). The control command (in V) 5 - 10 pressurizes the systems and 5 - 0 exhausts. The pressure inside the front chamber is measured with a solid-state pressure sensor (SMC, model PSE540-IM5H). The sensor data are sampled at 50 KHz, and averaged in batches of 500 to yield a very clean signal at 100 Hz. The difference between the pressures in the two chambers of each cylinder (denoted D) is proportional to the linear force exerted on the piston. The minimum pressure was hand tuned by raising the pressure in small incremental steps until the cylinder was able to correct for the slacks while finger was moved around. For protection of the finger, each cylinder's piston contraction is limited by excursion of the tendon it acts upon. Tendon lengths were measured using SICK-cylinder magnetic sensors (sensor resolution is 0.01mm) which linearly scale 32mm over 0-10 volts. SICK sensors were added later, and therefore were not used in the experiments on the kinematic tendon model.



(a) 3D model of the actuation system



(b) Experimental setup

Figure 4.10: The actuation system of the anthropomorphic robotic finger.

4.3.1 Modeling of the human finger

The definition of the three joints of the index finger is illustrated in Figure 4.11. The PIP joint is located at the distal end of the proximal phalangeal bone, and the DIP joint is located at the distal end of the middle phalangeal bone. The MCP joint has two DOFs:

one to achieve flexion-extension and another to realize abduction-adduction finger motion. According to the anatomical joint properties of the human index finger, the abduction-adduction joint axis is oriented at 60° with respect to the metacarpophalangeal bone as shown in Figure 4.11.

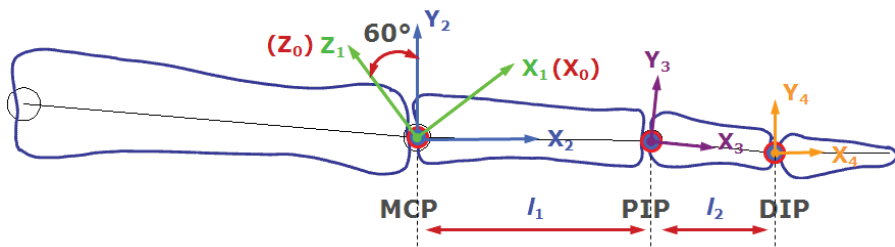


Figure 4.11: Model of the human index finger.

Frame 0: Fixed frame (palm phalange)

Frame 1: Adduction/Abduction frame

Frame 2: MCP flexion frame

Frame 3: PIP flexion frame

Frame 4: DIP flexion frame

After choosing the correct finger model, kinematic analysis of the index finger is conducted based on Denavit-Hartenberg (DH) notation, and corresponding parameters are summarized in Table 4.4.

A key benefit of the using model-based joint angle estimation is that we can extract all the joint information from knowing only the information at the fingertip. In this way, by implementing sensors or tracking the location and orientation of the fingertip, the information of the four joint angles (θ_1 , θ_2 , θ_3 , ω) can be recovered through a series of matrix transformations as follows:

$${}_4^0T = {}_1^0T \cdot {}_2^1T \cdot {}_3^2T \cdot {}_4^3T \quad (4.4)$$

The final format of the transformation matrix ${}_4^0T$ can be further sorted into the following format:

Table 4.4: Denavit-Hartenberg parameters used in the index finger model

| Linkage No. i | α_{i-1} | a_{i-1} | d_{i-1} | θ_i |
|-----------------|----------------|-----------|-----------|-------------------------------------|
| 1 | 0° | 0 | 0 | ω (MCP ab-ad) |
| 2 | 90° | 0 | 0 | $\theta_1 - 30^\circ$ (MCP flexion) |
| 3 | 0° | l_1 | 0 | θ_2 (PIP flexion) |
| 4 | 0° | l_2 | 0 | θ_3 (DIP flexion) |

The z -axis is in the direction of the joint axis.

α_{i-1} : Angle about common normal, from old z -axis to new z -axis.

a_{i-1} : Length of the common normal. Assuming a revolute joint, this is the radius about previous z .

d_{i-1} : Offset along previous z to the common normal.

θ : Angle about previous z , from old x to new x .

$$\begin{aligned} {}^0_4T = \left\{ \begin{array}{cccc} f(\theta_{1,2,3}, \omega) & f(\theta_{1,2,3}, \omega) & \sin \omega & f(\theta_{1,2,3}, \omega, l_{1,2}) \\ f(\theta_{1,2,3}, \omega) & f(\theta_{1,2,3}, \omega) & \cos \omega & f(\theta_{1,2,3}, \omega, l_{1,2}) \\ f(\theta_{1,2,3}) & f(\theta_{1,2,3}) & 0 & f(\theta_{1,2,3}, l_{1,2}) \\ 0 & 0 & 0 & 1 \end{array} \right\} \end{aligned} \quad (4.5)$$

4.3.2 Dynamics of the robotic finger system under PID control

This section presents experimental results on the dynamic behavior of the robotic finger system under PID control. In particular, the experiment investigated the combined dynamic behavior of the artificial finger and pneumatic actuation system in three tasks, which are (1) stabilization of the finger at pre-specified positions (set-points) and disturbance rejection; (2) set point change tracking; and (3) trajectory tracking. The PID control policies are constructed over tendon lengths to stabilize the finger at the prespecified set-point. Essentially, the PID control policy of each tendon is only a function of its own tracking error. Thus, control policies do not share tracking error information.

While choosing feasible set-points, each tendon was set to maintain some minimum tension (small pressure in each cylinder thus ensuring that tendons don't go slack) while

the finger was manually moved to a desired configuration. In the human hand, muscles switch from being active and pulling to being passive and stretched. Air cylinders were controlled in the same way in our experiments. Therefore this pulling-only transmission places an interesting constraint to the control system so that a tendon (e.g. PIP extensor) can only correct for the error in one direction (positive errors) and any error in the opposite direction (negative error) is regarded as a positive error for the antagonistic tendon(e.g. PIP flexor) and the artificial finger has to rely on the flexor to correct it.

The robustness of the PID controller and the nonlinearities of the underlying dynamics were investigated, by manually perturbing the finger (in opposite directions) at different set points. Disturbances are applied at $t = 5$ sec and 12 sec. To further investigate the dynamics of the robotic finger system we performed a second experiment in which we changed the set points periodically. Finally in our last experiment we tested the performance of the PID controller for the task of tracking sinusoidal-like trajectories in tendon space. The analysis of results focuses on the three tendons, namely, the central extensor, DIP and PIP flexors. Due to space limitations, this section only provides the results for trajectory tracking. Figure 4.12 illustrates the results.

Our observations regarding the dynamics of the pneumatic index finger under PID control are summarized below:

- The stabilization experiment demonstrates that PID control not only stabilizes the artificial finger around a set point but it can also quickly reject disturbances without creating unstable or marginally stable oscillations. It is characteristic that PID control responds within 2-4 ms of perturbations and can correct for disturbances of magnitude 1.5 cm to the finger tip (2.25 mm for central extensor) within 20 ms.
- The response of the robotic finger system to disturbances depends a lot on the tuning of the PID gains. Different levels of sensitivity were found to be tendon and posture dependent. Overall, the dynamics of the index finger are more sensitive with respect to the PID gains of the central extensor tendon and the two flexors PIP and DIP and less sensitive to the other two tendons.

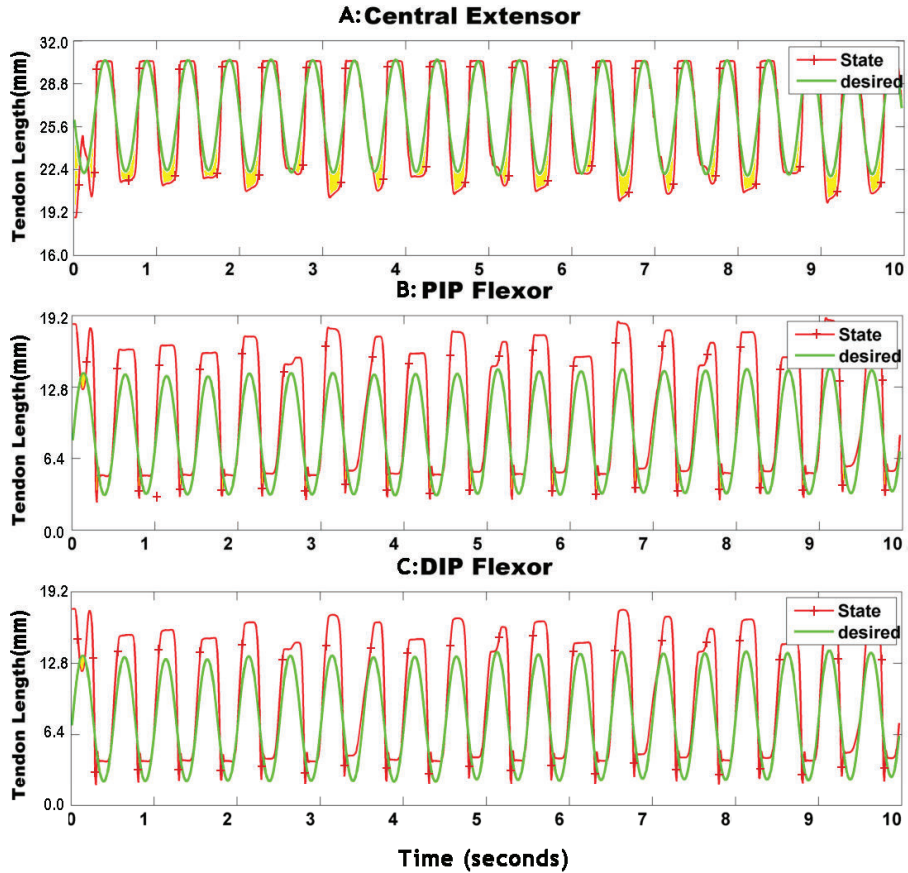


Figure 4.12: Desired and actual tendon excursion for central extensor (A), PIP (B) and DIP (C) tendons for the trajectory tracking task.

- For every stabilization point there is a different set of PID gains (Horizontal Position: $K_p = 0.4$, $K_i = 0.3$, $K_d = 0.005$). Thus, there are no universal PID gains for stabilization and disturbances rejection at different joint space configurations of the finger. The aforementioned observation is an indication of the strong nonlinearities of the underlying dynamics.
- The performance of the PID control varies in the three tasks of stabilization around one set point, set point tracking and trajectory tracking. Tuning the P, I and D gains for tracking error minimization of a particular tendon does not imply total tracking error minimization.

This nonlinear effect arises from the fact that control policies can correct only for positive errors and they have to rely on their opponent(antagonist) for the case of negative errors. Moreover the feedback control of individual tendon does not incorporate tracking errors of other tendons. For such a nonlinear system, a linear controller (PID) can no longer take care of the nonlinearities of the system.

The human fingers are actuated through flexors and extensors whose routing and pathway are highly nonlinear, particularly when bones slide over each other at the joints and are constrained by the surrounding soft tissues. The artificial finger biomechanically resembles its human counterpart, therefore the manner in which the tendons interact with the artificial joint capsule change the moment arms as a function of the joint space with respect to different configuration of the artificial finger.

The limitations mentioned above motivate the need for the development of a model based controller that makes informed policy decisions using the entire state space of the tendons while it also takes into account the moment arms at different joint space configurations of the artificial finger.

4.3.3 Model based control

Ideally the piston force can be controlled with minimal delay. This is difficult to achieve in pneumatic systems because the air dynamics have non-negligible time constants that depend on multiple factors such as compressor pressure, valve throughput and response time, length of the air tubes between the valve and the cylinder, volume of the chamber, and air temperature. These effects are hard to model accurately, yet for control purposes it is important to have a model that enables the controller to anticipate the resulting delays and compensate for them. To this end, a simple model of how the pressure difference D evolves over time was constructed:

$$dD/dt = A(V) + B(V)D \quad (4.6)$$

This is a first-order linear filter, modeling the rate of change of D as a function of the current value of D , and the coefficients A, B which are some to-be-determined functions of

the command voltage V . The shape of these functions was measured empirically as follows. A sequence of step voltages (with 2.5 sec duration) was applied, such that D settled into one of its extreme values (V_e), and then was driven towards some intermediate value using an intermediate voltage command (V_i) as shown in Figure 4.13. The piston was fixed in these experiments, so that changes in chamber volume did not affect the results. Figure 4.14 shows that our simple model is actually quite reasonable. Note that the valves have an internal delay of around 6-7 msec, but after that delay very rapid changes in pressure were observed, with rates on the order of thousands of PSI per second.

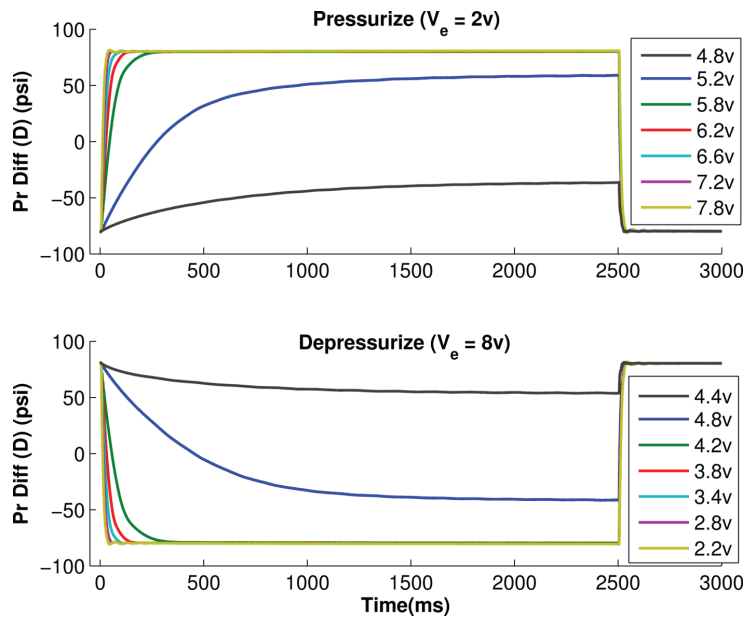


Figure 4.13: Pressure difference (D) behavior of pressurization and depressurization at different voltage levels (V_i).

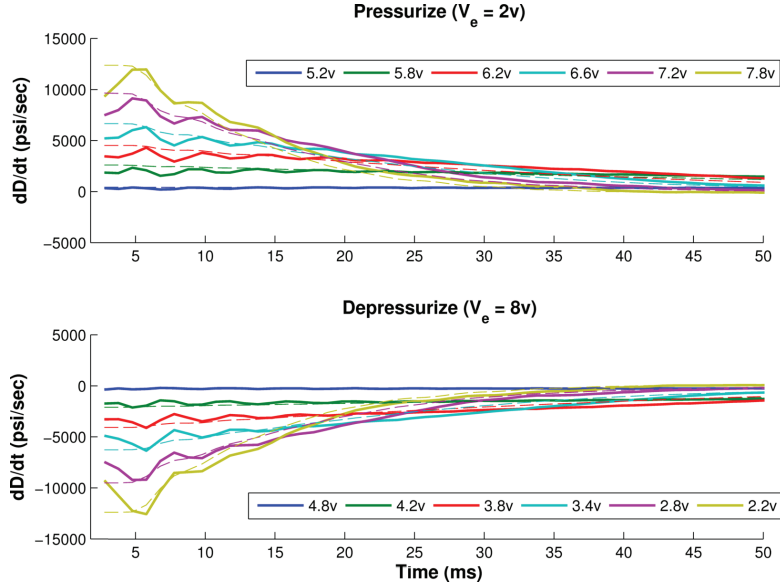


Figure 4.14: Pressure difference rate (dD/dt) of pressurization and depressurization at intermediate voltage levels (V_i). Solid lines represent original values and dashed lines represent values predicted by model. Pneumatics incurs a latency of 6-7 msec before reaching its maximum effect.

These curves were fitted with exponentials so as to determine the coefficients A and B for every value of V . This model enables us to implement a high-level controller whose output specifies the desired rate of change in D . We can then invert the functions $A(V)$ and $B(V)$ numerically while keeping D fixed to the currently measured value, and in this way calculate the voltage command V needed to achieve the specified rate of change of D .

4.3.4 Kinematic model of the robotic finger system

A kinematic model of the artificial finger and its tendon paths was constructed [33]. This was done by taking the numeric data from the CAD file used to 3D-print the finger, and importing it in an XML file that was then read by our modeling software. The software – called MuJoCo which stands for Multi-Joint dynamics with Contact – is a full-featured new physics engine, with a number of unique capabilities including simulation of tendon actuation [85]. In this chapter the kinematic modeling features of the engine is employed,

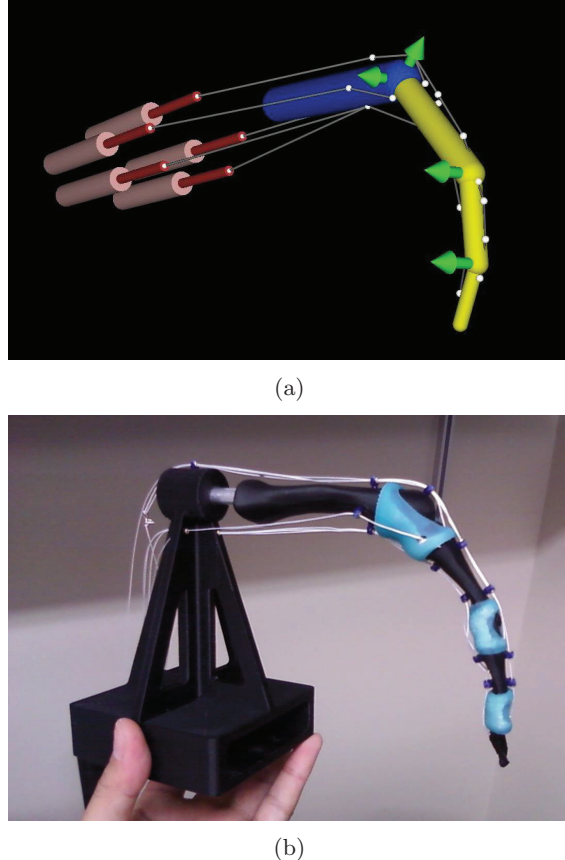


Figure 4.15: Comparison between the MuJoCo based simulation model and the physical prototype. (a) 3D Visualization of the kinematic model of the robotic finger in OpenGL. (b) Proposed biomimetic artificial finger.

as well as the built-in OpenGL visualization illustrated in Figure 4.15.

The skeletal modeling approach is standard: the system configuration is expressed in joint space, and forward kinematics are used at each time step to compute the global positions and orientations of the body segments along with any objects attached to them (such as sites used for tendon routing). Tendon modeling is less common and so our approach will be explained in more detail. The artificial finger is designed so that the tendons can be routed through special attachment points (as opposed to wrapping over curved surfaces). This greatly simplifies the model, because the tendon length is simply the sum of the linear segments connecting the routing points. Of course these lengths change as a function of

joint configuration.

Let \mathbf{q} denote the vector of joint angles, and $\mathbf{s}_1(\mathbf{q}), \dots, \mathbf{s}_N(\mathbf{q})$ denote the 3D positions (in global coordinates) of the routing points for a given tendon. These positions are computed using forward kinematics at each time step. Then the tendon length is

$$L(\mathbf{q}) = \sum_{n=1}^{N-1} \left((\mathbf{s}_{n+1}(\mathbf{q}) - \mathbf{s}_n(\mathbf{q}))^T (\mathbf{s}_{n+1}(\mathbf{q}) - \mathbf{s}_n(\mathbf{q})) \right)^{1/2} \quad (4.7)$$

The terms being summed are just the Euclidean vector norms $\|\mathbf{s}_{n+1} - \mathbf{s}_n\|$, however they are written explicitly to clarify the derivation of moment arms below.

Moment arms are often defined using geometric intuitions – which work in simple cases but are difficult to implement in general-purpose software that must handle arbitrary spatial arrangements. Instead the more general mathematical definition of moment arm was used in this chapter, and is defined as the gradient of the tendon length with respect to the joint angles. Using the chain rule, the vector of moment arms for the tendons is

$$\frac{\partial L(\mathbf{q})}{\partial \mathbf{q}} = \sum_{n=1}^{N-1} \left(\frac{\partial \mathbf{s}_{n+1}(\mathbf{q})}{\partial \mathbf{q}} - \frac{\partial \mathbf{s}_n(\mathbf{q})}{\partial \mathbf{q}} \right)^T \frac{\mathbf{s}_{n+1}(\mathbf{q}) - \mathbf{s}_n(\mathbf{q})}{\|\mathbf{s}_{n+1}(\mathbf{q}) - \mathbf{s}_n(\mathbf{q})\|} \quad (4.8)$$

This expression can be evaluated once the site Jacobians $\partial \mathbf{s} / \partial \mathbf{q}$ are known. MuJoCo automatically computes all Jacobians, and so the computation of moment arms involves very little overhead.

The extensor tendon of the artificial finger uses a pulley mechanism, which is modeled as follows. The overall tendon length L is equal to the sum of the individual branches, weighted by coefficients which in this case are 1/2 for the long path and 1/4 for the two short paths. Once L is defined, the moment arm vector is computed as above via differentiation.

Numerical values for the moment arms computed by the model in the resting finger configuration (45° at the MCP, 35° at the PIP, and 25° at the DIP) are shown in Table 4.5. These values change with finger configuration in a complex way, and are automatically recomputed at each time step. Moment arms are useful for computing the tendon velocities given the joint velocities:

Table 4.5: Moment arms that the simulator computed in the default posture (in mm)

| <i>Finger joint</i> | <i>Central extensor</i> | <i>DIP flexor</i> | <i>PIP flexor</i> | <i>Abduction tendon</i> | <i>Adduction tendon</i> |
|---------------------|-------------------------|-------------------|-------------------|-------------------------|-------------------------|
| MCP (ab/ad.) | 0.00 | -0.00 | 0.00 | -8.44 | 8.86 |
| MCP (fl/ex.) | 10.93 | -13.47 | -13.47 | -6.17 | -6.06 |
| PIP (fl/ex.) | 1.81 | -7.99 | -7.99 | 0.00 | 0.00 |
| DIP (fl/ex.) | 1.13 | -6.14 | 0.00 | 0.00 | 0.00 |

$$\dot{L} = \frac{\partial L(\mathbf{q})}{\partial \mathbf{q}} \dot{\mathbf{q}} \quad (4.9)$$

and also for computing the vector of joint torques τ caused by scalar tension f applied to the tendon by the corresponding linear actuator:

$$\tau = \left(\frac{\partial L(\mathbf{q})}{\partial \mathbf{q}} \right)^T f \quad (4.10)$$

Note that these are the same mappings as the familiar mappings between joint space and end-effector space, except that the Jacobian $\partial L/\partial \mathbf{q}$ here is computed differently. Another difference of course is that tendons can only pull, so $f \leq 0$.

To validate the kinematic model, the following experiment was conducted. Infrared markers (PhaseSpace, 120 Hz sampling rate) were attached to the fingertip, proximal finger segment, and the moving part of each cylinder. Another 3 markers were attached to the immobile base so as to align the reference frames of the motion capture system and the model. All markers were attached at known positions which we entered into our kinematic model as sites (discrepancy is within 2mm), similar to the sites used to route tendons. The cylinders were pressurized slightly so that they always pulled on the tendons and prevented tendon slack. The artificial finger was manually moved to different poses in its workspace, attempting to span the entire workspace. After each repositioning an interval of a few seconds was used, so as to let everything "settle" and obtain clean position data.

The data analysis began with frame alignment, by subtracting the translational bias

between the centers of mass of the modeled and measured base marker positions, and then performing orthogonal Procrustes analysis to compute the optimal rotation between the motion capture and model frames. The data for the moving markers were then transformed into the model coordinate frame, and were further processed as follows. Our approach implemented a MATLAB script that automatically identified non-overlapping time intervals in which every marker position remained within a ball of radius 2 mm (i.e. all markers were stationary), and averaged the position data for each marker within each time interval. This yielded 460 data points, each consisting of the 3D positions of the 7 mobile markers (5 on the cylinders, 2 on the finger).

The next step was to infer the joint angles of the finger given the positions of the two finger markers. This was done by an automated procedure (which is part of the MuJoCo engine), whereby the residual difference between the observed and predicted marker positions is minimized with respect to the set of joint angles (note that the predicted positions are functions of the joint angles). The minimization is done using a Gauss-Newton method with cubic line-search. Even at the optimal joint angles, there was some residual in the marker positions (around 5 mm on average) which we believe is mostly due to the fact that the finger is somewhat flexible and has additional degrees of freedom (even though their range of motion is very limited). Data points where the residual was larger than 7 mm were excluded from further analysis, leaving us with 400 data points.

Once the joint angles in each pose were inferred, our proposed tendon model was applied to compute the predicted tendon lengths, and the results were compared to the measured positions of the cylinder markers. The comparison is shown in Figure 4.16 for all five tendons. Overall good fit was observed, especially for the flexors and extensor that have larger excursions. The adduction tendon shows saturation, which might be caused by the position limiter on the cylinder (those limiters were just placed outside the range of the finger motion, but this one ended up inside the range) causing the tendon to go slack in some extreme poses. The abduction tendon is the most noisy, which we believe is due to the fact that it presses on the joint capsule and curves over it. This can be corrected by adjusting the routing points.

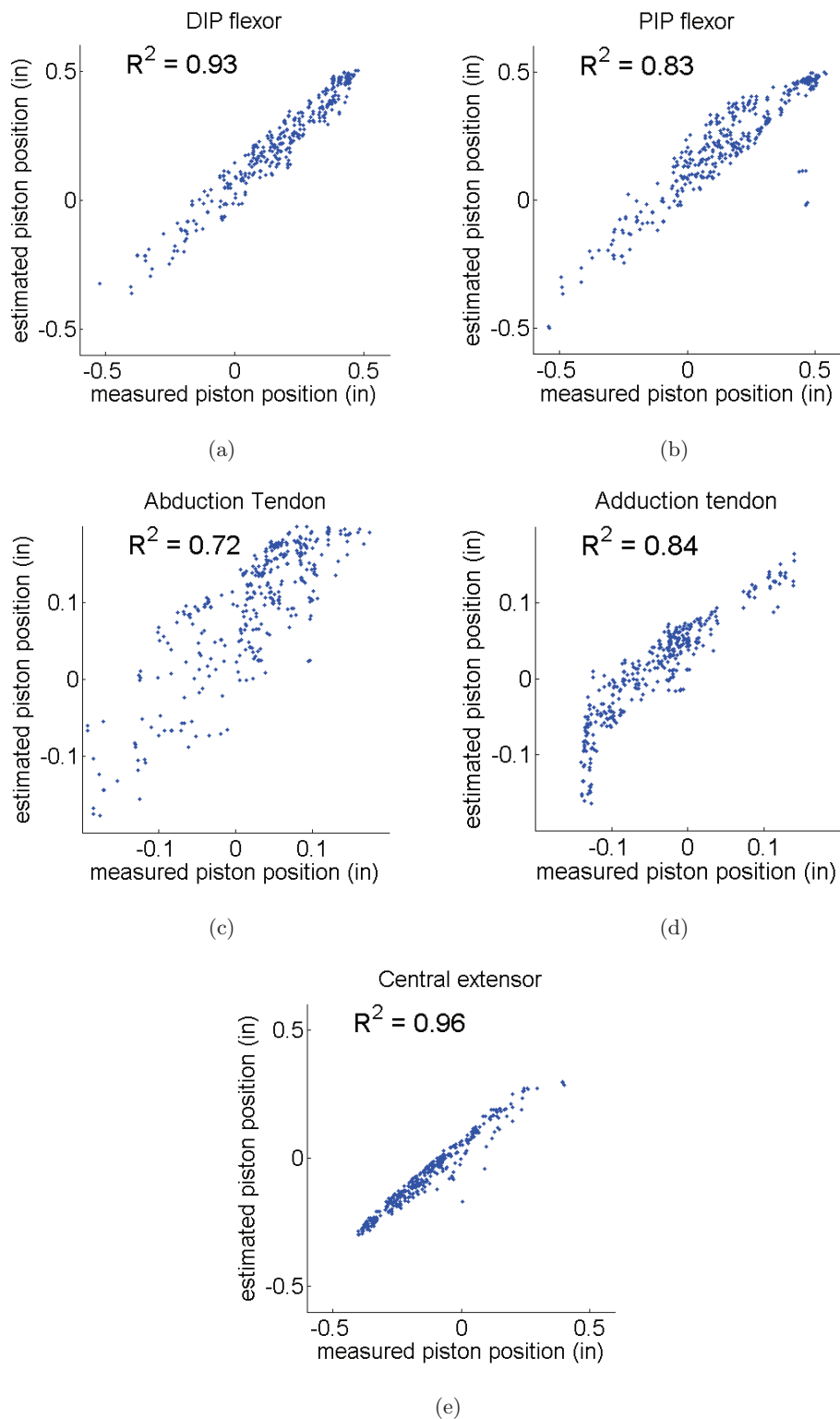


Figure 4.16: Comparison of measured and estimated tendon excursion data.

4.4 Discussion

This chapter described the design and modeling of a biomimetic artificial finger that has the potential to become a close replica of the human finger. The robotic finger system makes use of three main components: a modular design of the 3D printed finger segments, a series of simplified pulley based tendon mechanism, and a model based pneumatic actuation system for mimicking the contraction-only muscle behavior. The series of experiments on stabilization, disturbance rejection and tracking under PID control suggest that our robotic finger system presents a highly non-linear dynamics. The kinematic model of the artificial finger system is constructed with help of MuJoCo - a physics engine custom-developed - to simulate the interaction between the finger's joints and tendons. Experimental data of the tendon excursions are used to validate the efficacy of the simulation model. Overall good fits have been observed in the DIP, PIP flexors ($R^2 = 0.93$ and $R^2 = 0.83$) and central extensor ($R^2 = 0.96$) along which large excursions commonly occurred.

Thus far the entire actuation system and models of the kinematics and air dynamics have been built and established for the artificial finger. Our experimental results on stabilization and tracking with PID control motivate our future research towards system identification and model based control. At the system identification level, the next step is to identify the dynamics of the pneumatics and integrate the resulting model with the proposed kinematic model of the artificial finger and its tendons. On the control theoretic aspect, additional future work is to use model based techniques with variable sensitivity to model errors and contact discontinuities. These methods span the range of optimal, model predictive control and nonlinear methods such as back-stepping control. We also believe that a deeper understanding of the unique biomechanical features of human hands will provide greater insight into future designs of anthropomorphic robotic hands.

Chapter 5

ARTIFICIAL SKIN

In order to design an anthropomorphic robotic hand that can reproduce human level dexterity the challenge of providing adequate tactile sensing has to be overcome, largely because of its importance for dexterous manipulation. In order to better understand the complexity of touch we must examine the sensorial organs of the hand.

The human hand's sensory receptors are distributed underneath different layers of skin and serve different haptic modalities. For instance, Meissner's corpuscles and the Merkel disk receptors are the most numerous and are distributed preferentially on the distal half of human's fingertip. Due to their different embedded depths, the former are most sensitive to mid-range stimuli (20-50 Hz), whereas the latter are most responsive to low frequencies (5-15 Hz) [86]. It has been shown that the human hand's dexterity is largely affected by the sensory feedback from those receptors; with less sensory information the time for human subjects to complete a dexterous task can be increased up to 80% [87].

Similarly, the need for tactile sensing is a basic requirement for robotic manipulation during tasks such as precision grip, grasping point determination, pressure/force measurement, and pre-slip detection. So far numerous efforts have been put into the design of artificial skin. And, researchers have developed tactile sensors based on the characteristics of different materials such as, conductive rubber [88], fabric [89], gel [90], and ink [3]. Meanwhile, optical or vision based sensing [6, 91], ultrasonic [92], and piezoelectric sensors [93] have been proposed. Integrated systems such as, a tactile sensing system for the Utah/MIT Dextrous Hand [94], a soft fingertip with randomly distributed receptors [95], a robust biomimetic tactile sensor array [96], and a seashell effect based pretouch sensor [97] have also been developed. Other issues such as cost effectiveness, complexity, fusion with the different existing robotic hand systems, design of the thumb web, and optimization of the skin design are often omitted. Consequently, many anthropomorphic robotic hands perform

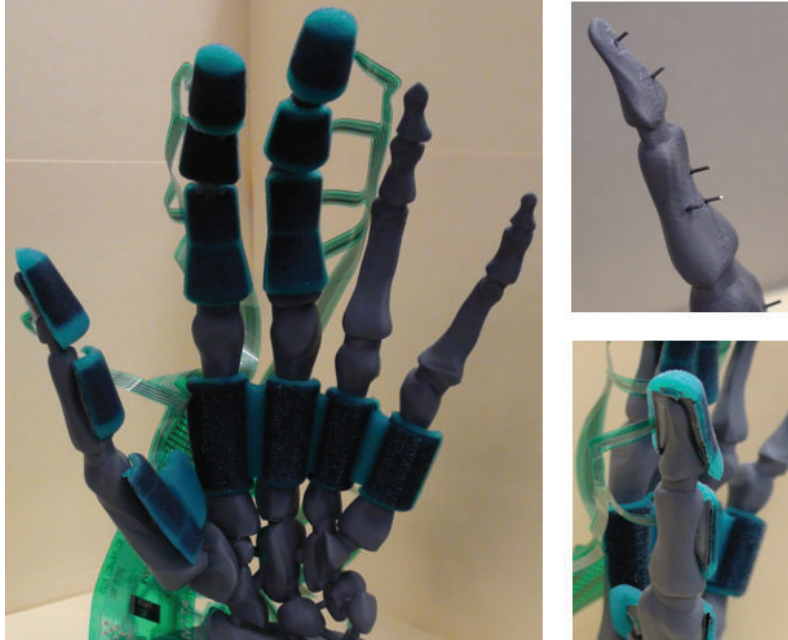


Figure 5.1: Detachable artificial skin pads attached onto the ACT Hand model. *Top right:* A side view of the thumb’s skeleton with steel pins attached. *Bottom right:* A back view of artificial skin pads mounted onto the thumb.

manipulation tasks without tactile sensors, precluding potential performance increases.

Previously, in the NeuroRobotics lab we have developed the Anatomically Correct Testbed (ACT) Hand as a platform for exploring dexterous hand motions and neural control strategies [8, 75–77]. The ACT hand provides a unique and compelling opportunity to study tactile sensation with an anthropomorphic robotic hand that closely mimics a human’s. In this chapter, we present the design for a set of tactile skin pads that can be attached to their corresponding phalanges of the ACT Hand (as shown in Figure 5.1). Each of the skin pads is designed based on the unique shape of its finger’s counterpart and can be easily snapped on and off from the ACT hand’s skeleton. Because of our flexible design methods these skin pads can be easily adapted for use with any other robotic hand.

The goal of this chapter is to detail a design strategy that can be directly applied to most of the existing anthropomorphic robotic hands with little effort or modification. Although, there are other important factors like visual feedback [29], fingertip position [98], and hand

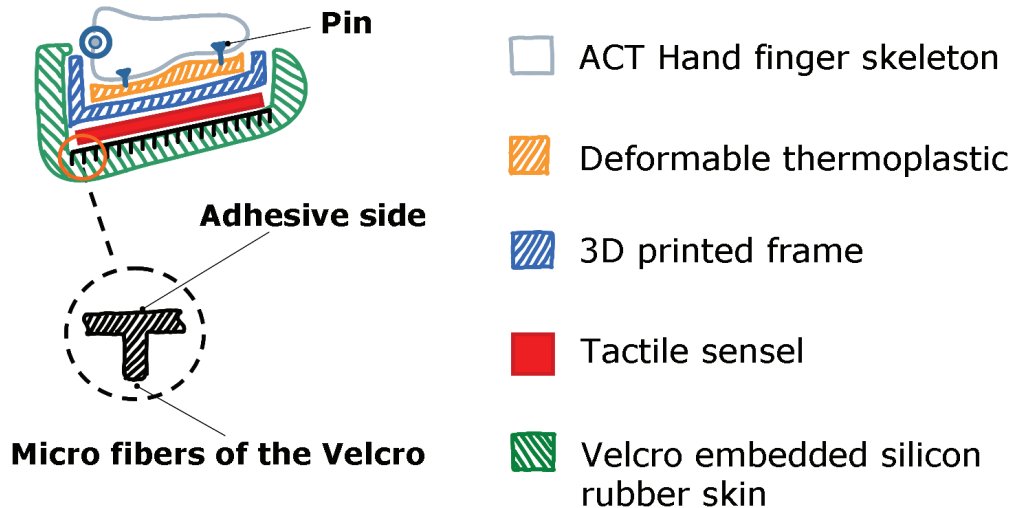


Figure 5.2: Schematic drawing of artificial skin’s multi-layered structure (Note: Differently colored regions are not in proportion to the real distributions of those layers.)

preshape [99] which affect object manipulation, we are interested in how the design of the artificial skin itself can potentially improve the functionality of a robotic hand. In the following sections our proposed design methods are explained, then the importance of fingertip shape on precision grip and the future work are addressed [100].

5.1 Development of the artificial skin

This section describes the mechanical design and prototyping process of our artificial skin. Although it is designed for the ACT hand, the method itself is compatible with other robotic hands.

5.1.1 Multi-layered design

The sensing field of the artificial skin is composed of 16 independent skin pads, each of which consists of four layers as shown in Figure 5.2. From the skin’s surface (top) to the skeleton (bottom), they are: Velcro embedded in artificial skin (silicon rubber), a tactile sensing element (sensel), a 3D-printed frame, and some reshaping thermoplastic.

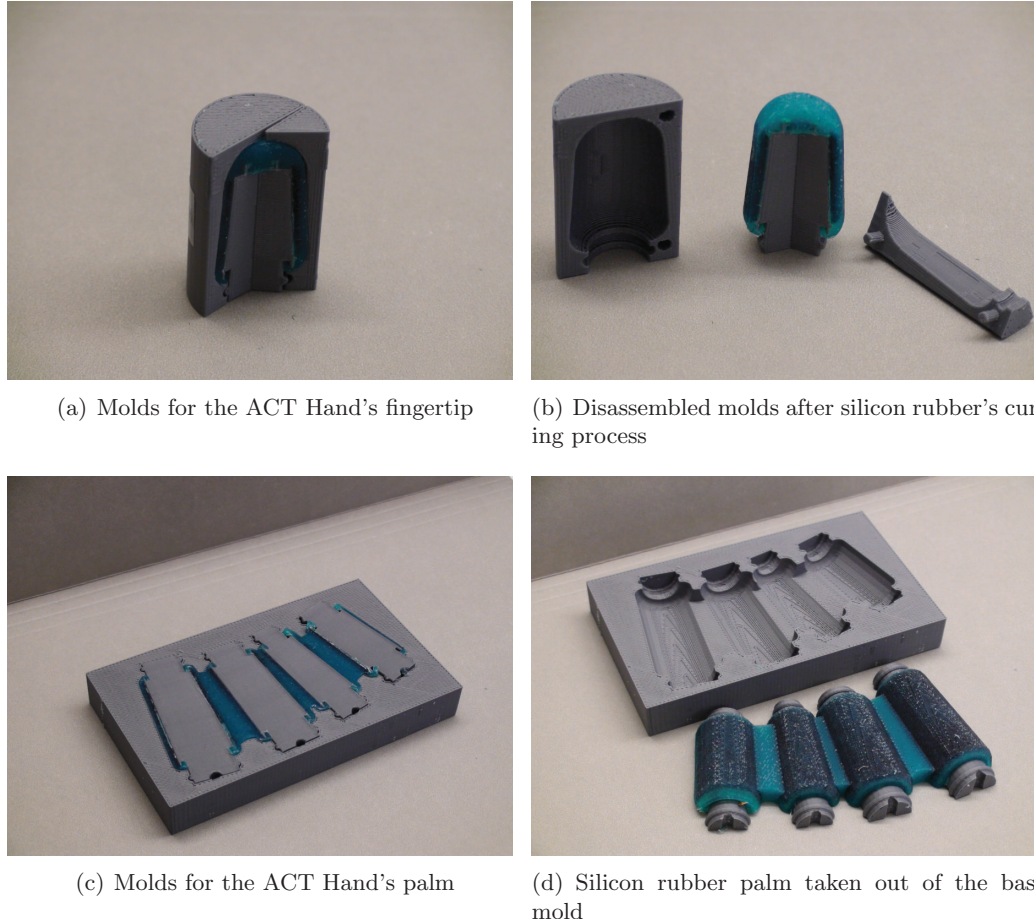


Figure 5.3: Components of the molds used for prototyping ACT Hand's fingertip and palm.

The layer of artificial skin is made of silicon rubber (PlatSil® 71 Series RTV, Polytek Development Corp., Easton, PA) with high shear strength. Its shape is cast by a set of 3D printed molds (see Figure 5.3) which forms a tapered shape resembling the pad of the human's fingertip. The fingerprint on its contacting surface can be custom designed to possess different surface textures which will affect its sensing performance. The hydrophobic property of the silicon rubber provides the artificial skin with beneficial properties such as easy-clean, water and oil resistant, and anti-smudge coatings but this also prohibits the silicon from sticking to any adhesive. This poses a big challenge when bonding it with neighboring layers. This problem has been innovatively solved by making the most of

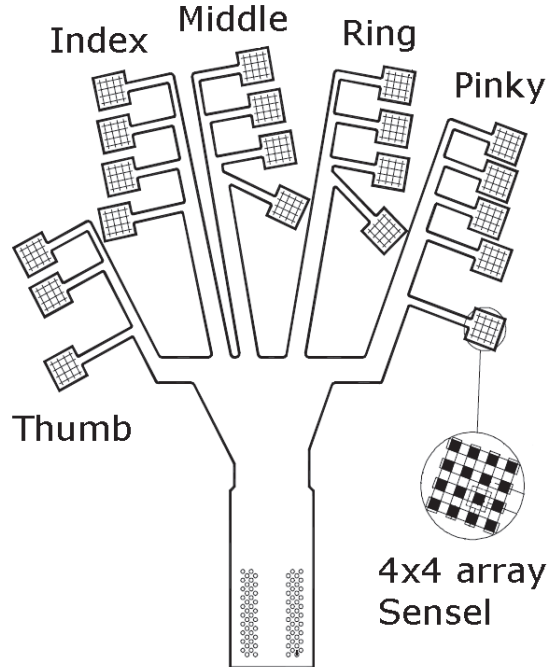


Figure 5.4: Configuration of the tactile sensor (Tekscan Inc., South Boston, MA) as the 2nd layer of the artificial skin.

Velcro as follows: Before the silicon rubber becomes fully cured, a slice of Velcro (loop side) is embedded into the skeletal side of the skin layer. After the curing process, the Velcro is securely bonded due to the strong interaction between a large number of micro fibers and their surrounding silicon rubber. The whole skin layer can then be easily adhered to the sensel through the adhesive surface of the Velcro. The total thickness of this top most layer through to the Velcro is about 2.5mm. To achieve optimal performance (and durability) of the silicon rubber a vacuum chamber is used to remove any air bubbles from the silicon mixture before curing.

The second layer is formed by a 4×4 (20×20mm in dimension) sensel array from an off-the-shelf five finger Grip TM system (Tekscan Inc., South Boston, MA) for identifying the location and magnitude of pressure points on the hand (see Figure 5.4). The Grip TM system made in this way has paper-thin flexibility (0.1mm in thickness). After binding

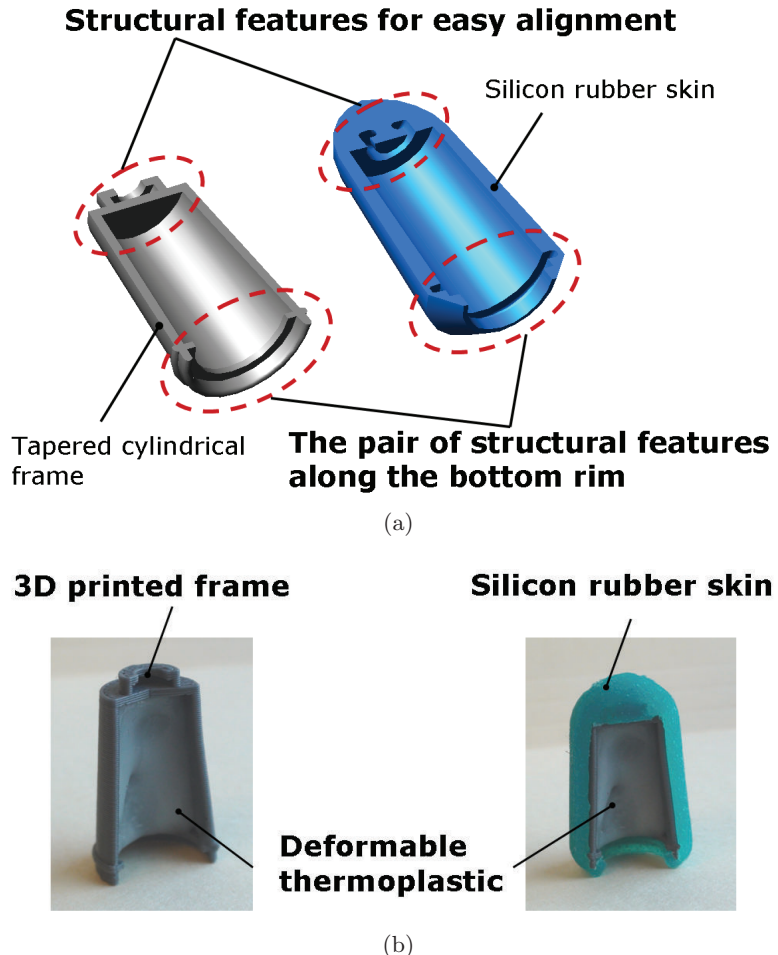


Figure 5.5: Tapered cylindrical frame (index fingertip) functioning as the skeleton of the artificial skin.

with the Velcro's adhesive surface, the sensor layer is carefully wrapped onto the 3D printed frame and attached with an adhesive (3M 77 spray adhesive). The sensel is more strongly bound to the printed frame than the Velcro; the bonding on either side of the sensel prevents slippage.

The third layer is a tapered cylindrical frame which is 3D printed by the Dimension BST 768 (Stratasys Corp., Eden Prairie, MN). It works as a skeletal component of the whole structure, and determines the basic shape and contour of the artificial skin. As we

mentioned, its outer surface is bonded with the tactile sensel, while its other side is fused with the thermoplastic layer. Along the rim of this printed frame, structural features such as the ones shown in Figure 5.5 are designed to fit corresponding spots "Lego-style" on the silicon rubber skin. This module design makes maintenance of the artificial skin possible, worn silicon rubber can easily be snapped off and replaced with a new one. Because the Velcro's bonding with the sensel is weaker than the sensel's bond to the frame the sensel remains attached to the frame during replacement.

The last layer is used to couple the artificial skin with its corresponding finger skeleton on the ACT hand, this layer is made of deformable thermoplastic (Shapeloock Corp., Sunnyvale, CA). After being heated and becoming soft, the thermoplastic is first molded onto the printed frame, and then shaped by the complex surface of the finger bone. After cooling down, small pins (0.5 mm in diameter, 3 mm in length) are attached onto the palm side of the ACT Hand (see Figure 5.6 (b)) to pair with the holes pre-drilled on the corresponding thermoplastic sections. The entire skin pad can be easily snapped on and off from the finger skeleton without affecting the robotic hand's functionality.

5.1.2 Modular design and the thumb web

On the ACT Hand the thumb, index, and middle fingers are actuated by tendons (routed anatomically) and muscle-equivalent actuators (motors). As addressed above, the artificial skin designed for the ACT Hand, has 16 total sensels fitted into its multi-layered structure. In order to avoid possible interference with the complex extensor hood of the ACT Hand's tendons [75], each segment of the artificial skin is designed to cover 180° of the palm side's sensor field; where receptors have been known to have the highest density in human's hand [86] (see Figure 5.6 (a)). Depending on the phalange to which the skin pad is attached the total sensing area can be further categorized into 4 components namely thumb, index, middle, and palm.

For the index and middle fingers, each segment of the artificial skin has four sensels fitted in three sections: one distally, one in the middle, and two in the proximal phalange. The contour of their skin shapes is uniquely designed to mimic their human counterparts.

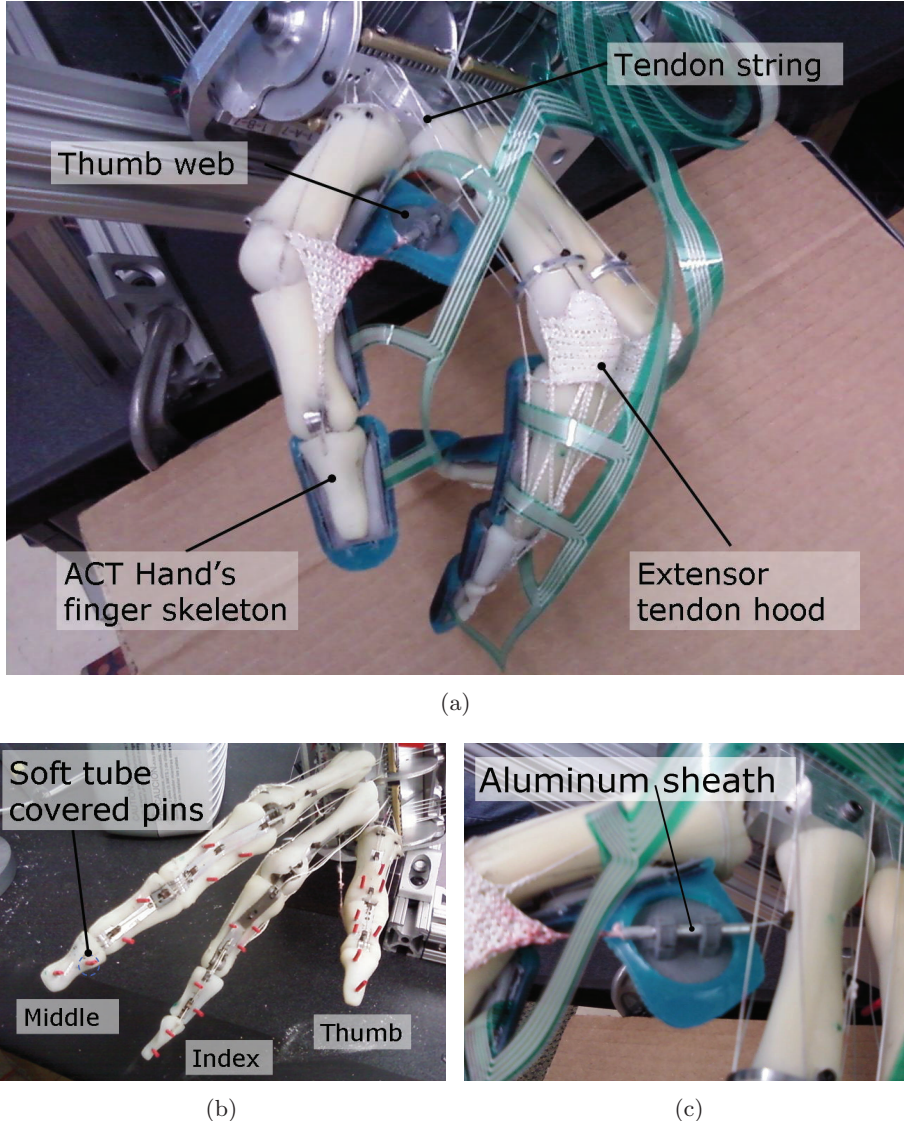


Figure 5.6: *Top Row:* The pictures of the ACT Hand with artificial skin attached. *Bottom Left:* Small pins attached onto the ACT Hand's thumb. *Bottom right:* Unique design of the thumb web.

The design of the thumb's skin components is quite different from the rest of fingers. This is due to the thumb's webbing (the flap of flesh between the thumb and index finger) whose function has been found to be critical to the use of trigger-operated tools [101, 102]. However, none of the existing anthropomorphic robotic hands take this important factor

into their design. As shown in Figure 5.6 (c), the artificial thumb web designed in our work incorporates a simple mechanism - a 15mm aluminum sheath - to enable the tendon string, which mimics the adductor pollicis (ADP) of the human hand, to serve the function of adducting the thumb. This sheath also maintains the correct position of the thumb's webbing between the thumb and index finger during motion. One sensel is fitted into each of the distal, middle, and proximal phalanges with a fourth placed into the thumb's webbing.

Four more sensels are reserved for the palm region that is directly under the index and middle fingers. These sensels provide supplementary information during the ACT hand's grasping tasks.

5.1.3 Adaptable design

3D printing technology provides a cost-effective way to make the adaptability of our proposed artificial skin flexible enough to meet different design requirements.

For robotic hands that need different fictional contact during object manipulation tasks, the shape, thickness, and surface of the skin pad can be easily modified and patterned with distinct textures by using different sets of 3D printed molds as shown in Figure 5.7. In addition, based on the different needs of tactile sensing, a variety of off-the-shelf tactile sensors [103] can also be directly integrated with our design.

Secondly, the combination of using 3D printed frame and deformable thermoplastic as the third and last layers makes our proposed skin design compatible with different finger topologies. In the case of the ACT Hand, the study of variable moment arms at each finger joint requires the coupling of skin pads to be compatible with bumpy finger surface while having no interference with the complex network of the tendon hood at the same time. And the effectiveness of the corresponding design solution has already been detailed in previous sections. Compared to the degree of complexities that the shape of the ACT Hand's finger bone has, most of existing robotic hands use simple geometric shapes (e.g. smooth circle and rectangle) for the finger's cross section, and do not have the constraints from complex, human-like tendon hood. Therefore when our proposed artificial skin design is adopted by other anthropomorphic robotic hands, the similar coupling strategy can be used with little

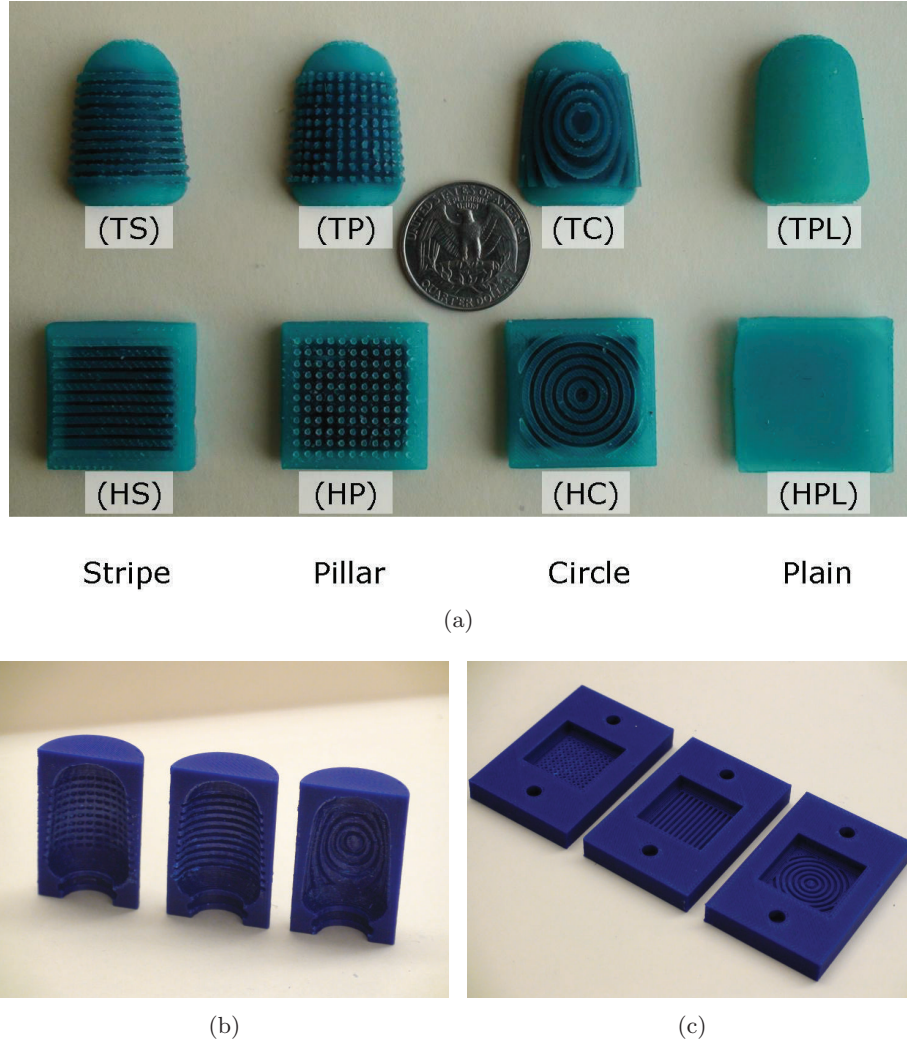


Figure 5.7: Adaptable design of the skin pads. *Top Row:* Eight sets of skin pads with four different textures (from left to right: stripe, pillar, circle and plain) on two types of skin shapes. *Bottom left:* Molds for tapered cylindrical skin pads. *Bottom right:* Molds for hexahedral skin pads.

effort or modification.

As detailed above, the concept of artificial skin with multi-layered detachable and modular design is compatible with most anthropomorphic robotic hands. This design can potentially improve manipulation performance by providing tactile sensing and more reliable grasping forces, as is discussed in the following section.

5.2 Experimental evaluation

A Precision grasp/grip is required when the object is small and can only be held between the fingertips of the thumb and fingers, for example in cases of grasping a pen or a needle. The precision grip forms an important category under the scope of dexterous manipulation, however the effects of skin design on the performance of the precision grasp are often omitted. Instead, a lot of the previous work focuses on providing enough grip forces during the power grasps; in these cases the contact areas between the robotic hand and an object are adequate for maintaining the dynamic stability of the task, thus the skin design is less critical. However, when an anthropomorphic robotic hand performs a precision grasp, the success of the task mainly relies on small contact areas at fingertips.

During a precision grasp, the artificial skin should be able to detect the magnitude and location of normal forces. Additionally the ability of detecting the occurrence of a slip, and ultimately preventing it from happening, is also preferred. Towards this goal, it is of our interest to investigate how the design of artificial skin can affect its performance during important precision grasp.

5.2.1 Experimental design and methods

We designed a series of experiments to identify the important factors that can potentially affect the detection of pre-slip with a 3-DOF Phantom Premium 1.5A (SensAble Technologies, Inc., Wilmington, MA). This hardware is back-drivable and accurate (0.03 mm resolution with 0.04 N backdrive friction), is capable of providing controllable force of a magnitude sufficient for simulating precision grasps.

Two different shapes of the probe were chosen to investigate the effect of pressure distribution on the artificial skin when pre-slip occurs. The length of the probe is designed in such a way that the center of the contacting point on the probe (as labeled as a red dots in Figure 5.8) could match that of the Phantom's end-effector. The spherical probe is chosen to test the artificial skin's sensing ability when the robotic hand performs precision grasp, where small contact areas are often limited to the fingertips. The size of the spherical probe

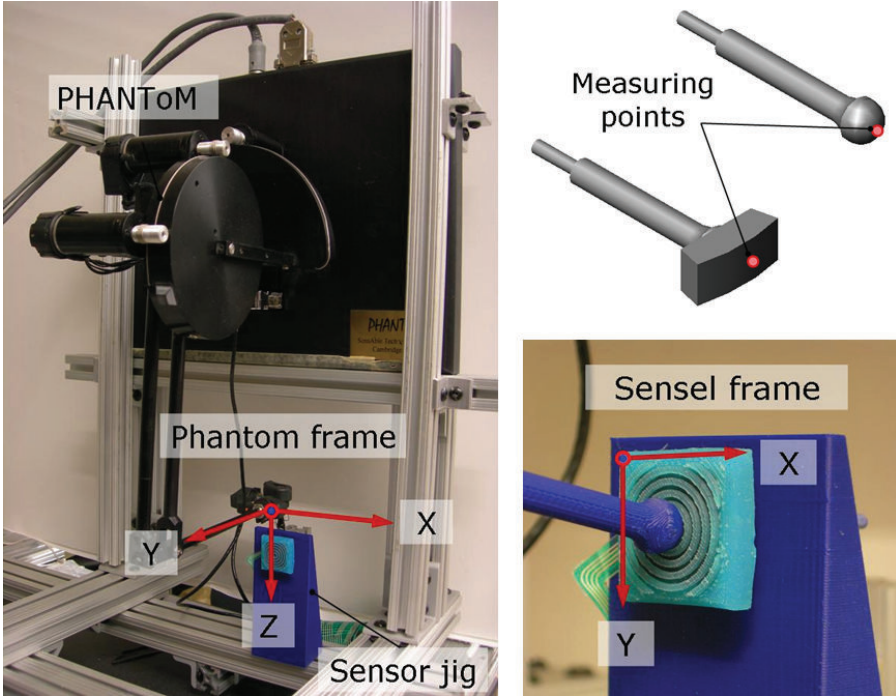


Figure 5.8: *Left:* Experimental setup. *Top right:* Two different shapes of the probes: the sphere (10 mm in diameter) and the curved surface (47 mm in radius). *Bottom right:* Initial test position. *Note:* The difference between the Phantom and sensel frames.

was decided based on a contacting surface test: A piece of planar glass was used to push against the artificial fingertip firmly, through the transparent glass the average diameter of the deformed area on the fingertip was then used as the diameter of spherical probe. The curvature of the second probe is extracted from a regular coffee mug in order to cover situations when power grasps are chosen with larger contact areas.

We also investigated the effects of different shapes and texture patterns of skin pads on the detection of pre-slip (as shown in Fig. 5.7 and Fig. fig:taperedFingertip). In total, we tested eight sets of skin pads with four different ridge patterns. The tested textures of the skin pad are defined as follows: stripe, pillar, circle, and plain. The different geometrical patterns of the texture are formed by the same type of ridges. The dimensions of the ridges are 1 mm in width and 1 mm in length with 1 mm interval between two ridges. The two

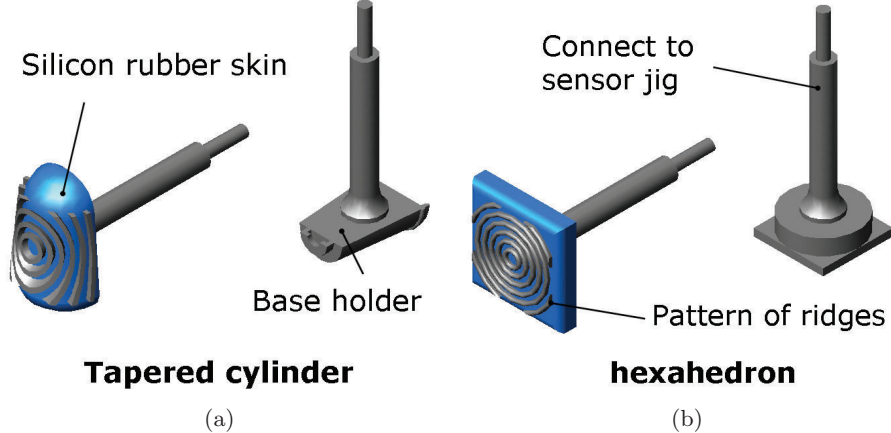


Figure 5.9: Examples of the skin pad used in the test. (a) CAD model of a tapered cylindrical skin pad. (b) CAD model of a hexahedral skin pad.

types of fingertip shapes are a tapered cylinder, and a hexahedron. Besides the human-like circle pattern firstly tested in this work, our variation of textures cover the most popular designs reported by previous research groups, e.g., smooth surface without ridges [6,95,104], pillars [105,106] and parallel ridges [107,108].

The experiment is to simulate the process of a gradually relaxed pinch grasp. Three trials were taken for each skin pad during the experiment. At the beginning of each trial, the probe was manually placed onto the spot close to the center of the skin pad fixed onto the sensor jig. And then the displacement, velocity, and forces of the probe at the contacting point were recorded at 1000 Hz. The average sampling rate of the force sensor used in this work is 20 Hz. Once the probe was positioned properly, 3.5 N of normal force in Y-direction, and a 1 N of tangential force in Z-direction (both in the Phantom frame) were simultaneously commanded onto the surface of the skin pad through the probe. While keeping the tangential force consistent, the normal force was controlled to gradually decrease with a constant rate of 0.3N/s. Each trial ends at the moment when the probe eventually slips off from the skin pad.

Raw data from the sensel were used to estimate the displacement of pressure center along vertical direction (in Sensel frame) by using the following equation:

$$D_{centroid} = \frac{\sum f_i y_i}{\sum f_i} \quad (5.1)$$

The force reading from the sensel at the center of pressure, with respect to the sensel frame is calculated as,

$$F_{centroid} = \frac{\sum f_i y_i}{\sum y_i} \quad (5.2)$$

In order to provide a metric to evaluate the design of each skin pad, in both shape and texture, we employ the slip ratio. Slip ratio has been used as an important factor to evaluate human subject's strategy to avoid slippage while performing a precision grasp [109, 110]. As shown in the equation below, it is proportional to the inverse of the coefficient of static friction and measured at the moment when slip occurs. A higher slip ratio corresponds to a more slippery surface.

$$\text{Slip ratio} = \frac{\text{Normal force}}{\text{Tangential force}} \quad (5.3)$$

The next section details the results collected from running our experiments on all skin pads with both the spherical and curved probes.

5.2.2 Results

Fig. 5.10 shows the results from the case of a spherical probe and hexahedral skin pad (with circled texture). The shaded areas in Fig. 5.10 (a) and (d) represent initial probe adjustment before trial onset. The contacting force was measured by the skin pad (see Fig. 5.10 (a)). The magnitude of the normal forces are gradually reduced to zero until the contact breaks. When the slip eventually occurs, the end time of each trial is marked by the peak reading from the probe's velocity curves (Fig. 5.10 (b) and (c)). Onset of each trial is defined by the peak of the sensels force readings. The calculated and actual displacements of the pressure center are compared in Fig. 5.10 (d). It is clear that the estimated center of pressure agrees quite well with the recorded data. And the trend of slip could also be

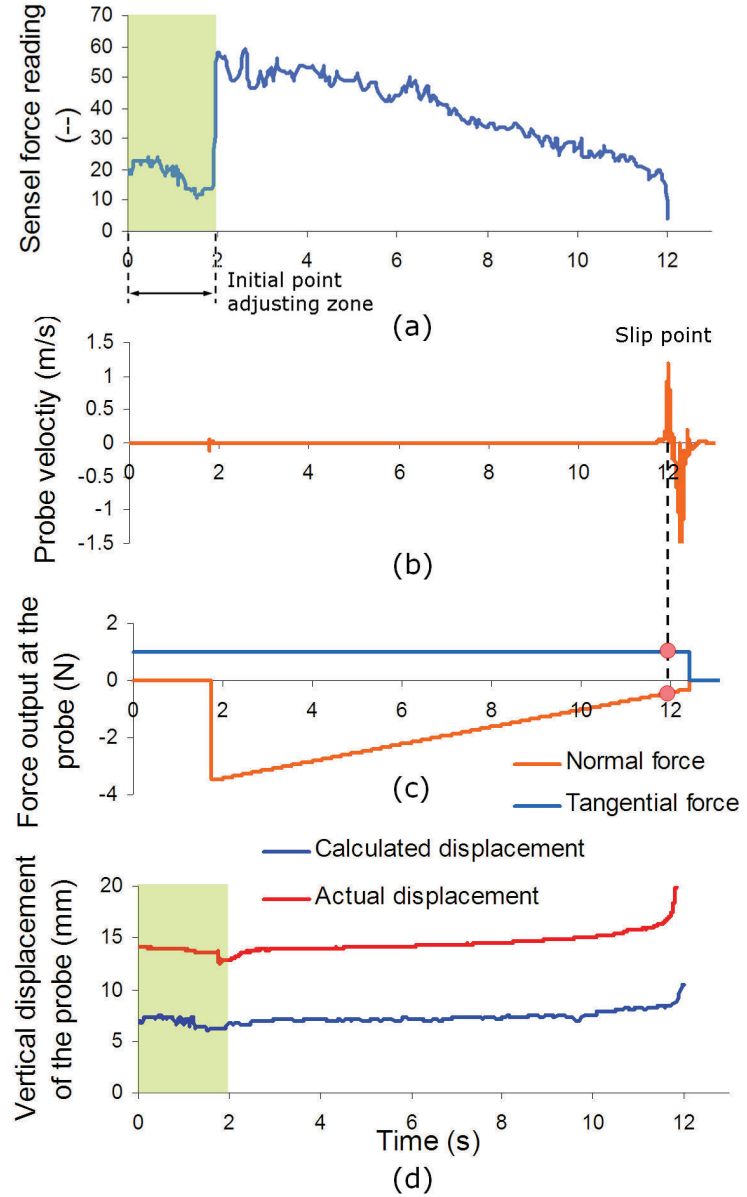


Figure 5.10: Outputs from the experimental setup. (a) Force reading from the sensel. (b) The probe velocity measured from the Phantom's end-effector. (c) The controlled normal and tangential forces from the Phantom robot. (d) Comparison of the calculated (in sensel frame, along Y-axis) and measured (in Phantom frame, along Z-axis) displacement of the probe along vertical direction.

Table 5.1: Results of slip ratios measured with spherical probe.

| <i>Skin pad type</i> | <i>The mean slip ratio (-)</i> | <i>The standard deviation (δ)</i> |
|----------------------|--------------------------------|---|
| TS | 0.344 (H. stripe) | 0.046 |
| | 0.392 (V. stripe) | 0.074 |
| TP | 0.509 | 0.014 |
| TC | 0.261 | 0.018 |
| TPL | 0.304 | 0.015 |
| HS | 0.363 (H. stripe) | 0.024 |
| | 0.510 (V. stripe) | 0.010 |
| HP | 0.559 | 0.041 |
| HC | 0.390 | 0.048 |
| HPL | 0.447 | 0.014 |

observed.

The time stamp labeled as the end of each trail is used to determine the slip ratio. Before the contact breaks, the pre-slip motion of the probe develops very slowly, therefore we can assume a quasi-static condition when the contact between the probe and the skin pad still exists. In 5.10 (b) and (c), the vertical dashed line represents the end time.

The slip ratios of the skin pads tested with the spherical and curved probes are listed in Table 5.1 and 5.2, respectively. Averaged values from three trials are presented. In the case of curved probe, only the results from hexahedral skin pads were collected because the inclination from the tapered cylindrical skin pad successfully prevented the slip-off from happening.

5.3 Discussion

In this section, the experimental results are discussed based on the comparison between hexahedral and tapered cylindrical skin pads in four categories: effects of skin textures on pre-slip detection, effects of ridge patterns on slip ratio, effects of contact areas on slip, and

Table 5.2: Results of slip ratios measured with curved probe.

| <i>Skin pad type</i> | <i>The mean slip ratio (-)</i> | <i>The standard deviation (δ)</i> |
|----------------------|--------------------------------|---|
| HS | 0.196 | 0.045 |
| | 0.421 | 0.019 |
| HP | 0.338 | 0.030 |
| HC | 0.349 | 0.016 |
| HPL | 0.351 | 0.010 |

the importance of choosing the right shape for the fingertip.

5.3.1 Effects of skin textures on slip detection

Fig. 5.11 shows the comparison of the pre-slip curves (along Z-direction in Phantom frame) between two types of skin pads when normal forces are gradually reduced at the contact point. The shaded areas are bounded by the start and end time of each trial. It is interesting to observe that under the same initial conditions, a smaller increase of the displacement (δ) was always identified in the case of using skin pads with plain surfaces. In contrast, larger displacement changes were prevailing among those skin pads implemented with ridges.

Various textures of skin pads can be easily achieved by using different geometric patterns of the ridges. Ridges on the artificial skin are often made of soft and elastic materials (e.g. silicone rubber) extruding out of the base materials (see Fig. 5.12). During object manipulation tasks, when the contact forces are large enough, soft ridges are bent and compressed forming an extra layer on top of base materials. As the contact gradually breaks with gradually reduced normal forces (F_N), since the ridges are softer than the base materials, many of them can still make good contact with surfaces of the object, but get locally stretched out along the pre-slip direction of the object under the effect of the tangential forces (F_T). In other words, the existence of ridges prolongs the slipping process and allows us to more easily detect the pre-slip by monitoring the values calculated for estimating the center of the contact forces. If the orientation of the ridges on the skin pad is

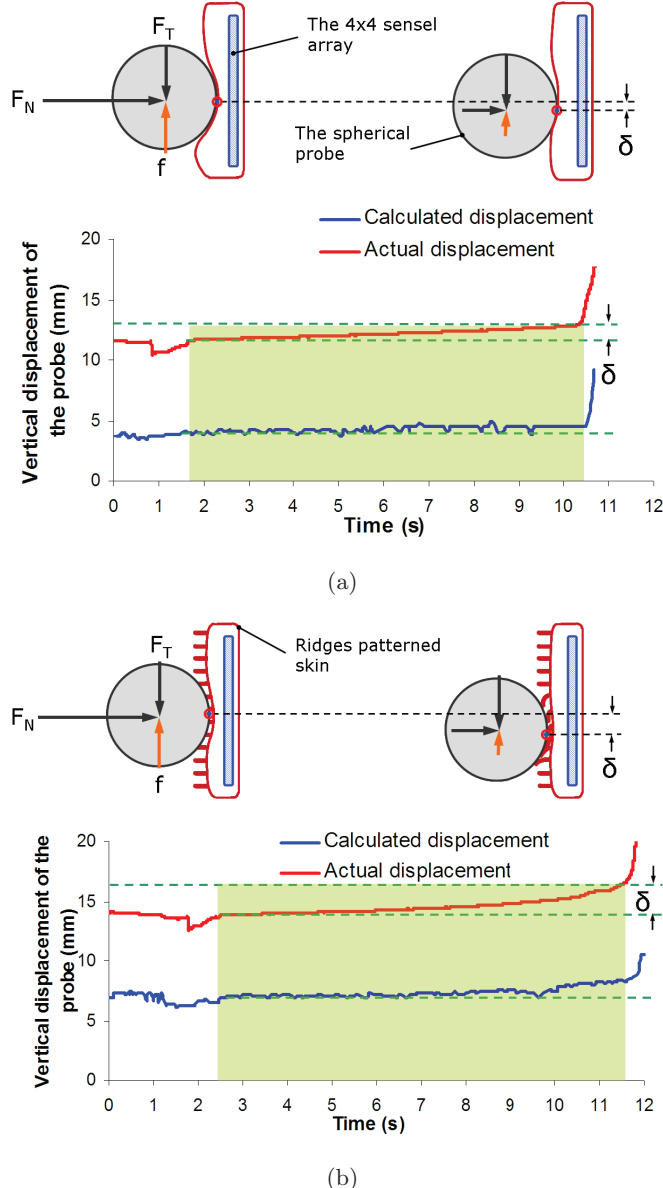


Figure 5.11: Comparison of the pre-slip curves between skin pads with/without texture. (a) Probe displacement on hexahedral skin pad with plain surfaces (HPL). (b) Probe displacement on stripe patterned, hexahedral skin pad (HS). *Note:* Spherical probe was used; The location of the forces are moved from the contact point to the center of the probe for easy reading; δ denotes the change of the vertical displacement.

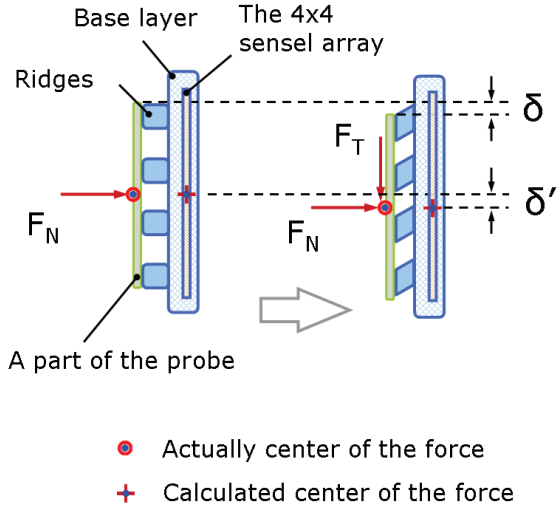


Figure 5.12: Schematic drawing showing the advantage of having ridges on pre-slip detection.

perpendicular to the sliding direction of the object, the resulting artificial skin design could potentially help prevent slip from happening.

On the contrary, in the case of using plain surfaces, a bump will be formed at the beginning of the contact when the normal force is strong enough to push the top layer of the soft materials down to a certain distance. Compared to these small ridges, the size of the bump is much larger and therefore won't be easily stretched. Although the bump can be pushed downward under the tangential forces, the existence of the bump functions more like a micro "wall" and therefore prohibits the occurrence of further displacement of the probe towards the pre-slip direction. Thus, when the slip of the probe eventually occurs, the abrupt moment of the probe is caused by the sudden disappearance of the "wall hump" effect. This effect can be clearly observed from the abrupt change of curves at the end of the experiment (see Fig. 5.11).

The result of the comparison experiment suggests that textured skin pads are more capable of detecting the occurrence of slip than the plain skin pads. Thus, when implementing the function of slip detection for a robotic hand, instead of upgrading force sensing system

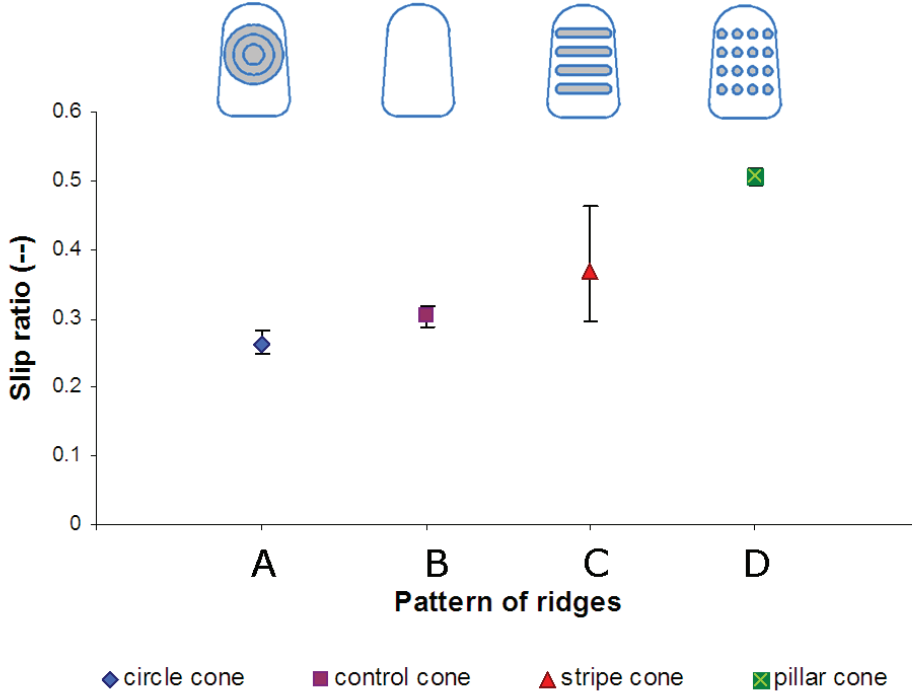


Figure 5.13: Slip-ratio measured on tapered cylindrical skin pads with spherical probe. *circle cone* stands for circle ridges pattern tested on the cylindrical skin pad.

to support high frequency sampling (higher 250 Hz), it can be more cost-effective to equip artificial skin with proper textures.

5.3.2 Effects of different texture patterns on slip ratio

Under the same testing conditions, a smaller slip-ratio suggests that the corresponding skin pad can provide more reliable gripping forces and better slip resistance. In this section, we compare the performance of different texture patterns on both tapered cylindrical and hexahedral skin pads.

In Fig. 5.13 and 5.14, an interesting trend is observed in both of the two cases: the average performance of the circle pattern is always above the rest of ridge patterns. Two

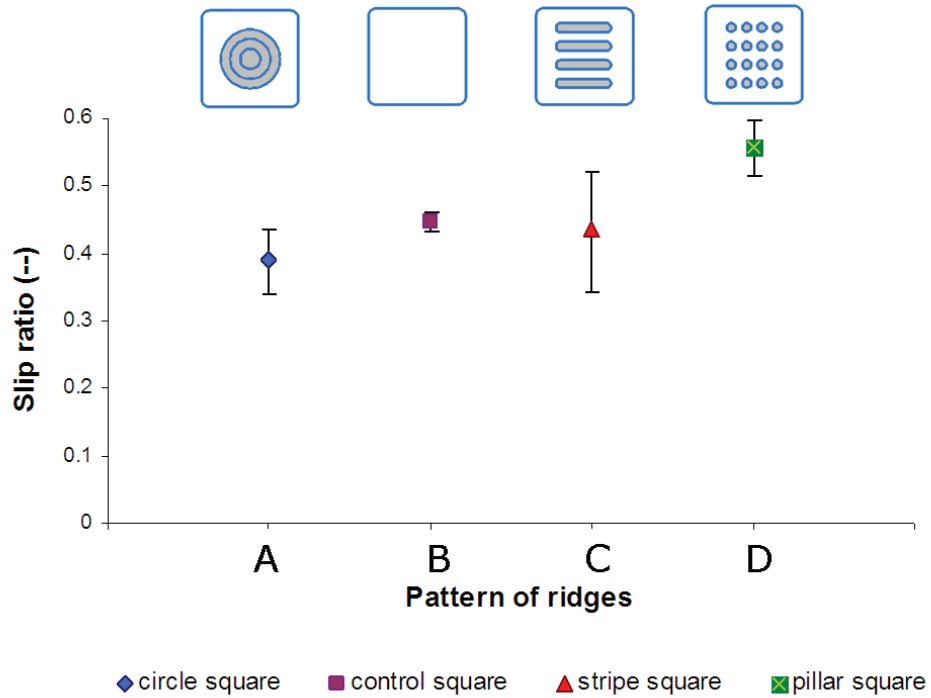


Figure 5.14: Slip-ratio measured on hexahedral skin pads with spherical probe. *circle square* stands for circle ridges pattern tested on the hexahedral skin pad.

factors can be used to explain the effects of ridge patterns on the slip-ratio.

The first one is the contact area. In spite of different texture patterns, at the beginning of contact, the maximum normal forces (3.5 N) can always generate the largest contact areas on the skin pads. Because the normal force is commanded to gradually decrease, every instance after that, the contact area should gradually decrease together with the restoration of compressed silicon rubber skin. The more the pattern of the ridges can conform to the contour of the object, the more effective contact areas can be maintained during the decreasing process of the contact area. In the case of having circled ridges, the contour of the object near the contact point can always be supported by the soft circle ridges with different sizes. Although locally formed bump on the plain skin pad can provide a better contacting conditions than the stripe and pillar patterns, their existence is still relying on the magnitude of the normal forces. However, when slip occurs, the gradually

reduced normal forces also result in the slow dissipation of the bump.

The second one is originated from the angle lever. In order to better explain this phenomenon, we assume that it's always the bottom half of the circled ridge makes the last contact with the object before the slip. As illustrated in Figure 5.15, assume that all the three textures are subject to the same normal and tangential and forces at the beginning. When a tangential force (F_T) is initially applied onto a soft ridge, a pair of symmetrically aligned reaction forces ($F_{elastic}$) are formed to counteract the tangential force. Compared to other ridges, it is obvious that the circled ridge is able to deform less in order to provide a pair of symmetric forces ($2 \cdot F_{elastic}$) that are big enough to counteract the same F_T , because it possesses a larger angle leverage ($\theta_1 > \theta_2$) than the others. The less deformation of the ridge is required to maintain the similar pre-slip status, the longer the probe can stay contact with the skin pad, and thus a smaller slip-ratio can be achieved. That's why the skin pads with circled ridges seemed to be stickier than the others when conducting the slip-ratio experiments (see Table 5.1 and 5.2).

It needs to be pointed out that the large deviation occurred in the case of using stripe pattern (see Fig. 5.13 and 5.14) was caused by its directional friction, because the stripe ridges can be mounted either parallel or perpendicular with respect to the object's slipping direction (see Table 5.1). The plotted data points were averaged values from a group of six trials.

5.3.3 The effects of contact areas on slip-ratio

To investigate how the contact areas will affect the performance of a precision grip, the probe with the curved surface was used in the slip-ratio experiment. Because all the tapered cylindrical skin pads successfully prevented probe from slip during the experiments, we only present the data collected from hexahedral skin pads.

The results of the experiments are plotted in Fig. 5.14 and 5.16. It is interesting to find that the averaged slip-ratios from the hexahedral skin pads are quite similar to each other when curve probe was used. The curved probe provides more contact areas than the spherical one (see Fig. 5.8), therefore under the same force conditions, the pressure

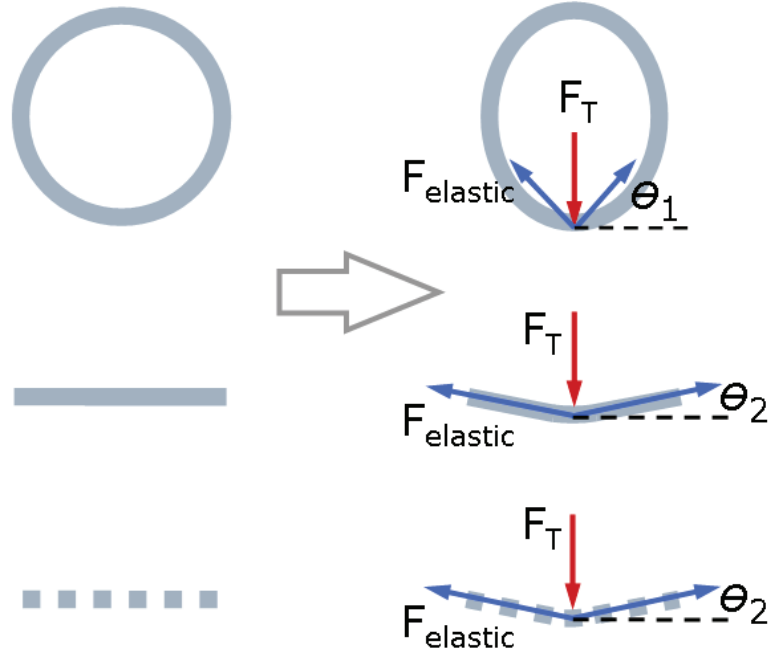


Figure 5.15: Schematic drawing showing the deformation of the three ridge patterns (circle, strip, and pillar) under the same tangential force conditions. *Left:* Shape of the ridges before the start of deformation. *Right:* Force analysis of ridges during the deformation process, but before the contact breaks. *Note:* The direction of the normal forces is perpendicular to the paper surface, but the drawing is omitted for easy reading.

applied onto the skin pads become smaller. In these cases, the ridges on the skin pads can not be compressed as hard as they would when spherical probe was used. Without enough local forces to trigger the viscoelastic behavior of the ridges, the effects from different ridge patterns on the slip-ratio are not obvious any more. Instead, the property of the soft materials at macroscale becomes the dominant factor. Since all the skin pads were made of the same silicone rubber, the slip-ratios exhibit very similar behavior as shown in Fig. 5.16.

In addition, the error bar is still bigger than others when the stripe pattern was tested. This again originates from the directional friction of the stripe ridges. Therefore the stripe texture is not recommended for the design of artificial skin.

In summary, when having large amount of contact surfaces (e.g., using robotic hand to perform envelop grasp), the quality of the the grasp is more decided by the friction

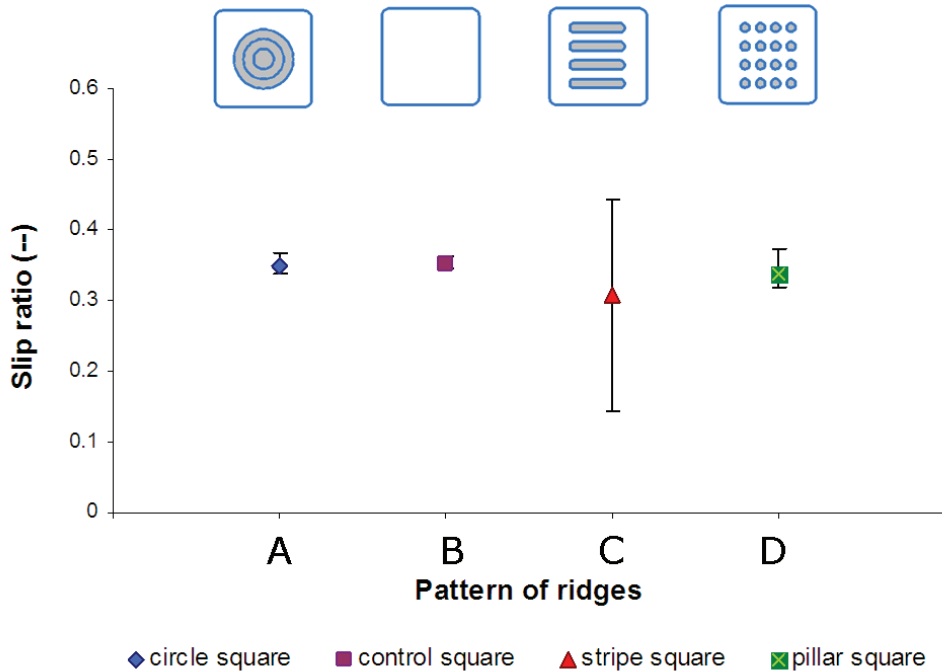


Figure 5.16: Slip-ratio measured on hexahedral skin pads with curved probe. *circle square* stands for circle ridges pattern tested on the hexahedral skin pad.

coefficient of the two materials and less affected by skin's textures.

5.3.4 The importance of mimicking a human's tapered fingertip

The role of evolution in human history has had a dramatic impact on the shape of our fingertips, therefore its shape should be considered in our skin design. As often omitted in the literature, the shape of artificial skin near a fingertip actually plays an important role in dexterous manipulation.

During dexterous tasks, such as threading a needle or twisting a nut, the human hand needs to reliably hold a slim or small object and consistently control its orientation to comply with some other external constraints. Therefore, while performing a precision grip, it is crucial to the success of the task to maintain a certain amount of contact area and force between the fingertips. The human hand is designed in a clever way to minimize the stress

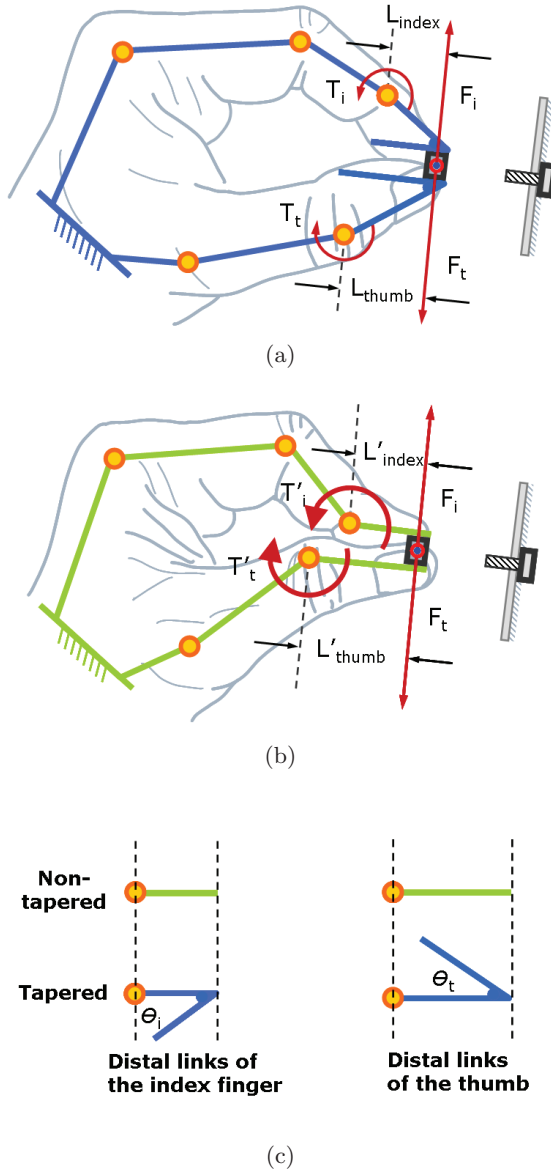


Figure 5.17: Comparison of tapered and non-tapered fingertip during dexterous manipulation. (a) Tapered fingertip possesses smaller moment arm at distal joints. (b) Hyper-extended, non-tapered fingertip achieving the same task with a larger moment arm at distal joints. (c) Transformation from non-tapered to tapered fingertips.

applied at the distal joints. To see this we perform a thought experiment as illustrated in Figure 5.17. First assume two separate pairs of hands pinch an identical object with the

same amount of normal force while maintaining the same orientation of the object. One hand has tapered finger pads at its tips, while the other has prismatic (or cylindrical) finger tips representing canonical robot hand design.

The torque exerted at each distal joint equals the moment arm from the contact center to the center of the distal joint (L_{index} , L_{thumb} and L'_{index} , L'_{thumb}) times the magnitude of normal force (F_i and F_t). The object is pinched at the same distance from the fingertip's tip in both cases. Also we assume that the distal links are of the same length, as depicted in Figure 5.17 (c). When tapered fingertips are adopted smaller moment arms ($L_{index} = L'_{index} \cdot \cos \theta_i$ and $L_{thumb} = L'_{thumb} \cdot \cos \theta_t$) are caused by the incline, and thus exert less torque at the distal joints compared to the robotic hand using blocky or cylindrical fingertips.

Further examination of the kinematics in the case of a non-tapered fingertip reveals excessive hyper-extension. In order for the non-tapered fingertip to achieve the same precision grip the distal link of the index finger, and the thumb, need to move beyond their normal range of motion to achieve the same posture as the tapered fingertip. This unusual finger posture is hyper-extended, which is known to be the cause of common joint injuries in the human hand [69]. Because this posture requires larger torques (T'_i and T'_t) to maintain the stability of an object it will also result in the formation of higher stiffness at the distal joint due to co-contraction. This may in return impair the compliant characteristics of the finger joint. If a robotic hand is designed to work in the human environment, an increased stiffness will place more hazards against the human being around it [111].

Chapter 6

DESIGN OF A 3-AXIS FINGERTIP SENSOR

During manipulation and exploration tasks, robotic hands/grippers are often required to respond effectively to unknown objects and obstacles. Without detailed models of the operating environment, real-time measurement of the contact force is essential for the success of a robotic hand/gripper to perform dexterous tasks. As thoroughly summarized in a recent review [112], many different types of force/torque sensors have been developed over the past decade in order to equip the robotic hands with the tactile sensing ability in various applications.

When it comes to choosing the suitable fingertip sensors for a robotic hand/gripper, besides taking into consideration the sensing ability, the cost still plays an important role. So far, high-end fingertip sensors have been widely employed by many advanced robotic hands [113–116]. However, the cost of those sensors accounts for large portions of the robotic hand. The price of a commercially available 6-axis force/torque sensor starts at \$2000. Although the performance of those advanced tactile/force-torque sensors is very appealing, there also exist situations where the researchers have to comply with their limited budgets on fingertip sensors and would like to reasonably relax the sensing requirement.

Durability and maintainability are the other two parameters that were often ignored during the design of fingertip sensors. The skin of the human hand can regenerate itself, and therefore normal wear and tear won't cause permanent damages to sensing modalities. The increasing roles of robots in human environments require robotic hands to be operated in harsh conditions where a fingertip sensor may be exposed to corrosive chemicals, metal objects with sharp edges, and coarse surfaces of certain objects that can all cause severe damages to the fingertip sensors beyond the normal repair. However, most of existing fingertip sensors have either embedded sensing elements [95] at the contact region or layered flexible circuit [100, 113] under the elastic materials of fingertips. These features

can potentially raise the risk of damaging the sensors. Therefore, important factors such as low-cost, maintainability and durability have to be taken into consideration during the design of future fingertip sensors.

In recent years, many researchers have started using 3D-printed parts directly for their robots, or sometimes fabricating the entire working prototype using only 3D printed parts with a few fasteners [14, 117]. 3D-printed molds and frames were also developed for making different soft skin textures [78, 100, 118]. Therefore, it is of our interest to investigate the possibility of designing and fabricating a 3D-printed fingertip sensor, and to understand essential characteristics that may potentially affect the performance of fingertip sensors.

To this end, we describe a fingertip sensor that makes the most of the appealing features of low-cost force sensors, innovative mechanism, and 3D-printing technology. In contrast to conventional approaches, our proposed design moves the sensing components away from the contacting areas to the base of the fingertip and keeps only the low-cost, compliant fingertip for direct contact with objects. These changes can potentially reduce the cost, allow more task-oriented design, and make the maintenance of the fingertip sensors easier than using complicated/expensive sensors.

In the following sections, the design concept of the fingertip sensor is explained, the important components are detailed, and then we optimize the configurations of our proposed fingertip sensor based on the hysteresis analysis. An optimized fingertip sensor is then used for calibration. At the end, based on what we learn from the 3D-printed fingertip sensor, we demonstrate a case study of our proposed design adapted to a robotic manipulation task with little modification efforts [119].

6.1 Development of the fingertip sensor

This section describes the working principle, the mechanical structure, and the electronic components of our proposed fingertip sensor.

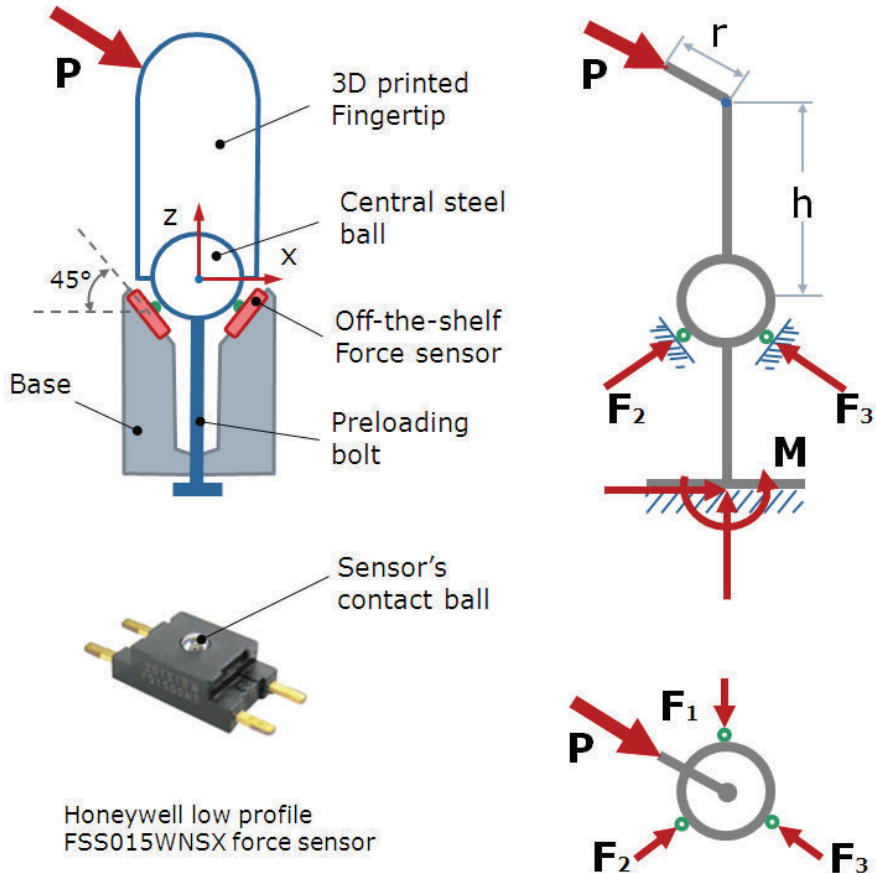


Figure 6.1: Schematic drawing and force analysis of our proposed fingertip sensor. *Top left:* Schematic drawing of the fingertip sensor showing relative positions of all components. *Bottom left:* The picture of a Honeywell force sensor used in this paper. *Right column:* Beam structure of the fingertip sensor when external force (P) applied at the fingertip.

6.1.1 Sensor description and the working principle

As shown in Fig. 6.1, the working principle of the fingertip sensor is based on a cantilever mechanism. The fixed end is located at the bottom of the base; the free end is attached to the bottom of the fingertip through a central steel ball. The central steel ball is then supported by three symmetrically arranged Honeywell FSS015WNSX force sensors (FSS sensor hereinafter) via three pairs of sphere contacts. The three FSS sensors are placed at the inclined opening of the well structure of the base. The external forces applied at the

fingertip will result in a combined reaction force from the three sensor balls and get detected by three FSS sensors.

As represented as a beam structure in Fig. 6.1, important parameters that are related to manipulation task contains the radius (r) and the height (h) of the fingertip. The diameter of the central steel ball decides the size of the base structure which is designed to not have contact with external objects, and therefore won't be considered as a design parameter. Additionally, because the exposed surfaces of the central steel ball and three sensor balls are all plated, the contact between them can be treated as frictionless sphere contacts, thus the sensor reading should mainly reflect the change from the normal forces (F_1 , F_2 , and F_3) at the contact sites.

6.1.2 Mechanical design of the fingertip sensor

As shown in Fig. 6.2, our proposed fingertip sensor is composed of five components, namely, a fingertip (can be coated with silicone rubber), a plated central steel ball, a force sensor enclosed base, a cantilever-bolt mounted bottom cap, and three FSS force sensors. Except for the extended cantilever-bolt (a M2.5 steel screw), the central steel ball (9.4 mm in diameter) and the FSS sensors, all the other parts were 3D printed by the Dimension BST 768 (Stratasys Corp., Eden Prairie, MN) within one hour.

6.1.3 Electrical wiring

The Honeywell FSS sensor is powered by 5V DC source. Its output is then fed into an instrumentation amplifier LT1920 from Linear Technologies, where the signal is differentially amplified by a factor of 5. The output is fed to a NI-DAQ PCI 6229 card where it is digitized as shown in Fig. 6.3. And the detail specifications of the FSS sensor are listed in Table 6.1.

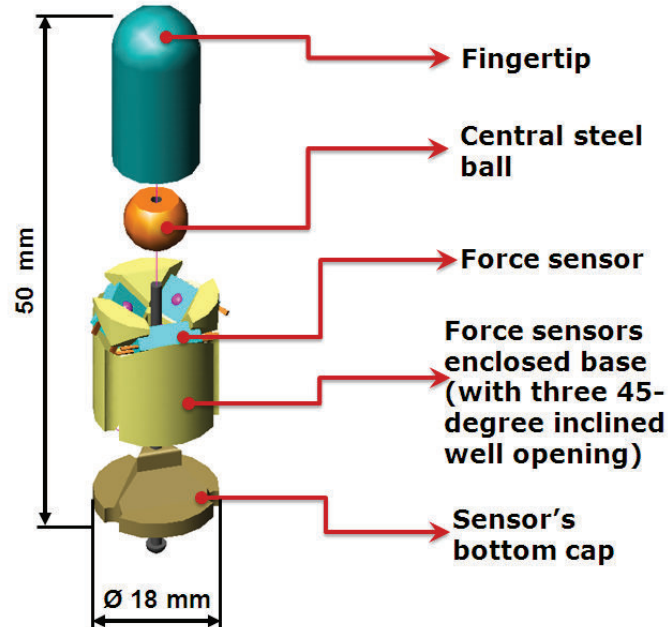


Figure 6.2: 3D CAD model of the fingertip sensor.

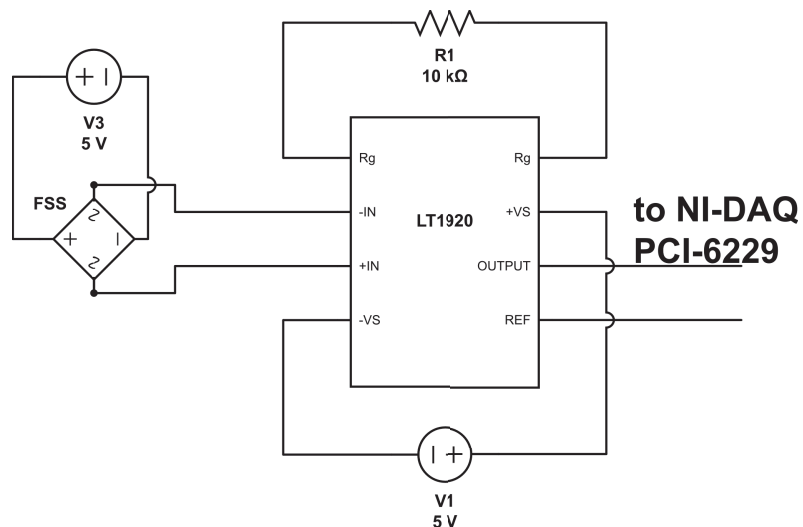


Figure 6.3: The electrical wiring diagram of a single FSS sensor.

Table 6.1: Performance characteristics of the FSS force sensor

| <i>Characteristic</i> | <i>Unit</i> | <i>sensor FSS015WNSX</i> | | |
|---------------------------------------|-------------|--------------------------|-------------|-------------|
| | | <i>Min.</i> | <i>Typ.</i> | <i>Max.</i> |
| Force sensing range(FS) | N | 0 | – | 15 |
| Operating voltage | Vdc | 3.3 | 10 | 12.5 |
| Zero offset | mV | -30 | 0 | +30 |
| Zero shift (25 to 0°C, 25 to 50°C) | mV | – | ± 0.5 | – |
| Linearity | % span | – | ± 0.5 | – |
| Sensitivity | mV/V/N | 2.2 | 2.4 | 2.6 |
| Repeatability | % span | – | ± 0.2 | – |
| Response time (10% to 90%FS) | ms | – | 0.1 | 0.5 |
| Safety overforce | N | – | – | 45 |

6.2 Design optimization of the fingertip sensor

According to the factory's specification, the performance of the Honeywell FSS sensor is very good (as detailed in Table 6.1), and therefore they are often adopted by medical devices [120]. However, due to the special structure we adopted for our design, once the three FSS sensors are installed inside the fingertip sensor, the central steel ball would exert compression force through the three contacting balls of the FSS sensors. It is of interest to understand how the FSS sensors behave under pre-loading. Besides, the overall performance of our proposed fingertip sensor relies heavily on its mechanical design. Important factors such as the friction between the central steel ball and the three sensor's contacting balls, and the elastic behavior of the ABS plastic used for 3D printing can all be greatly affected by the configurations of the fingertip sensor. In order to investigate how the mechanical design will affect the performance of our proposed fingertip sensor, we conducted hysteresis analysis with respective to two groups of forces (*G1*-type and *G2*-type) under six different rotational conditions as illustrated in Fig. 6.4.

At the beginning of each loading test [121], a small tray was hanged from the fingertip (at *h1..h9* or *r1..r5*) through a pair of strings. The tray and strings weigh 5 grams in total. During the experiments, known weights were added and removed from the tray manually,

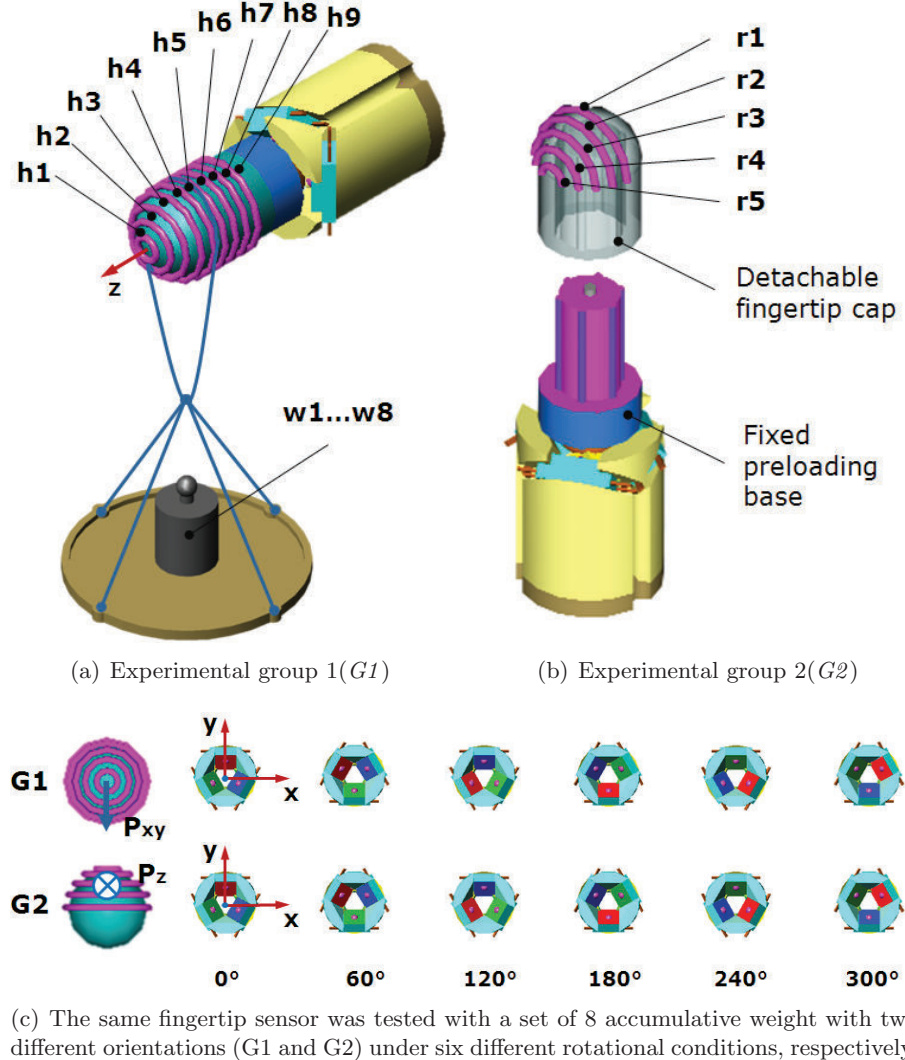


Figure 6.4: Varying conditions for design optimization. (a) Detachable fingertip cap for minimizing the disturbance to the pre-loading status. (b) Hanging weight method used for loading/unloading difference forces. (c) Under the same force conditions, six different rotational cases were tested during the experiments. (Note: the red, green, and blue colors were used to label the three FSS sensors.)

and force readings from the FSS sensors were recorded by NI DAQ PCI-6229 at 2KHz. In order to obtain the hysteresis curves we initialized the fingertip sensor with the empty tray. We then successively added weights to the tray so that we obtained measurements

at different weights. After that we removed the weights in the reverse order. After each addition/removal we waited until the weight stabilized and marked the time in our recording with the corresponding weight. We then averaged the values from the 3 seconds after the time marker and treated that number as the voltage output of the sensor under the loaded weight.

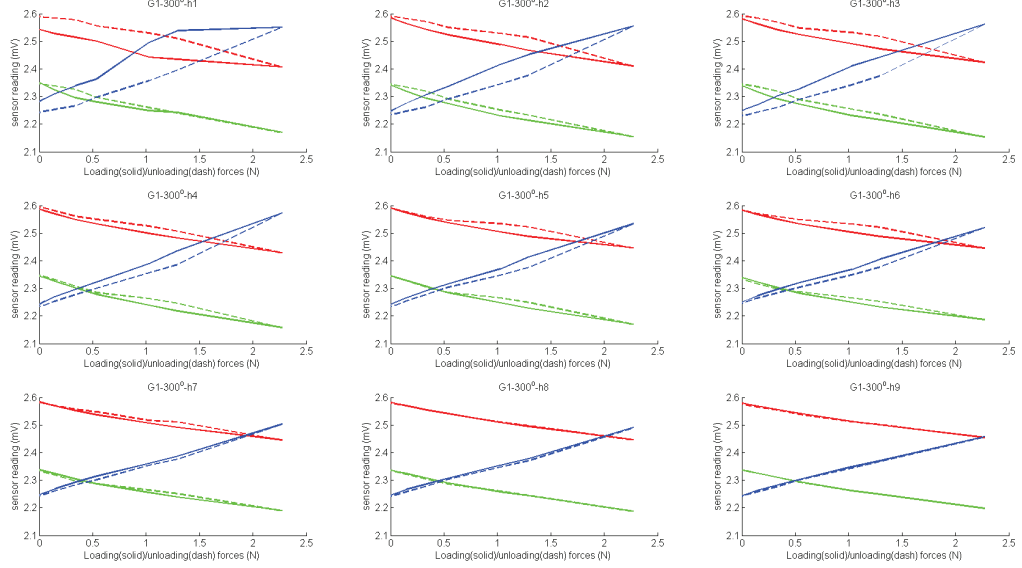
Group 1 and group 2 each have distinctively nine and five testing locations. And for every testing location, loading and unloading experiments were conducted with eight different weights. The information of the tested fingertip sensor is listed in Table 6.2. Examples of processed data are as shown in Fig. 6.5. Due to the small non-linearity effects found from the data, we chose to use the following, simplified equation to calculate the midpoint hysteresis for every testing location:

$$Hysteresis\% = \left| \frac{S_{mp} - S_{mn}}{S_{start} - S_{end}} \right| \times 100\% \quad (6.1)$$

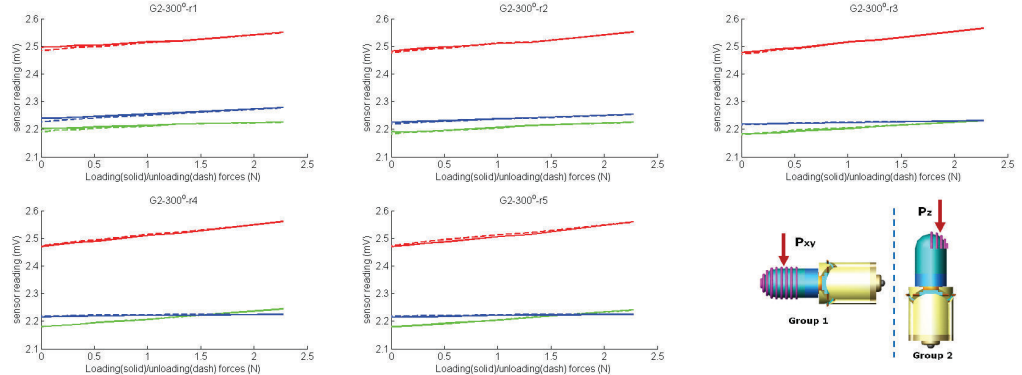
where S_{start} and S_{end} are the sensor readings from the start and end points of the hysteresis loop; S_{mp} and S_{mn} are the readings in a positive and negative going directions, respectively. Based on Eq. (5.1), the mechanical hysteresis of the fingertip sensor was statistically analyzed as shown in Fig. 6.6.

Table 6.2: Specifications of the tested fingertip force sensor

| <i>Term</i> | <i>Unit</i> | <i>Value</i> |
|------------------------------------|-------------|---|
| Tested height($h_1 \dots h_9$) | mm | 22.76 21.92 20.52 18.72 16.76 14.76 12.76 10.76 8.76 |
| Tested radius($r_1 \dots r_5$) | mm | 0 1.90 3.69 5.12 6.03 |
| Hanging weights($w_1 \dots w_8$) | gram | 0 5 15 35 55 105 132 232 |
| Total weight | gram | 18 |
| Total height | mm | 48.50 |
| Total diameter | mm | 18.00 |
| FSS sensor's price | \$/unit | 60 |



(a) A set of P_{xy} (8 accumulative weights) applied at 9 different axial locations when the rotation-angle is fixed at 300° for G1.



(b) A set of P_z (8 accumulative weights) applied at 5 different radial locations when rotation-angle is fixed at 300° for G2.

Figure 6.5: Examples of the data collected for hysteresis analysis. (Note: the red, green, and blue data points were collected from the three sensors defined in Fig. 6.4(c), respectively.)

In both group 1 and 2's experiments, a cantilever effect is formed when the external forces (P_{xy} or P_z) are applied at the fingertip (the free end) of our 3D-printed force sensor. The readings of the three FSS sensors located at the base (the fixed end) will increase if they are on the compression side, or decrease if they are on the tension side.

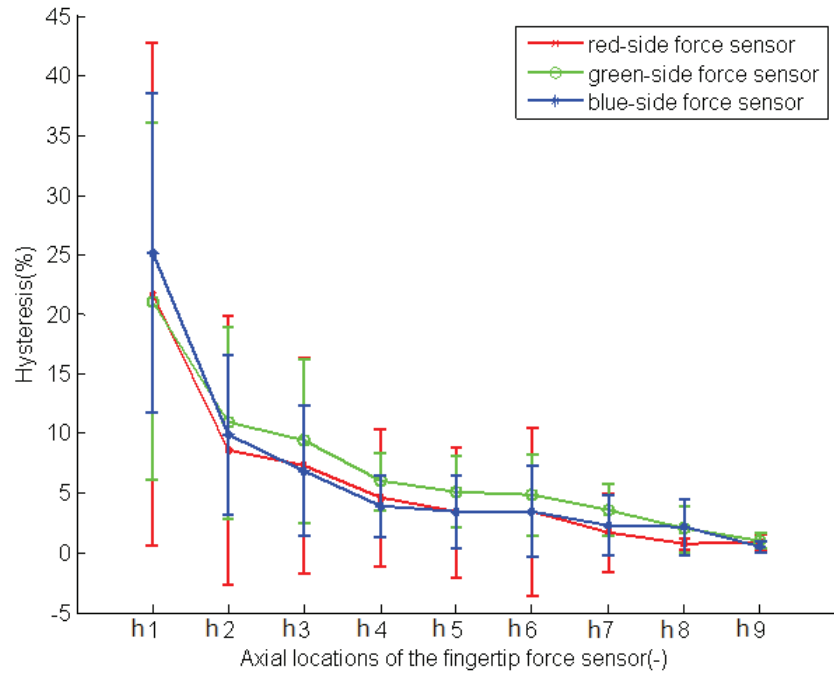
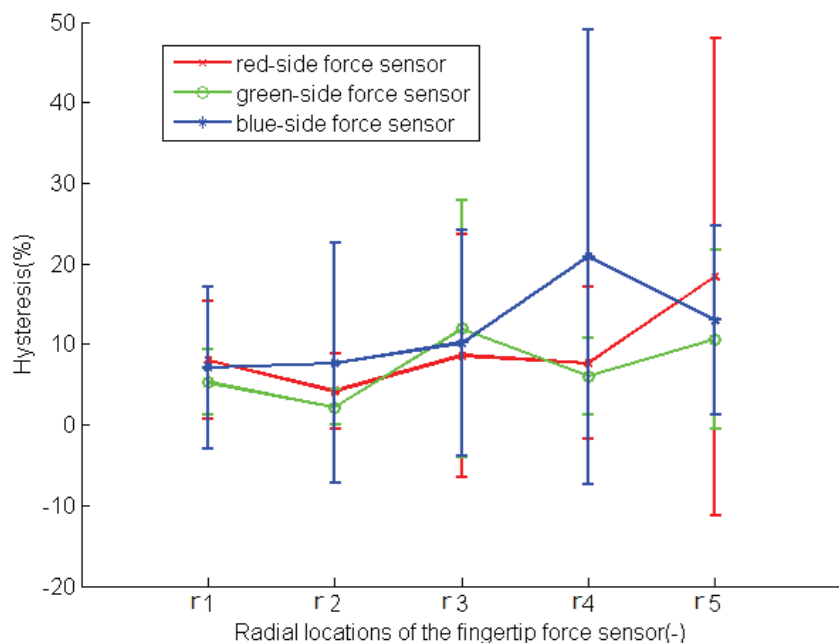
(a) The hysteresis along axial direction of the finger force sensor(*G1*)(b) The hysteresis along radial direction of the finger force sensor(*G2*)

Figure 6.6: The change of the hysteresis of the proposed fingertip sensor at different testing locations.

A typical loading/unloading process is shown in Fig. 6.5(a) for group 1's data. An exponential decrease of the hysteresis with the height of the fingertip was observed. This can be resulted from the decreasing torque effect on the mechanical hysteresis as the loading/unloading forces moving towards the base of the fingertip sensor. When the external force P is applied according to the group 1's setup, in the x-y plane of the fingertip sensor, torques are simultaneously generated at the contact sites between the central steel ball and three FSS sensors' contacting balls. Although the friction between two plated metal balls is seemly small compared to the force applied to the fingertip, the induced friction could still cause the reading of a compressed FSS sensor (see the blue curves in Fig. 6.5(a)) to increase from 2.46 to 2.56 mV under the same maximum loading force, accounting for a 33.9% of the total increasing force from 0 to 2.27 N, as shown in Fig. 6.5(a) from moving the test location from $h9$ to $h1$.

Interestingly, a similar but smaller, 9.6% increase of the sensor reading under the maximum compression force was observed in group 2's data (see the red curve in Fig. 6.5(b)) as the z-direction forces P_z moving from $r1$ to $r5$. This is because the change of moment arm decreases by two times when the same amount of testing forces are moved from group 1 to group 2.

On the contrary, the lowest, averaged hysteresis for group 2's data (2.19%) still appears to be over two times larger than the lowest one from group 1's data (0.98%)(see Fig. 6.6). This is because the total span of the sensor readings (the denominator $S_{start}-S_{end}$ in Eq. (1)) in group 2 becomes very small (about 0.005 mV) for the sensors on the tension side of the fingertip during the six different rotations (see blue curve in Fig. 6.5(b)).

Based on the above analysis, we found that the height of the 3D-printed fingertip sensor will affect the hysteresis performance of the sensor most, therefore we redesigned an optimized fingertip force sensor that has a height (h) of 0 mm and a radius (r) of 9 mm based on the schematic drawing in Fig. 6.1. The calibration of the optimized force sensor will be detailed in the following section.

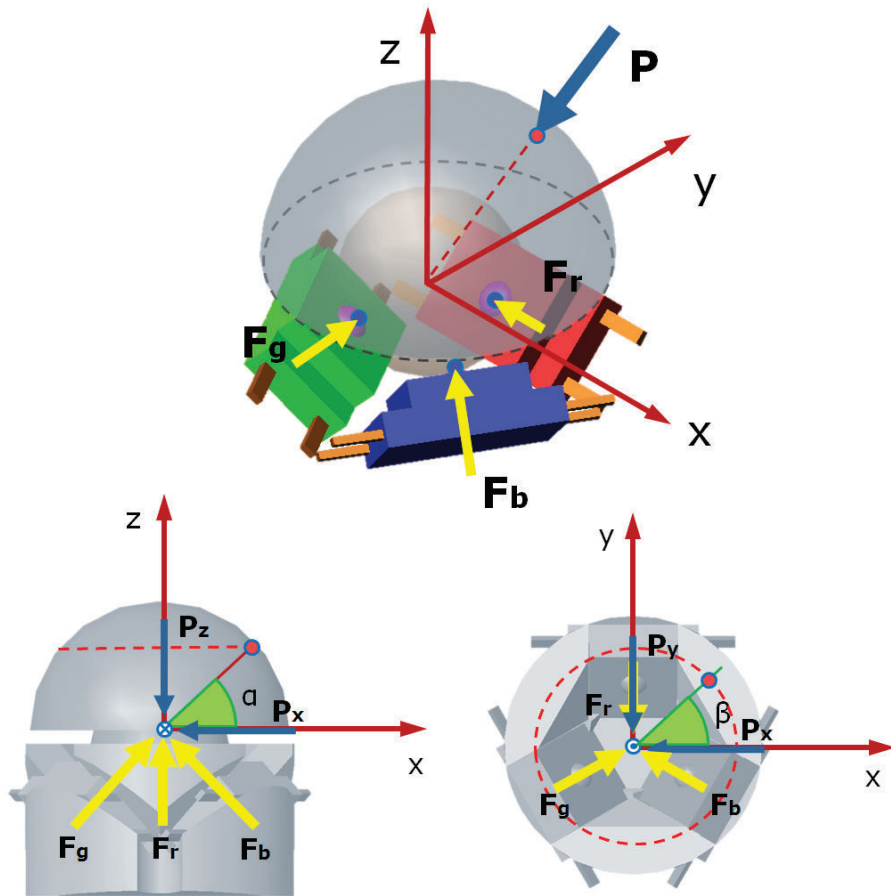


Figure 6.7: Force analysis of the fingertip force sensor.

6.3 Calibration of an optimized fingertip sensor

The specifications of our optimized fingertip sensor is summarized in Table 6.3.

Before the calibration, a frictionless hard-finger model is chosen for the force analysis of the optimized fingertip sensor as shown in Fig. 6.7. When there is an external force applied on the surface of fingertip, its normal component (\vec{P}) can be further decomposed into three force vectors (\vec{P}_x , \vec{P}_y , and \vec{P}_z) in the fingertip's coordinate system. For the fingertip at equilibrium, three counteracting forces (\vec{F}_r , \vec{F}_g , and \vec{F}_b) will be transmitted simultaneously through the three FSS sensor's contacting balls. Since we have already reduced the height

Table 6.3: Specifications of the optimized fingertip force sensor

| <i>Term</i> | <i>Unit</i> | <i>Value</i> |
|---------------------------------------|-------------|---------------------------------|
| Tested height($h_1 \dots h_6$) | mm | 8.41 7.71 6.62 5.19 3.51 1.65 |
| Tested radius($r_1 \dots r_6$) | mm | 1.65 3.51 5.19 6.62 7.71 8.41 |
| Hanging weights($w_1 \dots w_{10}$) | gram | 0 5 15 35 55 82 109 136 163 213 |
| Total weight | gram | 14 |
| Total height | mm | 20 |
| Total diameter | mm | 18.00 |

of the fingertip after the optimization, the torque induced friction is neglected at the contact point between the central ball and the three FSS sensors. And the following force balance can be achieved:

$$\vec{P} = \vec{F}_r + \vec{F}_g + \vec{F}_b \quad (6.2)$$

where the normal force component (\vec{P}) can be further decomposed with location information α and β :

$$\begin{pmatrix} \vec{P}_x \\ \vec{P}_y \\ \vec{P}_z \end{pmatrix} = \begin{pmatrix} \vec{P} \cdot \cos\alpha \cdot \cos\beta \\ \vec{P} \cdot \cos\alpha \cdot \sin\beta \\ \vec{P} \cdot \sin\alpha \end{pmatrix} \quad (6.3)$$

From the 3D model of the fingertip sensor, the geometric information containing the locations of the three FSS sensors is used to formulate the counteracting forces:

$$\vec{F}_r = (0, -\cos 45^\circ, \sin 45^\circ)^T \cdot k_r \cdot S_r \quad (6.4)$$

$$\vec{F}_g = (\cos 45^\circ \cos 30^\circ, \cos 45^\circ \sin 30^\circ, \sin 45^\circ)^T \cdot k_g \cdot S_g \quad (6.5)$$

$$\vec{F}_b = (-\cos 45^\circ \cos 30^\circ, \cos 45^\circ \sin 30^\circ, \sin 45^\circ)^T \cdot k_b \cdot S_b \quad (6.6)$$

Where k_r , k_g , k_b , and S_r , S_g , S_b are the calibration coefficients and the sensor readings from the correspondingly colored FSS sensors (see Fig. 6.7), respectively.

Then by substituting Eq. (3)-(6) into Eq. (2), we derive the fingertip model as follows:

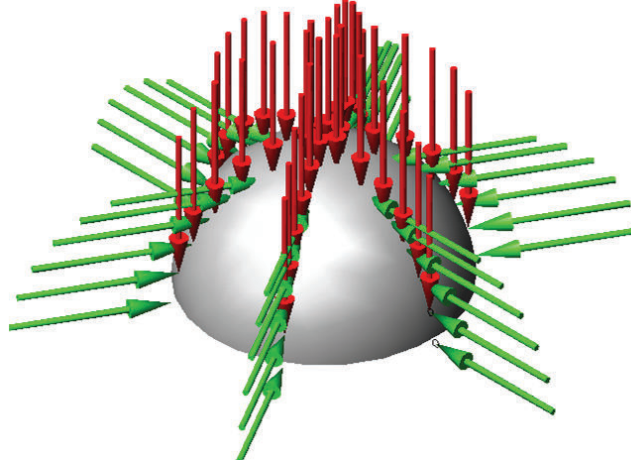


Figure 6.8: 72 sets of loading forces applied at different locations on an optimized fingertip sensor for calibration purpose. Note: G1 and G2-type forces are labeled with green and red colors, respectively.

$$\begin{pmatrix} \vec{P}_x \\ \vec{P}_y \\ \vec{P}_z \end{pmatrix} = \mathbf{A} \cdot \begin{pmatrix} S_r \\ S_g \\ S_b \end{pmatrix} \quad (6.7)$$

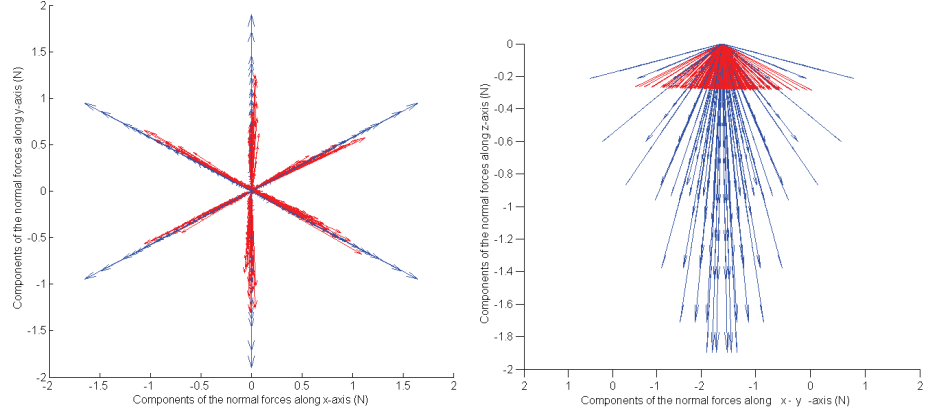
where coefficient matrix A is in the form of:

$$\mathbf{A} = \begin{pmatrix} 0 & 0.6124 & -0.6124 \\ -0.7071 & 0.3536 & 0.3536 \\ 0.7071 & 0.7071 & 0.7071 \end{pmatrix} \cdot \begin{pmatrix} k_r & 0 & 0 \\ 0 & k_g & 0 \\ 0 & 0 & k_b \end{pmatrix} \quad (6.8)$$

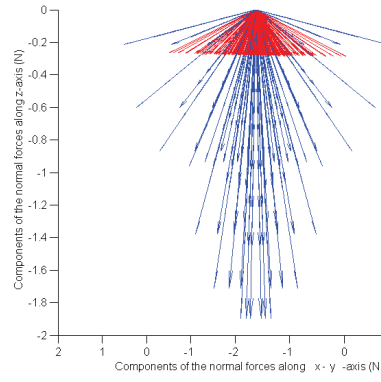
As shown in Fig. 6.8, a total of 72 sets of loading forces were applied at 36 different locations¹ on the optimized fingertip sensor in two groups. The normal component of forces (\vec{P}) together with their acting locations (α and β) were extracted for the calibration process.

The calibration matrix was computed by using least square optimization method from Matlab. For the optimized fingertip sensor, a full rank coefficient matrix \mathbf{A}_{opt} suggests that

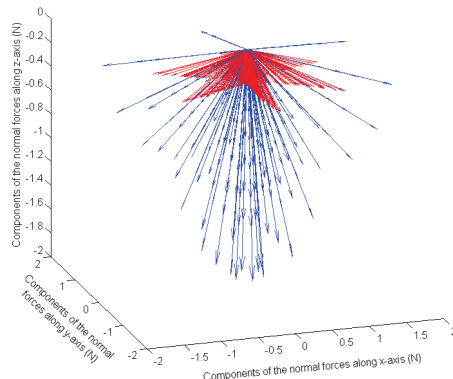
¹a set of 0 5 15 35 55 82 109 136 163 213 grams of hanging weights were used for each location



(a) Applied and estimated forces in the x-y plane.



(b) Applied and estimated forces in z-x/y plane.



(c) Comparison of the measured and estimated forces in 3D.

Figure 6.9: Comparison of applied (blue) and measured (red) normal forces of our proposed force sensor.

three force components of the external force (\vec{P}) can be independently decomposed. And the condition number of A_{opt} is 34.92.

$$A_{opt} = \begin{pmatrix} -0.1569 & -2.7179 & 0.0155 \\ 2.3755 & 1.4390 & 0.1033 \\ -2.1593 & 1.3978 & 0.0545 \end{pmatrix} \quad (6.9)$$

The comparison between applied and estimated forces is shown in Fig. 6.9. It is interesting to find that our proposed fingertip sensor is able to estimate the rotation of the external

force in the x-y plane quite well, but has difficulties of measuring the force (\vec{P}_z) in axial direction. One possibility is that the direction of the \vec{P}_z is coincident with, but opposite to the direction of the pre-loading force, thus the bigger the \vec{P}_z , the more the pre-loading bolt is pushed out (in a non-detectable way). It is out of the scope of this design paper, but will be addressed for future version of the fingertip sensor.

6.4 A case study – designing fingertip sensors for Phantom robots' manipulation tasks

In this section, our goal is to equip a group of 3-DOF Phantom robots (SensAble Technologies, Inc., Wilmington, MA) with adjustable fingertip sensors so that Phantom robots can perform manipulation tasks cooperatively. The design requirements are listed below:

1. The fingertip sensor needs to be connected to the end-effector of a 3-DOF Phantom robot with a 1-DOF adjustable base.
2. The fingertip used for manipulation objects are expected to be compliant, and can be easily changed to other shapes with little effort.
3. During manipulation tasks, only the radial side of the fingertip sensor is expected to contact with the objects. Therefore the fingertip sensor should be able to detect the directions of the external forces coming sideways. The resolution should be within 60 degrees in the radial plane.
4. The replacement of the fingertip should be easy and fast; the budget of each fingertip should not exceed \$20.

At this stage, the design requirements of the fingertip sensor are all met for the manipulation tasks of the Phantom robots as shown in Fig. 6.10. More information about the sensor can be found in our video submission. In the rest of this section, we are going to validate the efficacy of our proposed method through experiments.

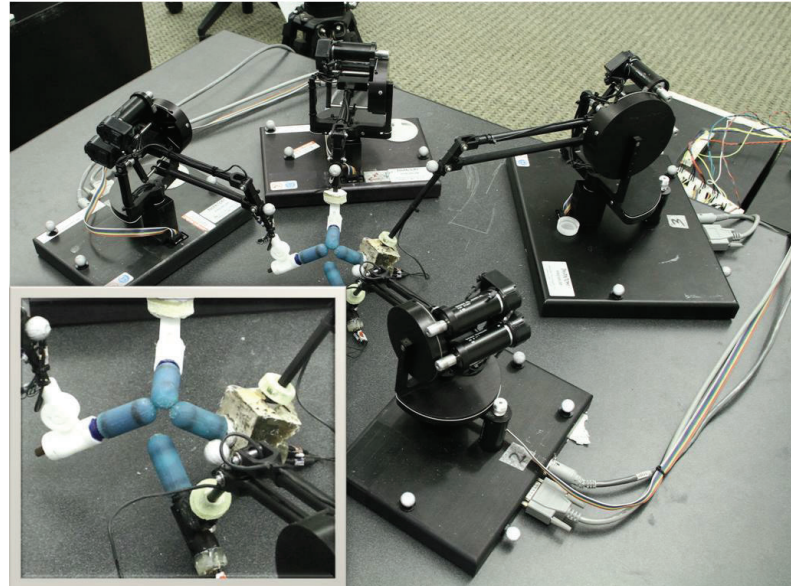


Figure 6.10: Fully assembled fingertip sensors mounted at the end-effectors of four 3-DOF Phantom robots for cooperative manipulation tasks.

As illustrated in Fig. 6.11, a fully assembled fingertip sensor for the Phantom robot was tested in the experiments. A MLP-25 load cell (Transducer techniques, CA) was attached to a probe stylus. Infrared markers were used to track the motion of the stylus. The 3D marker coordinates were measured at 480 Hz using a 7-camera system (PhaseSpace Inc., San Leandro, CA) with respect to the camera (global) frame. The direction of the contact force applied to the fingertip in the radial plane was first calculated in the finger frame and then transformed to global frame for comparison.

The magnitude and the orientation of the contact force were recorded by the the load cell and collected by the motion capture system, respectively. Those values were used to label and validate our experimental results. The FSR sensor changes its resistance based on the force applied to it. We measured the resistance using a voltage divider that divides the 5V supply voltage between 10K Ω resistor and the sensor. We then converted the voltage reading to resistance for reporting.

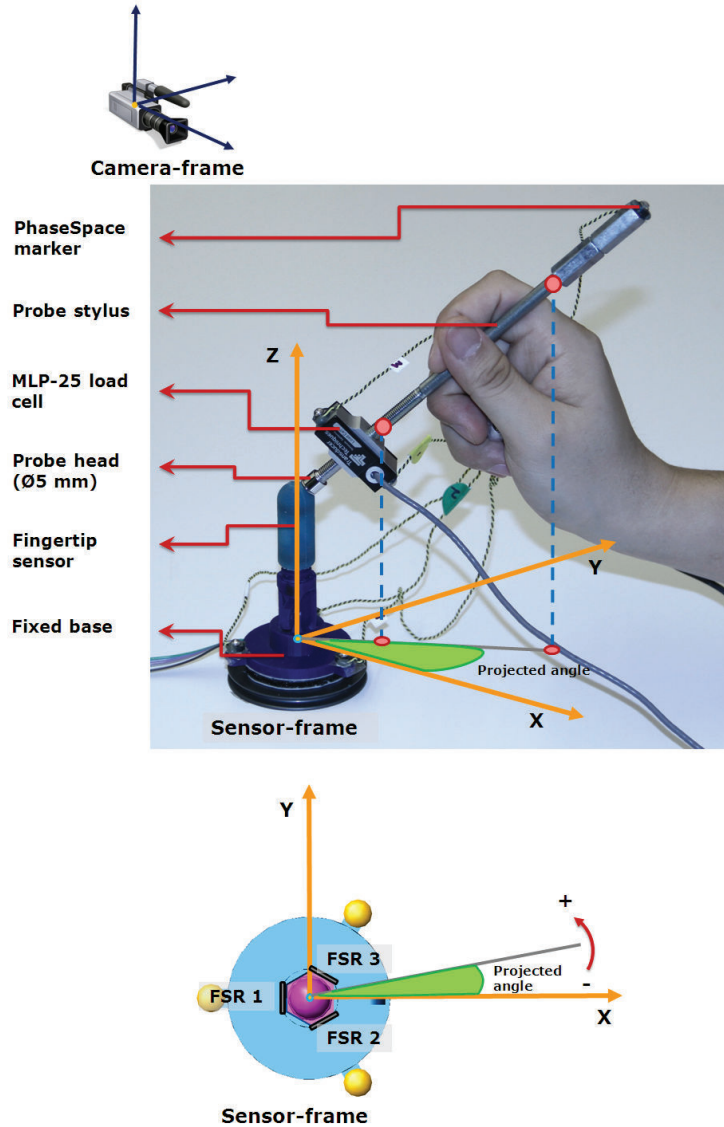


Figure 6.11: Experimental setup of the fingertip sensor and definition of different frames. *Top:* Labeled pictures of a typical trial illustrating the definition of projected angle, sensor-frame, camera-frame, and important components of the experiment. *Bottom:* Locations of the three FSRs (\$6/unit) in sensor-frame whose X-Y plane is the radial plane).

As shown in Fig. 6.11, the force vectors measured from the probe stylus were first projected onto the X-Y plane (the radial plane) in the sensor-frame. Then the projected angles were calculated based on their X and Y coordinates. The projected angle is equivalent

to the β value as modeled in the section IV, and therefore its value can be calculated by using Eq. (3) and (4).

The comparison result between the measured and the estimated projected angles is shown in Fig. 6.12. Note that the readings from the load cell are only used as the contact-event indicator. When the contact occurs, a spike would be observed in the load cell data. The differences between measured and estimated angles are all within 60 degrees. This means the fingertip sensor could successfully meet our design requirements for the Phantom robot. The sources of the discrepancies between the measured and estimated angles most likely result from the hysteresis and non-linearity of the FSRs [122]. In addition, the contacts between the probe head and the silicone rubber coated fingertip seemed to be more complicated than we expected – the effect of the deformation of the silicone rubber around the probe head combined with the relatively large friction made it hard to accurately measure the direction of the applied force.

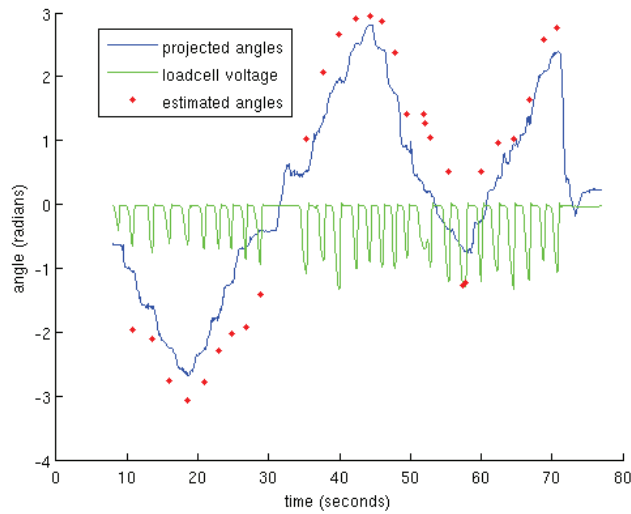


Figure 6.12: Comparison of the contact angles between measured and estimated values in the radial plane.

6.5 Conclusion

We have detailed the design of a low-cost, 3-axis fingertip sensor that is made of 3D-printed materials. Our proposed fingertip sensor is composed of a fingertip, a FSS sensor enclosed base, a cantilever-bolt, and a set of low-cost sensors. In order to improve our design concept, experiments were conducted on optimizing the effects of configurations on the performance of the fingertip forces. In total, over 2000 loading/unloading tests were conducted for collecting data used in statistical analysis. We found that there was no obvious effects on the linearity of the sensor by pre-loading the FSS sensors with the cantilever bolt. However the height of the 3D-printed fingertip appears to be an important factor that affects the hysteresis performance of the FSS sensor. Thus, an optimized fingertip sensor was used for the calibration in the later experiments. The results of the calibration prove that our proposed fingertip sensor can detect the normal component of the contact forces. However it was challenging for the fingertip sensor to estimate the forces acting along the axial direction of the fingertip sensor, the discrepancy is likely from the elastic deformation of the bottom cap. In our future work, we are planning to add this effects into the fingertip model.

At the end, a case study was presented to validate the adaptive feature of our design concept. Four Phantom robots were equipped with modified fingertip sensors. And each of them costs less than \$20 to fabricate. Design requirements such as compliance, resolution, and low-cost were all achieved through combining 3D-printing technology and innovative design. Next we are going to perform manipulation with those Phantom robots.

As for improving the functionality of the 3D-printed sensor itself, we are interested in incorporating three more sensors into the design so that the resulting sensor will have the potential to measure all the six degrees of freedom of a contact force. As we demonstrated in our case-study, similar design concept can be easily adapted to different applications with little effort. Due to its compact size, our optimized fingertip sensor will be implemented into a 20-DOF anthropomorphic robotic hand that was previously developed in our lab [14]. Eventually, we would like to make our 3D model of the fingertip sensor an open-source sensor so that more researchers can benefit from the convenience and low-cost of the 3D printing technology.

Chapter 7

LOW-COST ROBOTIC HAND

In this chapter, we take an alternative approach to the question of how the anthropomorphic robotic hand can be designed such that the fabrication of the robotic hand is fast, the cost of the modification and maintenance is cheap, and the control of the robotic hand is feasible by presenting the design, actuation, and modeling of a 20-DOF anthropomorphic robotic hand (as shown in Figure 7.1). Our proposed method combines adaptive design, rapid prototyping, and modeling with a custom-designed software [85]. The resulted anthropomorphic robotic hand is composed of 31 parts in comparison to other existing robotic hands using hundreds of parts, and can be 3D-printed in 20 hours and fully assembled in 4 hours. Its size, DOFs, ROM, and actuation type can all be adjusted/changed with little effort or modification.

In the following sections, the innovative design methods of the robotic hand are detailed, the actuation system is described, and then the modeling of the robotic hand system is established to demonstrate how our custom modeling software could help to speed up the control. At the end a fully assembled robotic hand system is prepared for our future work [14].

7.1 *Development of the anthropomorphic robotic hand*

Although the anatomy of the human hand provides detailed sources of static models, such as joint structure, tendons routing, and layered skin, how to organically incorporate state-of-the-art engineering advances into a fully functional robotic hand system is what we want to achieve in this chapter. This section describes the mechanical design and prototyping process of our robotic hand.

As shown in Figure 7.2, Our proposed robotic hand is composed of four articulated



Figure 7.1: The 3D-printed 20-DOF anthropomorphic robotic hand.

fingers and one opposable thumb. The size of our robotic hand matches that of the ACT Hand [8] whose biomechanical properties were extracted from a laser-scan model of a human left hand (Stratasys Corp., Eden Prairie, MN).

There are three joints in each finger of the human hand: namely, the metacarpophalangeal (MCP), proximal interphalangeal (PIP), and distal interphalangeal (DIP). Each DIP and PIP joint possesses one DOF. The MCP joint has two DOFs: one to achieve flexion-extension and another to realize abduction-adduction finger motion. The three joints of the thumb are the carpometacarpal (CMC), metacarpophalangeal (MCP), and interphalangeal (IP) joints. Its IP and MCP joint were designed to possess one DOF in the flexion-extension direction respectively. In contrast with other fingers MCP joints, the CMC joint of the thumb has two DOFs with two non-intersecting, orthogonal axes [8]. Table 7.1 lists the

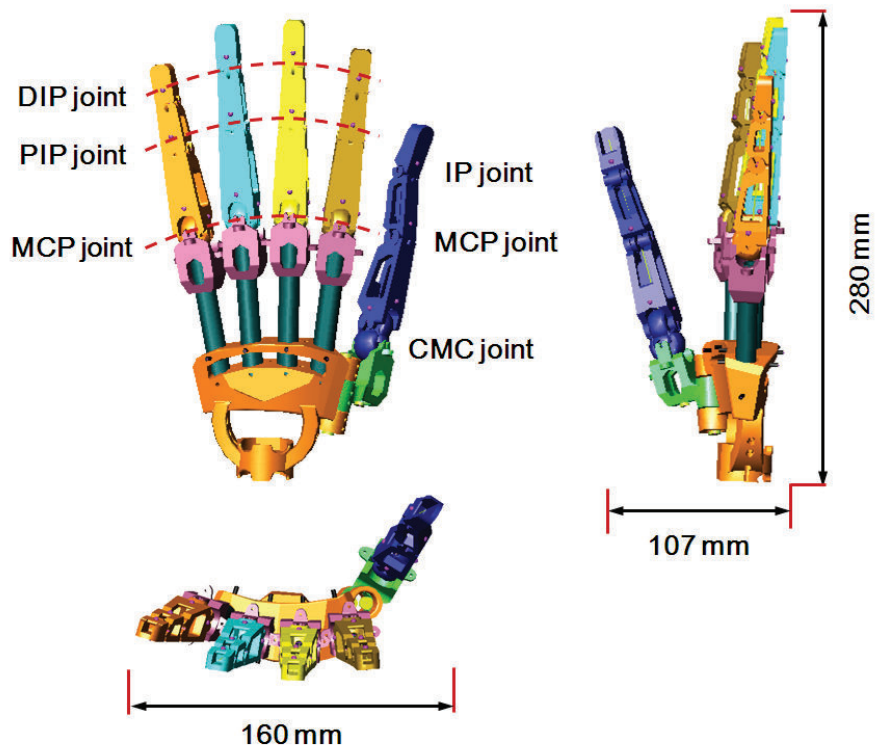


Figure 7.2: 3D model of the anthropomorphic robotic hand.

ROM of our proposed robotic hand.

7.1.1 3D-printed Lego-style, modular finger design

As previously mentioned, one of the major barriers that prevents researchers from adding modification to any existing anthropomorphic robotic hands is that the cost of time and grand funding. However this cost can be side stepped through the innovation of rapid prototyping technologies. As shown in Figure 7.3, each segment of a finger is 3D printed by the Dimension BST 768 (Stratasys Corp., Eden Prairie, MN). The resolution of the 3D printed parts is 0.025mm, and it takes only one hour to print all the components of an entire finger. Additionally the strength of the ABS plastic is sufficient to resist the induced stress of cables.

One of the important factors we believe that makes LEGO toy popular is because it

Table 7.1: The joint motion limits of the anthropomorphic robotic hand

| Finger | Joint | Minimum | Maximum |
|--|-------|---------------|---------------|
| Index, Middle, Ring, & Little | MCP | 20° extension | 90° flexion |
| | | 30° abduction | 30° adduction |
| | PIP | 0° extension | 90° flexion |
| | DIP | 0° extension | 90° flexion |
| Thumb | CMC | 40° extension | 90° flexion |
| | | 40° abduction | 40° adduction |
| | MCP | 0° extension | 80° flexion |
| | IP | 20° extension | 90° flexion |

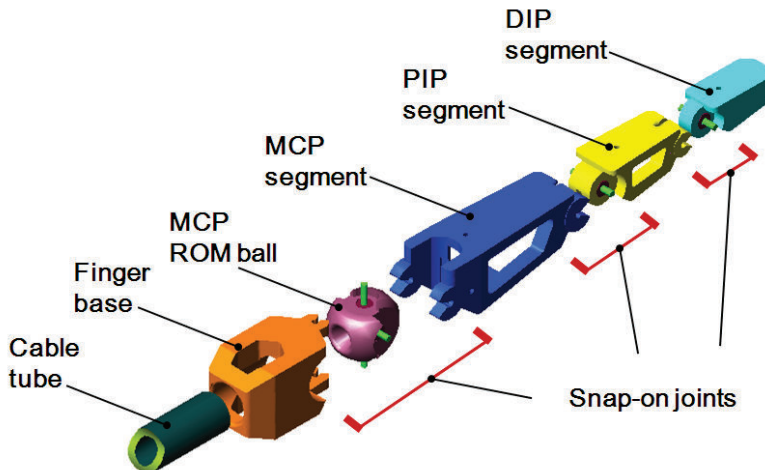


Figure 7.3: Components of each finger unit.

allows players to inspiringly prototype their design ideas via a number of interlocking plastic bricks within a short period time. Following the same principle, our proposed robotic hand was designed to be modular and adaptable. The joint connection between two finger segments was formed by one LEGO-style Snap-On joint. As shown in Figure 7.3, there are three Snap-On joints in one finger. The interlocking mechanism of the Snap-On joint is composed of a 3D printed C-shaped clip on one side of the joint and a steel shaft passing

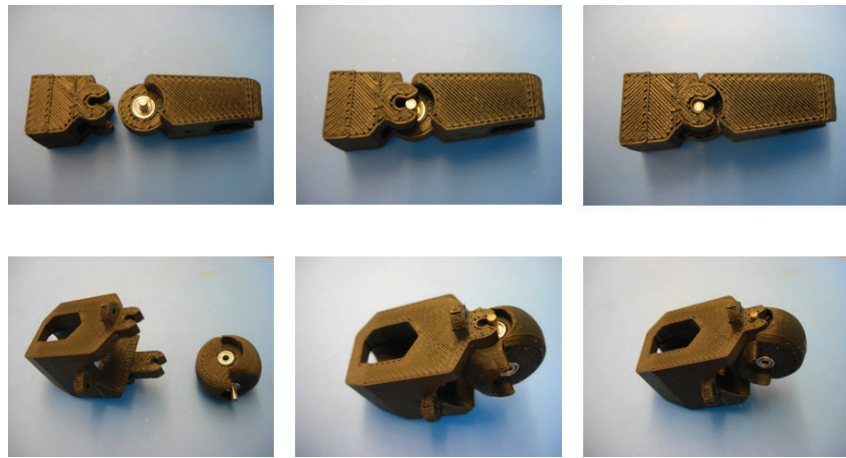


Figure 7.4: Two examples of assembling a Snap-On joint. *Top row:* Assembling a DIP hinge joint. *Bottom row:* Assembling a MCP ROM-ball on to the finger base.

through the center of the other side of the joint. After snapping into the clip, the steel shaft can be secured by the friction engagement, and a Snap-On joint is thus formed (as shown in Figure 7.4).

The ROM of a joint is limited by the mechanical constraints between adjacent finger segments in extreme postures and can be modified in CAD model without affecting other sites of the part. For instance, by snapping on a new MCP ROM-ball with different mechanical constraints, the ROM of abduction/adduction can vary from 20 degrees to 40 degrees easily.

In addition to simplifying the robotic hand design, the Snap-On mechanism can also help to ease the burden on assembly: by replacing a set of finger segments with shorter ones, a smaller hand will be reformed in minutes.

7.1.2 Adaptable tendon routing

The tendon routing plays an important role in control of anthropomorphic robotic hands. As shown Figure 7.5(a), our proposed robotic hand uses four pairs of antagonistic tendons to control each of its 4-DOF fingers. The tendons are made of 0.46 mm Spectra® fiber (AlliedSignal, Morristown, NJ). The fiber was chosen because of its strength (200N breaking

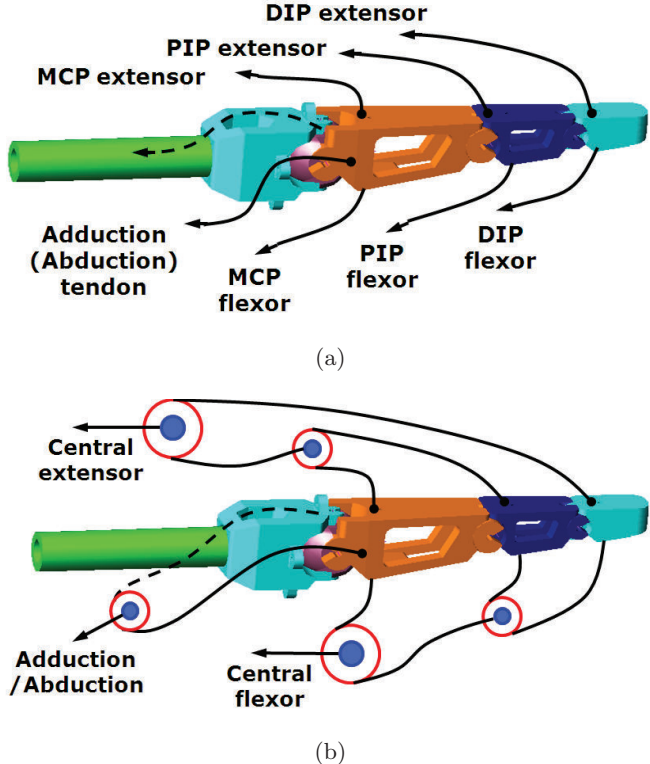


Figure 7.5: Schematic drawing of two possible cable routing types. (a) A 4-DOF finger with four pairs of antagonistic cables (*Note*: cables originated from the DIP and PIP finger segments were passing through the center of the cable tubes in the real robotic hand, for better illustration, their routings are drawn explicitly). (b) A 3-DOF under-actuated finger with pulley systems.

strength), high stiffness, flexibility, and its ability to slide smoothly through the cable tube. Compared to other types of transmission, such as linkages, gears, and belts, choosing cable-driven system enables the anthropomorphic robotic hand to quickly switch between being fully actuated and being under-actuated with little modification as shown in Figure 7.5. This in return broadens the application of the anthropomorphic robotic hand ranging from dexterous manipulation research to practical prosthetics.

Although changing the tendon routing is a good way to explore the potentials of an anthropomorphic robotic hand, it is also the most time-consuming process during the assembly (e.g., 90% of the total time in our case). How to efficiently optimize the cable routing

and paths so that each of the finger joints can be controlled properly plays an important role in our proposed robotic hand design.

Before rushing to prototype/modify the robotic hand, our custom modeling software provided us an unique platform to evaluate our design ideas. For instance, the STL files generated for 3D printing can be directly loaded into the software for detecting mechanical conflicts.

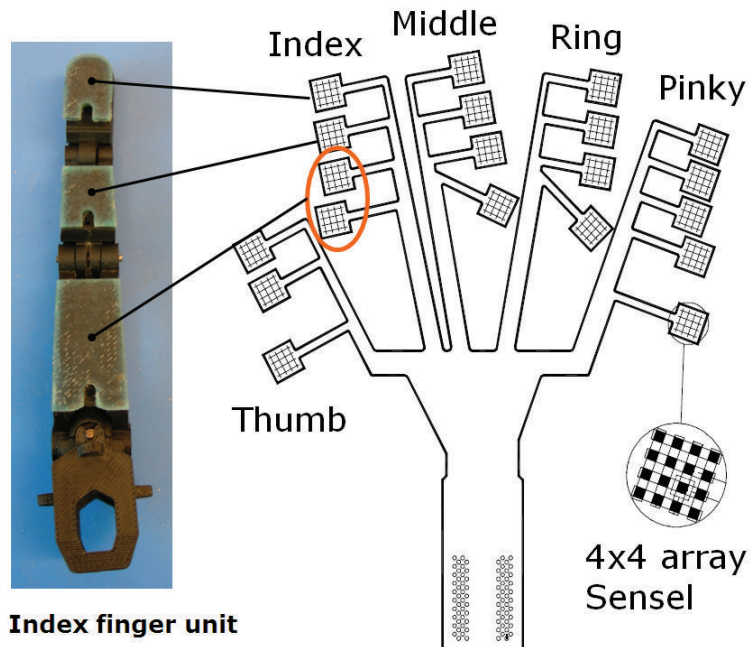


Figure 7.6: The configuration of the tactile sensor as the second layer of the artificial skin.

7.1.3 Tactile sensing of the robotic hand

As shown in Fig. 7.6, the tactile sensing of our 20-DOF robotic hand adopted the layered skin pad design that are described in Chapter 5 (see Fig. 5.2 for comparison). Since the design and performance of the artificial skin has been systemically investigated in the previous chapter, we are not going to repeat the description in this section.

7.1.4 Actuation system

As shown in Figure 7.7 the actuation system consists of two major components: pneumatic control unit, and robotic hand's actuation unit.

The actuation unit contains 36 of the M9 Airpel cylinders (Airpot Corp., CT) for finger tendons, and 4 of the M16 Airpel cylinders for wrist tendons (also used for finger actuation in this work). Double-acting cylinders were selected for complete control over the actuation force in both directions (although this feature is not yet utilized). The fully assembled actuation unit forms the base of the hand and weighs 660 grams. It can sustain about 75 N from each air cylinder with a safety factor of 3. When attached to a robot arm, most of this mass is near the base (elbow), thus won't cause mechanical conflicts during manipulation tasks. Detailed specifications of the actuation system can be found from our previous work [123].

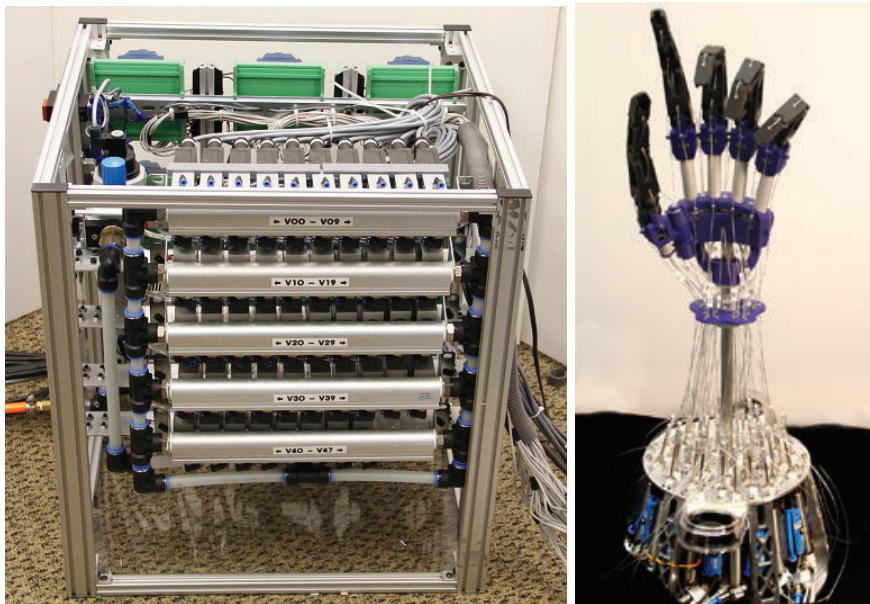


Figure 7.7: The actuation system of the robotic hand. *Left:* the pneumatic control unit. *Right:* Fully assembled actuation unit.

7.2 Modeling of the robotic hand

The variable moment arms of our proposed robotic hand closely mimic its human counterpart (as shown in Figure 7.8), and provide us an unique opportunity to investigate dexterous manipulations tasks. However, it also poses a series of challenges to the robotic hand control. Together with the information of the tendon excursion, knowing accurate moment arms at each joint of the finger can allow us to easily compute the kinematic configuration including joint angles and velocities for the corresponding finger.

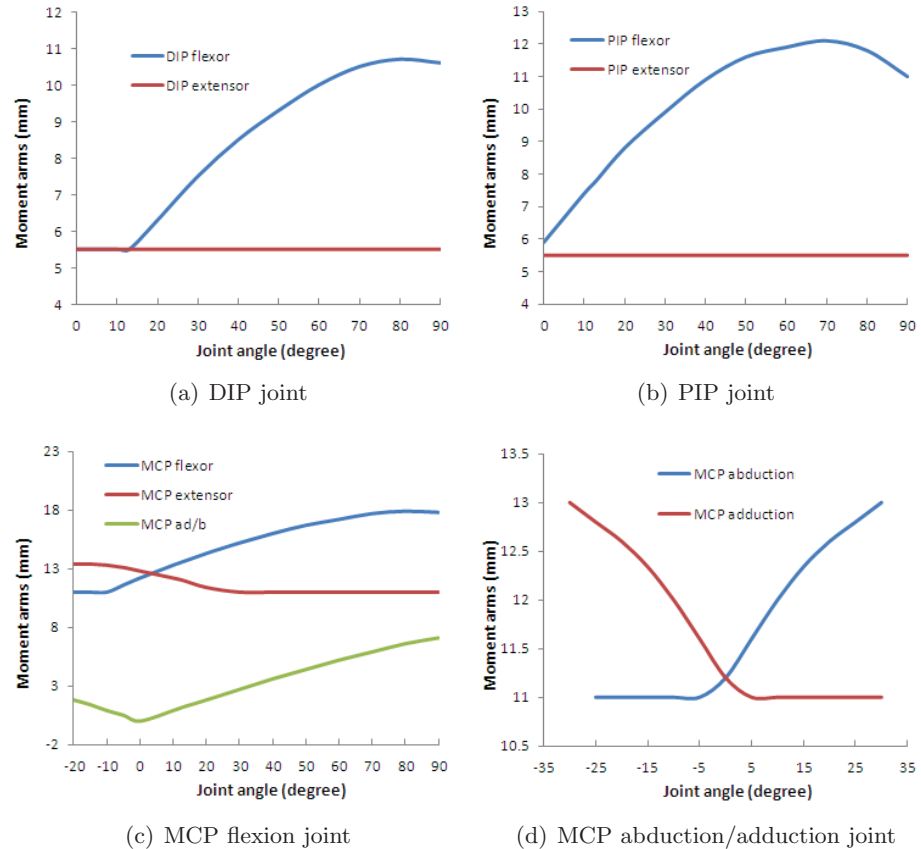


Figure 7.8: Moment arms at different joints of the index finger of the robotic hand (data are measured from the 3D CAD model). (a) Moment arms at the DIP joint. (b) Moment arms at the PIP joint. (c) Moment arms at the MCP flexion joint. (d) Moment arms at the MCP abduction/adduction joint.(Note: Flexion and abduction motions have positive angles, flexion; extension and adduction motions have negative angles.)

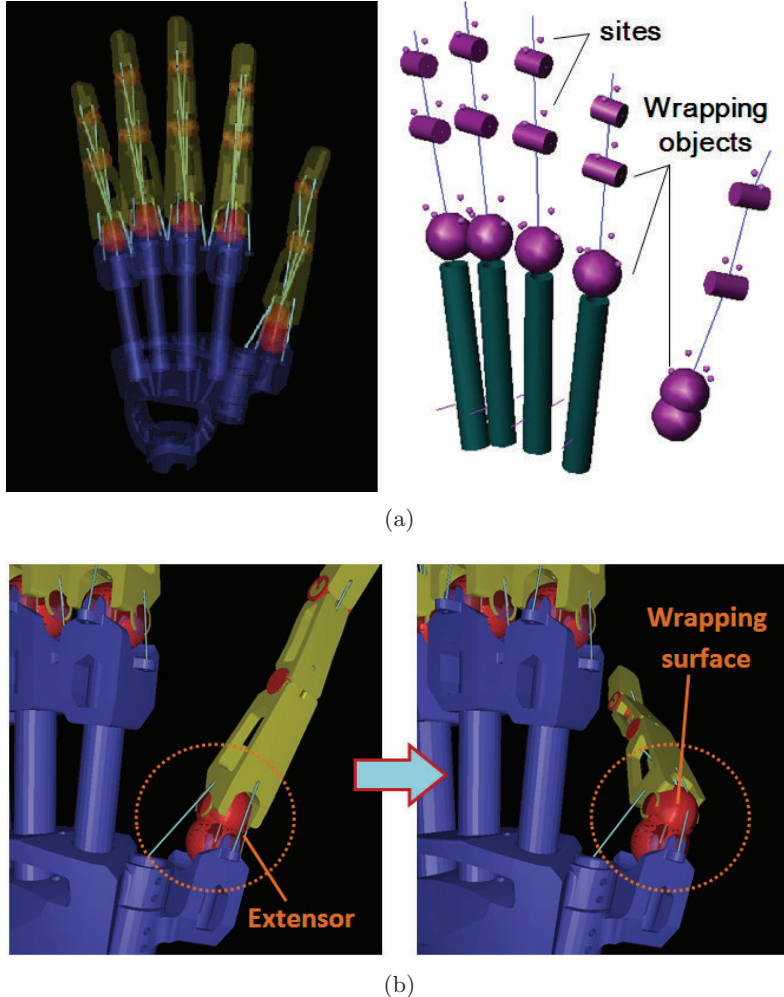


Figure 7.9: Modeling of our low-cost robotic hand. (a) Kinematic model of the robotic hand visualized in OpenGL(*left*) and the model of the tendon paths(*right*). (b) The thumb extensor wrapping at the CMC joint during the flexion motion.

Instead of complicating the mechanical structure of our robotic hand by adding multiple joint sensors, we chose to construct a kinematic model of the hand and its tendon paths in order to estimate the finger status(as shown in Fig. 7.9(a)) This was done by taking the numeric data from the CAD file used to 3D-print the robotic hand, and importing it in an XML file that is then read by our modeling software MuJoCo. The same process has been

explained in detail in Chapter 4, therefore only the important figures are presented here.

As shown in Figure 7.9(b) MuJoCo computes the shortest path that passes through all sites defined for a given tendon, and does not penetrate any of the wrapping objects (i.e. the tendon wraps smoothly over the curved surfaces).

7.3 Performance evaluation of the robotic hand

In this section, we conducted a series of experiments to test the performance of the compliance, and speed of our proposed robotic hand. Preliminary results are reported.

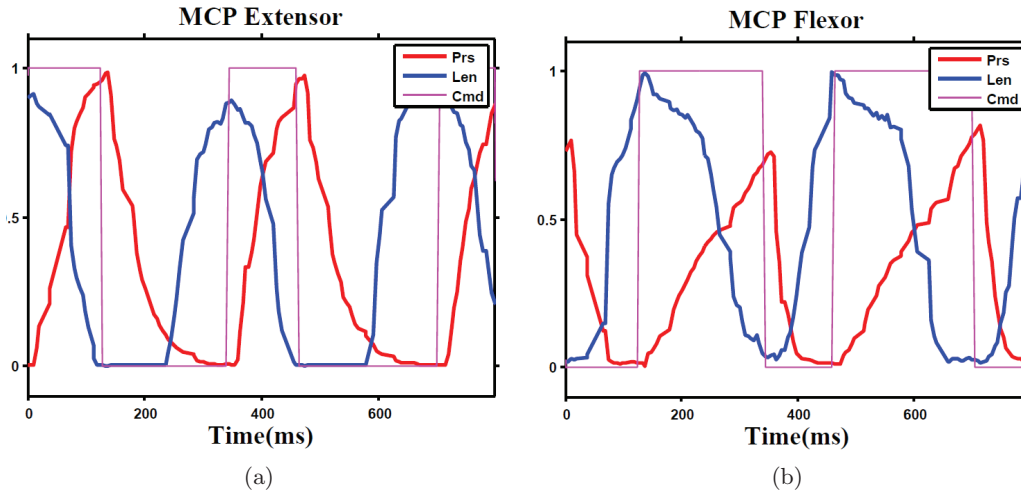
7.3.1 The force behaviors and speed of the robotic hand

In order to investigate the characteristics of the force and compliance of the actuation system, we conducted experiments using a Shadow hand in our previous work [123]. In this chapter, we conducted the same experiments on our proposed robotic hand and compare its performance with the Shadow hand in Table 7.2. An external force of 2 grams at the index finger tip was enough to flex the MCP joint thus confirming the exceptional compliance of our fully actuated robotic hand. During the test of the maximum fingertip forces, all the index fingers of the two robotic hands were commanded to be fully extended, the moment arm of our proposed robotic hand is 13 mm (104 mm finger length) compared to Shadow hand’s 10 mm moment arm (96 mm finger length), but produced over doubled forces in both flexion and extension directions.

The actuation system we developed was mainly prepared for the tendon-driven hands and performing dexterous hand manipulation experiments. Any dexterous hand manipulation demands agility and responsiveness from its actuation hardware. The speed capabilities of our robotic hand were evaluated using a simple open loop bang-bang control strategy over the index finger. The goal was to achieve full stroke movements (joint limit to joint limit) at maximum frequency. Control switching frequency was gradually increased until finger started making incomplete strokes, i.e. reversed before hitting the joint limits. Using this simple strategy, a frequency of about 3Hz was achieved for a full finger motion (from

Table 7.2: Comparison of characteristic force behaviors

| <i>Specifications on force behaviors</i> | <i>Our proposed robotic hand</i> | <i>The Shadow hand</i> |
|--|----------------------------------|------------------------|
| Minimum actuation force at finger tip to move MCP joint(vertical actuator, at atm pressure) | 0.020 N (2.0 g weight) | 0.039 N (4.0 g weight) |
| Minimum actuation force at finger tip to move MCP joint(vertical actuator, at min slack correction pressure) | 0.078 N (8.0 g weight) | 0.059 N (6.0 g weight) |
| Maximum flexion force at index finger tip | 6.91 N (705 g weight) | 2.94 N (300 g weight) |
| Maximum extension force at index finger tip | 6.86 N (700 g weight) | 4.31 N (439 g weight) |

Figure 7.10: Full finger motion at 3 Hz. *Left\Right:* Response of the valve pressure (prs) and length sensor (len) of the MCP extensor\fexor with respect to the command signal.

fully extended to fully flexed for all the three joints) as shown in Figure 7.10 and 7.11. We are working towards a more principled way to further improve actuation speed by carefully modelling valve and pneumatics of our system.

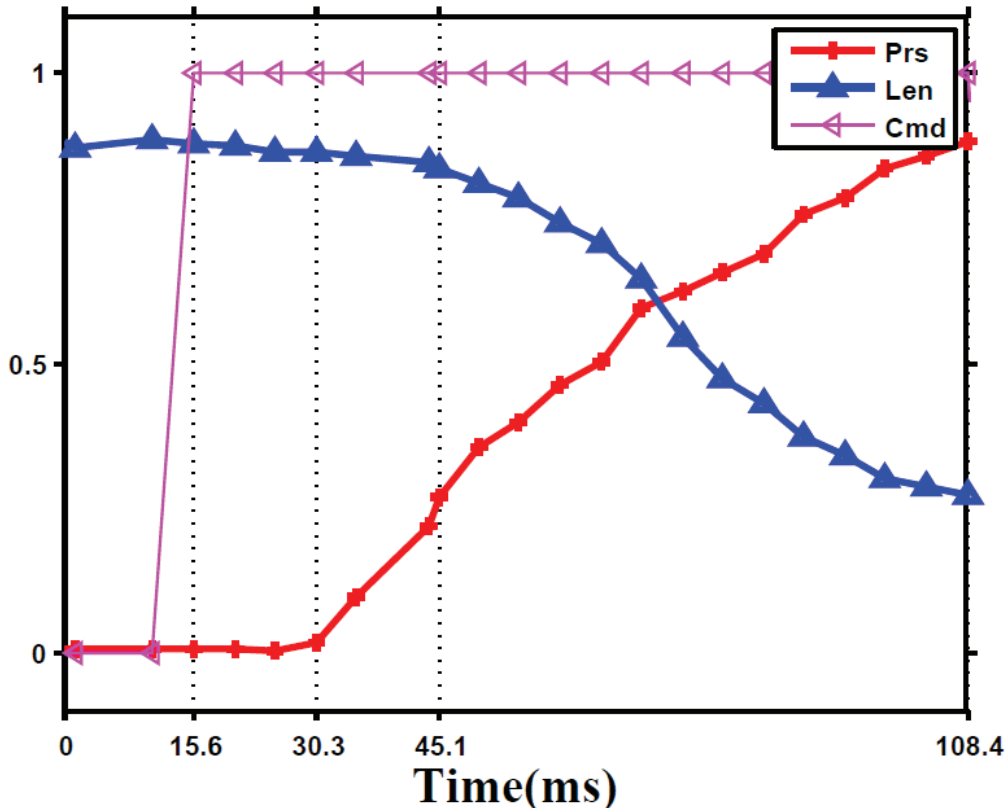


Figure 7.11: Time stamps. *From left to right:* T1 – Event Trigger, command written to the pneumatic value, T2 – Pressure wave arrival, T3 – Index finger MCP movement detected.

7.3.2 The cost of the robotic hand

The cost of our proposed robotic hand itself is very low – approximately \$100 for all materials. Of course this does not include the tactile sensing (\$300) and actuation system. However, a ShadowHand robot with similar mechanical capabilities and also without actuation costs around \$60,000. Thus the proposed design offers a dramatic reduction in cost, as well as time required to manufacture and test a modified version of the system when needed.

A notable advantage of having an inexpensive hand (and instead investing in the actuation system) is that only the hand will typically interact with the environment. Thus any damage is likely to occur in parts that are inexpensive to replace. The modular design of

the robotic hand and its tactile sensing can further reduce the cost as well.

7.4 Conclusion

We have described the method of designing and modeling of a 20-DOF anthropomorphic robotic hand. Our proposed robotic hand has 31 components, and can be manufactured in 24 hours. Important parameters such as finger length, DOF, and ROM of the robotic hand can all be individually changed with little effort or modification. Skin pads for tactile sensing were also developed. For evaluating design ideas and speeding up our design cycle, we used our custom modeling software to establish the kinematic model of the robotic hand. Experimental results on tactile sensing, force behaviors and actuation speed suggested that our robotic hand has comparable performance to the ShadowHand robot, but requires only a fraction of the latter's cost. Our proposed design has the potential to become an important tool for assisting robotic hand researchers to cost-effectively and efficiently investigate different control methods.

Chapter 8

PROOF-OF-CONCEPT PROTOTYPE OF THE ANTHROPOMORPHIC ROBOTIC HAND

In the previous chapters, we reviewed the important anatomy of the human hand, fabricated and tested the crocheted extensor hood, designed artificial fingers that possess human-like compliance, actuated the artificial finger with pneumatic system, proposed the design of artificial skin, and fingertip sensors. Based on what we learn from these investigation, in this chapter, we conclude the work by briefly describing the prototyping process of our proposed anthropomorphic robotic hand. This robotic hand is composed of one thumb and four fingers. Different from all the existing robotic hands, its joints highly mimic their human counterparts by matching not only the structure, but also the working principles that allow the fluent motions of the human hand.

The structure of this chapter is organized as follows: The first part focuses on the design and prototyping process of our proposed robotic hand. And the second part addresses the design of the novel data glove.

8.1 The rapid prototyping process of the anthropomorphic robotic hand

As shown in Fig. 8.1, all the parts of the robotic hand can be printed out on a 20×20 cm tray (Dimension BST 768, Stratasys Corp., Eden Prairie, MN)). Depending the setting of the inner structure and resolution of the parts (0.025 mm), the total printing time could be less than 20 hours.

After cleaning the support materials off from the parts, each robotic finger can be quickly assembled as explained in Fig. 4.3. The design of the joint capsule was further improved. As show in Fig. 8.2, one pair of the crocheted ligaments is used to mimic the two collateral ligaments located on the sides of each finger joint. Similarly, the function of the volar plate (see Fig. 2.10) is replaced by two crocheted ligaments anchored across each joint (as shown



Figure 8.1: The full set of 3D-printed finger segments made of ABS plastic.

in Fig. 8.2). Instead of using the silicone rubber sleeve, laser-cut rubber sheet was used to provide the human-like compliance (80W CO^2 1100 series laser, Legacy Laser, Defiance, PA). Based on the ROM of each joint, the dimensions of these components vary in size. The design improvement greatly reduced the fabrication time. The longest joint ligaments can be manually crocheted within five minutes. And the laser-cut rubber sheet can be prepared in few seconds. Coating the thermoplastic onto the joint base (as shown in Fig. 4.3) becomes the most time-consuming part of the prototyping process. However, it still can be finished within 20 minutes for each finger.

The next step is to attach the laser-cut extensor hood onto the dorsal side of each finger. In the previous chapters, we have detailed the important roles of the extensor hood during

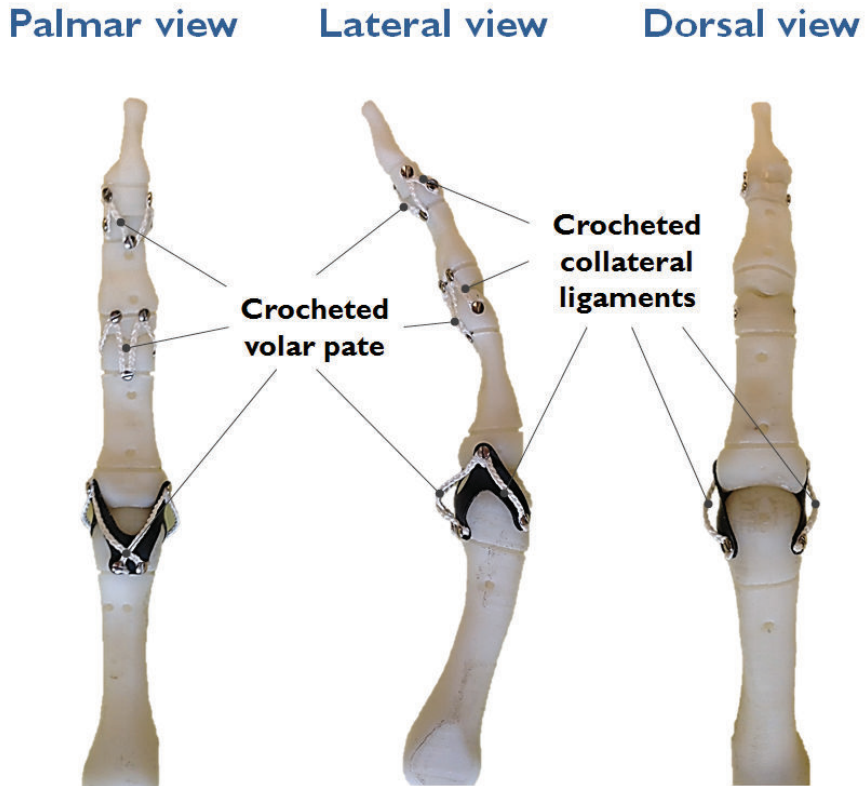


Figure 8.2: Simplified joint capsule composed of crocheted Spectra kite string and laser-cut high strength rubber sheet.

both finger extension and flexion motions. When finger straightens, the extensor hood acts as a force transmission mechanism that actively delivers torques at each finger joint. However, most of grasping movements of human hand heavily rely on the contraction of flexor muscles to execute different types of grips. With the help of flexor tendons, when co-contraction (like stiffening all the finger joints) of agonist and antagonist muscles is not required, the extensor hood is mainly functioning as a passive breaking mechanism that smartly facilitates the motion during finger flexion. In human hand, these two roles of the extensor hood are perfectly regulated by different groups of muscles controlled by our brain. Yet it is very challenging to replicate all the behaviors of those muscles with one set of actuators in robotic hand control. We thus propose to design a hierarchical extensor

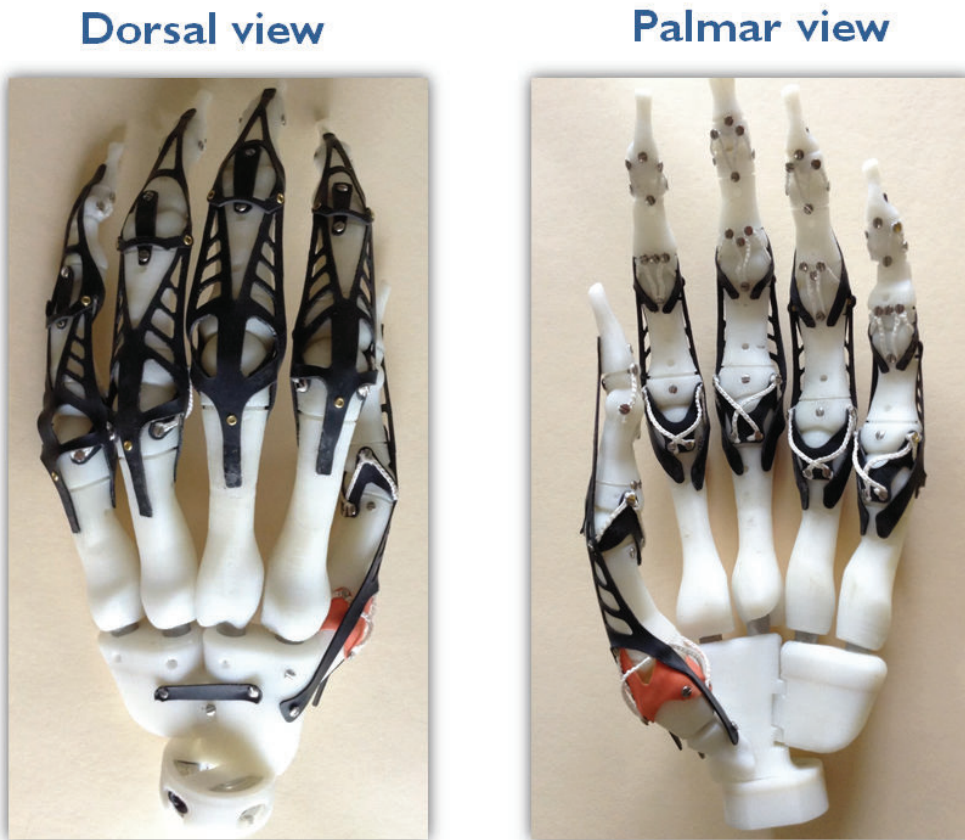


Figure 8.3: The fully assembled biomimetic hand containing the 3D-printed ABS bones from the scan of cadaveric hand bones. *Note:* The wrist of the hand is immobilized since it is not the focus of this thesis at this stage.

mechanism in order to handle the two roles of the extensor hood separately.

As shown in Fig. 8.3, highly resilient rubber sheet was laser cut into the shape of an extensor hood to mimic the passive behaviors of the extensor tendons, leaving the active part of control to the electric servos that enable the finger extension through cable-driven mechanism. By doing so, the control of the robotic hand can be greatly simplified.

Before each finger was mounted onto the wrist of the robotic hand, another important mechanism was implemented in order to mimic the function of tendon sheaths on the palmar side of the fingers. We name them as the elastic pulley system, which consists of 14 patches of

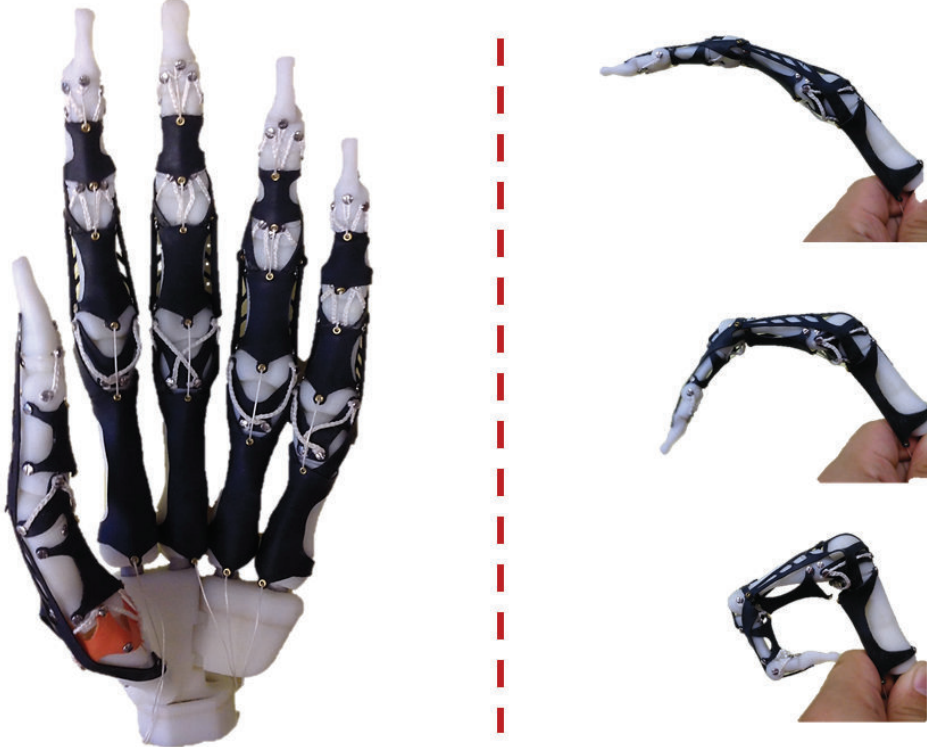


Figure 8.4: The elastic pulley system implemented on the palmar side of the biomimetic hand. *Left:* The flexor tendons of the robotic hand are running underneath the laser-cut, elastic tendon sheaths. *Right:* Snapshots of a separate finger showing the bulging process of the elastic pulleys during finger flexion.

laser-cut rubber sheets. The rubber sheets were slightly pre-stretched before being attached onto the finger so that they could closely conform to the contour of the bone. Then flexor tendons made of high strength Spectra® strings (200 N yield strength) were routed through the rubber tendon sheaths via several rivet reinforced ports (see Fig. 8.4). One end of the flexor was to be inserted into the distal joints of the hand, and the other end was directly connected to the electric servo. Once the servo starts rotating, each robotic finger bends with the retraction of the strings during which the bulging process of the elastic pulleys occurs simultaneously. The design of the rubber tendon sheaths closely mimics that of the human counterpart (see Fig. 2.4) by providing mechanical advantages that allow torques

at the finger joints to gradually increase as long as the servos keep pulling the strings.

The final step was to mount the thumb and fingers onto the wrist of robotic hand. The wrist of our proposed robotic hand has 1-DOF at the base of the ring and little fingers. As we addressed at the beginning of this thesis, the biomimetic design of the wrist is left for future work, the current version only serves as a static base for testing the fingers. But the strings' routing paths at the wrist are closely mimicking the carpal tunnel of the human hand. In total, ten Dynamixel servos [124] (nine MX-12W and one AX-12A) are used to actuate the robotic hand (as shown in Fig. 8.5). Two servos are used to control the flexion and extension of the ring and little fingers through a differential pulley transmission. The index and middle fingers are separately controlled by two pairs of servos so that each of them can bend and straighten independently. But they also share an extra servo for a coupled control at their MCP joints. We use three actuators to control the thumb. One of them is an AX-12A Dynamixel servo that has a larger gear ratio (254/1) than others (32/1) and is used for the extension/abduction of the thumb. The other two servos of thumb are assigned to control the flexion and adduction motions, respectively. The diameter of the pulley that is directly attached to the shaft of the servo is 20 mm.

The specifications of the two types of servos are listed in Table 8.1.

Table 8.1: The specifications of the Dynamixel servos.

| <i>Dynamixel Servo Model</i> | <i>AX-12A</i> | <i>MX-12W</i> |
|------------------------------|--------------------------|--------------------------|
| Working voltage (V) | 12 | 12 |
| No load speed (RPM) | 59 | 470 |
| Stall torque (N·m) | 1.5 | 0.2 |
| Gear ratio | 254/1 | 32/1 |
| Resolution (°) | 0.29 | 0.088 |
| Range of Motion (°) | 300 | 360 |
| Communication Speed | 7343bps 1Mbps | 8000 bps - 4.5 Mbps |
| Weight (g) | 55 | 54.6 |
| Dimensions (mm) | $32 \times 40 \times 50$ | $32 \times 40 \times 50$ |

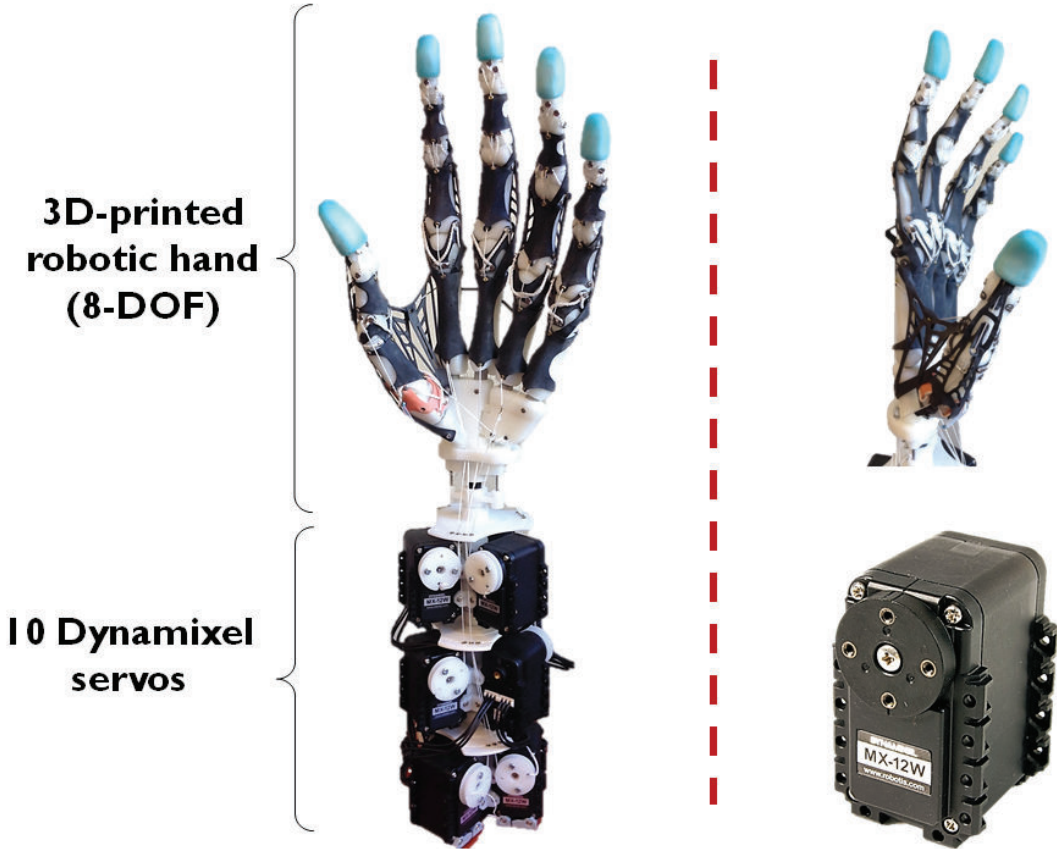


Figure 8.5: The fully assembled biomimetic hand incorporated with the electric actuators. *Left:* The palmar aspect of the anthropomorphic robotic hand. *Top right:* The lateral view of the robotic hand showing the structure of the thumb web. *Bottom right:* The MX-12W dynamixel servo.

8.2 Teleoperation of our proposed robotic hand

Currently, no tactile or joint angle sensor was implemented into our proposed robotic hand yet. But the designs we developed for the artificial skin and fingertip sensor could all be modified to work with the existing robotic hand prototype. For this proof-of-concept prototype, the next critical step is to validate its functionality with teleoperation. To this end, a new type of data glove was designed in order to achieve the one-to-one easy mapping from the human hand to the robotic hand (see Fig. 8.6).

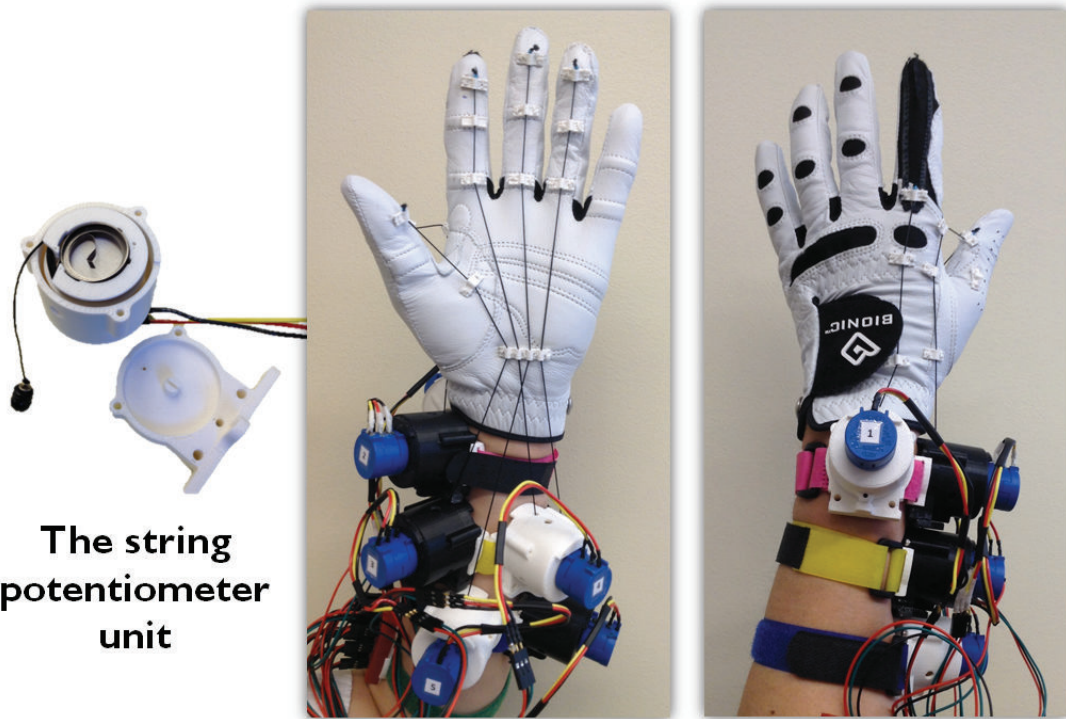


Figure 8.6: The string-potentiometer based data glove. *Right:* A disassembled string-potentiometer unit. *Middle:* The palmar view of the data glove showing the four flexors connected to the thumb, index, middle, and coupled ring and little fingers. *Right:* The dorsal view of the data glove showing the control inputs from the index finger's PIP joint and the ad/b motion of the thumb.

Since our proposed anthropomorphic robotic highly mimics the human hand, it is straightforward to consider of extracting movement information from the latter and sending them as control inputs for the former. This idea is not new, in fact, most of the dexterous motions demonstrated by the existing anthropomorphic robotic hands were all realized by using this method known as the teleoperation. During this process, in order to map the motion from the human hand to the robotic hand, joint angles are often collected by a data glove, and then translated into commands that can be used to control the actuators. Depending on the type of the transmission system, the translated commands could contain information ranging from the gear-ratio values, configurations of a linkage system, to an

$m \times n$ Jacobian matrix that correlates m joint angles with n actuators. However, none of those data gloves can realize the one-to-one mapping from the human hand to the robotic hand for two reasons. First, very few robotic hands directly implement electric motors at their joints because small motors are neither compact enough to fit into the finger joint nor strong enough to generate enough torques at the fingertip to perform any meaningful task. So the actuation system of the robotic hand always requires a certain type of transmission system. Therefore the readings of joint angles measured from a data glove could not be directly used for the control of any robotic hand without taking into consideration of the transmission system. Second, the kinematics of these robotic hands are based on simplified mechanical joints whose configurations and rotational axes could be very different from the specific human hand that is used in the teleoperation, posing an inherent mismatch in the calibration procedure.

In contrast, our proposed anthropomorphic robotic hand can be categorized as a cable-driven system in which all the strings mimicking the extensor/flexor tendons of the human hand. Different from all the existing anthropomorphic robotic hands, the kinematics of our proposed robotic hand inherently matches that of the human hand. This means if we could directly provide information about how much the tendons should travel back and forth, the control problem of our proposed robotic hand can be greatly simplified by bypassing the complicated mapping conversion process that often involves the non-linear relationships in the $m \times n$ Jacobian matrix.

As shown in Fig. 8.6, our data glove uses six custom-made string potentiometers whose original design was adopted from the online open-source STL files [125]. Each string potentiometer works as a key retractor with an anchor point at the corresponding tendon insertion site near the distal joint of each finger. It can measure the length of the string when it travels back and forth along with the finger movement.

As demonstrated in Fig. 8.7, the data glove was successfully used to teleoperate our anthropomorphic robotic hand via an off-the-shelf servo controller (CM-530) [124]. During this process, information of natural hand motions of the human operator were extracted by the data glove, and transformed into data about how much each string (tendon) should travel. These data were simultaneously converted to rotational angles of each servo based

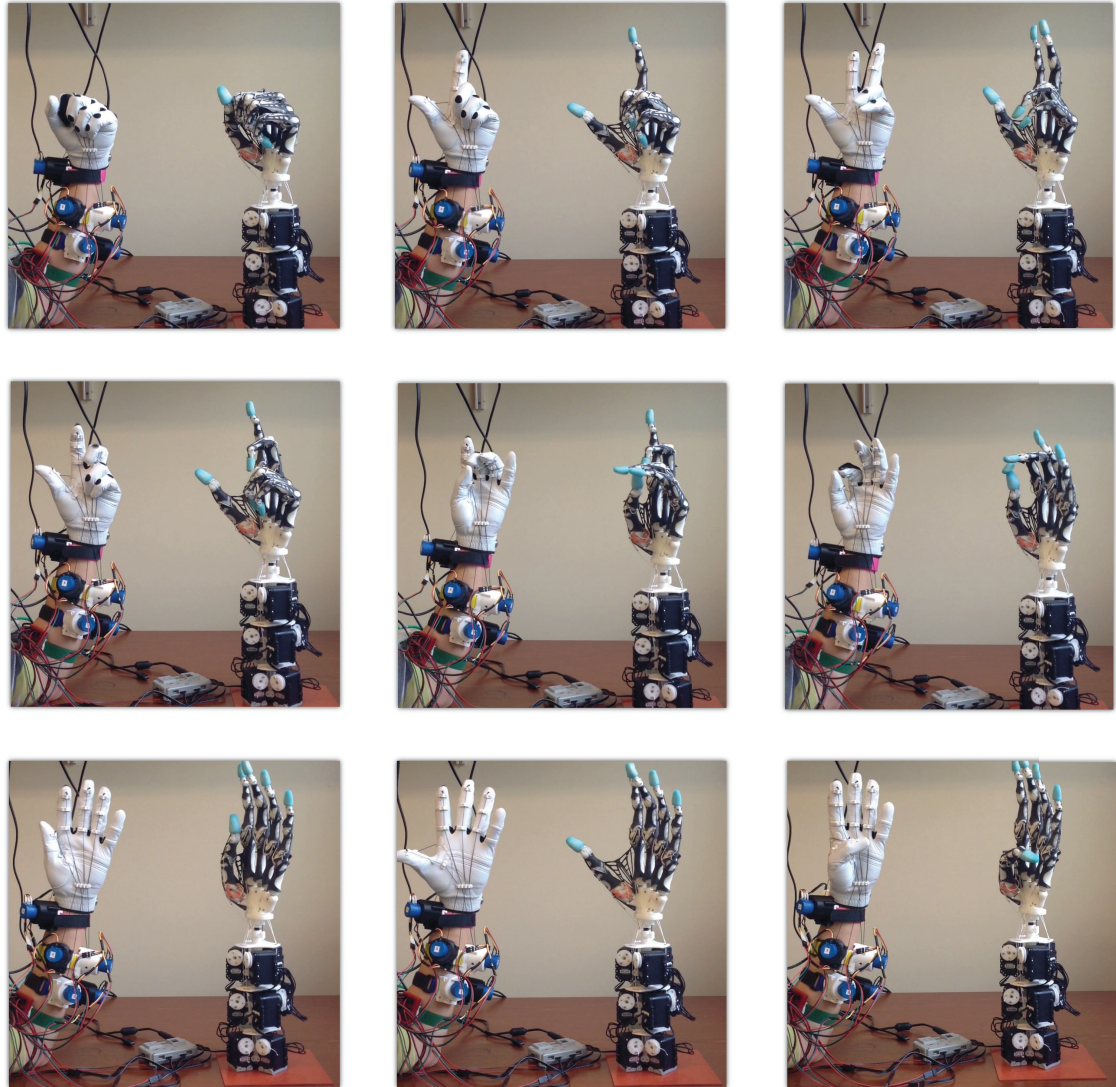


Figure 8.7: Snapshots showing the teleoperation process of our proposed anthropomorphic robotic hand. *Top row:* The index and middle fingers can move independently from the coupled ring and little fingers. *Middle row:* The precision grasp between the index/middle finger and the thumb. *Bottom row:* The abduction, adduction, and opposition motions of the thumb.

on the diameter of the pulley directly connected to its shaft.

8.3 Performance of the biomimetic robotic hand

In addition to the qualitative evaluation mentioned above. We also quantitatively investigated the performance of our robotic hand in terms of its fingertip forces and trajectories. The experimental setup, procedures, and results are discussed in following subsections.

8.3.1 The effects of finger postures on fingertip force

Although the MCP joint of each finger potentially allows any motion ranging from 45° in extension to 90° in flexion, our human hands are not always operated at these extreme postures. Instead, a smaller range of motion were found to be prevailing during the reach and grasp motions of the human hand. And therefore two metrics, namely openness and flatness were introduced to define the boundary of this smaller set of hand postures for ergonomic applications by Bae [27].

As shown in Fig. 8.8, the changes of joint angles in the index finger can be used to distinctively represent the four boundary postures. In the order of MCP, PIP, and DIP joint angles, there are $(9.9^\circ, 60.3^\circ, 40.2^\circ)$, $(29.7^\circ, 9.9^\circ, 6.6^\circ)$, $(50.4^\circ, 39.6^\circ, 26.4^\circ)$, and $(60.3^\circ, 19.8^\circ, 13.2^\circ)$ for postures 1, 2, 3, and 4, respectively. Because most of our daily objects can be picked up by using the grasp bounded by those four postures, it is of our interest to investigate how the fingertip force of our robotic hand changes with respect to the four different finger postures.

To this end, we designed an experimental setup that is compatible with the four different situations. As shown in Fig. 8.9, a separate index finger was securely mounted on a 3D-printed base. And four detachable jigs, which were also attached to the base, were alternated to position the same load cell (MLP-25 , Transducer techniques, CA) so that the force sensing side of the load cell could always be in good contact with the fingertip during each trial. Besides using these jigs, the fingertip of the index finger was modified to incorporate a small socket to further prevent slip during the test (see Fig.8.10).

The flexor tendon of the finger was connected to a plastic tray that weights 20 grams.

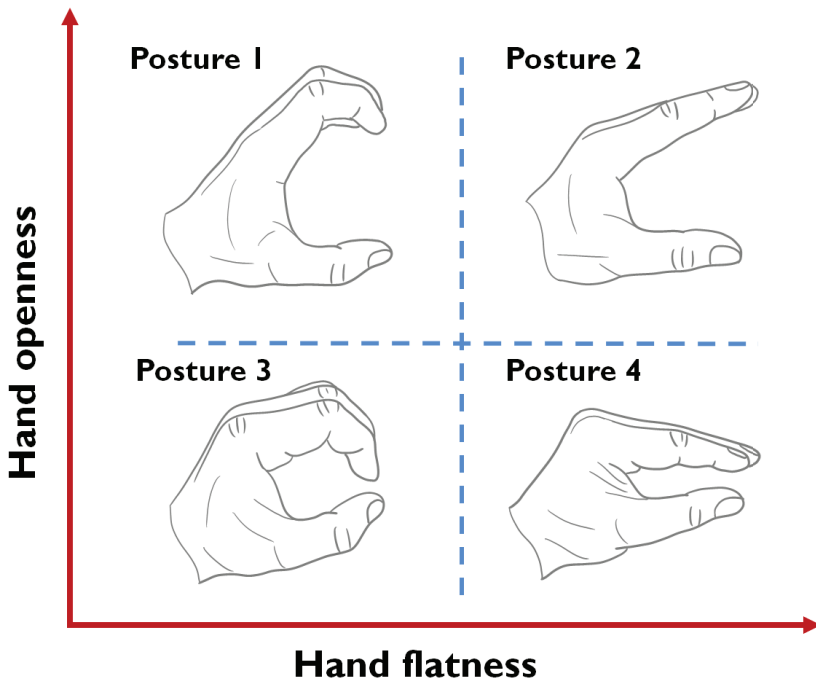


Figure 8.8: The four hand postures that can be used to bound the common reach and grasp motions of the human hand (adopted from [27]).

Ten known weights¹ were cumulatively added into tray during each loading test. After calibration, the force readings from the load cell were recorded by NI DAQ PCI-6229 at 200 Hz. At each finger postures, six loading trials were first conducted. Then we discarded all the first trials to avoid system errors caused by switching jigs and repositioning the load cell. The fingertip forces from each trial were calculated by subtracting the force readings when no weight was added.

The result is plotted in Fig. 8.11. It is interesting to observe that the output of fingertip force is greatly affected by hand postures. When the finger bends into the palm, both the flatness and openness of the hand are reduced, generating the smallest flexor to fingertip force ratio (4.50, $R^2 = 0.98$) at posture 3. Similarly, when the finger straightens, both the flatness and openness of the hand are increased, resulting in the largest flexor to fingertip

¹98, 104, 104, 104, 104, 104, 108, 180, 208, 212 grams

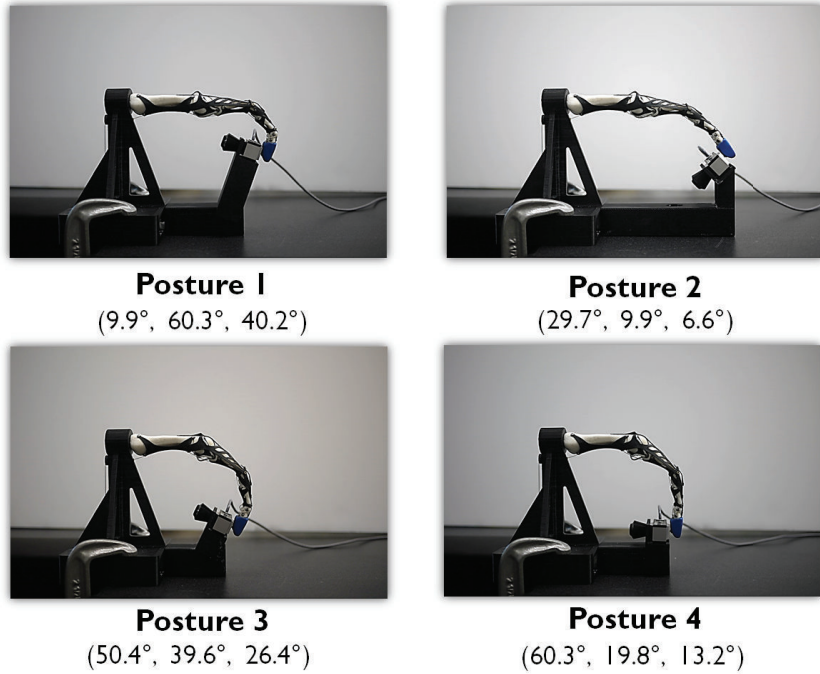


Figure 8.9: Experimental setups for testing the fingertip forces at four different boundary postures. *Note:* The joint angles are denoted in the form of (MCP, PIP, DIP).

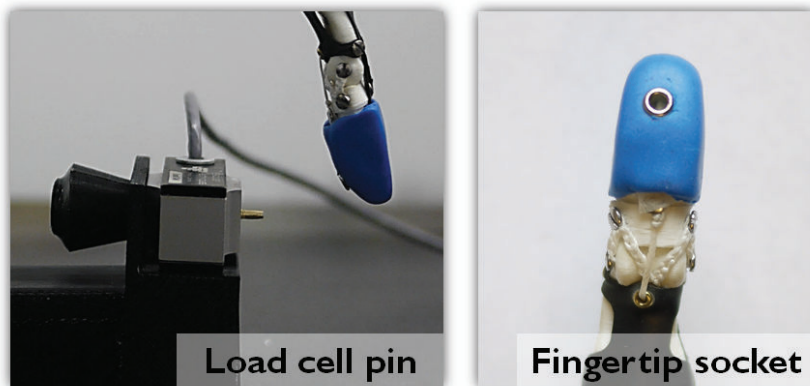


Figure 8.10: The mechanical coupling between the fingertip and the load cell.

force ratio (6.90, $R^2 = 0.99$) at posture 2. Since the flexor mechanism of our robotic hand closely mimics the elastic pulley system of its human counterpart (see Fig. 8.4), the

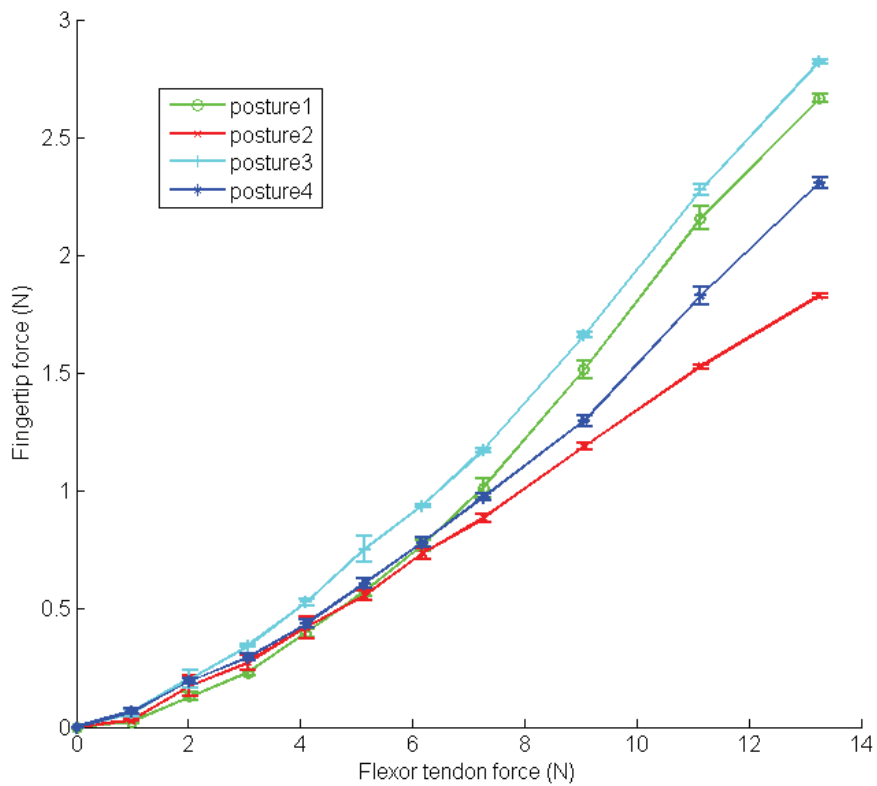


Figure 8.11: The relationship between the flexor tendon's forces and fingertip forces at four different finger postures. *Note:* Data are reported as mean +/- standard deviation.

phenomenon suggests that under the same amount of muscle forces, the human hand is inherently more compliant when all the fingers are extended to reach objects, but becomes stiffer when fingers wrap around objects to form a firm grip.

The result of the flexor to fingertip force ratios is summarized in Table 8.2. The flexor tendons of our robotic hand mimic the flexor digitorum profundus (FDP) tendon of human hand by having the same insertion site at the distal joint. Although the human finger has another flexor tendon – the flexor digitorum superficialis (FDS) tendon – inserted to the base of the PIP joint, we chose to not incorporate the FDS in this version of the robotic hand, because it is reported that the FDP tendon generates greater fingertip forces than

Table 8.2: The flexor to fingertip force ratios at different finger postures

| <i>Posture Number</i> | <i>Flexor vs. tip force slope</i> | <i>R</i> ² | <i>The Max measured fingertip force</i> ¹ (N) | <i>The Max predicted fingertip force</i> ² (N) |
|-----------------------|-----------------------------------|-----------------------|--|---|
| 1 | 4.61 | 0.96 | 2.68 | 32.54 |
| 2 | 6.90 | 0.99 | 1.84 | 21.74 |
| 3 | 4.50 | 0.98 | 2.84 | 33.33 |
| 4 | 5.60 | 0.98 | 2.34 | 26.79 |

¹The force readings are from the MLP-25 load cell.

²The fingertip forces are predicted based on the stall torque of the AX-12A Dynamixel servo.

the FDS tendon during isometric tasks [126]. Compared to our results listed in Table 8.2, it was found that the ratio of FDP tendon to fingertip force in the human hand is 7.9 ± 6.3 during pinch grasp [127]. The smaller ratio observed in our robotic hand suggests that our biomimetic pulley mechanism can transmit tendon forces to the fingertip more efficiently.

The origin of this transmission efficiency comes from the bulging process which was also clearly observed across all the four trials. As shown in Fig. 8.12, the moment arm at each finger joint continues to grow as the tendon force increases (by adding more weights into the tray). Since the tendon sheaths were made of highly resilient rubber sheet, this bulging process can be reversed without any noticeable deformation once the tendon force reduces. As shown in Fig. 8.11, the small errorbar of the results also confirms that our proposed robotic hand is quite consistent in term of outputting fingertip force. As shown in the last column of Table 8.2, our proposed robotic index finger can potentially generate over 30 N force at its fingertip if stronger servo motor (Dynamixel AX-12A) is used. This amount is comparable with that of the human index finger reported in past [128].

A repeatable experimental setup is crucial to all the scientific investigation. However, most of the in-vivo studies conducted on cadaver hands could not be repeated by other researchers since the decay process of the organic tissues is irreversible. Besides, the biological variations caused by individual differences could also result in a long lasting debate. In contrast, our proposed robotic hand highly resembles its human counterpart and can be

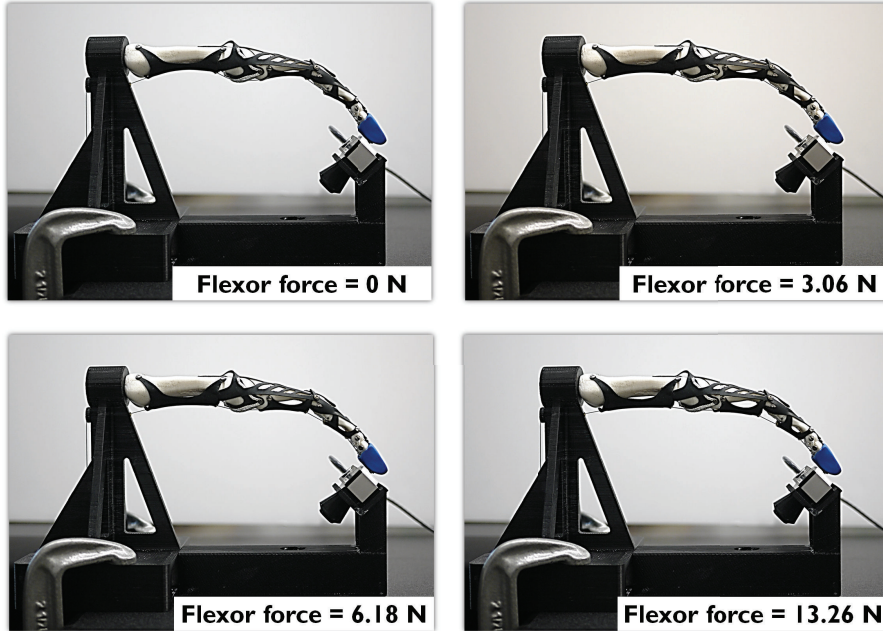


Figure 8.12: The bulging process of the tendon sheaths (from Posture 1 as shown in Fig. 8.9) when the flexor tendon force increases.

easily duplicated with variations in anatomical details, therefore it can help to document these important scientific findings by serving as an open-source platform.

8.3.2 Trajectory of the fingertip

Because our robotic hand system is underactuated with elastic components at each finger joint, it is of our interest to investigate the repeatability of our proposed mechanism, especially when the finger' ROM is controlled in between full flexion and extension postures.

As we briefly mentioned, the ring and little fingers are coupled considering their collaborative relationship as the grasping fingers. Their flexion and extension motions are controlled by a pair of Dynamixel servos through a differential pulley transmission as shown in Fig. 8.13. The benefit of using such a pulley structure is to provide an extra source of hand compliance in addition to the build-in compliance at each finger joint, since it allows the two grasping fingers to conform to the contour of an object by automatically adjusting

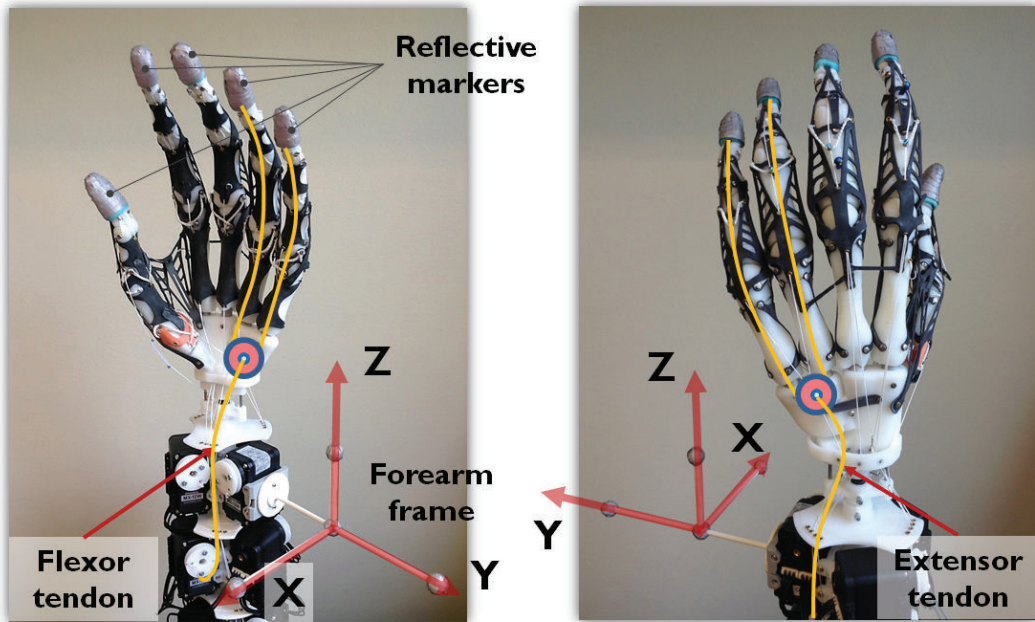


Figure 8.13: Labeled pictures showing the differential pulley transmission for ring and little fingers and the locations of the reflective makers. *Note:* All the marker coordinates were recorded with respect to the forearm frame.

the shared string length between the two insertion sites. But the drawback is that the underactuation mechanism could also become a source of uncertainty bringing the two fingers into some unknown postures when they bend and straighten between the two extreme postures.

Compared to the ring and little fingers, the index, middle, and thumb are each actuated by more than two servos, therefore can be better controlled in this case. During the fingertip tracking experiment, we chose two known postures for the coupled ring and little fingers, and then controlled the two servos to bend and straighten the coupled fingers approximately once every two seconds. The coordinates of the reflective markers attached to the fingertip of the fingers are recorded by a motion capture system (Vicon Bonita) composed of 7 infrared cameras at 240 Hz VGA resolution. The Vicon system was calibrated, and is able to detect 0.5 mm displacement in all directions.

In order to ease the marker occlusion and confusion issues, we attached a forearm frame (see Fig. 8.13) near the wrist of our robotic hand, so that we can record the marker trajectories for one fingertip at a time, and then transform their coordinates from the default world frame to this forearm frame when processing the data. The use of this forearm frame also allows us to constantly change the orientation of our robotic hand during hand motions in order to achieve better visibility for the reflective markers.

The XYZ coordinates of the fingertips from the ring and little fingers are plotted in Fig. 8.14(a) and (b), respectively. 20 repetitions of the full flexion and extension motions were recorded. The data show a highly repeatable pattern both from the the ring and little fingers, which suggests that the built-in joint compliance and differential pulley system do not affect the repeatability performance of our proposed robotic finger design. The patterns of their repetitions look very similar to each other since their actuation is coupled. Thus, in the following discussion, we are going to use the ring finger as a representative case.

After being projected onto the X-Z plane, the flexion and extension trajectories of the ring finger's tip can be clearly observed in Fig. 8.15. It is interesting to find that the flexion and extension motions of our biomimetic robotic finger were not following the same trajectory. Instead, the area bounded by the two trajectories covers a big portion of the reachable workspace of the ring finger [129]. The flexion trajectory closely resembles that of the logarithmic spiral curve observed from human finger's flexion motion [130]. However, the extension trajectory was rarely reported in the past literature mainly because researchers were more interested in the grasping phrase of hand motion. The difference between the flexion and extension fingertip trajectories results from the sequential joint movements which can be affected by the corresponding joint stiffness. As shown in Fig. 2.3 and 2.4, the constantly changing joint stiffness can be potentially regulated by changing the structures and mechanical properties of both the extensor hood and the elastic pulleys of each robotic finger.

The fingertip trajectories of other digits were also recorded. Unlike the pre-determined inputs for the ring and little fingers, the repetitive movements of the index, middle, and

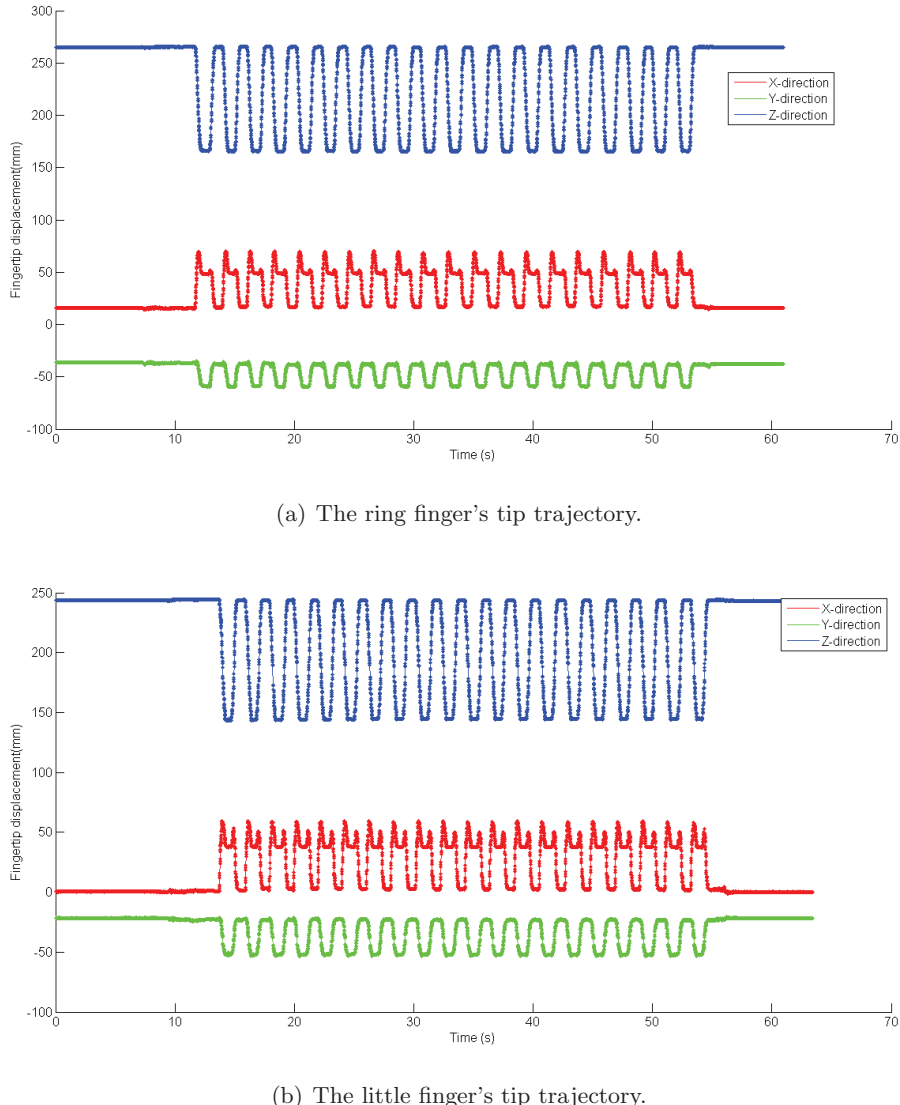


Figure 8.14: The displacement of the fingertips during 20 repetition of flexion and extension motions. (a) XYZ coordinates data from the ring finger. (b) XYZ coordinates data from the little finger. *Note:* The tracking data were separately recorded for the ring and litter fingers to avoid marker occlusion and confusion.

thumb were controlled by the human operator through our custom-made data glove, since our goal is to demonstrate the general workspaces of the robotic hand in the case of teleoperation. The two principal components of the thumb motions, namely the flexion/extension

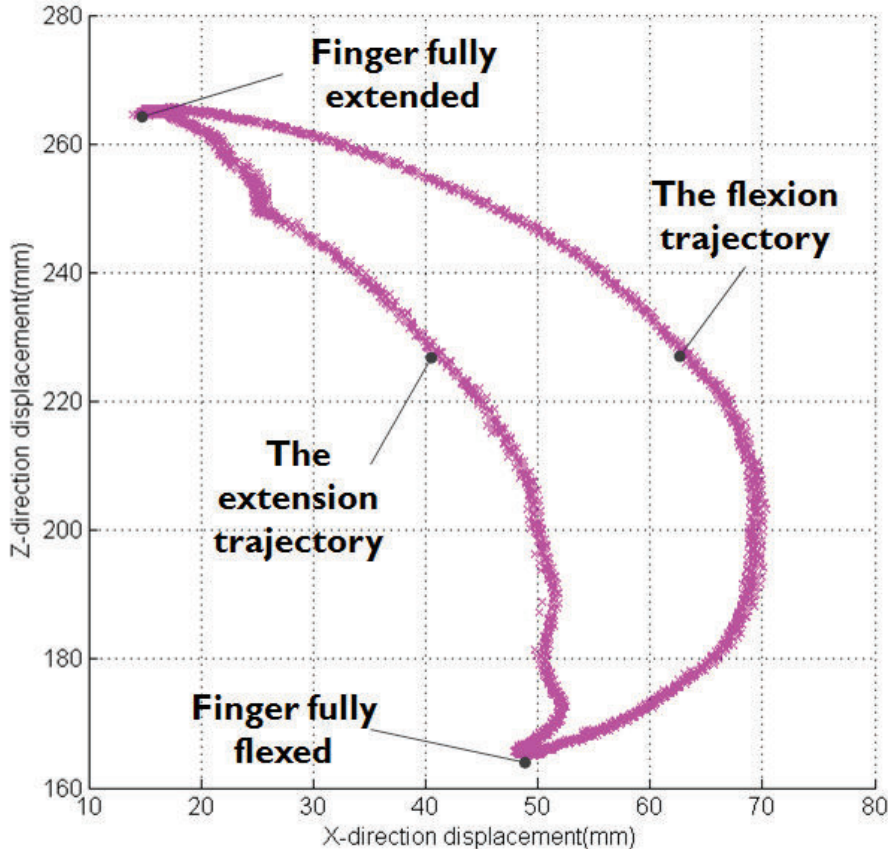


Figure 8.15: The ring fingertip's trajectories projected onto the X-Z plane. (Note: The scatter plot is from the 20 repetitions of the full flexion and extension motions.)

and the abduction/adduction were tested separately. As shown in Fig. 8.16, the teleoperation results in more scattered data points compared to the ones collected from the ring and little fingers.

As we explained when we discussed the ring and little fingers. The trajectory of each fingertip (except for the coupled ones) was first individually recorded to avoid marker occlusion and confusion issues, and it was then plotted in the same forearm frame during post-processing. The overlapping points between the thumb and fingertips' trajectories clearly indicate the capability of the thumb opposition.

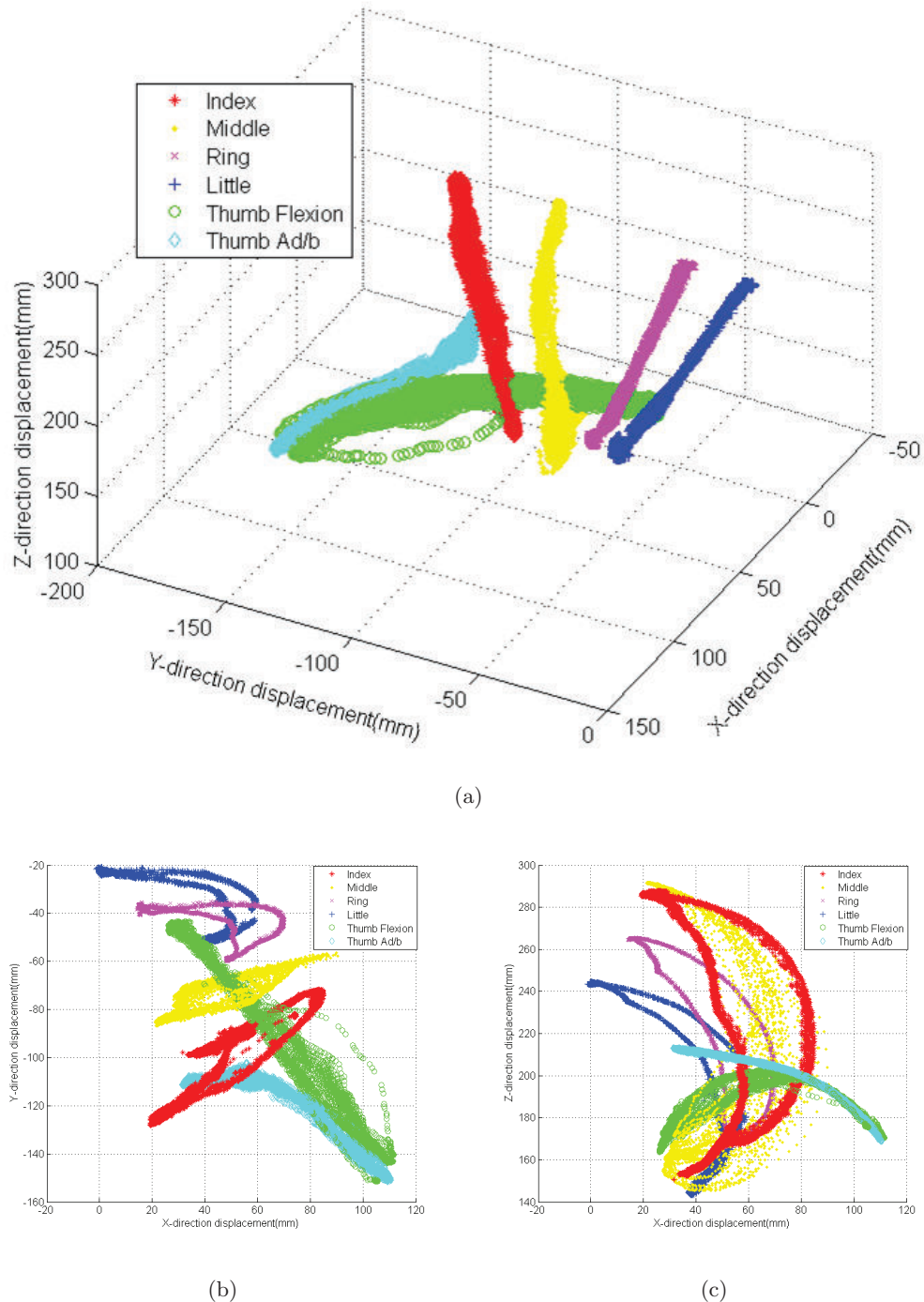


Figure 8.16: The trajectories of the fingertips during our robotic hand movement. *Top:* 3D scatter plot of fingertip trajectories. *Bottom left:* The trajectories of the fingertips projected onto the X-Y plane showing the thumb opposition and adduction/abduction motions. *Bottom right:* The trajectories of the fingertips projected onto the X-Z plane showing the workspaces of the fingers.

During the flexion/extension motions, all the fingertip trajectories of the four fingers exhibit very similar patterns, only vary in size due to their finger length difference. It is also very obvious to observe that the fingertips were moving closer to each other as they gradually bend into the palm. Compared to the fingers, the thumb followed a relatively consistent trajectory during both the flexion/extension and abduction/adduction motions. And therefore the entire workspaces of our robotic thumb are bounded by three parts, namely the palmar side of hand, the flexion/extension, and the abduction/adduction movements.

8.3.3 Object grasping and manipulation tasks

After the investigation of the fingertip forces and trajectories. In order to further evaluate the overall performance of our robotic hand, we conducted the grasping and manipulation experiments using 31 objects from the prioritized list [18]. The experiments were divided into three categories, namely picking up objects from a table, cooperative grasping between the human and robotic hands, and the demonstration of simple in-hand robotic manipulation tasks.

In the first part of the grasping experiment, human operator used his right hand to manually hold the forearm of our robotic hand, meanwhile, used his left hand to teleoperate the digits of the robotic hand via the data glove. This process is known as the tele-manipulation during which the movement of the robotic hand is both controlled and guided by the human operator's hand motion and visual feedback. Since the total weight of our robotic hand system is only 942 grams including the 10 Dynamixel servos, the human operator could easily maneuver the entire robotic hand to achieve suitable position and orientation before and during each grasping test.

As shown in Fig. 8.17, our robotic hand successfully picked up 29 out of 31 objects that were initially placed on the table. The weights of these objects range from less than 1g (a piece of tissue paper) to 518g (a bottled water). And their shapes and compliance are also varied. It is very interesting to observe how the complicated pre-grasp planning of many other robotic hands can be effortlessly tackled by the human operator in our experiment. This is because our data glove and robotic hand system can be seen as an effective portal



Figure 8.17: The list of objects used in the grasping tasks during tele-manipulation. *Note:* All the objects were initially placed on the table. The two objects enclosed in the dashed box are the ones that our robotic hand failed to grasp within four trials due to the flatness of the object, the slippery surface of the table, and limited vision at the grasping site.

that truthfully transfers the motor skills from the human brain to robotic hand's actions.

The biggest challenge during the tele-manipulation tasks was the occlusion of the grasping site, since the human operator could only see the back of the robotic hand with very limited visual clues about what occurs at the finger tips. As the objects getting smaller, flatter and lighter, the number of failed grasps were more commonly observed, particularly when the robotic hand were trying to grasp the almost empty toothpaste tube and the single coin (see Fig. 8.17). We argue that this problem could be solved by implementing

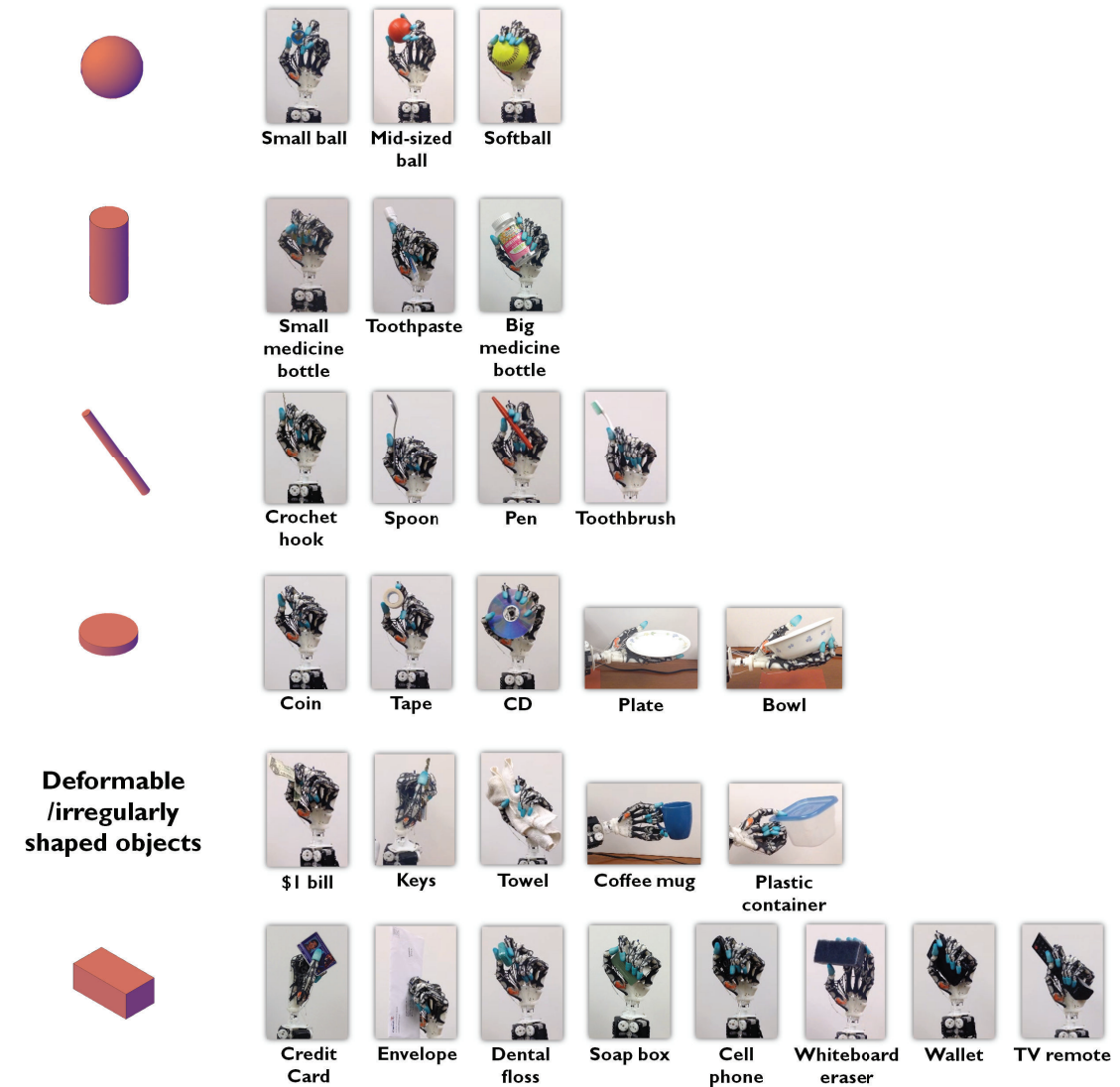


Figure 8.18: The classification of grasped objects based on their geometrical types.

overhead cameras and fingertip forces sensors to provide better visual and force feedback during each grasping task.

In addition, the compliance of our robotic hand also plays an important role during each grasping trial by allowing the fingers to naturally conform to the shapes of different objects. Due to this built-in compliance at each finger joint, our robotic hand could successfully

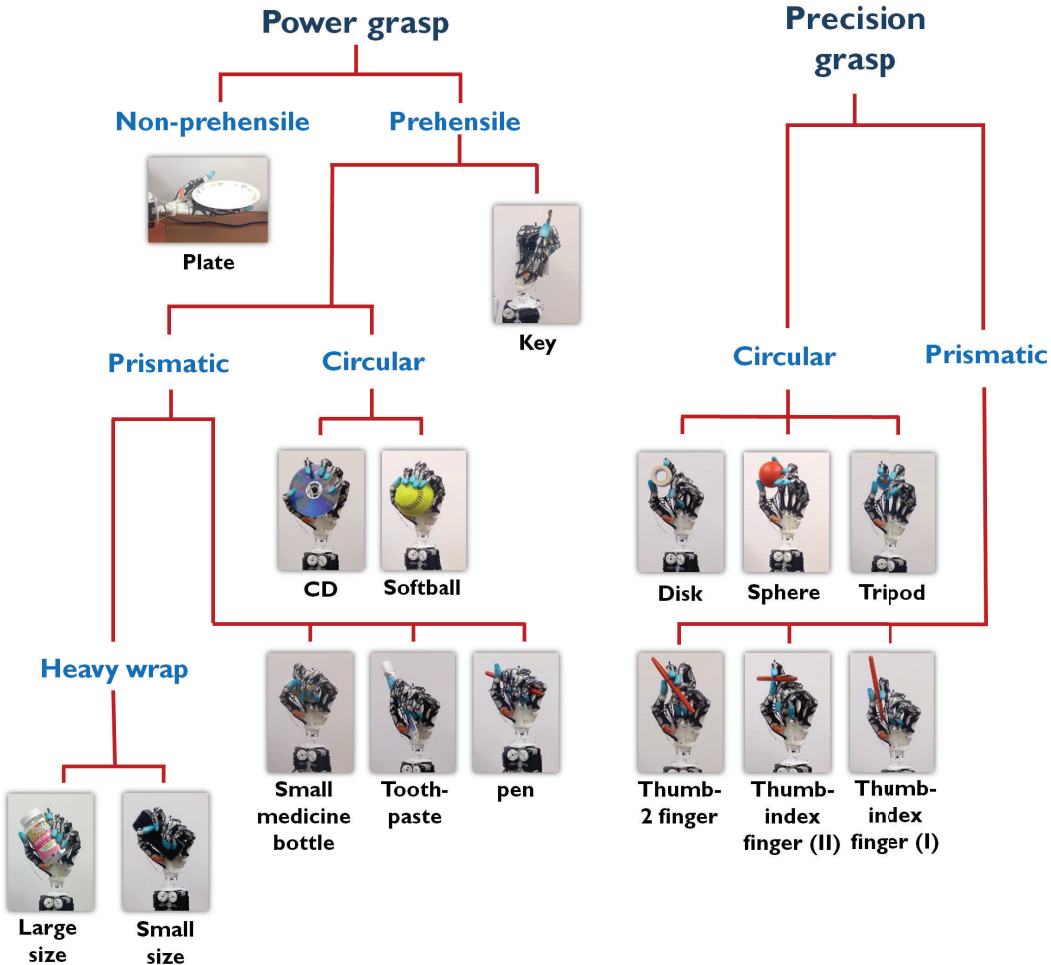


Figure 8.19: The hand taxonomy realized by our robotic hand (*Note:* see Fig.1.3 for comparison).

pick up a wide range of objects with very few number of grasping postures. From telemanipulation point of view, this also suggests that our robotic hand system (including the data glove) can effectively transfer the hand synergies [53] from the human operator to the robotic hand.

In the second part of the grasping tests, we kept the robotic hand in its upright position most of the times, and manually handed it different objects. This experiment can be seen

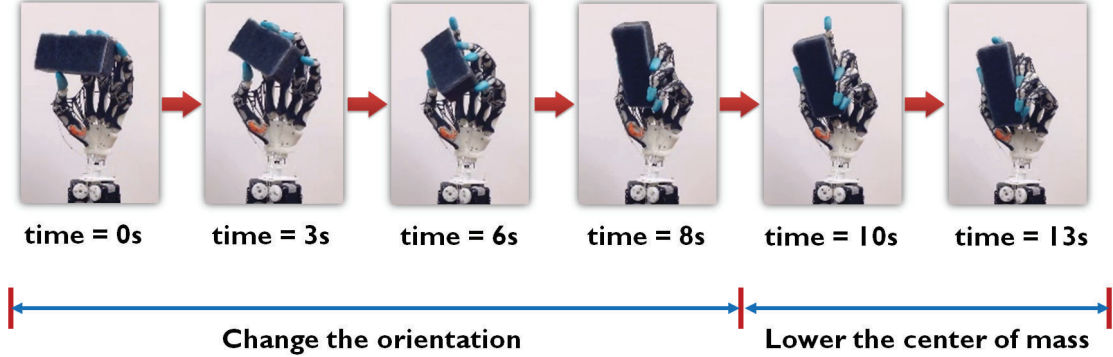


Figure 8.20: Snapshots of our robotic hand performing re-grasp of a whiteboard eraser.

as a series of cooperative grasping tasks between the human operator and the robotic hand during which the former could clearly monitor the status of the grasped object without the occlusion issue at the grasping site. As shown in Fig. 8.18, representative objects were further divided into six categories based on their geometrical types. Note that, without the problem of occlusion coin and cell phone can be successfully grasped by the robotic hand this time.

Differing from the few grasping postures observed in the first part of the tests, more variations in grasping postures were found in this second part of the experiments, especially the frequent occurrence of different precision grasps. In fact, the resulting grasps covered most of the grasping types defined by human hand taxonomy, except for the ones that require independent control of the ring and little fingers (see Fig. 8.19).

Last but not least, we tested the in-hand manipulation ability of our biomimetic robotic hand. As shown in Fig. 8.20, the orientation of a whiteboard eraser was first changed from being horizontal to vertical through a series of continuous hand motions in the first 8 seconds. And then the eraser was further pushed downwards by the coordination of the index finger and other gradually released digits during the last 5 seconds.

Chapter 9

CONCLUSION AND FUTURE WORK

In this thesis, we have detailed the design process that leads us to build the final prototype of our anthropomorphic robotic hand. The goal of this work is to answer the question of how to design an anthropomorphic robotic hand that highly mimics the salient biological features of the human hand with state-of-the-art technologies. In this chapter, first, we summarize the contributions of this work to different aspects of the anthropomorphic robotic hand design; Second, we discuss the potential investigation that can further help to improve the work.

9.1 Contributions

Recent advances in rapid prototyping technologies have offered many new approaches to efficiently manufacture complex parts at low cost. As reviewed in Chapter 1, the prosthesis nose, exhaust turbine, and small parts of the surgical robot can all be 3D-printed with different high resolution materials. However, the design of advanced anthropomorphic robotic hand has not taken advantages of these cutting-edge technologies to the extent we expected. We argue that this limitation originates from our intentional omission of the important anatomy of human hand in robotic design due to its alleged complexity. In medical research, those complexities are studied as valuable details that are crucial to hand surgeons when they create precise surgical plans, but in robotics, those seemingly excessive information of the hand anatomy often discourages researchers from initiating any attempt to replicate the human hand. Therefore, most of anthropomorphic robotic hands only mimic the most obvious features of the human hand such as the range of motion, the number of fingers, and the size of the human hand.

In Chapter 2, we translated the important anatomy of the human hand into the “language” that a roboticist can appreciate. Those salient features of the human hand include:

the structure of the extensor/flexor tendons, the mechanical advantages in gliding ligaments and bulging tendon sheaths during finger movements, the complex bone shapes that decide the joint type, last but not least, the ligaments that form different ROM at each joint. We argue that these anatomical features are essential for the functions of our human hand, and should be mimicked with necessary modification when being implemented into robotic hand design. We regard these interpretation and observations as the first mile stone of our contribution to the community of robotic hand research.

We then started our investigation of fabricating the artificial extensor hood in Chapter 3. The extensor hood of the human hand is a thin film of fibrous tissues. It works as a transmission system by converting muscle forces to joint torques during finger movements. After finding that biosolid behavior of the fibrous tissues could potentially be replaced by Spectra string made of high strength polyester fibers, we innovatively brought in the crochet technique into robotic hand design by creating the first crocheted extensor hood for the anatomically corrected testbed (ACT) hand. The finger of the ACT hand could move smoothly after being implemented with the artificial extensor hood. In order to validate the efficacy of this new method, a series of tensile tests were conducted to quantitatively compare mechanical properties between different crocheted structures used in the prototype. We regard this as the second contribution of our research, since its success encouraged us to explore more unconventional methods on the way of designing of our anthropomorphic robotic hand.

After prototyping the artificial extensor hood, we focused on the design of a highly biomimetic finger joint in the first half of Chapter 4. The finger joint is probably the smallest moving unit that facilitates the hand motions. However, it still could be further divided into several salient features that are hard to mimic simultaneously, including the unique shape of the bones at different joints, the joint capsule formed by fine ligaments, and the smooth cartilage that enables low-friction contact between two articulated surfaces. In order to tackle this design challenge, we prototyped an artificial MCP joint that is composed of a 3D-printed ball joint, crocheted ligaments, and a silicon rubber sleeve, which as a whole realizes the functions typical of a human finger joint. Parameter estimates of stiffness and damping for the artificial joint are found to be similar to those reported for the human joint.

And eventually a biomimetic finger was built based on the same concept of joint design. In the second half of Chapter 4, we connected the biomimetic finger with the pneumatic actuation system that consists of five air cylinders. The kinematics of the resulting system was modeled in MuJoCo, and tested with PID control based on real time tracking in tendon space. A series of experiments on stabilization and disturbance rejection suggested that our robotic finger system presents a highly non-linear dynamics. For the first time we proved that an artificial finger composed of highly biomimetic and compliant joints can be actuated *in vitro*.

In addition to the biomechanical features of the human hand, tactile perception is a very important but complex system composed of several different receptors in layers of our skin. Inspired by this multi-layered structure, we developed the artificial skin pads in Chapter 5. Different from the previous chapters, the resulting design of the artificial skin is not to fully replicate the human-level tactile sensing, but more towards equipping the anthropomorphic robotic hand with a generic force sensing system that is compatible to our existing design. Through experiments we found that the skin pad can better prevent slip from happening if its texture is designed to have small circled ridges. And tapered fingertip is an important feature for avoiding joint hyper-extension.

Independent of the artificial skin design, in Chapter 6 we proposed a low-cost fingertip that features a detachable fingertip made of 3D-printed materials and a cantilever mechanism that allows the detection of contact forces via three off-the-shelf, low-cost force sensors. To improve our design concept, optimization on the configuration of the fingertip sensor was performed under statistical analysis of the hysteresis performance. We demonstrated that our proposed design can measure the direction of contact forces in the radial plane of the fingertip sensor.

The first trial of designing and prototyping an 20-DOF anthropomorphic robotic hand with 3D-printing technology was detailed in Chapter 7. Our proposed artificial skin design was also integrated into the robotic hand. The resulting robotic hand is composed of 31 components, and can be manufactured in 24 hours.

Last but not least, based on the knowledge we learn from the above investigation, our proposed anthropomorphic robotic hand was eventually prototyped and tested in Chapter

8. To efficiently validate its design efficacy, a new type of data glove was also fabricated with six string potentiometers. The total weight of this robotic is less than 1 *kg* (942 grams), including the 10 Dynamixel servos used in actuation system. In order to further evaluate the performance of our robotic hand, the fingertip forces and trajectories were systematically tested. Our experimental results suggest that the elastic pulley system can transmit tendon forces to the fingertip more efficiently. We also found that this efficiency changes with different finger postures commonly used by the human hand during reach and grasp motions. The fingertips' trajectories clearly demonstrate the workspace of each finger and the thumb during flexion/extension motions. The highly repeatable motions of the coupled ring and little fingers also proved that the underactuation mechanism and built-in compliance of the fingers were successfully designed and implemented.

Our proposed anthropomorphic robotic hand incorporates all 15 human-like joints and can be teleoperated by using our custom-made data glove. As demonstrated by the object grasping and manipulation tasks, it can smoothly follow the human hand motions with one-to-one mapping in tendon space and easily form different hand postures that are originally categorized for human hand taxonomy. The success prototype of this robotic hand has the potential to bring the following immediate impacts:

- Current hand research has been heavily relying on the cadaver hands. Besides always being in short supply, the data collected from the cadaver hand are not repeatable. In contrast, our proposed anthropomorphic robotic hand can be personalized and 3D printed with the biomechanical information of any cadaver hand.
- Instead of performing thought experiments on the static hand models, medical students can use our proposed robotic hand, which is inherently similar to the human hand, to understand the important hand anatomy.
- The manufacturing cost of our robotic hand is under \$1500, including the actuation units. All the parts including the bone segments, artificial joints, and forearm brackets can be either 3D-printed or laser cut in 24 hours.

- Our design presents a paradigm shift from using mechanical hinge joints to artificial joint with crocheted ligaments, which broadens our scope of biomimetics and robotics. The unique artificial joint we proposed can be used in the design of other synovial joints of the human body with necessary modification.

9.2 Future work

In order to further improve the functionality of our proposed anthropomorphic robotic hand, we believed efforts towards the following directions will be worth investigating:

- As shown in Fig. 9.1, we have already prototyped a 3D-printed connector that is compatible with the existing elbow design of the WAM arm for the rotation of the forearm. However, our current version of the robotic hand does not include a biomimetic design of the wrist. It will be interesting to add a 2-DOF wrist in order to fully explore the dexterity of our anthropomorphic robotic hand. Meanwhile, the modification could be challenging since all the flexor/extensor tendons will route through an articulated wrist joint.
- Artificial skin and fingertip sensors will be incorporated into our current design of the robotic hand in order to equip it with tactile sensing ability. The required knowledge has been prepared in Chapter 5 and 6, and therefore the modification process should be straightforward.
- In terms of testing different control strategies to realize autonomous manipulation, we would like to first model the entire robotic hand system in MuJoCo environment, and then investigate the feasibility of using optimal control method to perform dexterous manipulation tasks.
- At the same time, we believe the teleoperation will still be an important alternative for easy control. To this end, we are going to improve the design of the data glove so that the volume of the string potentiometers can be further reduced to the size of a small key retractor.

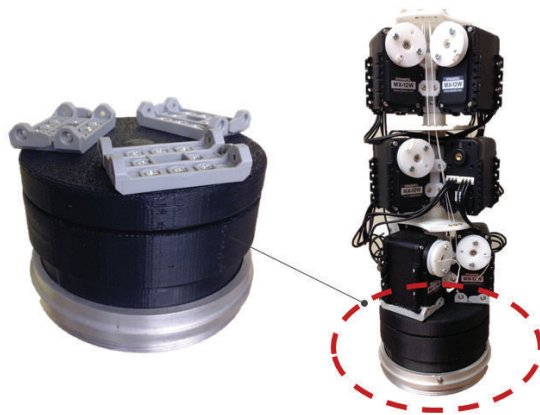


Figure 9.1: The 3D-printed connector that allows 1-DOF forearm rotation.

- We are also interested in developing different models of the anthropomorphic robotic hands so that each of them can have a focus on different applications, such as prothesis, space exploration, healthcare robotics, and etc.
- Our functional robotic hand system can serve as a working biological scaffold. For example, the bone of the anthropomorphic hands can be 3D printed with bio-compatible materials with localized porous structure; the ligament and tissue can be crocheted by using strings made of biodegradable carbon nanotube [131]. Living cells can therefore be cultivated onto the flexible and porous crocheted structure. Existing tissue engineering technologies of mass transfer, cell cultivation, and cell-migration can be used to cultivate the living ligaments on the robotic hand system.

BIBLIOGRAPHY

- [1] S. Jacobsen, E. Iversen, D. Knutti, R. Johnson, and K. Biggers, “Design of the Utah/M.I.T. dextrous hand,” vol. 3, pp. 1520–1532, Apr 1986.
- [2] C. Lovchik and M. Diftler, “The Robonaut hand: a dexterous robot hand for space,” in *Proceedings of the 1999 IEEE International Conference on Robotics and Automation.*, vol. 2, 1999, pp. 907–912.
- [3] T. Mouri, H. Kawasaki, Y. Keisuke, J. Takai, and S. Ito, “Anthropomorphic robot hand: Gifu hand III,” in *Proc. Int. Conf. ICCAS*, 2002.
- [4] Shadow Robot Company, “www.shadowrobot.com,” 2008.
- [5] I. Yamano and T. Maeno, “Five-fingered robot hand using ultrasonic motors and elastic elements,” in *Proceedings of the 2005 IEEE International Conference on Robotics and Automation.*, April 2005, pp. 2673–2678.
- [6] J. Ueda, Y. Ishida, M. Kondo, and T. Ogasawara, “Development of the NAIST-Hand with vision-based tactile fingertip sensor,” 2005.
- [7] M. C. Carrozza, G. Cappiello, S. Micera, B. B. Edin, L. Beccai, and C. Cipriani, “Design of a cybernetic hand for perception and action,” *Biol. Cybern.*, vol. 95, no. 6, pp. 629–644, 2006.
- [8] A. D. Deshpande, Z. Xu, M. J. V. Weghe, B. H. Brown, J. Ko, L. Y. Chang, D. D. Wilkinson, S. M. Bidic, and Y. Matsuoka, “Mechanisms of the Anatomically Correct Testbed Hand,” *IEEE/ASME Transactions on Mechatronics*, no. 99, pp. 1–13, 2011.
- [9] “Elumotion - elu-2 hand,” <http://www.elumotion.com/Elu2-hand.htm>, (Visited on 05/12/2015).
- [10] M. Grebenstein, M. Chalon, W. Friedl, S. Haddadin, T. Wimböck, G. Hirzinger, and R. Siegwart, “The hand of the dlr hand arm system: Designed for interaction,” *The International Journal of Robotics Research*, vol. 31, no. 13, pp. 1531–1555, 2012.
- [11] M. S. Johannes, J. D. Bigelow, J. M. Burck, S. D. Harshbarger, M. V. Kozlowski, and T. Van Doren, “An overview of the developmental process for the modular prosthetic limb,” *Johns Hopkins APL Technical Digest*, vol. 30, no. 3, pp. 207–216, 2011.

- [12] C. Melchiorri, G. Palli, G. Berselli, and G. Vassura, “Development of the ub hand iv: Overview of design solutions and enabling technologies,” *Robotics & Automation Magazine, IEEE*, vol. 20, no. 3, pp. 72–81, 2013.
- [13] Sandia National Laboratories, Sanddia hand, “www.sandia.gov,” 2013.
- [14] Z. Xu, V. Kumar, and E. Todorov, “A low-cost and modular, 20-DOF anthropomorphic robotic hand: Design, actuation and modeling,” in *IEEE-RAS International Conference on Humanoid Robots (Humanoids)*, 2013.
- [15] R. Deimel and O. Brock, “A novel type of compliant, underactuated robotic hand for dexterous grasping,” in *Proceedings of Robotics: Science and Systems*, Berkeley, USA, July 2014.
- [16] M. Cutkosky, “On grasp choice, grasp models, and the design of hands for manufacturing tasks,” *Robotics and Automation, IEEE Transactions on*, vol. 5, no. 3, pp. 269–279, Jun 1989.
- [17] A. M. Dollar, “Classifying Human Hand Use and the Activities of Daily Living,” *The Human Hand as an Inspiration for Robot Hand Development*, pp. 201–216, 2014.
- [18] Y. S. Choi, T. Deyle, T. Chen, J. Glass, and C. Kemp, “A list of household objects for robotic retrieval prioritized by people with als,” in *Rehabilitation Robotics, 2009. ICORR 2009. IEEE International Conference on*, June 2009, pp. 510–517.
- [19] “3ders.org - the future of prosthetics: 3d printed nose, ear and eye — 3d printer news & 3d printing news,” <http://www.3ders.org/articles/20131108-the-future-of-prosthetics-3d-printed-nose-ear-and-eye.html>, (Visited on 05/12/2015).
- [20] “Direct metal laser sintering (dmls) — solid concepts inc.” <https://www.solidconcepts.com/technologies/direct-metal-laser-sintering-dmls/>, (Visited on 05/12/2015).
- [21] “Sintering 3d parts from powdered metal is on the rise — micromanufacturing,” <http://www.micromanufacturing.com/content/sintering-3d-parts-powdered-metal-rise>, (Visited on 05/12/2015).
- [22] “Master forklift driver - drops coin into plastic bottle - youtube,” <https://www.youtube.com/watch?v=b1dvh1bREvA>, (Visited on 05/12/2015).
- [23] “da vinci surgical system - folding origami - youtube,” <https://www.youtube.com/watch?v=s6VZLkrIe1M>, (Visited on 05/12/2015).

- [24] Wikipedia, “Trapezium (bone) — wikipedia, the free encyclopedia,” 2014, [Online; accessed 12-May-2015]. [Online]. Available: [http://en.wikipedia.org/w/index.php?title=Trapezium_\(bone\)&oldid=634623814](http://en.wikipedia.org/w/index.php?title=Trapezium_(bone)&oldid=634623814)
- [25] “Crochet chart symbols — welcome to the craft yarn council,” http://www.craftyarn council.com/chart_crochet.html, (Visited on 05/12/2015).
- [26] J. Clavero, P. Golano, O. Farinas, X. Alomar, J. Monill, and M. Esplugas, “Extensor mechanism of the fingers: MR imaging-anatomic correlation,” *RADIOGRAPHICS*, vol. 23, no. 3, pp. 593–611, MAY-JUN 2003.
- [27] S. C. Bae, “Investigation of hand posture during reach and grasp for ergonomic applications,” Ph.D. dissertation, University of Michigan, 2011.
- [28] A. Miller and P. Allen, “Graspit! a versatile simulator for robotic grasping,” *Robotics Automation Magazine, IEEE*, vol. 11, no. 4, pp. 110 – 122, dec. 2004.
- [29] F. Rothling, R. Haschke, J. Steil, and H. Ritter, “Platform portable anthropomorphic grasping with the bielefeld 20-DOF Shadow and 9-DOF TUM hand,” in *IEEE/RSJ International Conference on Intelligent Robots and Systems*, 2007.
- [30] M. Grebenstein, M. Chalon, G. Hirzinger, and R. Siegwart, “Antagonistically driven finger design for the anthropomorphic DLR Hand Arm System,” in *2010 10th IEEE-RAS International Conference on Humanoid Robots (Humanoids)*, Dec. 2010, pp. 609 –616.
- [31] V. Bundhoo and E. Park, “Design of an artificial muscle actuated finger towards biomimetic prosthetic hands,” in *12th International Conference on Advanced Robotics, 2005. ICAR '05. Proceedings.*, July 2005, pp. 368 –375.
- [32] F. Lotti, P. Tiezzi, G. Vassura, L. Biagiotti, G. Palli, and C. Melchiorri, “Development of UB Hand 3: Early results,” in *Proceedings of the 2005 IEEE International Conference on Robotics and Automation*, April 2005, pp. 4488–4493.
- [33] Z. Xu, V. Kumar, Y. Matsuoka, and E. Todorov, “Design of an anthropomorphic robotic finger system with biomimetic artificial joints,” in *2012 4th IEEE RAS EMBS International Conference on Biomedical Robotics and Biomechatronics (BioRob)*, june 2012, pp. 568 –574.
- [34] H. D. Corporation, “Body-powered prosthetic hand,” September 2009, <http://www.hosmer.com/products/hooks/index.html>.
- [35] Motion Control, Inc., “The motion control ETD,” September 2009, <http://www.utaharm.com/>.

- [36] Liberating Technologies, Inc., “Upper extremity prosthetics,” September 2009, <http://www.liberatingtech.com>.
- [37] OttoBock HealthCare, Inc., “Cable-controlled arm prostheses,” September 2009, <http://www.ottobock.com>.
- [38] G. Bekey, R. R. Tomovic, and I. Zeljkovic, “Control architecture for the belgrade/USC hand,” *Dextrous Robot Hands.*, pp. 136–149, 1990.
- [39] A. Dollar and R. Howe, “Simple, robust autonomous grasping in unstructured environments,” in *2007 IEEE International Conference on Robotics and Automation*, April 2007, pp. 4693–4700.
- [40] Z. Xu, T. Deyle, and C. Kemp, “1000 Trials: An empirically validated end effector that robustly grasps objects from the floor,” in *Proceedings of the 2009 IEEE International Conference on Robotics and Automation.*, May 2009, pp. 2160–2167.
- [41] W. Townsend, “The Barrett hand grasper - programmably flexible part handling and assemble,” *The International Journal of Industrial Robot*, vol. 27, no. 3, pp. 181 – 188, 2000.
- [42] Touch Bionics Inc., “www.touchbionics.com,” 2009.
- [43] P. J. Kyberd, C. Light, P. H. Chappell, J. M. Nightingale, D. Whatley, and M. Evans, “The design of anthropomorphic prosthetic hands: A study of the southampton hand,” *Robotica*, vol. 19, no. 6, pp. 593–600, 2001.
- [44] T. Senoo, Y. Yamakawa, S. Mizusawa, A. Namiki, M. Ishikawa, and M. Shimojo, “Skillful manipulation based on high-speed sensory-motor fusion,” in *Proceedings of the 2009 IEEE International Conference on Robotics and Automation.*, May 2009, pp. 1611–1612.
- [45] J. K. Salisbury and J. J. Craig, “Articulated Hands: Force Control and Kinematic Issues,” *The International Journal of Robotics Research*, vol. 1, no. 1, pp. 4–17, 1982.
- [46] DEKA Research and Development Corp., “www.dekaresearch.com,” 2008.
- [47] J. Butterfass, M. Fischer, M. Grebenstein, S. Haidacher, and G. Hirzinger, “Design and experiences with DLR hand II,” vol. 15, 2004, pp. 105–110.
- [48] Aesthetic Prosthetics, Inc., “Aesthetic hand introduction,” September 2009, <http://www.aestheticprosthetics.com>.

- [49] M. Nicolelis, “Actions from thoughts,” *NATURE*, vol. 409, no. 6818, pp. 403–407, JAN 18 2001.
- [50] M. Velliste, S. Perel, M. C. Spalding, A. S. Whitford, and A. B. Schwartz, “Cortical control of a prosthetic arm for self-feeding,” *Nature*, vol. 453, no. 7198, pp. 1098–1101, June 2008.
- [51] T. Kuiken, G. Dumanian, R. Lipschutz, L. Miller, and K. Stubblefield, “The use of targeted muscle reinnervation for improved myoelectric prosthesis control in a bilateral shoulder disarticulation amputee,” *Prosthetics and Orthotics International*, vol. 28, no. 3, pp. 245–253, DEC 2004.
- [52] Barrett Technology, Inc., “Wam arm specification,” September 2009, <http://www.barrett.com/robot/products-arm-specifications.htm>.
- [53] E. Todorov and Z. Ghahramani, “Analysis of the synergies underlying complex hand manipulation,” in *26th Annual International Conference of the IEEE Engineering in Medicine and Biology Society (IEMBS)*, vol. 2, 2004.
- [54] W. Penfield and E. Boldrey, “Somatic motor and sensory representation in the cerebral cortex of man as studied by electrical stimulation.” *Brain: A journal of neurology*, 1937.
- [55] “blacksmith’s workshop — flickr - photo sharing!” <https://www.flickr.com/photos/eorus/11104047705>, (Visited on 05/12/2015).
- [56] “Legacy products — stratasys,” <http://www.stratasys.com/customer-support/legacy-products>, (Visited on 05/13/2015).
- [57] “1100 series laser engraver / cutter,” <http://www.legacylasers.com/1100-Series-Laser-Engraver-Cutter.php>, (Visited on 05/13/2015).
- [58] “Nextengine 3d laser scanner,” <http://www.nextengine.com/>, (Visited on 05/13/2015).
- [59] B. Hannaford, J. M. Winters, C.-P. Chou, and P.-H. Marbot, “The anthroform biorobotic arm: a system for the study of spinal circuits,” *Annals of biomedical engineering*, vol. 23, no. 4, pp. 399–408, 1995.
- [60] I. Mordatch, Z. Popović, and E. Todorov, “Contact-invariant optimization for hand manipulation,” in *Proceedings of the ACM SIGGRAPH/Eurographics symposium on computer animation*. Eurographics Association, 2012, pp. 137–144.

- [61] Y. Ye and C. K. Liu, “Synthesis of detailed hand manipulations using contact sampling,” *ACM Transactions on Graphics (TOG)*, vol. 31, no. 4, p. 41, 2012.
- [62] T. A. Kuiken, L. A. Miller, R. D. Lipschutz, B. A. Lock, K. Stubblefield, P. D. Marasco, P. Zhou, and G. A. Dumanian, “Targeted reinnervation for enhanced prosthetic arm function in a woman with a proximal amputation: a case study,” *The Lancet*, vol. 369, no. 9559, pp. 371–380, 2007.
- [63] J. L. Collinger, B. Wodlinger, J. E. Downey, W. Wang, E. C. Tyler-Kabara, D. J. Weber, A. J. McMorland, M. Velliste, M. L. Boninger, and A. B. Schwartz, “High-performance neuroprosthetic control by an individual with tetraplegia,” *The Lancet*, vol. 381, no. 9866, pp. 557–564, 2013.
- [64] V. S. Polikov, P. A. Tresco, and W. M. Reichert, “Response of brain tissue to chronically implanted neural electrodes,” *Journal of neuroscience methods*, vol. 148, no. 1, pp. 1–18, 2005.
- [65] J. L. Skousen, M. J. Bridge, and P. A. Tresco, “A strategy to passively reduce neuroinflammation surrounding devices implanted chronically in brain tissue by manipulating device surface permeability,” *Biomaterials*, vol. 36, pp. 33–43, 2015.
- [66] D. Lee, A. Franchi, P. Giordano, H. I. Son, and H. Bulthoff, “Haptic teleoperation of multiple unmanned aerial vehicles over the internet,” in *Robotics and Automation (ICRA), 2011 IEEE International Conference on*, May 2011, pp. 1341–1347.
- [67] W. P. Cooney and E. Chao, “Biomechanical analysis of static forces in the thumb during hand function,” *The Journal of Bone & Joint Surgery*, vol. 59, no. 1, pp. 27–36, 1977.
- [68] S. W. Lee, H. Chen, J. D. Towles, and D. G. Kamper, “Effect of finger posture on the tendon force distribution within the finger extensor mechanism,” *Journal of biomechanical engineering*, vol. 130, no. 5, p. 051014, 2008.
- [69] P. W. Brand and M. H. Anne, *Clinical Mechanics of the Hand*. St. Louis: Mosby-Year Book, Inc., 1993.
- [70] S. Dalley, T. Wiste, T. Withrow, and M. Goldfarb, “Design of a multifunctional anthropomorphic prosthetic hand with extrinsic actuation,” *IEEE/ASME Transactions on Mechatronics*, vol. 14, no. 6, pp. 699–706, dec. 2009.
- [71] M. Carrozza, B. Massa, S. Micera, R. Lazzarini, M. Zecca, and P. Dario, “The development of a novel prosthetic hand-ongoing research and preliminary results,” *IEEE/ASME Transactions on Mechatronics*, vol. 7, no. 2, pp. 108–114, jun. 2002.

- [72] M. C. Carrozza, C. Suppo, F. Sebastiani, B. Massa, F. Vecchi, R. Lazzarini, M. R. Cutkosky, and P. Dario, “The spring hand: development of a self-adaptive prosthesis for restoring natural grasping,” *Autonomous Robots*, vol. 16, no. 2, pp. 125–141, 2004.
- [73] H. Kawasaki, T. Komatsu, and K. Uchiyama, “Dexterous anthropomorphic robot hand with distributed tactile sensor: Gifu hand II,” *IEEE/ASME Transactions on Mechatronics*, vol. 7, no. 3, pp. 296 – 303, sep. 2002.
- [74] A. Dollar and R. Howe, “A robust compliant grasper via shape deposition manufacturing,” *IEEE/ASME Transactions on Mechatronics*, vol. 11, no. 2, pp. 154 –161, april 2006.
- [75] D. Wilkinson, M. Vande Weghe, and Y. Matsuoka, “An extensor mechanism for an anatomical robotic hand,” in *Proceedings of the 2003 IEEE International Conference on Robotics and Automation.*, 2003.
- [76] M. Vande Weghe, M. Rogers, M. Weissert, and Y. Matsuoka, “The ACT hand: Design of the skeletal structure,” in *Proceedings of the 2004 IEEE International Conference on Robotics and Automation.*, 2004.
- [77] L. Y. Chang and Y. Matsuoka, “A kinematic thumb model for the ACT hand,” in *Proceedings of the 2006 IEEE International Conference on Robotics and Automation.*, 2006.
- [78] Z. Xu, E. Todorov, B. Dallon, and Y. Matsuoka, “Design and analysis of an artificial finger joint for anthropomorphic robotic hands,” in *2011 IEEE International Conference on Robotics and Automation (ICRA)*, 2011.
- [79] J. R. Ralphs and M. Benjamin, “The joint capsule: structure, composition, ageing and disease,” *Journal of Anatomy*, vol. 3, pp. 503–509, 1994.
- [80] T. Joyce, “Currently available metacarpophalangeal prostheses: their designs and prospective considerations,” *EXPERT REVIEW OF MEDICAL DEVICES*, vol. 1, no. 2, pp. 193–204, NOV 2004.
- [81] D. Beevers and B. Seedhom, “Metacarpophalangeal joint prostheses: A review of the clinical results of past and current designs,” *The Journal of Hand Surgery: Journal of the British Society for Surgery of the Hand*, vol. 20, no. 2, pp. 125 – 136, 1995.
- [82] D. Henderson and D. Taimina, “Crocheting the hyperbolic plane,” *MATHEMATICAL INTELLIGENCER*, vol. 23, no. 2, pp. 17–28, SPR 2001.
- [83] F. H. Netter, *Atlas of Human Anatomy*, 2nd ed. Teterboro, New Jersey: Icon Learning Systems, 1997.

- [84] D. G. Kamper, T. G. Hornby, and W. Z. Rymer, “Extrinsic flexor muscles generate concurrent flexion of all three finger joints,” *Journal of Biomechanics*, vol. 35, no. 12, pp. 1581 – 1589, 2002.
- [85] E. Todorov, T. Erez, and Y. Tassa, “Mujoco: a physics engine for model-based control,” *Under Review*.
- [86] E. R. Kandel, J. H. Schwartz, and T. M. Jessell, *Principles of Neural Science*, 4th ed. McGraw-Hill Medical, July 2000.
- [87] K. Shimoga, “A survey of perceptual feedback issues in dexterous telemanipulation. I. finger force feedback, IEEE,” *Virtual Reality Annual International Symposium*, pp. 263–270, Sep. 1993.
- [88] M. Shimojo, M. Ishikawa, and K. Kanaya, “A flexible high resolution tactile imager with video signal output,” in *Proceedings of the 1991 IEEE International Conference on Robotics and Automation*, 1991.
- [89] M. Inaba, Y. Hoshino, K. Nagasaka, T. Ninomiya, S. Kagami, and H. Inoue, “A full-body tactile sensor suit using electrically conductive fabric and strings,” in *Proceedings of the 1996 IEEE/RSJ International Conference on Intelligent Robots and Systems*, 1996.
- [90] R. Kageyama, S. Kagami, M. Inaba, and H. Inoue, “Development of soft and distributed tactile sensors and the application to a humanoid robot,” in *1999 IEEE International Conference on Systems, Man, and Cybernetics*, 1999.
- [91] H. Maekawa, K. Tanie, K. Komoriya, M. Kaneko, C. Horiguchi, and T. Sugawara, “Development of a finger-shaped tactile sensor and its evaluation by active touch,” in *Proceedings of the 1992 IEEE International Conference on Robotics and Automation*, 1992.
- [92] H. Shinoda and S. Ando, “Ultrasonic emission tactile sensor for contact localization and characterization,” in *Proceedings of the 1994 IEEE International Conference on Robotics and Automation*, 1994.
- [93] K. Motoo, T. Fukuda, F. Arai, and T. Matsuno, “Piezoelectric vibration-type tactile sensor with wide measurement range using elasticity and viscosity change,” in *2006 IEEE/RSJ International Conference on Intelligent Robots and Systems*, 2006.
- [94] D. Johnston, P. Zhang, J. Hollerbach, Z. Hollerbach, and S. Jacobsen, “A full tactile sensing suite for dextrous robot hands and use in contact force control,” *IEEE International Conference on Robotics and Automation*, 1996.

- [95] K. Hosoda, Y. Tada, and M. Asada, “Anthropomorphic robotic soft fingertip with randomly distributed receptors,” *Robotics and Autonomous Systems*, 2006.
- [96] N. Wettels, J. Santos, Veronica, S. Johansson, Roland, and E. Loeb, Gerald, “Biomimetic tactile sensor array,” *Advanced Robotics*, vol. 22, no. 8, pp. 829–849, 2008.
- [97] L.-T. Jiang and J. R. Smith, “Seashell effect pretouch sensing for robotic grasping,” in *Robotics and Automation (ICRA), 2012 IEEE International Conference on*. IEEE, 2012, pp. 2851–2858.
- [98] P. Michelman, “Precision object manipulation with a multifingered robot hand,” *IEEE Transactions on Robotics and Automation*, vol. 14, no. 1, pp. 105 –113, Feb. 1998.
- [99] C. Baysal and A. Erkmen, “Preshape induced grasp controller for dexterous manipulation with a multifingered robot hand,” in *Proceedings of the 2004 IEEE International Conference on Mechatronics*, 2004.
- [100] Z. Xu, B. Dallon, and Y. Matsuoka, “Design of artificial skin with integrated tactile sensors for anthropomorphic robotic hands,” in *2011 IEEE International Conference on Robotics and Biomimetics (ROBIO)*, 2011.
- [101] J. J. Hebert, “Hand size counts in safe handgun use,” *Ergonomics in Design*, vol. 8, 2000.
- [102] S. Kumar, *Biomechanics in Ergonomics, Second Edition*. Boca Raton, FL, USA: CRC Press, Inc., 2007.
- [103] J. Dargahi and S. Najarian, “Advances in tactile sensors design / manufacturing and its impact on robotics applications - a review,” *Industrial Robot: An International Journal*, vol. 32, 2005.
- [104] A. Caffaz, G. Cannata, G. Panin, and E. Massucco, “The DIST-hand, an anthropomorphic, fully sensorized dextrous gripper,” in *First IEEE-RAS Int. Conf. on Humanoid Robots*, 2000.
- [105] K. Nakamura, “Tactile sensing device instantaneously evaluating friction coefficients,” in *DIGEST OF THE SENSOR SYMPOSIUM, 18TH*, 2001.
- [106] D. Goeger, N. Ecker, and H. Woern, “Tactile sensor and algorithm to detect slip in robot grasping processes,” in *IEEE International Conference on Robotics and Biomimetics.*, 2009.

- [107] D. Yamada, T. Maeno, and Y. Yamada, “Artificial finger skin having ridges and distributed tactile sensors used for grasp force control,” in *Proceeding of the 2001 IEEE/RSJ International Conference on Intelligent Robots and Systems.*, 2001.
- [108] D. Damian, H. Martinez, K. Dermitzakis, A. Hernandez-Arieta, and R. Pfeifer, “Artificial ridged skin for slippage speed detection in prosthetic hand applications,” in *2010 IEEE/RSJ International Conference on Intelligent Robots and Systems (IROS)*, 2010.
- [109] M. Burstedt, B. Edin, and R. Johansson, “Coordination of fingertip forces during human manipulation can emerge from independent neural networks controlling each engaged digit,” *EXPERIMENTAL BRAIN RESEARCH*, vol. 117, no. 1, pp. 67–79, 1997.
- [110] J. R. Flanagan, R. S. Johansson, M. K. O. Burstedt, and M. K. O. Burstedt, “Control of fingertip forces in multidigit manipulation,” *Journal of Neurophysiology*, vol. 81, pp. 1706–1717, 1999.
- [111] M. Zinn, O. Khatib, B. Roth, and J. Salisbury, “Playing it safe [human-friendly robots],” *Robotics Automation Magazine, IEEE*, vol. 11, no. 2, pp. 12 – 21, 2004.
- [112] R. Dahiya, G. Metta, M. Valle, and G. Sandini, “Tactile sensing – from humans to humanoids,” *IEEE Transactions on Robotics*, vol. 26, no. 1, pp. 1–20, 2009.
- [113] A. Schmitz, M. Maggiali, L. Natale, B. Bonino, and G. Metta, “A tactile sensor for the fingertips of the humanoid robot icub,” in *IEEE/RSJ International Conference on Intelligent Robots and Systems (IROS)*, 2010, pp. 2212–2217.
- [114] N. Wettels and G. Loeb, “Haptic feature extraction from a biomimetic tactile sensor: Force, contact location and curvature,” in *IEEE International Conference on Robotics and Biomimetics (ROBIO)*, 2011, pp. 2471–2478.
- [115] B. Edin, L. Beccai, L. Ascari, S. Roccella, J.-J. Cabibihan, and M. Carrozza, “Bio-inspired approach for the design and characterization of a tactile sensory system for a cybernetic prosthetic hand,” in *IEEE International Conference on Robotics and Automation(ICRA)*, 2006, pp. 1354–1358.
- [116] T. B. Martin, R. Ambrose, M. Diftler, J. Platt, R., and M. J. Butzer, “Tactile gloves for autonomous grasping with the nasa/darpa robonaut,” in *IEEE International Conference on Robotics and Automation (ICRA)*, vol. 2, 2004,.
- [117] R. R. Ma, L. U. Odhner, and A. M. Dollar, “A modular,open-source 3d printed underactuated hand,” in *IEEE International Conference on Robotics and Automation(ICRA)*, 2013.

- [118] B. Winstone, G. Griffiths, C. Melhuish, T. Pipe, and J. Rossiter, “TACTIP-tactile fingertip device, challenges in reduction of size to ready for robot hand integration,” in *2012 IEEE International Conference on Robotics and Biomimetics (ROBIO)*, 2012.
- [119] Z. Xu, S. Kolev, and E. Todorov, “Design, optimization, calibration, and a case study of a 3d-printed, low-cost fingertip sensor for robotic manipulation,” in *Robotics and Automation (ICRA), 2014 IEEE International Conference on*. IEEE, 2014, pp. 2749–2756.
- [120] I. Honeywell International, “Honeywell fss015wnsx specification,” 2013.
- [121] Y.-C. Huang, Y.-H. Chang, and W.-S. Chang, “A new structure for a fingertip force sensor,” *IEEE/ASME Transactions on Mechatronics*, vol. 4, no. 3, pp. 293–300, 1999.
- [122] A. Hollinger and M. M. Wanderley, “Evaluation of commercial force-sensing resistors,” in *NIME06, Paris, France*, 2006.
- [123] V. Kumar, Z. Xu, and E. Todorov, “Fast, strong and compliant pneumatic actuation for dexterous tendon-driven hands,” in *2013 IEEE International Conference on Robotics and Automation*, 2013.
- [124] “:::ROBOTIS:::,” http://www.robotis.com/xe/dynamixel_en, (Visited on 05/27/2015).
- [125] “String potentiometer complete kit (am-2674),” <http://www.andymark.com/product-p/am-2674.htm>, (Visited on 05/12/2015).
- [126] K. Kursa, E. Diao, L. Lattanza, and D. Rempel, “In vivo forces generated by finger flexor muscles do not depend on the rate of fingertip loading during an isometric task,” *Journal of biomechanics*, vol. 38, no. 11, pp. 2288–2293, 2005.
- [127] F. Schuind, M. Garcia-Elias, W. P. Cooney, and K.-N. An, “Flexor tendon forces: in vivo measurements,” *The Journal of hand surgery*, vol. 17, no. 2, pp. 291–298, 1992.
- [128] F. J. Valero-Cuevas, F. E. Zajac, and C. G. Burgar, “Large index-fingertip forces are produced by subject-independent patterns of muscle excitation,” *Journal of biomechanics*, vol. 31, no. 8, pp. 693–703, 1998.
- [129] S. Venema and B. Hannaford, “A probabilistic representation of human workspace for use in the design of human interface mechanisms,” *Mechatronics, IEEE/ASME Transactions on*, vol. 6, no. 3, pp. 286–294, Sep 2001.
- [130] D. G. Kamper, E. G. Cruz, and M. P. Siegel, “Stereotypical fingertip trajectories during grasp,” *Journal of neurophysiology*, vol. 90, no. 6, pp. 3702–3710, 2003.

- [131] B. M. Baker, R. P. Shah, A. M. Silverstein, J. L. Esterhai, J. A. Burdick, and R. L. Mauck, “Sacrificial nanofibrous composites provide instruction without impediment and enable functional tissue formation,” *Proceedings of the National Academy of Sciences*, vol. 109, no. 35, pp. 14 176–14 181, 2012.